General Disclaimer

One or more of the Following Statements may affect this Document

- This document has been reproduced from the best copy furnished by the organizational source. It is being released in the interest of making available as much information as possible.

- This document may contain data, which exceeds the sheet parameters. It was furnished in this condition by the organizational source and is the best copy available.

- This document may contain tone-on-tone or color graphs, charts and/or pictures, which have been reproduced in black and white.

- This document is paginated as submitted by the original source.

- Portions of this document are not fully legible due to the historical nature of some of the material. However, it is the best reproduction available from the original submission.

Produced by the NASA Center for Aerospace Information (CASI)

Final Report:

STUDY OF A SCANNING CELESTIAL ATTITUDE DETERMINATION SYSTEM (SCADS) FOR A SYNCHRONOUS SATELLITE

Contract No. NAS 5-10372
Control Data Project No. 9575

February 28, 1968

Prepared for:

National Aeronautics and Space Administration
Goddard Space Flight Center
Greenbelt, Maryland

Aerospace Research Department
CONTROL DATA CORPORATION
8100 34th Avenue South
Minneapolis, Minnesota 55440

RD 2006

N 69-19335
(ACCESSION NUMBER)
326
(PAGES)
CR 100149
(NASA CR OR TMX OR AD NUMBER)
(THRU)
1
(CODE)
21
(CATEGORY)
FACILITY FORM 602

Final Report:

STUDY OF A SCANNING CELESTIAL ATTITUDE DETERMINATION SYSTEM (SCADS) FOR A SYNCHRONOUS SATELLITE

Contract No. NAS 5-10372
Control Data Project No. 9575

February 28, 1968

Prepared for:

National Aeronautics and Space Administration
Goddard Space Flight Center
Greenbelt, Maryland

Aerospace Research Department
CONTROL DATA CORPORATION
8100 34th Avenue South
Minneapolis, Minnesota 55440

RD 2006

PRECEDING PAGE BLANK NOT FILMED.

ABSTRACT

A detailed feasibility and preliminary design study for the application of a Scanning Celestial Attitude Determination System (SCADS) to a synchronous satellite is presented. Two operational modes are considered--a spin stabilized phase in which the synchronous orbit is established from an inclined transfer ellipse and a three-axis controlled phase in which the synchronous spacecraft is pointed along directions close to local vertical. The mission profile for the ATS F & G program is used as reference. Accuracy requirements in the spinning mode are $0^{\circ}.1$ in pointing and 0.03 percent in spin period. For the three axis mode a precision of $0^{\circ}.01$ in each axis--yaw, pitch, and roll--is desired.

Three SCADS sensor configurations are investigated--a spin mode sensor in which the scan is provided by the vehicle motion, a three-axis mode sensor in which the scan is provided by a synchronous motor, and a dual mode sensor which combines both capabilities in one instrument. With minimum restrictions on the launch window to avoid interference from the sun and moon, it is found that all three configurations are feasible and suitable SCADS designs are evolved. However, it is found that the combination of the two single-purpose sensors gives superior accuracy performance and higher reliability than the dual mode sensor. The approach employing separate SCADS sensors for the two phases is therefore recommended for the ATS F & G missions.

PRECEDING PAGE BLANK NOT FILMED.

FOREWORD

This report was prepared by Control Data Corporation, Research Division, for the National Aeronautics and Space Administration, Goddard Space Flight Center, under Contract No. NAS 5-10372.

The Control Data Project Engineer was A. E. LaBonte. Other contributing authors of this report were C. B. Grosch, D. F. Nickel, R. W. Peterson, and B. D. Vannelli.

Control Data Corporation would particularly like to acknowledge the technical guidance provided by the National Aeronautics and Space Administration Project Technical Officer, Irving B. Loven and by Dr. James Gatlin representing the NASA ATS F & G Program.

PRECEDING PAGE BLANK NOT FILMED.

TABLE OF CONTENTS

TITLE PAGE		i
ABSTRACT		iii
FOREWORD		v
TABLE OF CONTENTS		vii
LIST OF FIGURES		xi
LIST OF TABLES		xv
I.	INTRODUCTION	1
	A. The SCADS Concept	1
	1. Star Transit Measurements	1
	2. Star Identification	4
	a. Determination of a Mean Period	5
	b. Scan-to-Scan Correlation	8
	c. Star Identification by Azimuth Differences	9
	3. Attitude Determination	10
	B. Orbital Configurations: SCADS Operational Requirements	21
	1. Transfer Ellipse Mode, Spin Stabilized	21
	2. Synchronous Circular Orbit, Spin Stabilized	21
	3. Synchronous Circular Orbit, Three Axis Controlled	24
	C. The Study	26
II.	SCADS CELESTIAL ENVIRONMENT ANALYSES	27
	A. SCADS Operation in the Presence of the Sun, Earth, and Moon	27
	1. The Earth	29
	2. The Sun	33
	3. The Moon	39
	4. Bright Object Interference in the Three Axis Controlled Mode	45
	B. SCADS Stellar Target Availability	49
	1. Possible Scan Axis Directions: SCADS/ATS F&G	51
	2. Stellar Target Distributions - Spin Mode SCADS Sensor	52
	3. Stellar Target Distributions - Dual Mode SCADS Sensor	70
	4. Stellar Target Distributions - Three Axis Controlled Mode SCADS Sensor	82

III. SCADS PARAMETER SELECTION 89

A. Parameters Related to Celestial Constraints 89

1. Bright Object Shield 90
2. SCADS Geometric Parameters: Spin Mode Sensor 93
3. SCADS Geometric Parameters: Dual Mode Sensor 102

B. Parameters Related to Star Detection and Identification 109

1. Slit Configuration 109
2. Photodetector Performance 112
3. Signal Filter 122
4. Optical Aperture 143

C. Parameters Related to Measurement Accuracy 151

1. Scan Period 152
2. Blur Spot Size and Slit Width 153
3. Time Measurement Resolution and Clock Stability 157

IV. SCADS SENSOR DESIGNS 161

A. Spin Stabilized Mode 161

1. Optical Sensor Head 161
2. Electronic Signal Processor 165

B. Three Axis Controlled Mode 185

1. Optical Sensor Head 185
2. Electronic Signal Processor 189

C. Dual Mode 192

1. Optical Sensor Head 192
2. Electronic Signal Processor 195

D. Spinning Mode; Possible Modifications of the ATS-C Design 197

1. Optical Sensor Head 197
2. Electronic Signal Processor 198

E. Sensor Volume, Weight, and Power Estimates 201

1. Spinning Mode Sensor Estimates 203
2. Three Axis Controlled Mode Estimates 205
3. Dual Mode Estimates 207

V. SCADS PERFORMANCE ANALYSES 209

A. Star Transit Detection 209

B. Attitude Determination Error Analysis 215

1. Method of Determination of Errors 216
2. Spin Mode Sensor Errors 217
3. Dual Mode Sensor Errors 219
4. Three Axis Mode Sensor Errors 222

C. Radiation Susceptibility 225

1. Optically Bright Objects 225
   a. Photomultiplier Overload Protection 225
   b. Radiation Heating Protection 227
2. High Energy Radiation 229
   a. Photocathode Shield 230
   b. Protection of the Optics 235

D. Reliability 236

VI. CONDITIONS REQUIRED FOR OPTIMAL SCADS OPERATION 239

A. Spacecraft and Mission Constraints 239

B. Suggested Spacecraft Location of SCADS 240

C. SCADS Information Bandwidth Requirements 241

VII. RECOMMENDED SCADS DESIGN 243

REFERENCES 251

GLOSSARY OF PRIMARY SCADS SYMBOLS 253

APPENDIX A: Attitude Determination for the Three Axis Controlled Phase of ATS F&G 257

APPENDIX B: Data Sheets for the EMR-541N and EMR-543N Photomultipliers 265

APPENDIX C: Photomultiplier Noise Induced by Exposure to the Van Allen Belts 277

APPENDIX D: Radiation Damage to Circuitry 305

PRECEDING PAGE BLANK NOT FILMED.

LIST OF FIGURES

Figure	1	Schematic Representation of SCADS	3
	2	Computed and Measured Azimuths for Star Identification	15
	3	Iterative Star Identification Scheme	16
	4	Relation Between the Slit and a Star at the Instant of Transit	18
	5	Orbital Configurations	23
	6	Nominal SCADS Scan Axis Directions	25
	7	SCADS Annular Scan Pattern	28
	8	The Earth from the Transfer Ellipse: $\delta_{spin} = -20.^{\circ}7$	31
	9	The Earth from the Transfer Ellipse: $\delta_{spin} = -23^{\circ}$	32
	10	Principal Angles for the Spinning Mode SCADS Sensor	35
	11	SCADS Solar Launch Window: $\delta_{spin} = -20.^{\circ}7$	37
	12	SCADS Solar Launch Window: $\delta_{spin} = -23^{\circ}$	38
	13	Combined Solar-Lunar Launch Window for Day-Mode Insertion	43
	14	Combined Solar-Lunar Launch Window for Night-Mode Insertion	44
	15	A Priori Limiting Stellar Magnitude	50
	16	Possible SCADS Scan Axis Pointing Directions	53
	17	Spin Mode Sensor Second, Third, Fourth, and Fifth Brightest Stars in the Field of View: $\delta_{scan} = -10^{\circ}$	55
	18	Spin Mode Sensor Second, Third, Fourth, and Fifth Brightest Stars in the Field of View: $\delta_{scan} = 0^{\delta}$	56
	19	Spin Mode Sensor Second, Third, Fourth, and Fifth Brightest Stars in the Field of View: $\delta_{scan} = 10^{\circ}$	57
	20	Spin Mode Sensor Second, Third, Fourth, and Fifth Brightest Stars in the Field of View: $\delta_{scan} = 20^{\circ}$	58
	21	Spin Mode Sensor Second, Third, Fourth, and Fifth Brightest Stars in the Field of View: $\delta_{scan} = 30^{\circ}$	59
	22	Number of Stars in the Field of View with Limiting Magnitudes Parametric: $\delta_{scan} = -10^{\circ}$, Spin Mode Sensor	60
	23	Number of Stars in the Field of View with Limiting Magnitudes Parametric: $\delta_{scan} = 0^{\circ}$, Spin Mode Sensor	61

Figure 24	Number of Stars in the Field of View with Limiting Magnitudes Parametric: $\delta_{scan} = 10^{o}$, Spin Mode Sensor	62
25	Number of Stars in the Field of View with Limiting Magnitudes Parametric: $\delta_{scan} = 20^{o}$, Spin Mode Sensor	63
26	Number of Stars in the Field of View with Limiting Magnitudes Parametric: $\delta_{scan} = 30^{o}$, Spin Mode Sensor	64
27	Spin Mode Sensor: Cumulative Probability Distribution for the Third and Fourth Brightest Stars in the Field of View	65
28	Range in the Number of Stars for the Spin Mode Sensor: $\delta_{scan} = 20^{o}.7$	67
29	Range in the Number of Stars for the Spin Mode Sensor: $\delta_{scan} = 23^{o}$	68
30	Range in the Number of Stars for the Spin Mode Sensor: $\delta_{scan} = 0^{o}$	69
31	Dual Mode Sensor Second, Third, Fourth, and Fifth Stars in the Field of View: $\delta_{scan} = -10^{o}$	71
32	Dual Mode Sensor Second, Third, Fourth, and Fifth Stars in the Field of View: $\delta_{scan} = 0^{o}$	72
33	Dual Mode Sensor Second, Third, Fourth, and Fifth Stars in the Field of View: $\delta_{scan} = 10^{o}$	73
34	Dual Mode Sensor Second, Third, Fourth, and Fifth Stars in the Field of View: $\delta_{scan} = 20^{o}$	74
35	Dual Mode Sensor Second, Third, Fourth, and Fifth Stars in the Field of View: $\delta_{scan} = 30^{o}$	75
36	Number of Stars in the Field of View with Limiting Magnitude Parametric: $\delta_{scan} = -10^{o}$, Dual Mode Sensor	76
37	Number of Stars in the Field of View with Limiting Magnitude Parametric: $\delta_{scan} = 0^{o}$, Dual Mode Sensor	77
38	Number of Stars in the Field of View with Limiting Magnitude Parametric: $\delta_{scan} = 10^{o}$, Dual Mode Sensor	78
39	Number of Stars in the Field of View with Limiting Magnitude Parametric: $\delta_{scan} = 20^{o}$, Dual Mode Sensor	79
40	Number of Stars in the Field of View with Limiting Magnitude Parametric: $\delta_{scan} = 30^{o}$, Dual Mode Sensor	80

Figure 41	Dual Mode Sensor: Cumulative Probability Distribution for the Third and Fourth Brightest Stars in the Field of View	81
42	Range in the Number of Stars for the Dual Mode Sensor: $\delta_{scan} = 20.7^{\circ}$	83
43	Range in the Number of Stars for the Dual Mode Sensor: $\delta_{scan} = 23^{\circ}$	84
44	Range in the Number of Stars for the Dual Mode Sensor: $\delta_{scan} = 0^{\circ}$	85
45	Three Axis Mode Sensor: Cumulative Probability Distribution for the Third and Fourth Brightest Stars in the Field of View	87
46	Bright Object Shield Geometry	91
47	Geometry of the Shield Problem for the Spin Mode Sensor	94
48	Optical Field of View for the Spin Mode Sensor	97
49	Central Blocking for the Spin Mode Sensor	98
50	Normalized Bright Object Shield Height for the Spin Mode Sensor	99
51	Normalized Bright Object Shield Diameter for the Spin Mode Sensor	100
52	Parametric Design Curves for the Spin Mode SCADS Sensor: Second Level Optimization	101
53	System Limiting Magnitude for the Spin Mode Sensor	103
54	Geometry of the Dual Mode Sensor	104
55	Effective Field of View for the Dual Mode Sensor	107
56	Normalized Bright Object Shield Dimensions for the Dual Mode Sensor	108
57	Single Slit and Three Slit Reticle Configurations	110
58	Photocathode Radiant Sensitivity and Spectral Energy Distribution for Vega	116
59	Effective Instrument Spectral Energy Distribution for Vega	117
60	Spectral Energy Distributions of "Red" Stars	118
61	Effective Instrument Spectral Energy Distributions for "Red" Stars	119

Figure 62	Star Pulse Filtering	123
63	Percent of Star Radiation Passing Scanning Slit	127
64	Normalized Ratio of Peak Signal-to-RMS Noise for the Two-Pole Filter	137
65	Star Pulse Input Signal, Filter Impulse Response, and Output Signal	140
66	Circuit Configuration for Low Pass Active Filter	142
67	Schematic Representation of a Rotational Slit Width	155
68	Representative Blur Spot Diagrams	156
69	SCADS Dimensions for Optimal Spin Mode Sensor Design	163
70	SCADS Electronics Block Diagram	166
71	Waveforms Illustrating Background Filtering	170
72	Output Signals from High-Pass and Low-Pass Filters	172
73	Block Diagram for the High Voltage Power Supply	177
74	Voltage Doubler Circuit	179
75	Voltage Tripler Circuit	179
76	Interlaced Dual Even-Odd Multiplier	181
77	Cockroft-Walton Multiplier for EMR 14 Stage Photomultiplier	182
78	Charging Time of a Cockroft-Walton Multiplier	183
79	Exploded View of a SASI Motor	188
80	Electronic Block Diagram for SASI/SCADS	190
81	Detection Probability for the Spin Mode SCADS Sensor	211
82	Detection Probability for the Dual Mode SCADS Sensor	212
83	Detection Probability for the Three Axis Mode SCADS Sensor	213
84	Total Attitude Error for the Spin Mode as a Function of Right Ascension of the Scan Axis	218
85	Cumulative Distribution of the Total Attitude Error: Spin Mode Sensor	220
86	Cumulative Distribution of the Total Attitude Error: Dual Mode Sensor	221
87	Scan Axis Directions with Excessive Attitude Errors	224

Figure 88 Reticle Slit Reed Shutter Mechanism 228
89 Schematic of the Radiation Random Noise Process 232
90 Pictorial Representation of Spin Mode Sensor 244
91 Pictorial Representation of Three-Axis Sensor 245
92 Pictorial Representation of Dual Mode Sensor 246

LIST OF TABLES

Table I Dates in 1971 for Potential Lunar Interference 46
II Parameters for Recommended Spin Mode SCADS Sensor Configuration 164
III Parameters for Recommended Three Axis Mode SCADS Sensor Configuration 186
IV Parameters for Recommended Dual Mode SCADS Sensor Configuration 194
V Volume Estimates, Spin Mode Sensor 203
VI Weight Estimates, Spin Mode Sensor 204
VII Power Estimates, Spin Mode Sensor 204
VIII Volume Estimates, Three Axis Mode Sensor 205
IX Weight Estimates, Three Axis Mode Sensor 206
X Power Estimates, Three Axis Mode Sensor 206
XI Volume Estimates, Dual Mode Sensor 207
XII Weight Estimates, Dual Mode Sensor 208
XIII Power Estimates, Dual Mode Sensor 208
XIV Comparison of the Spin Mode Sensor-Three Axis Sensor Combination with the Dual Mode Sensor 248

STUDY OF A SCANNING CELESTIAL ATTITUDE DETERMINATION SYSTEM (SCADS) FOR A SYNCHRONOUS SATELLITE

I. INTRODUCTION

The results of a detailed feasibility and design study for a scanning celestial attitude determination system (SCADS) applicable to a synchronous satellite are presented. Where specific orbital or spacecraft parameters are required, they are taken from the preliminary specifications for the ATS-F&G satellites.

It may be noted here that the work performed specifically for this study emphasized those aspects of the application of SCADS which are peculiar to the launch and operation of a vehicle in an equatorial synchronous orbit. However, a number of more general results obtained in previous studies [1-4]* are included in order to make this report more nearly self-contained.

A. The SCADS Concept

SCADS represents a means for obtaining spacecraft attitude to very high precision with relatively simple instrumentation. In the three subsections which follow, the measurements required of this instrumentation, the data identification operations performed on these measurements, and the reduction of resultant known pattern of measurements to a determination of the spacecraft attitude are briefly described.

1. Star Transit Measurements

The measurement environment consists of the brighter stars of the night-time sky--stars which are bright enough so that an observer on Earth finds them clearly visible to the unaided eye. The positions of these stellar "targets" are carefully and completely documented and they are sufficiently far away so that they may be treated as point sources with negligible parallax for satellite operations in the vicinity of the earth. In short, the bright stars provide a nearly invariant fundamental frame of reference

*References indicated by [..] are tabulated at the end of the report.

which needs updating only very occasionally and then only in the star catalog, not in the physical alignment of the instrumentation on board the vehicle.

The SCADS instrument itself is designed to detect these stars in as nearly a passive manner as possible. To insure that a number of relatively bright stellar targets can be acquired by SCADS, the instrument employs a large optical field of view which covers a significant portion of the celestial sphere. Detection and "measurement" of the stars is achieved by placing a pattern of light-transmitting slits (often only one) in an otherwise opaque focal plane reticle in the optical system. The pattern of slits is caused to scan across a portion of the celestial sphere, either directly through the motion of the vehicle itself as with a spinning satellite or through some low-power reticle drive motor as would be required if the vehicle attitude were stationary in celestial space. As the slit scans across the focussed "point" image of a star, the starlight is gated through the reticle and sensed by a photodetector behind the image plane. The signal from the photodetector is used to gate another signal which characterizes either the time or the azimuth angle of the slit at which the star is centered in the slit. The process is shown schematically in Figure 1.

The fundamental raw data from the SCADS instrument thus consists of a set of transit times or transit angles. In order to solve the three-axis attitude problem, at least three spatially independent measurements must be taken. With a single slit, only one type of spatial measurement can be made for each star; thus, at least three different stars must be detected. If more than one slit is employed, a pattern may be arranged so that both azimuth and elevation angle values can be inferred. Under these conditions, each star can give two spatially independent measurements and a minimum of two detectable stars is required.

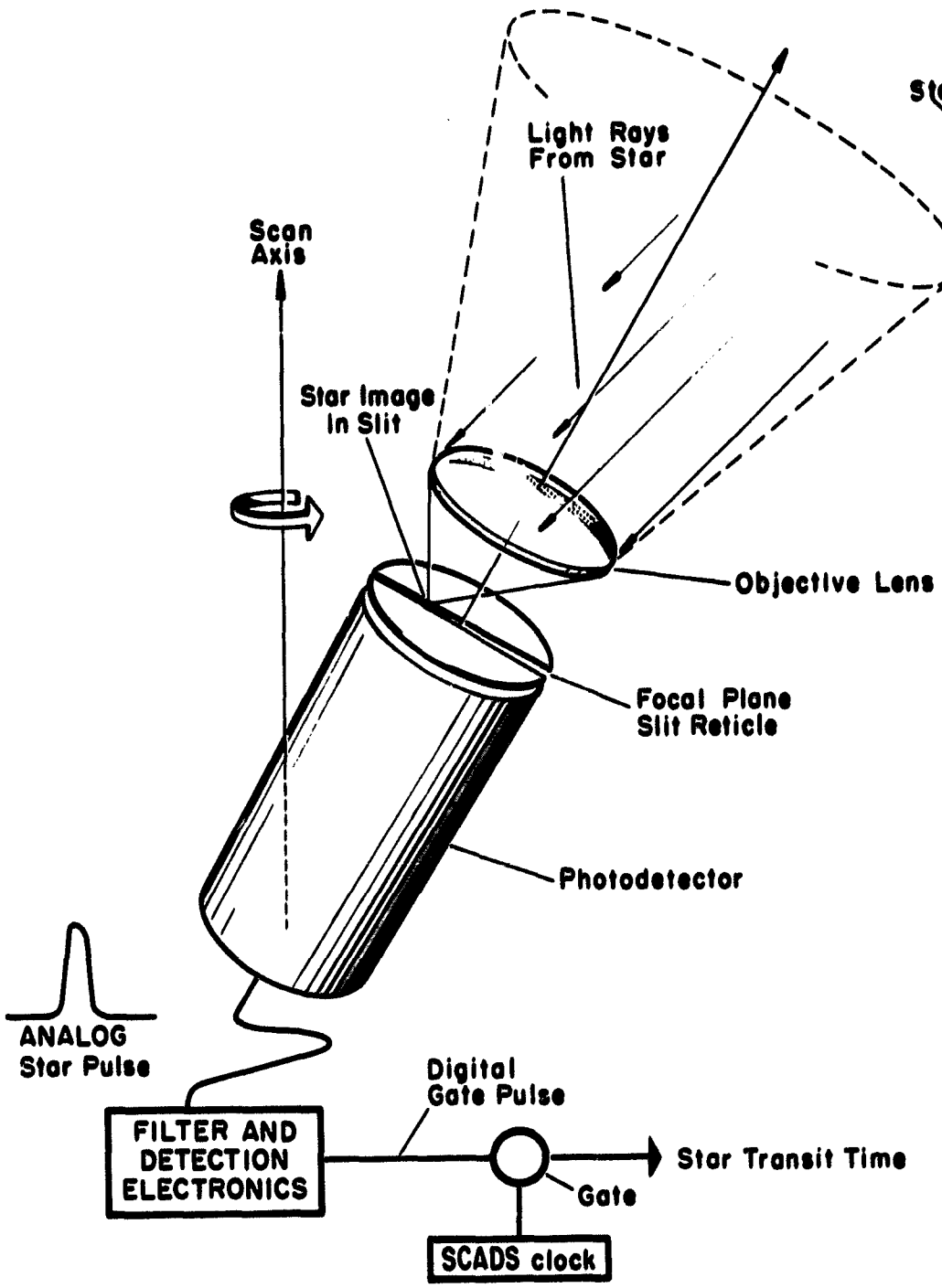


Figure 1: Schematic representation of a Scanning Celestial Attitude Determination System (SCADS)

If the attitude is changing with time, then rate information as well as the specific instantaneous attitude is desired. Each rate variable which is added requires an additional transit measurement. These, however, need only be independent in time from the others so repeated transits of the same three stars on successive scans would be sufficient. As a practical matter, the number of stars detected should exceed the minimum number to aid in identification of the pattern of transits with a known pattern of stars. Further, the number of transit measurements should exceed the number of variables sought in the solution; overdetermination of the system of equations coupled with a least-squares fit reduces the overall system error.

2. Star Identification

In the next section the problem of determining attitude is discussed in terms of an equation which must be satisfied whenever a known star is in the sensor slit. The key to the section which follows is the phrase "known star", for the problem of identifying stars from their transit times is discussed in the following paragraphs. The problem consists of establishing a one-for-one correspondence between transit times and star names (or catalog numbers). Since absolute stellar magnitudes will not be measured by the sensor, we must prescribe a method which does not utilize magnitude measurements for the identification process.

The problem of identifying stars when only the relative azimuth of a set of targets is measured (angle as measured from some arbitrary reference about an unknown optical axis) is a very difficult one. Only if the approximate pointing direction of the instrument is known can the method described here assure us of a relatively high probability of a successful identification.

One of the main reasons that the method of star identification described in this section is possible at all is because we have a fairly good idea of where to look (on the celestial sphere) for a star pattern similar to the

one detected by the sensor. The satellite is spin stabilized and consequently because the orbital parameters will be known and the time of day of any observation will be recorded, a simple computation will determine the nominal direction of the scan axis. From this very good starting point, it should not be too difficult to find a star pattern (from a star catalog) similar to the detected pattern and hence to identify the transited stars.

Much of the following star identification scheme depends on searching a list of possible stars for those having azimuth separations similar to the observed ones. Fortunately, we need only look at relatively small regions of the celestial sphere because of how well the pointing direction is already known, but also we are further assisted by a knowledge of how faint a star the optical and electrical sensor can detect.

The process of relating a sequence of transit times recorded chronologically to their associated star names or catalog numbers can be divided into three logically distinct tasks: (1) determination of a mean period, (2) establishing a scan-to-scan correlation, and (3) identification of the stars by azimuth differences. A brief outline of each of these tasks is given below.

a. Determination of a Mean Period

In order to establish where in the list of transit times one complete scan ends and the next one begins, one needs to determine the length of a single scan. This seems like a trivial task but can be difficult particularly when the satellite is undergoing nutation (not spinning about a single axis). The nominal spin period can be defined as the mean of all the periods during one nutation period.

To find a transit time corresponding to a particular star on successive scans, one need only add the nominal period to the transit time and search forward in the transit list until a second transit is found which agrees

with it to within some small tolerance. This period is required in order to filter out extraneous noise pulses and false targets from the raw data. The more accurately it is known, the better able we are to eliminate these "confusion pulses" and to subsequently identify the actual stars.

If one can be assured that the spin period of the satellite is well known and accurate, then this procedure can be bypassed. If, however, there is some doubt about the period and we are given a range of possible values ($T_{min} \leq T \leq T_{max}$), then a technique for determining the period is as follows:

Choose the geometric mean of the range of possible values for the period. Call this the nominal period T. Also define

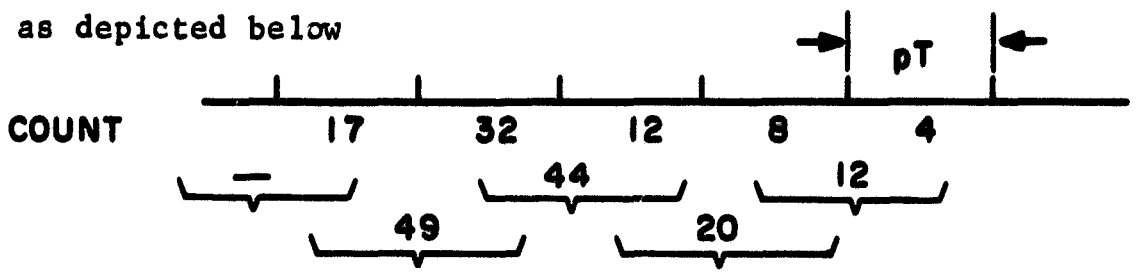
$$T'_{min} = T_{min} - pT$$

$$T'_{max} = T_{max} + pT$$

where p is some small number like .005 (½%).

Calculate all possible time differences $t_i - t_j$, $j < i$ such that $T'_{min} \leq t_i - t_j \leq T'_{max}$ for all i, where t_i is the i^{th} transit time. This produces a large array of differences which are to be sorted from smallest to largest. This sorted list is now divided into slots of length pT and a count is made of the number of differences in each slot. Since the period should appear most frequently among all these differences, we concentrate our efforts on the slot with the largest count.

Further, to eliminate possible overlap problems the counts for all pairs of adjacent slots are added together to form a new set of difference counts as depicted below



This revised list of counts is searched for the largest count and the new interval (of length 2pT) is considered to contain a good approximation of the new nominal period. One estimator of the nominal period is simply the mean of all differences in this slot and a good estimator of the tolerance assigned to this period might be the variance (σ) of these differences with respect to this mean.

A quick check to determine the quality of the estimator for the nominal period would be to run through the raw transit times taking differences again but this time counting the number of pairings which can be made by taking each transit, t_i, and searching an area $\pm 2\sigma$ about the time $t_i + T$ and counting the number of transits t_j which satisfy the inequality

$$|t_j - t_i - T| \leq 2\sigma, \; j > i \text{ all } i. \qquad (1)$$

If we count the number of times we have zero, one, and more than one matchings of this type, the number of single matches should dominate the other two. If the zero matches category dominates, we have missed the actual nominal period by making the difference slots too narrow and have computed too small a variance. If this is the case, we can adjust by returning to the original difference table and redefining the slot length (this could be done by, say, doubling p) and recounting as above. If the third category (more than one) dominates we have missed the actual nominal period by making the difference slots too wide and have computed too large a variance. We adjust for this by returning to the difference tables and redefining the slot length (e.g. by halving p) and recounting. By repeated use of this kind of processing, at some point the second category (one match) will dominate and the procedure stopped, or we may assume that we have a bad batch of data. The last mean period so found will be defined as the nominal period and its associated variance will be used as a tolerance in later portions of the identification process.

b. Scan-to-Scan Correlation

One method of eliminating as much noise as possible from the transit time raw data is to choose to consider only transits which occur "regularly" from one scan to the next. It seems clear that truly random noise pulses getting through the electronic gear to appear as a transit of a star in the transit list should not occur regularly in the same relative position on successive scans. For this reason, an attempt is made to pick only time pulses which repeat themselves on many scans, (say seven to nine scans out of ten). Clearly, the better the estimate of the actual scan period we have, the easier this task will be. Also, if the nutation rate is high and the coning angle is relatively large, then star transits are not apt to appear separated by exactly the same time difference from one scan to the next.

Using the period as determined by the above process and the variance as a measure of the allowable tolerance, each transit time is considered in sequence. A forward search is made in a region $\pm 2\sigma$ about the time $t_i + T$. Three situations are possible: (1) no transits t_j can be found to satisfy the inequality,

$$|t_i + T - t_j| \leq 2\sigma; \tag{2}$$

(2) a single transit satisfies the inequality; or (3) more than one transit falls in the range. If (1) is the case and t_i is not the second transit of a previously matched pair, we may assume that the transit time t_i was triggered by noise or a false target of some sort and can be discarded from the time list.

Clearly, if (2) is the case, we have found what we are looking for and all we need to do is tag the transit t_j with an identifier which associates it with t_i and eliminates it from further consideration. Using the new transit t_j, the process is repeated until we have been able to string

together several transits by this technique.

When (3) occurs, we are unable to choose from among several possibilities and we avoid coming to any decision at this point. We simply increment the subscript i and continue. It may be possible to eliminate some of the ambiguous matches just by sliding the process down to the next unchecked entry. The complete process is repeated until no new transits have been matched so that if any were matched from a previous pass, there exists a possibility that this may have enabled us to come to a decision about a previously unresolvable situation.

c. Star Identification by Azimuth Differences

In the discussion that follows, it cannot be over-emphasized that the technique depends heavily on the presence of an approximate attitude. This "guess" is used by the computer program to search its star catalog to find those stars which should lie in the scanned region of the celestial sphere. In this way a "computed azimuth pattern" (CAP) is generated. The measured azimuth pattern (MAP) provided by the sensor output is the one to be matched by varying the assumed pointing direction.

The actual matching technique, i.e. the method of varying the parameters from which CAP is generated until CAP = MAP, can be illustrated by a manual analog. On a transparent sheet, lay out the measured azimuths as a set of radial lines (starting from an arbitrary zero azimuth). Overlay this sheet on a rectangular projection of the celestial sphere in the area of the assumed pointing direction. Translate the azimuth sheet on the star pattern and rotate it about the azimuth pattern center until coincidence of the patterns is achieved.

The above procedure is closely followed by the computer in achieving a CAP and MAP match. The computer solution is, however, more numerical, less sophisticated, and considerably more accurate. (The manual method cannot

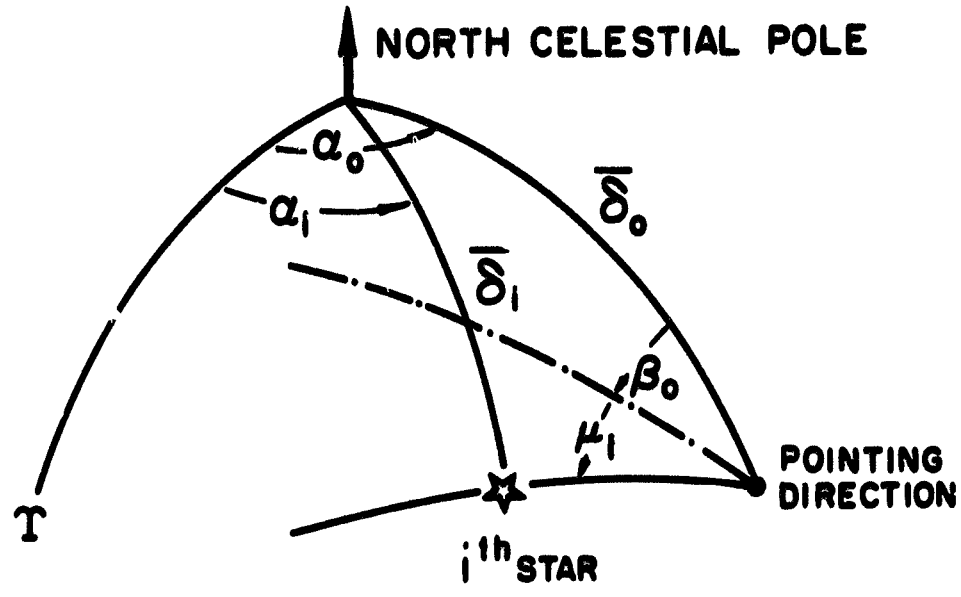
take full advantage of the instrument measurement accuracy without the aid of precision measuring machines. The computer--being in essence just such a machine--can realize the full potential accuracy of the data.)

Given the spacecraft orbital parameters and the time and date, one can compute an assumed pointing direction of the spin axis and azimuth zero direction accurate to within a few degrees. The first task is to pick stars from the catalog which lie in an enlarged region about this direction and which, of course, are brighter than the limiting magnitude. This will reduce the original catalog list numbering several hundred candidates down by at least an order of magnitude. Furthermore, those stars actually detected by the sensor are guaranteed to be in this reduced list (unless a false target comes through) provided that the assumed position and the true position do not differ greatly.

The reduced star list now contains the right ascension and declination of the candidate stars. For the pattern matching process we need to know the relative azimuth differences between the first and second stars, the second and third stars, etc. The computation of these azimuth angles is quite simple. Given the right ascension, α_i, and declination, δ_i, of the i^{th} star and the right ascension, α_o, and declination, δ_o, of the assumed pointing direction, the azimuth, μ_i, from north (measured counterclockwise) is given by the equation

$$\tan(\beta_o + \mu_i) = \frac{\sin(\alpha_o - \alpha_i)\cos\delta_i}{\sin\delta_i\cos\delta_o - \cos\delta_i\sin\delta_o\cos(\alpha_o - \alpha_i)} \qquad (3)$$

where the signs of the numerator and denominator determine the proper quadrant.



In this manner, an azimuth angle is calculated for all stars in the catalog within the augmented field of view. An array is then constructed of the relative azimuths of these stars where the entries are formed by a simple subtraction, $\mu_{i,\,j} = \mu_i - \mu_j$, $i > j$.

Note that all entries below the first row are redundant. That is, having the azimuth differences between any star and the first star enables one to find all other separations. In order to save many arithmetic operations in the computer program, however, this array is made up once at the beginning and just referenced thereafter. A second, and more important reason for filling in the complete array exists; namely, the expected difficulty with undetected targets. That is, with any detection equipment of the type described in this report, a theoretical limiting magnitude for the dimmest star can be calculated and the instrument calibrated for this limit. However, there will always be some slightly brighter targets than this limiting

j ↓ i →	1	2	3	4	5	...
1	0	5.6	14.7	39.2	101.0	
2		0	9.1	33.6	95.4	
3			0	24.5	86.3	
4				0	61.8	
5					0	
⋮						

magnitude which will go undetected on occasion, and some slightly dimmer objects which may occasionally be detected. To cope with the former (in the star identification process at least), we complete the array mentioned above so that it is possible, for example, to search for the separation of the fourth star and the second without insisting that the stars be detected in precisely the same order as the catalog indicates. Coping with the latter problem (dim stars) is easier; we simply extend our list of star candidates slightly beyond the limiting magnitude to insure including all possibilities (at the risk of making the task more difficult).

The technique of matching stars with their measured azimuth angles is relatively simple. The scanning instrument measures the angles, μ_i, $i = 1, \ldots, N$. Since the azimuth zero direction is not accurately known, we cannot depend on μ_i measured being equal to μ_i computed even if an exact

pointing direction could be used to obtain the μ_i computed. However, the relative azimuths would be exact under those circumstances, and for this reason we do not need to rely heavily on a knowledge of the azimuth zero reference.

At this point, the computer program will consider each of the measured azimuth differences and search through the separation array seeking angles (and associated indices i, j) agreeing to within some generous tolerance angle μ_ϵ. A list of index numbers is kept for each measured pair of angles. When all target pairs have been processed, these lists may look like this.

μ_{21}	μ_{32}	μ_{43}	---	μ_{N1}
4-3	6-4	7-6		5-1
4-8	7-1			11-3
5-4	7-2			11-4
				11-10

Note that the first target is used in both the first and last list to complete the scan. The actual identification process is now simply to scan across the lists looking for sets of indices of the form

b-a c-b d-c --- N-a.

The underlined indices exhibit such a form. We must conclude then that the identified stars are numbered a, b, c, ..., N, respectively. However, it may be possible to find other sets of N stars which also satisfy the above conditions, in this case each set must be further examined.

For every azimuth difference, a residual exists. Residuals are taken

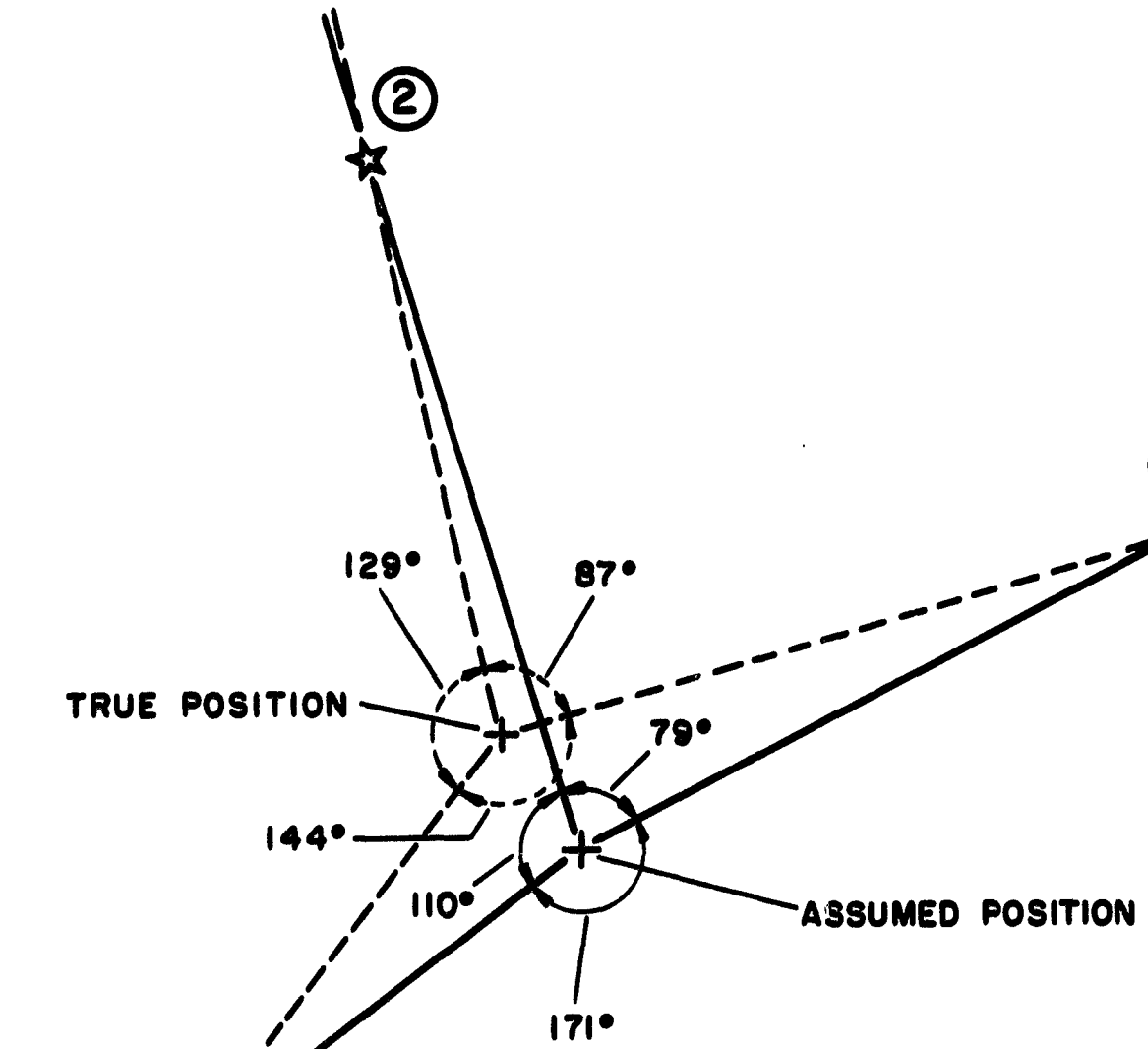
as the difference between measured and computed relative azimuths with careful attention paid to the sign. These residuals can be used to move the assumed pointing direction closer to the true position. Graphically, the scheme is as follows (the computer program would, of course, do the problem digitally, but in a similar manner).

Let the dotted lines (of Figure 2) refer to azimuths measured from the true pointing direction to each star, the solid lines are the azimuths from the assumed position. In this figure a sample case is illustrated using three stars for clarity. The residuals are, respectively, +8, +19, -27, and the sum of squares is 1154. From the sign of each residual we can determine which direction to move in order to reduce the residual (to zero, if possible). If the sign is positive, the computed angle is too small and we must move "toward" the pair of stars defining this angle. Toward as used here arbitrarily means along a line defined by bisecting the angle between the two stars. Positive residuals dictate moving toward the pair of stars along the bisector and negative residuals indicate motion away from the stars.

From the relative size of the residual an indication of how far to move can be computed. The example above (Figure 2) seems to indicate that moving more along the bisector of stars 3 and 1 (in the negative sense) should be the dominant change since it has the largest residual (in absolute value). The fractional motions for the three pairs can be arbitrarily chosen as

$$\frac{8}{\sqrt{1154}} = .235 \qquad \frac{19}{\sqrt{1154}} = .558 \qquad \frac{27}{\sqrt{1154}} = .794$$

of some total motion. Total motion can be taken as one-half the estimated tolerance Δ (Δ is an estimate of the difference between the true pointing direction and the assumed direction) to begin with and halved on each repetition of this method (if successive steps are necessary to resolve ambiguous



RELATIVE AZIMUTHS

MEASURED	COMPUTED	RESIDUAL
87	79	+8
129	110	+19
144	171	-27

SUM OF SQUARES: 1154

Figure 2: Computed and measured relative azimuths in the star identification process

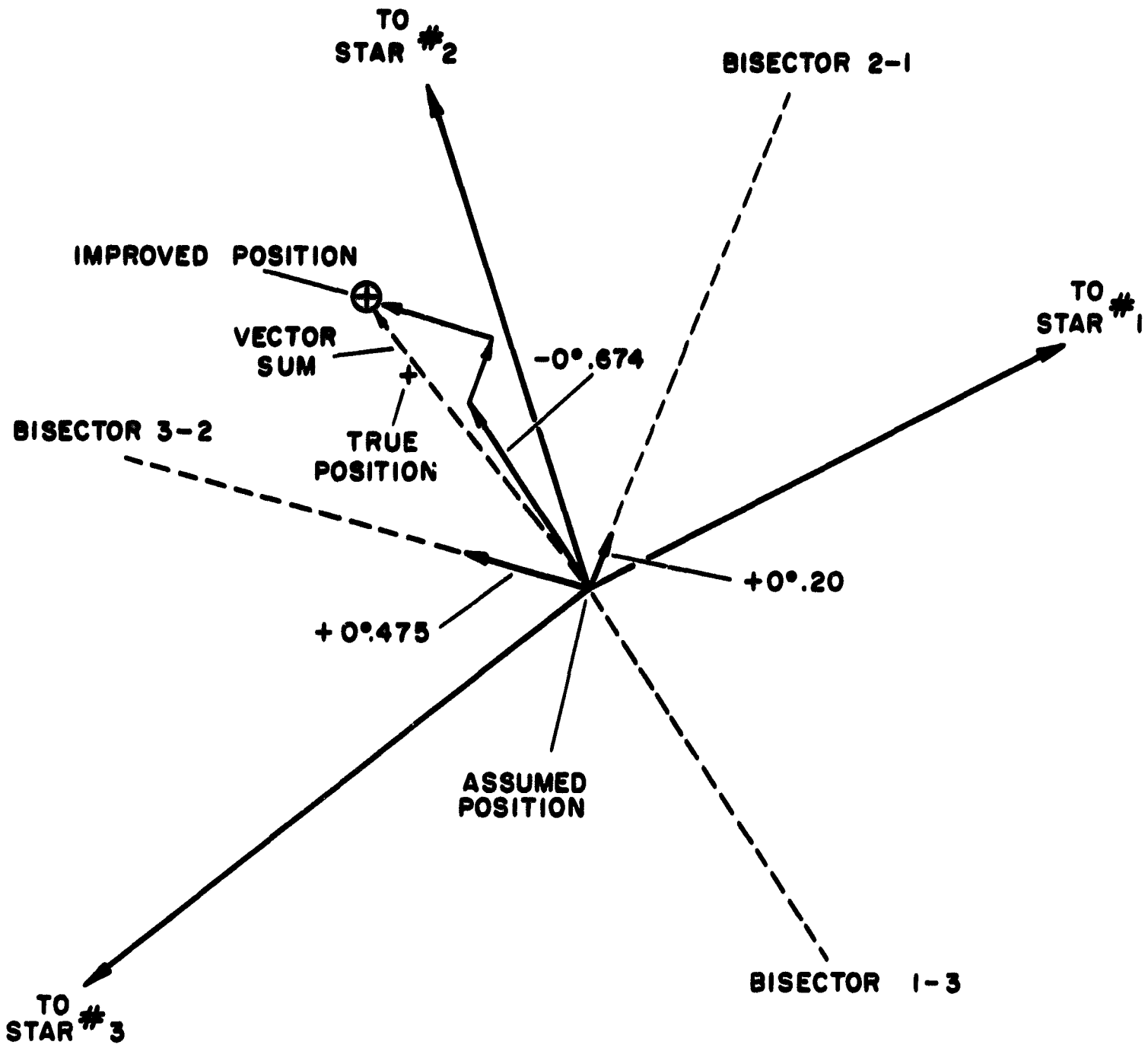


Figure 3: Star identification: example of an iterative step in the solution

star patterns). In Figure 3, the vector sum of the displacement of Figure 2 is shown using a tolerance of two degrees and the resultant next assumed pointing direction is indicated. We have improved our position from an error of 1.0 degree down to about 0.25 degree, a significant improvement.

3. Attitude Determination

The general method of attitude determination by use of transit times of known stars across a slit will now be discussed. Our discussion is not new here, but is taken from previous work supported by NASA.[1,4,5] At this point, we assume transit data has been received from the vehicle and has previously been tagged, i.e., known stars have been associated with each transit time.

A slit is scribed on the focal plane of an optical system. Such a slit describes a curve when projected on the celestial sphere. If the slit is a straight line and the optical system is distortion free, then the curve is a great circle. Such will be considered the case here.

The instrumentation is such that the slit is either fixed with respect to the satellite (spin stabilized satellites) or rotates with respect to the satellite in some precisely known manner (non-spin stabilized satellites). In either case, the great circle projection of the slit can be described by an equation which contains only known parameters if such an equation is written utilizing a coordinate system fixed in the satellite.

At the instant a star transits the slit, we know the star lies on the slit's projection. Hence, at this instant we may write,

$$\hat{n} \cdot \hat{s} = 0, \tag{4}$$

where $\hat{n}$ = unit vector normal to the plane determined by the slit's projection on the celestial sphere;

$\hat{s}$ = unit vector to the star (Figure 4).

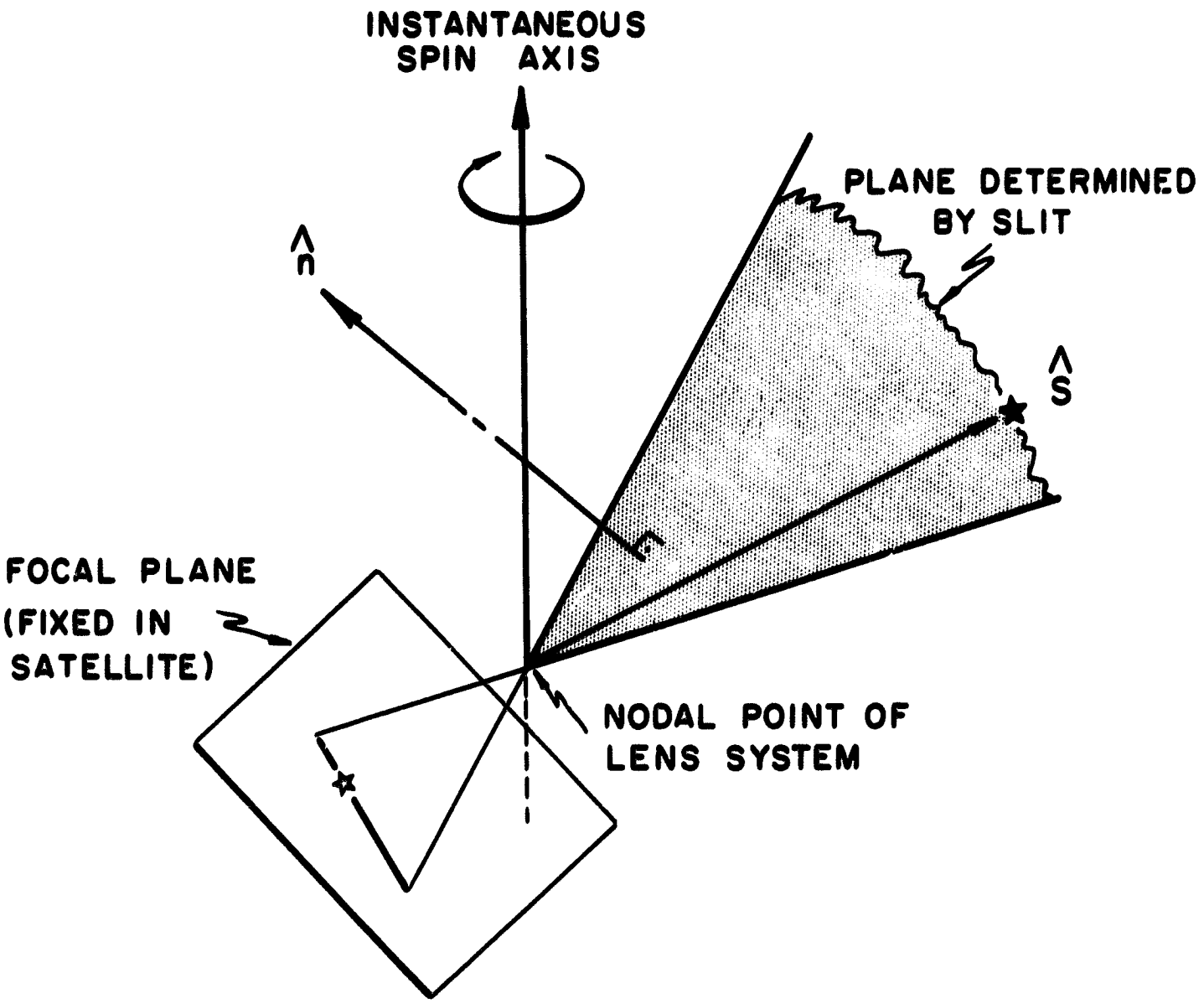


Figure 4: Relation between $\hat{n}$ and $\hat{s}$ at the instant of transit

Since the slit is in a known position with respect to the satellite, $\hat{n}$ is easily written in a coordinate system fixed in the satellite. On the other hand, $\hat{s}$ is most easily written in a celestial coordinate system (a system in which the star directions are catalogued). In order to write these vectors in the same coordinate system, parameters which specify the orientation of the coordinate system fixed in the body with respect to the celestial system must be introduced. However, these are the very parameters we are interested in determining.

In order to introduce parameters which allow $\hat{n}$ and $\hat{s}$ to be written in the same coordinate system, the physics which govern the attitude motion of the satellite must be considered. Two basic models are pertinent to the ATS-F & G. These models assume the following types of constraints on the satellite dynamics:

(a) rigid body, torque free, nearly symmetric, and spinning;

(b) attitude controlled such that roll, pitch, and yaw are slowly varying functions of time (slow with respect to the scan period of the slit which is rotated with respect to the satellite).

Of these models, (a) has been analyzed, programmed, and applied. A discussion may be found in References [1] and [5]. Model (b) has been analyzed, but not programmed. The total problem as it evolves about this model is given in Appendix A.

In general, model (a) can be applied to the spin stabilized phase of the ATS-F & G missions. During most of this phase, and fortunately that portion of the phase over which attitude is most important, the spacecraft's altitude is large. Hence, perturbing effects from the earth and corresponding torques will be small.

Model (b) will then be utilized during the attitude controlled mode of the mission. It is assumed that attitude information will be supplied only

at the end points of vehicle maneuvers and not during the sluing duration. Thus, the assumption of slow roll, pitch, and yaw rates is justified.

B. Orbital Configurations: SCADS Operational Requirements

As noted above, the specific orbital parameters considered are those proposed for the ATS-F&G satellites. Two distinct roles are seen for the SCADS application to these missions. Up through the completion of synchronous orbit insertion and correction, the vehicle will be spinning. SCADS would be used first to give the attitude information required for the firing of the kick stage to inject the vehicle into synchronous orbit at the apogee of the transfer ellipse. Continued use of SCADS in this mode would be required after each reorientation of the vehicle during the orbit correction phases designed to remove any residual eccentricity and inclination in the final orbit. In these spin stabilized portions of the mission, it is desired to determine three-axis attitude to $0^{\circ}.1$ and the spin period to within 0.03 percent.

After a satisfactory orbit has been achieved, the vehicle will be despun and placed in a three-axis controlled mode. During this portion of the mission, it is desired to use SCADS for very precise calibration of other instruments on board the vehicle provided that performance during the spinning mode operations is not degraded. In the three-axis controlled mode, an accuracy of $0^{\circ}.01$ in the three-axis attitude is desired.

The orbital parameters and special SCADS requirements in the various modes are summarized below.

1. Transfer Ellipse Mode, Spin Stabilized

At the inception of this study, a transfer ellipse with perigee at 100 nautical miles altitude, apogee on the equator at synchronous altitude (19,323 nautical miles), an orbital inclination of $22^{\circ}.3$, and eccentricity of 0.7306 was proposed. Later considerations suggest that an orbital inclination of $26^{\circ}.25$ may be used. In the work which follows, results for each of these parameters is presented.

In order to achieve a synchronous orbit from the inclined transfer ellipse, the vehicle kick motor (which is directed along the negative spin axis) must be aligned so that the spin axis is at right angles to the line of apsides and has a declination $\delta_{spin} = -20.^{\circ}7$ (for inclination $22.^{\circ}3$) or $\delta_{spin} \approx -23^{\circ}$ (for inclination $26.^{\circ}25$). After the initial launch and spin up phases, the error between the true spin axis and its nominal direction may be as much as 10°; it is required that SCADS be able to tolerate this uncertainty. It is further required that SCADS be operational for $\pm$ 2 hours about the first apogee of the transfer ellipse and from -2 hours to 0 hours (the time of synchronous insertion) before the second apogee. Note that the period of the transfer orbit is 10.513 hours.

Additional parameters or constraints which apply to the transfer ellipse and are relevant to the SCADS study are summarized here. The vehicle spin rate is 60 rpm. The line of apsides at second apogee (synchronous insertion) will be at 53°W longitude. The angle between the sun line and the spin axis may be in the range 50° to 130° as determined from solar panel power considerations.

The transfer orbit configurations for the two different cases of orbital inclination are summarized in Figure 5.

2. Synchronous Circular Orbit, Spin Stabilized

Once the kick motor has been fired and the vehicle is in a near synchronous orbit, SCADS will be used first to ascertain that the orientation of the spin axis is the same as it was prior to insertion. Thus, attitude must be measured with δ_{spin} near $-20.^{\circ}7$ or -23° over a portion of the synchronous orbit. Note that if Ω is the right ascension of the insertion point (the line of apsides for the transfer ellipse) then $\alpha_{spin} = \Omega + 90^{\circ}$ since the spin axis is perpendicular to local vertical at that point.

Four other possible orientations may arise during the spinning phase

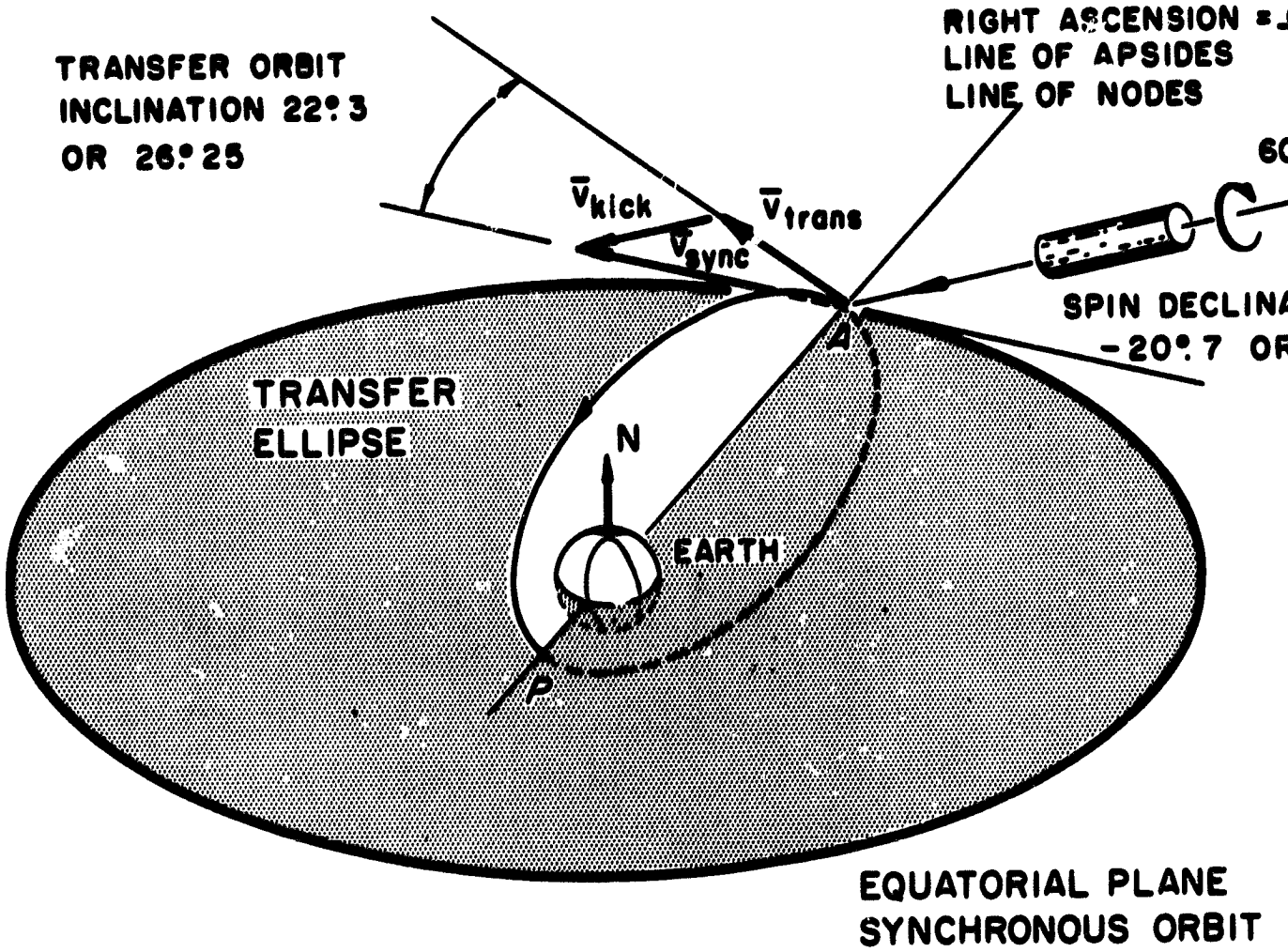


Figure 5: Orbital configurations. (Note: two possible inclinations for the transfer ellipse and corresponding spin declinations are considered.)

of the synchronous orbit. To remove residual inclination of the orbit, the vehicle may be oriented to ($\delta_{spin} = \pm 90^{o}$) and a vernier correction burn carried out. To remove residual eccentricity in an under-energy condition, the vehicle spin axis will be brought up into the orbital (equatorial) plane and a vernier burn to increase speed will be carried out. In this case the spin axis will be along ($\delta_{spin} = 0^{o}$, $\alpha_{spin} = \Omega + 90^{o}$). On the other hand, if an over-energy condition exists, the vehicle may be flipped all the way over to ($\delta_{spin} = 0^{o}$, $\alpha_{spin} = \Omega - 90^{o}$) before the correction. This latter condition may be avoided by intentionally achieving an under-energy state at insertion. However, since it is not certain whether this under-energy approach will be used, the implications of the various vehicle orientations will be considered both with and without the condition ($\delta_{spin} = 0^{o}$, $\alpha_{spin} = \Omega - 90^{o}$).

It is required that SCADS be operational for all of these expected spin axis directions during the spin stabilized portion of the synchronous orbit. Again, an uncertainty of 10^{o} for the actual spin axis relative to the nominal value is to be assumed. The nominal states are summarized in Figure 6.

3. Synchronous Circular Orbit, Three-Axis Controlled

In the three-axis controlled mode, the yaw axis will be swung to point at various points on the earth. From synchronous altitude, the yaw axis can take on any value within a cone of half angle approximately $8^{o}.7$; this becomes the effective angle of uncertainty which SCADS must tolerate. Note also that continuous SCADS operation is not required for this phase.

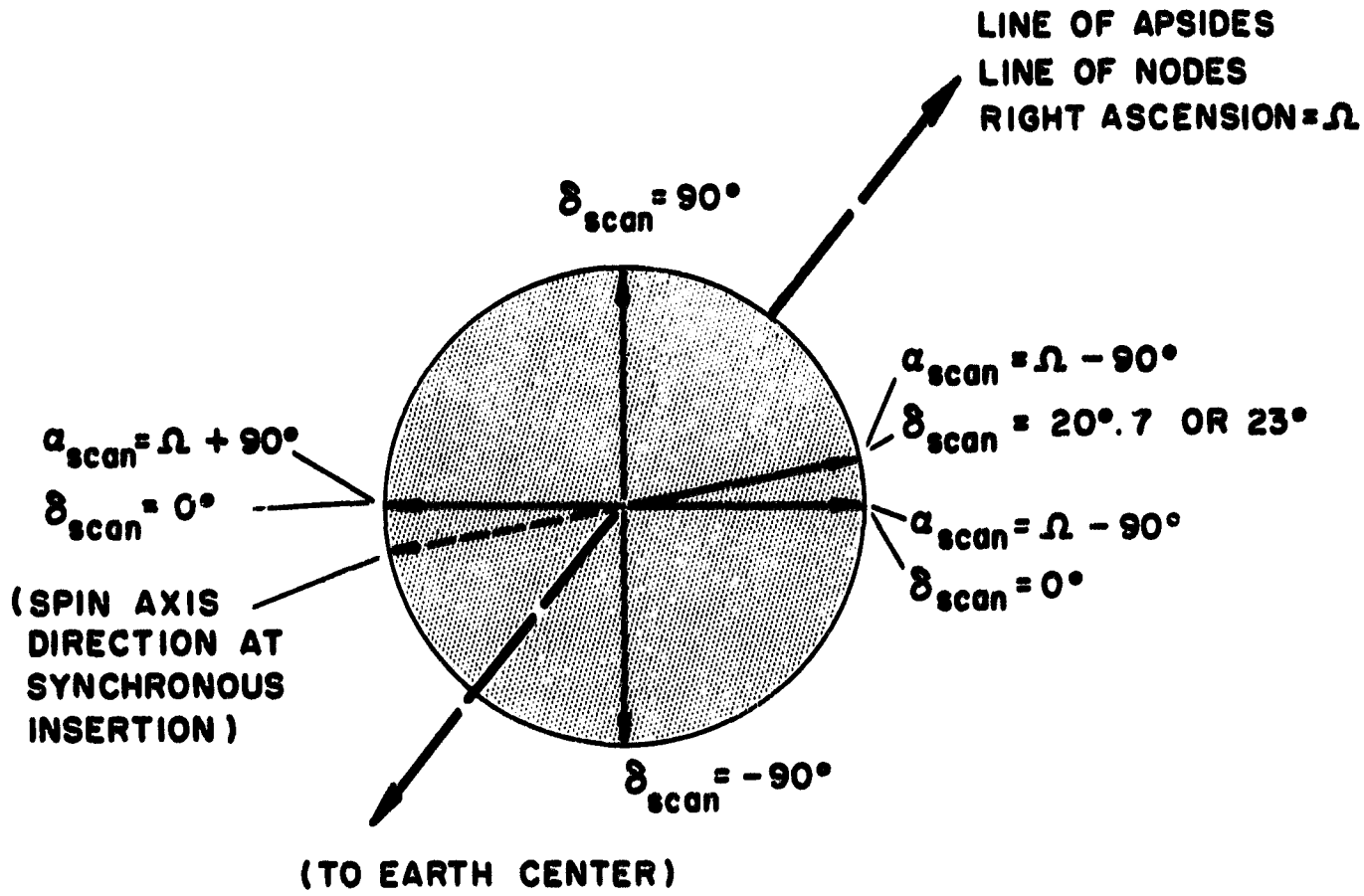


Figure 6: Nominal directions of the SCADS scan axis in the synchronous orbit. Note that the scan axis as defined here is along the negative spin axis. In all cases, the nominal scan axis is perpendicular to the spacecraft-earth line at synchronous insertion.

C. The Study

In the study which follows, three basic SCADS configurations are considered. The first of these is the spin mode SCADS sensor; it is a simple fixed-reticle system which is required to operate only in the spin-stabilized portions of the ATS F & G missions. The second is the three-axis-controlled mode SCADS sensor. This system has a driven reticle and is required to operate only in the three-axis controlled mission phases. Finally, a dual mode SCADS sensor is considered. This system has the capability of providing attitude information with a single instrument for both the spinning and controlled spacecraft operations.

The discussion proceeds as follows. In Section II, the celestial environment in which SCADS must operate is analyzed both in terms of the constraints imposed by the presence of the sun, earth, and moon and in terms of the distribution of stellar targets. In Section III, the general criteria for selecting SCADS parameters are developed and a series of parametric design curves and relations is presented. Section IV develops the specific recommended designs for the three configurations and presents estimates for the gross characteristics--power, weight, and volume--for each. In Section V, the expected performance of the recommended designs is further analyzed with emphasis on the target detection and accuracy achievable with the sensors. In Section VI, the operational conditions and constraints are briefly summarized. Finally, the basic resultant SCADS configurations are compared in Section VII and a particular SCADS approach is recommended.

Two principal conclusions arise in the study. First, SCADS is suitable for application to a multiphase synchronous satellite mission and thus to the ATS F & G program. Second, although the diverse requirements of the spinning and three-axis-controlled operations can be met with a dual mode SCADS sensor, the combination of separate spin mode and three-axis mode sensors provides significant advantages for this program. Justification of these conslusions and details of the corresponding designs are presented below.

II. SCADS CELESTIAL ENVIRONMENT ANALYSES

SCADS utilizes a wide field of view optical system to insure covering a relatively large portion of the celestial sphere and thereby guarantee that a sufficient number of suitable celestial targets will be acquired. The scanning operation typically traces out an annular region as illustrated in Figure 7. Although it is desirable to have a few more than the minimum number of targets available, it is an aim of this study to minimize the size, weight, and power of potential SCADS instrumentation within the constraints of sound design. Thus, the limiting stellar magnitude (i.e. the faintest consistently detectable star) for the system should be set as bright as possible. Unfortunately for the purposes of the SCADS application, the bright stars are distributed very nonuniformly over the celestial sphere; there is a strong concentration along the galactic plane--the Milky Way. However, a typical mission will contain possible pointing directions which lie close to the Milky Way and others which lie close to the sparsely populated galactic poles. Since a minimum number of targets must be detected for the problem to be solved at all, selection of the system limiting magnitude must be made on a worst case basis. Thus, a detailed star availability study must be made in order to match the sensor to the particular operational requirements of the proposed orbits and orientations.

Further, because SCADS employs a wide field of view, special care must be exercised to make certain that the bright celestial objects--the sun, earth, and moon--interfere with the detection of stars as little as possible. Note that the sun is 10^{12} times as bright as a fourth magnitude star; even a small fraction of the sun's total light scattered into the SCADS optical system would completely mask a star signal. The next two subsections treat the SCADS design implications of the presence of the bright objects and detailed star availability searches for this study.

A. SCADS Operation in the Presence of the Sun, Earth, and Moon

If sunlight has some scattering path into the SCADS optical system,

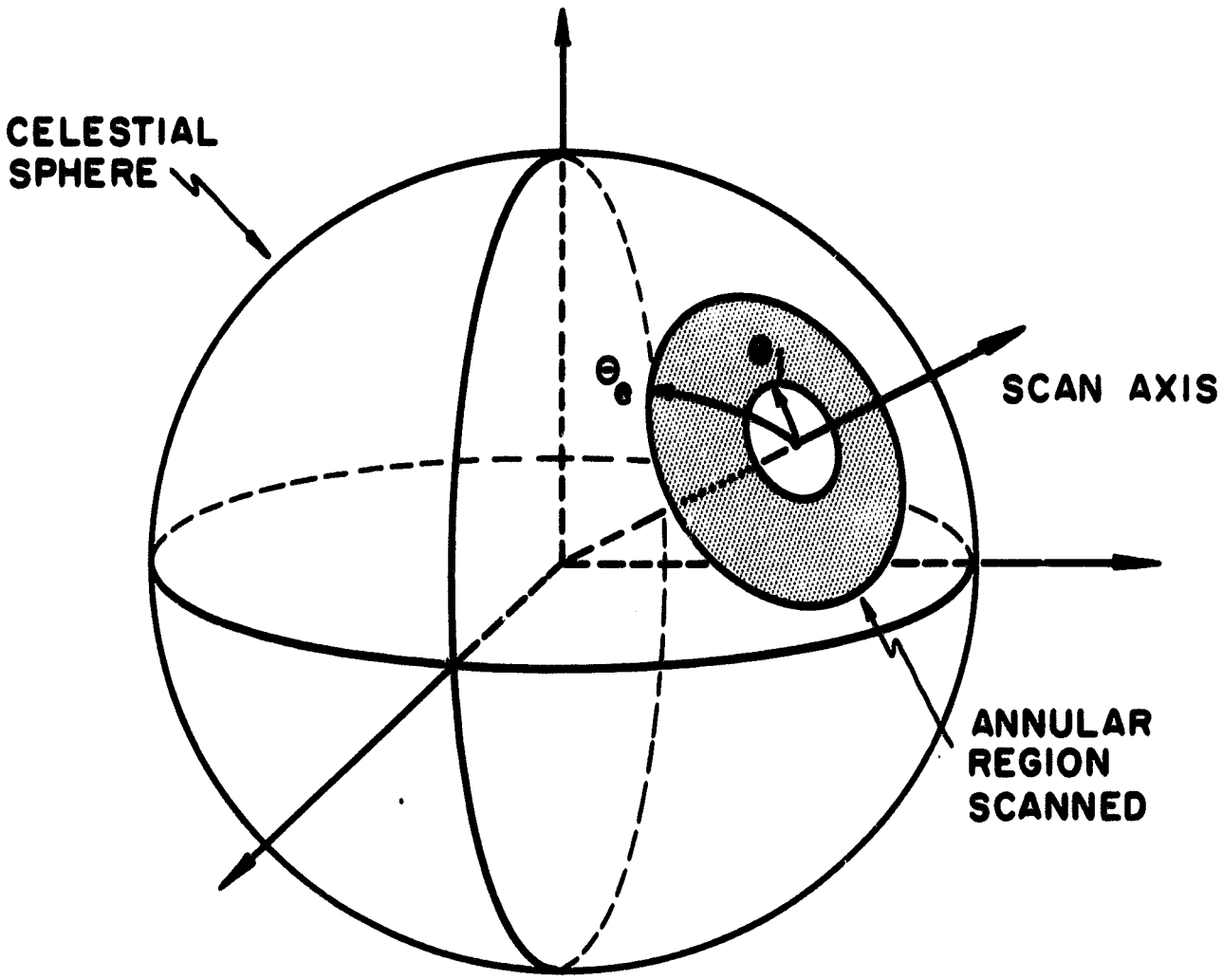


Figure 7: SCADS annular scan pattern

it must be attenuated by more than a factor of 10^{12} along that path to avoid overriding the light signals from stars near the system detection limit (assumed at this point to be somewhere in the stellar magnitude range between 3 and 5). Further, from the sunlit side, the earth as seen from synchronous altitude is only about two orders of magnitude less bright than the sun; at the altitude of the transfer ellipse perigee, it is almost four-tenths as bright as the sun. Thus, if either the sun or the sunlit earth are less than 90^{o} from the SCADS optical axis, fairly extensive bright object shielding will be required. Note here that the 90^{o} criteria is based on the fact that any direct sunlight which strikes the SCADS lens, even at an angle well outside the optical field of view, will encounter sufficient scattering within the glass to flood the photodetector through the slit.

The moon, on the other hand, is only about 10^{6} times as bright as the expected limiting magnitude star. In this case, sufficient attenuation should be provided by merely excluding the moon from the actual optical field of view.

1. The Earth

The annular scan field depicted in Figure 7 is created in the spinning case by canting the optical field of view away from the spin axis and allowing the vehicle motion to sweep the optic axis around in a cone. The dead zone in the middle of the annulus is placed there to simplify the star identification scheme and to avoid the large angular errors associated with azimuth measurements on points close to a center of rotation.

From the geometry of the transfer orbit (Figure 5) it is clear that the positive spin axis points at the earth or close to it over the half of the orbit from perigee to apogee and away from the earth on the half from apogee back to perigee. Since it is the time prior to apogee on the second transfer ellipse orbit which is particularly critical for the SCADS

determination, the optical axis should point away from the earth as much as possible on that orbital segment. Thus, the optical axis should make an obtuse angle with the positive spin axis and the negative spin axis becomes identified with the scan axis for the spinning mode. On the transfer ellipse, then, the scan axis will have a nominal direction of ($\alpha_{scan} = \Omega - 90^{\circ}$, $\delta_{scan} = 20^{\circ}.7$ or 23°). Figures 8 and 9 show the angle ψ_E from the scan axis to the earth's limb and also the half angle subtended by the earth at the spacecraft on the transfer ellipse as a function of the time after apogee. Note that in each case the angle ψ_E from the nominal scan axis to the earth's limb is about 92° at two hours prior to apogee and about 68° at two hours after apogee.

The earth's limb can approach as close as $\xi_E = (\psi_E - \Gamma - \epsilon_u)$ to the optical axis where Γ is the cant angle of the optical axis from the scan axis and ϵ_u is the uncertainty (10°) in the scan axis. The angle ξ_E becomes the angle to which the bright object shield must be designed. Note further that Γ is a constant for a particular design and ϵ_u is 10° throughout the study of the spinning mode. Thus, if a shield can be designed to handle $\psi_E = 68^{\circ}$ at two hours after apogee, the system will be shielded from the earth over the entire range from -5 hours to +2 hours after apogee, rather than just $\pm$ 2 hours. This gives the potential of five hours in which SCADS is continuously operational immediately prior to the critical second apogee point.

In the synchronous orbit, spin-stabilized mode, the scan axis will lie close to, ($\alpha_{scan} = \Omega - 90^{\circ}$, $\delta_{scan} = 20^{\circ}.7$ or 23°) or in, ($\alpha_{scan} = \Omega \mp 90^{\circ}$, $\delta_{scan} = 0^{\circ}$) the equatorial plane. Thus, no matter what the value of Γ may be, the optical field of view will scan through the earth on some portion of each synchronous orbit. However, if SCADS is adequately shielded on the transfer ellipse near the spacecraft apogee position ($\alpha_{S/C} = \Omega$, $\delta_{S/C} = 0$ relative to earth center), then it will remain adequately shielded near that same point on the synchronous orbit. This is sufficient to insure that SCADS will be operational in the presence of the earth for the final orbit corrections.

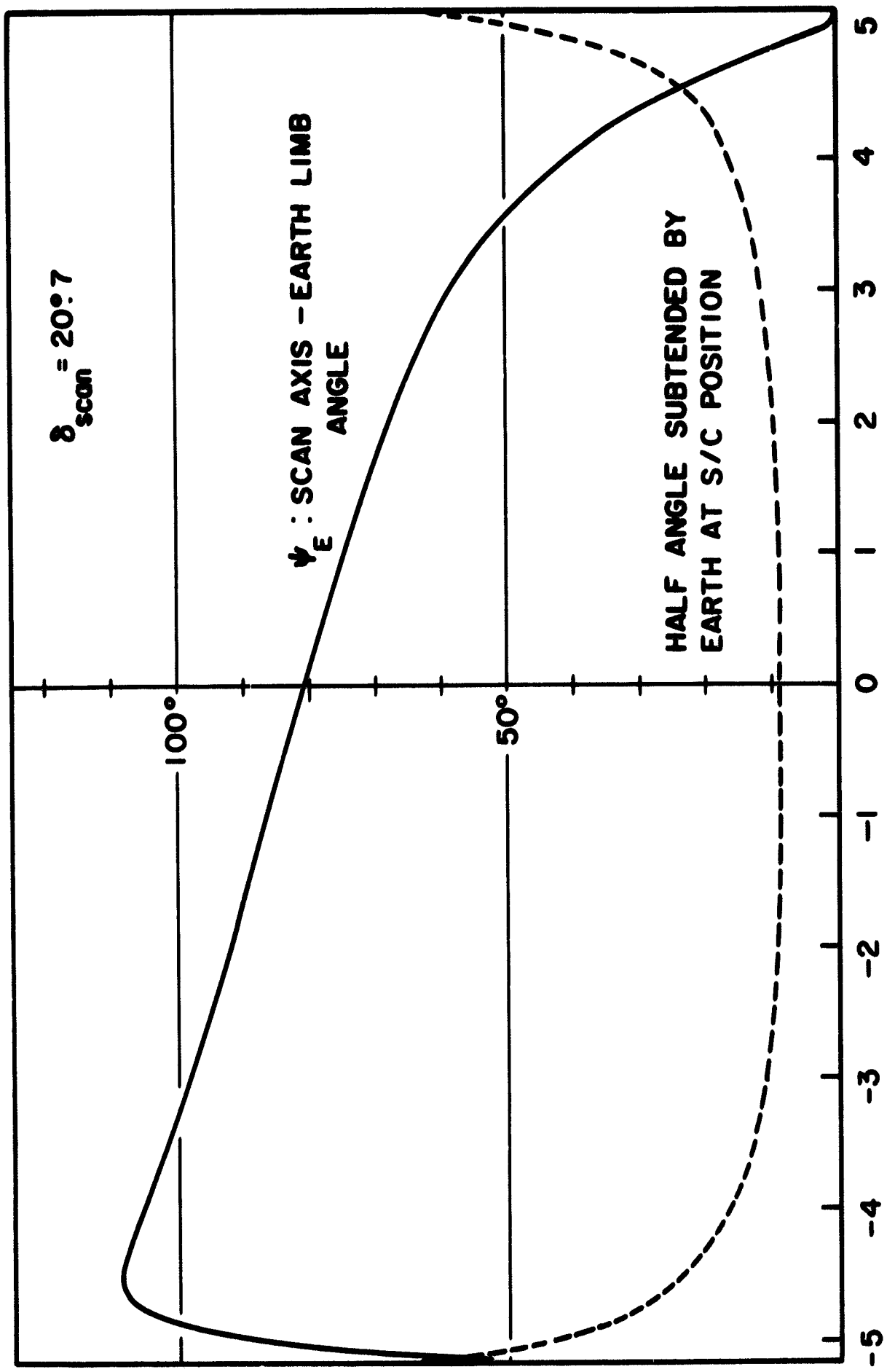


Figure 8: The Earth as seen from the spacecraft on the transfer ellipse with orbital inclination $i = 22^{o}.3$ and nominal spin axis declination $\delta_{spin} = -20^{o}.7$.

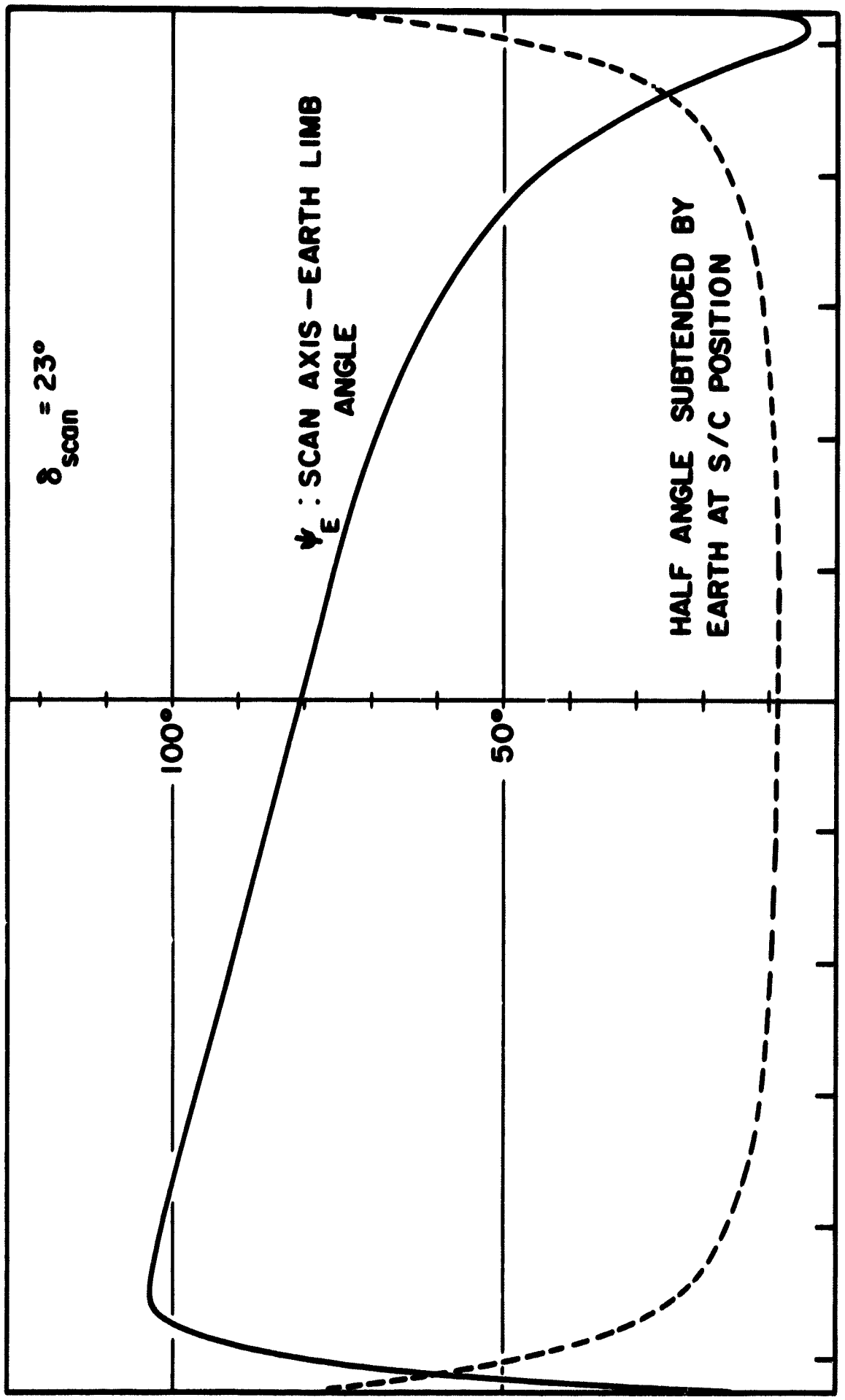


Figure 9: The Earth as seen from the spacecraft on the transfer ellipse with orbital inclination $i = 26^{o}.25$ and nominal spin axis declination approximately $\delta_{spin} = -23^{o}$.

In the three-axis controlled synchronous orbit, a dual mode sensor--i.e. one designed to operate as a completely passive scanner in the spinning mode and then provide its own reticle motion in the three-axis controlled mode--would look out at an acute angle with respect to the former negative spin axis which is now the negative yaw axis. Thus, the sensor would always be looking away from the earth. If a separate SCADS system is chosen ior the three-axis controlled mode, it can be oriented near the positive or negative pitch axis which points clcse to the north or south celestial pole. In this position, it would avoid all three objects since $|\delta_{SUN}|_{max} = 23^{\circ}.4$ and $|\delta_{MOON}|_{max} = 28^{\circ}.5$.

2. The Sun

For the transfer ellipse scan axis ($\alpha_{scan} = \Omega - 90^{\circ}$, $\delta_{scan} = 20^{\circ}.7$ or 23°) and for three of the five possible scan axes in the spinning synchronous mode--($\alpha_{scan} = \Omega - 90^{\circ}$, $\delta_{scan} = 20^{\circ}.7$ or 23°), ($\alpha_{scan} = \Omega - 90^{\circ}$, $\delta_{scan} = 0^{\circ}$), and ($\alpha_{scan} = \Omega + 90^{\circ}$, $\delta_{scan} = 0^{\circ}$)--the angle between the scan axis and the sun depends on both the time of year (i.e. on α_{SUN}, δ_{SUN}) and on the point of insertion of the spacecraft into the synchronous orbit ($\alpha_{S/C} = \Omega$, $\delta_{S/C} = 0$). However, for the other two possible scan axes ($\delta_{scan} = \pm 90^{\circ}$), the angle between the scan axis and the sun line depends only on the declination of the sun. Here, the nominal scan axis-sun line angle is given by $\Psi_S = 90^{\circ} \pm |\delta_{SUN}|$. The minimum value of Ψ_S occurs at the solstices when $|\delta_{SUN}|$ is maximum; this value is just $\Psi_S = 66^{\circ}.557$.

A number of observations may be made here. First, SCADS must operate in one of these two modes if an orbit inclination correction is required. Second, it is desirable that no SCADS-imposed restrictions be placed on the date of launch within the year; $\Psi_S = 66^{\circ}.557$ is possible. Third, the angle between the sun line and the optical axis can be as small as $\xi_S = \Psi_S - \Gamma - \epsilon_u$ where Γ and ϵ_u are the cant angle and scan axis uncertainty as before. Note further that if Θ denotes the full field of view of the SCADS optical system, then the outer edge of this optical system makes an angle of

($\Gamma + \Theta/2$) with the scan axis and can come to within ($\psi_S - \Gamma - \Theta/2 - \epsilon_u$) of the sun--see Figure 10. If the values $\psi_S = 66^\circ.557$ and $\epsilon_u = 10^\circ$ are used, the sun may come within ($56^\circ.557 - \Gamma - \Theta/2$) from the edge of the field of view. For the wide field of view optical system (large Θ) required by SCADS, this results in a rather difficult sun shielding problem. However, as noted above, SCADS must operate in the ($\delta_{scan} = \pm 90^\circ$) orientations so the condition

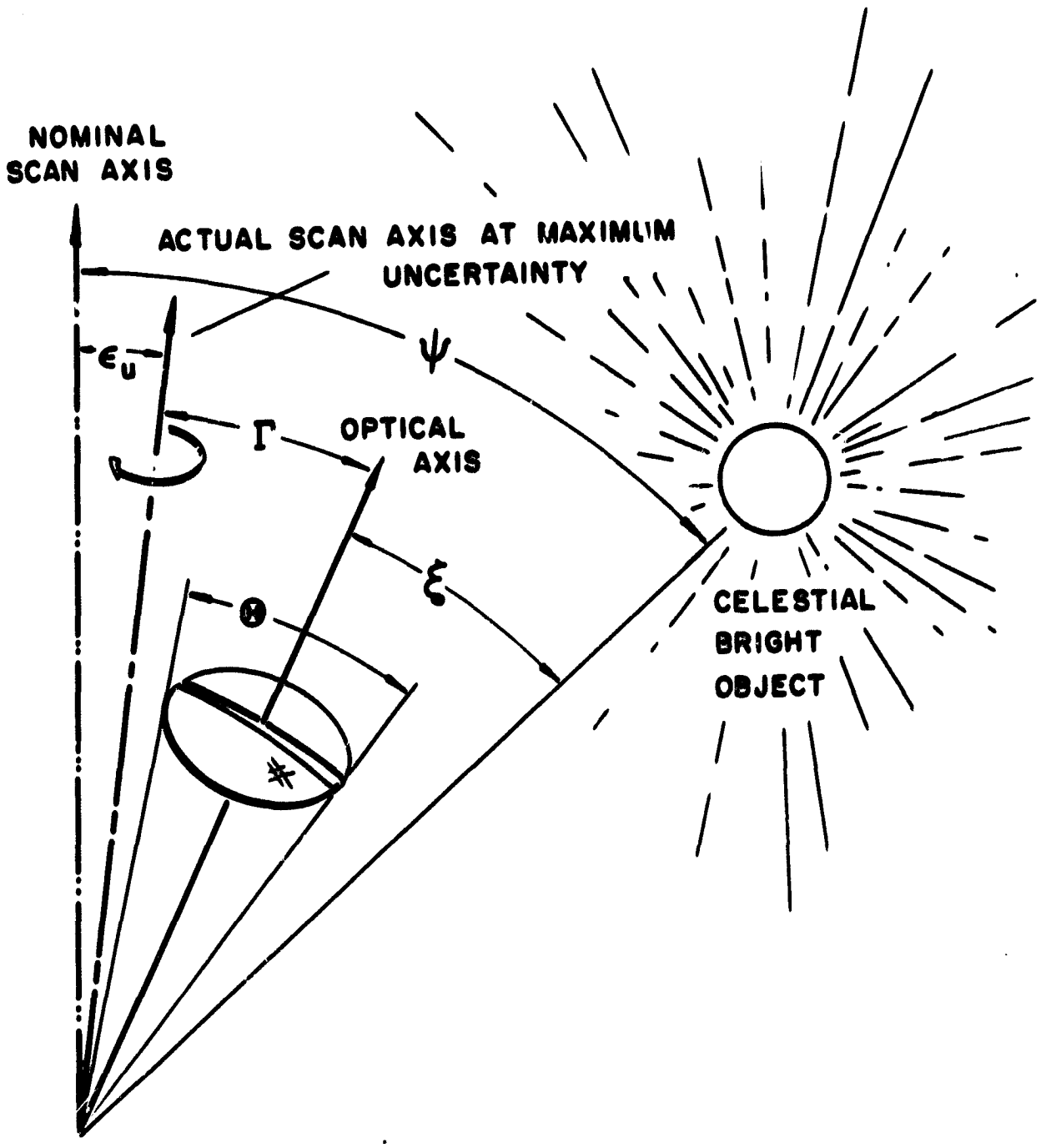
$$\psi_S \geq 66^\circ.557 \tag{5}$$

is chosen as a constraint.

This has three major consequences. First, a detailed study must be performed to optimize the joint selection of the cant angle Γ, the optical field of view Θ, and the sun shield design. Second, if a sun shield can be designed to meet this constraint, then the earth shield problem is solved automatically since $\psi_E \geq 68^\circ$. The shield problem is discussed later. Finally, the constraint in (5) is reflected back to the other three possible scan axis directions and implies a permissible range on Ω; that is, it specifies a SCADS imposed launch window as a function of the date in the year.

The range in permissible launch conditions is conveniently specified in terms of the angle between the sun line and the spin axis at synchronous insertion. Let the reference direction of the spin axis at insertion be characterized by (α^r_{spin}, δ^r_{spin}) where $\delta^r_{spin} = -20^\circ.7$ or -23°. Then, the three possible nominal directions for the scan axis are described by (α_{scan}, δ_{scan}) = ($\alpha^r_{spin} - 180^\circ$, $-\delta^r_{spin}$) at the moment of insertion, ($\alpha^r_{spin} - 180^\circ$, 0°) if under-energy corrections are to be made and (α^r_{spin}, 0°) if over-energy corrections are needed. The angle ψ_S between the sun line and the <u>scan</u> axis is specified by

$$\cos \psi_S = \cos \delta_{scan} \cos \delta_{SUN} \cos(\alpha_{SUN} - \alpha_{scan}) + \sin \delta_{scan} \sin \delta_{SUN}. \tag{6}$$



ψ = angle from nominal scan axis to celestial bright object

ϵ_u = uncertainty in actual scan axis direction with respect to the nominal scan axis

Γ = cant angle of optical axis with respect to the scan axis

Θ = optical field of view

ξ = required shield angle

Figure 10: Principal angles for the spinning mode SCADS sensor

Similarly, the angle Φ_{SS} between the sun line and the reference spin axis is given by

$$\cos \Phi_{SS} = \cos \delta^{r}_{spin} \cos \delta_{SUN} \cos(\alpha_{SUN} - \alpha^{r}_{spin}) + \sin \delta^{r}_{spin} \sin \delta_{SUN}. \quad (7)$$

Equations (6) and (7) may be combined with the relations describing the scan axis direction in terms of the reference spin direction. Further, the angle ψ_S from the nominal scan axis to the sun line must satisfy the inequality in (5) . The following three constraint relations on the permissible value of Φ_{SS}, the spin axis-sun line angle at insertion, result:

$$\cos \Phi_{SS} \geq -\cos 66^{\circ}.557 \quad (8)$$

from the scan axis direction at insertion,

$$\cos \Phi_{SS} > -\cos 66^{\circ}.557 \cos \delta^{r}_{spin} + \sin \delta_{SUN} \sin \delta^{r}_{spin} \quad (9)$$

from the scan axis direction in the under-energy eccentricity correction mode, and

$$\cos \Phi_{SS} \leq \cos 66^{\circ}.557 \cos \delta^{r}_{spin} + \sin \delta_{SUN} \sin \delta^{r}_{spin} \quad (10)$$

from the scan axis direction in the over-energy eccentricity correction mode. All three of relations (8), (9), and (10) must be satisfied. The smaller value of the two limits on Φ_{SS} from equations (8) and (9) yields an upper bound; the limit on Φ_{SS} from (10) yields a lower bound. The resulting SCADS-imposed "launch window" is shown as the range between curves I and II in Figure 11 for $\delta_{spin} = -20^{\circ}.7$ and in Figure 12 for $\delta_{spin} = -23^{\circ}$ as a function of the date in 1971. The flat portion of the upper bound (Curve I) corresponds to a region where relation (8) dominates; in the adjacent curved regions, constraint (9) dominates.

Note that the lower bound (Curve II) is imposed by the requirement that

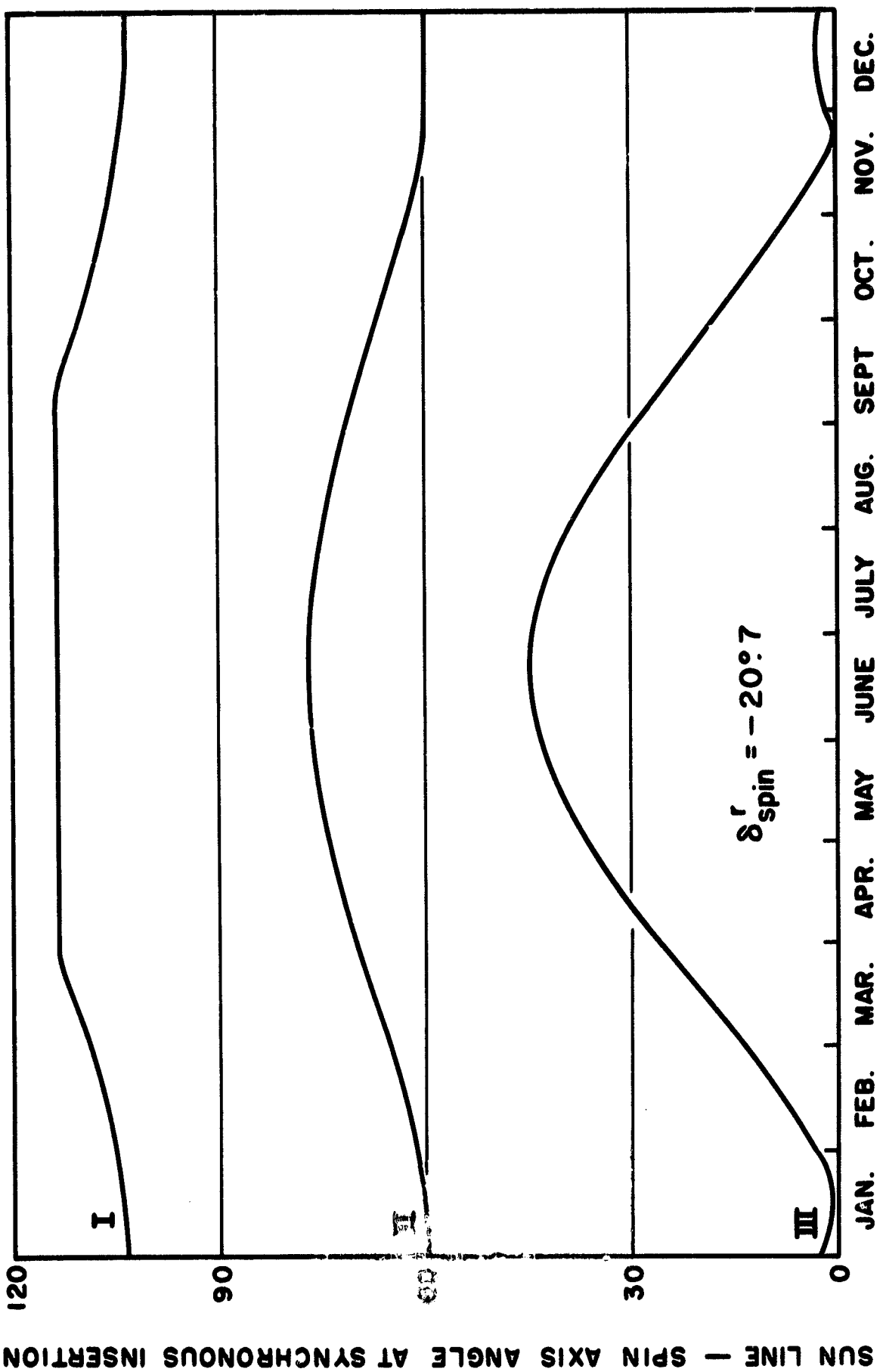


Figure 11: SCADS solar launch window; allowed range of the sun line-spin axis angle Φ_{SS}. Interference from the sun is avoided over all spin stabilized portions of the ATS F&G mission. The results correspond to a transfer ellipse orbital inclination i = $22.^{o}3$ and spin axis delination δ_{spin} = $-20.^{o}7$. The significance of Curve I, II, and III is described in the text.

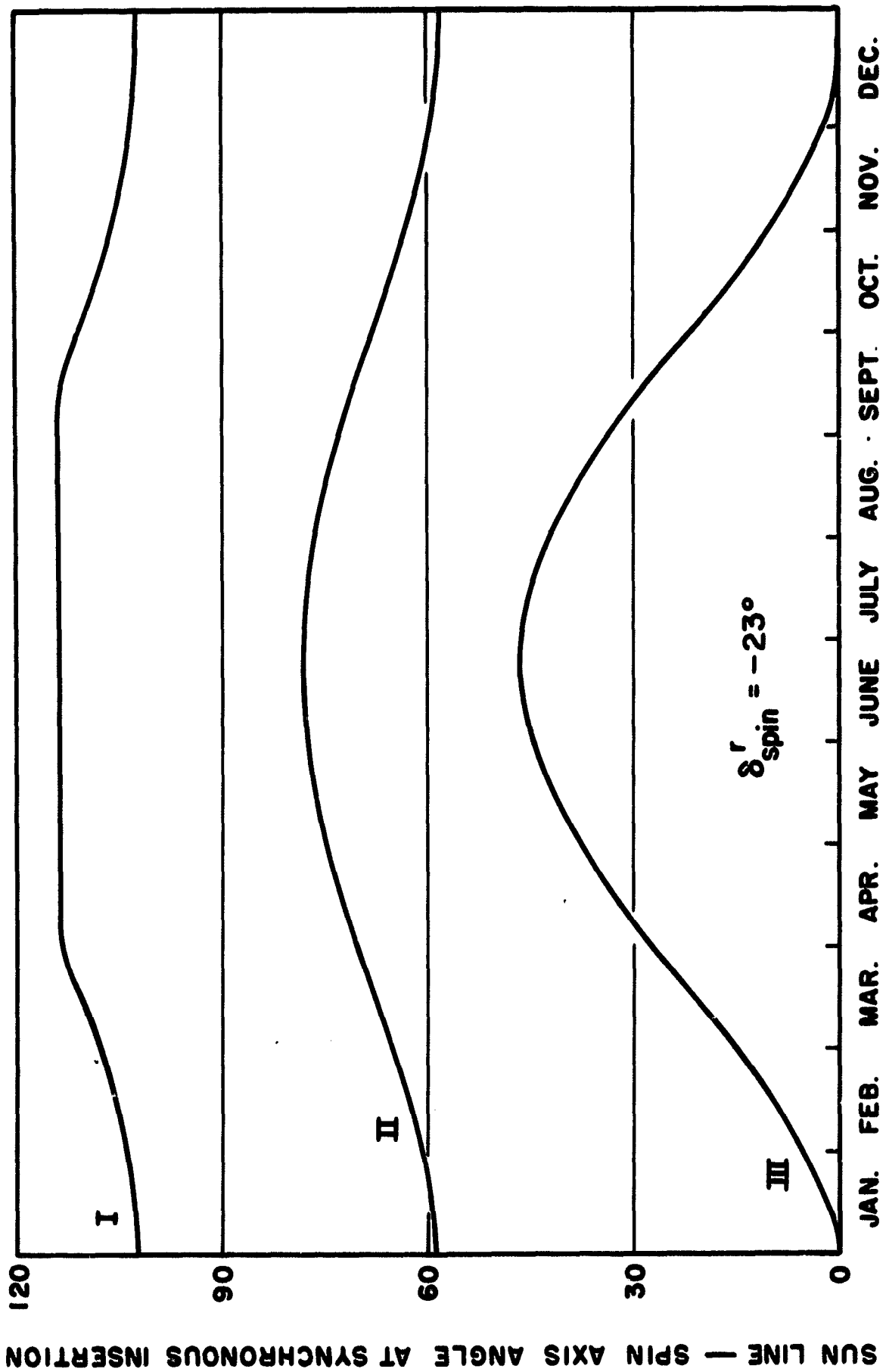


Figure 12: SCADS solar launch window; allowed range of the sun line-spin axis angle ϕ_{SS}. Interference from the sun is avoided over all spin stabilized portions of the ATS F&G mission. The results correspond to a transfer ellipse orbital inclination $i = 26.^{o}25$ and spin axis declination approximately $\delta_{spin} = -23^{o}$. The significance of Curve I, II, and III is described in the text.

SCADS operate when the scan axis is oriented in the direction appropriate to an "over-energy" eccentricity correction. If the mission is carried out in such a manner that an under-energy insertion is insured (or if the thrust of the orbit correction engines can be reversed without reversing the entire spacecraft), then the lower bound represented by Curve II and relation (10) can be removed. Under these circumstances, the minimum permissible angle, Φ_{SS}, between the sun line and the nominal spin axis at insertion is limited only by the difference in the declinations of the sun and the reference spin axis $|\delta_{SUN} - \delta^{r}_{spin}|$. This limitation is shown as curve III in Figures 11 and 12.

It should be pointed out that the curves presented here actually represent two launch windows per day. Once a value for Φ_{SS} within the launch window is specified, equation (7) implies a value for $|\alpha_{SUN} - \alpha^{r}_{spin}|$ or two possible values for α^{r}_{spin} -- one on either side of α_{SUN}. But $\alpha^{r}_{spin} = \Omega + 90^{o}$ where Ω is the right ascension of the transfer ellipse apogee and the point of synchronous insertion. Thus, each allowed value of Φ_{SS} corresponds to two possible insertion points. Since the allowed values of Φ_{SS} are near 90^{o} (see Figures 11 and 12), α^{r}_{spin} is near $\alpha_{SUN} \pm 90^{o}$ and Ω is near α_{SUN} (local noon) or $\alpha_{SUN} + 180^{o}$ (local midnight). Thus, the two different insertion points may be characterized as a "day mode" and a "night mode" with respect to local time--tentatively corresponding to 53^{o}W longitude.

3. The Moon

It was possible above to discuss the operation of SCADS in the presence of the sun and the sunlit earth in terms of the orbital and orientation configurations expected in the mission with very little reference to the detailed design of the SCADS instrument. Only the selection of a constraint on the minimum angle between the sun line and the nominal scan axis was required. However, investigation of possible lunar interference with SCADS requires more specific information about the system.

SCADS CELESTIAL ENVIRONMENT ANALYSES

The moon presents a serious problem only when it falls directly within the optical field of view over a portion of the scan. Further, the moon itself travels quite rapidly through the sky (about 13^{o} per day) so that it will pass across a chord of a typical SCADS annular field of view and beyond the point of interference in a relatively short time--usually in a day or two. Thus, the only critical problem with the presence of the moon occurs during the one and one-half traversals of the transfer ellipse--a time period of about 16 hours. The possible intrusion of the moon imposes additional restrictions on the launch window. These constraints are outlined below for the recommended designs--developed later in the report--for both the spin mode sensor and the dual mode sensor. As with the sun, these constraints will be expressed in terms of permissible values for the nominal spin axis-sun line angle ϕ_{SS} at synchronous insertion.

A series of factors must be taken into account. First, it is assumed that SCADS becomes inoperable whenever the moon's apparent direction lies closer to the scan axis than the outer angular radius of the annular field of view; this outer or exterior radius is denoted by θ_e. The constraint is then expressed as

$$\psi_M > \theta_e + \epsilon_u \tag{11}$$

where ψ_M is the angle from the nominal scan axis to the apparent moon line and ϵ_u is the uncertainty of the actual scan axis relative to its nominal direction.

Second, the geocentric position of the moon must be accurately known as a function of time. For this purpose, a truncated version of E. W. Brown's lunar position series such as that published in Battin[6] is appropriate. The coefficients in this series were first updated very accurately from the base date of Greenwich mean noon January 0, 1900 to midnight at the beginning of 1971. This removes the effect of the large number of complete lunar orbits

which would otherwise have to be carried along. This is important because only a fixed number of significant digits can be saved in a computer word and an angular position which must carry a large number of complete revolutions (high order digits) will lose accuracy in the last partial revolution (low order digits) due to round off error. It is, of course, only the last partial orbit which is of importance in determining the current position of the moon. The resulting expressions were encoded as a FORTRAN subroutine which requires the input of time in fractional Julian days from the beginning of 1971 and returns the corresponding geocentric position of the moon in terms of celestial direction cosines.

Third, the moon is sufficiently close so that its parallax may be significant for a spacecraft at synchronous altitude. Since the nominal scan direction is fixed in space for a particular transfer ellipse, the possibility of lunar interference is evaluated only at the critical times corresponding to the first and second apogee points when the spacecraft is at $\alpha_{S/C} = \Omega$, $\delta_{S/C} = 0^{\circ}$ and synchronous altitude. The apparent position of the moon as seen from the spacecraft is then expressed in terms of geocentric lunar coordinates and the right ascension Ω of the transfer ellipse apogee.

The last factors which must be accounted for are the relations among the sun line-spin axis angle Φ_{SS}, Greenwich time in fractional Julian days from the beginning of 1971, and the location of the transfer ellipse apogee characterized by Ω. Insertion into the synchronous orbit is to occur at the second apogee (and equatorial crossing) and will correspond nominally to a point at 53°W longitude. At Greenwich midnight, the right ascension of Greenwich is $[\alpha_{SUN}(D_{71}) + 180^{\circ}]$ modulo 360° where α_{SUN} is the right ascension of the sun at D_{71} integral Julian days after the beginning of 1971. If t represents current Greenwich time expressed as a fraction of one Julian day (i.e. $t < 1$), then the current right ascension of Greenwich is given by $[\alpha_{SUN}(D_{71}) + 180^{\circ} + 360^{\circ}.986t]$ modulo 360°; the coefficient $360^{\circ}.986$ is just the angle through which the earth turns in a mean solar day. The current

right ascension of 53°W longitude is then given by

$$\Omega = [\alpha_{SUN}(D_{71}) + 180^{\circ} + 360^{\circ}.986t - 53^{\circ}] \text{ modulo } 360^{\circ}. \quad (12)$$

This is the desired relation between Ω and time. Note that the current time in fractional Julian days from the beginning of 1971 is just

$$t_{71} = D_{71} + t. \quad (13)$$

For any given value of t, the current position of the sun and the geocentric position of the moon are to be evaluated at t_{71}; however, α_{SUN} in equation (12) is still to be evaluated at D_{71}.

Once $\Omega(t)$ and $[\alpha_{SUN}(t_{71}), \delta_{SUN}(t_{71})]$ have been found, the angle Φ_{SS} between the spin axis and the sun line can be found from $[\alpha_{spin} = (\Omega + 90^{\circ}), \delta_{spin} = -20^{\circ}.7 \text{ or } -23^{\circ}]$ and equation (7). Also, the angle Ψ_M between the scan axis and the spacecraft-moon line can be determined and tested in the constraint relation (11). If this constraint is not satisfied, the moon may intrude into the field of view and the time t_{71} (i.e. Greenwich time t on date D_{71} + 1) and corresponding Φ_{SS} are excluded as a possible point for synchronous orbit insertion.

The factors described above have been integrated into a computer program to determine the lunar restrictions on the satellite launch. A representative sample of the combined solar-lunar launch window results is shown for $\theta_e = 30^{\circ}.75$ and $\delta_{spin} = -20^{\circ}.7$ in Figures 13 and 14. The solar imposed limits have the same significance as that described in connection with Figure 11.

Note that the problem of interference from the moon is different for the "day" and "night" insertion modes. Fortunately, no more than one of the two modes is affected on any particular date. Thus, at least one launch window is available on each date in 1971. The results for other recommended

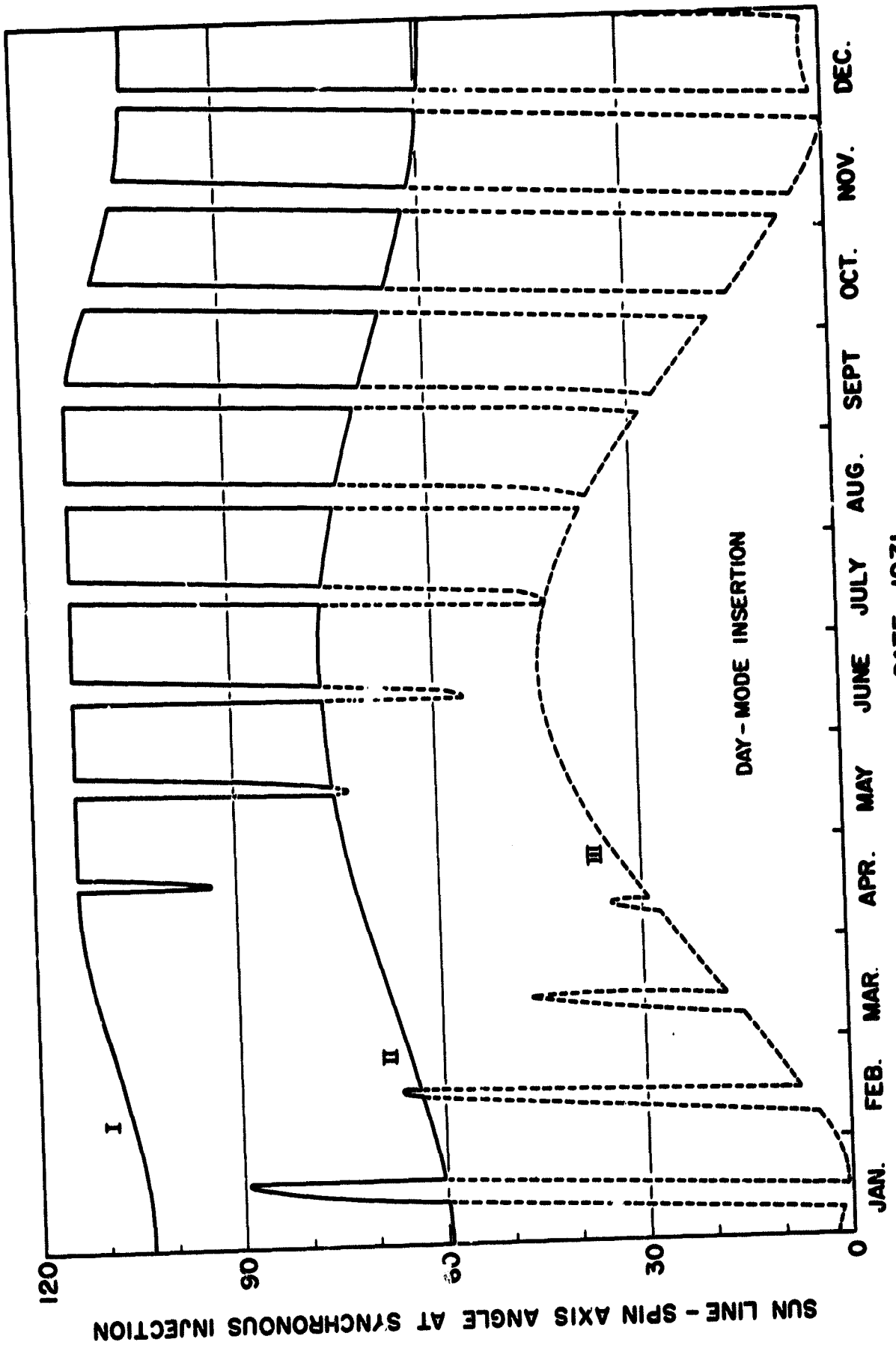


Figure 13: Combined solar-lunar launch window for day-mode insertion; allowed values of δ_{SS}. The transfer ellipse orbital inclination is $i = 22^{o}.3$, the nominal spin axis declination is $\delta_{spin} = -20^{o}.7$, and the outer radius of the annular field of view is $\theta_e = 30^{o}.75$.

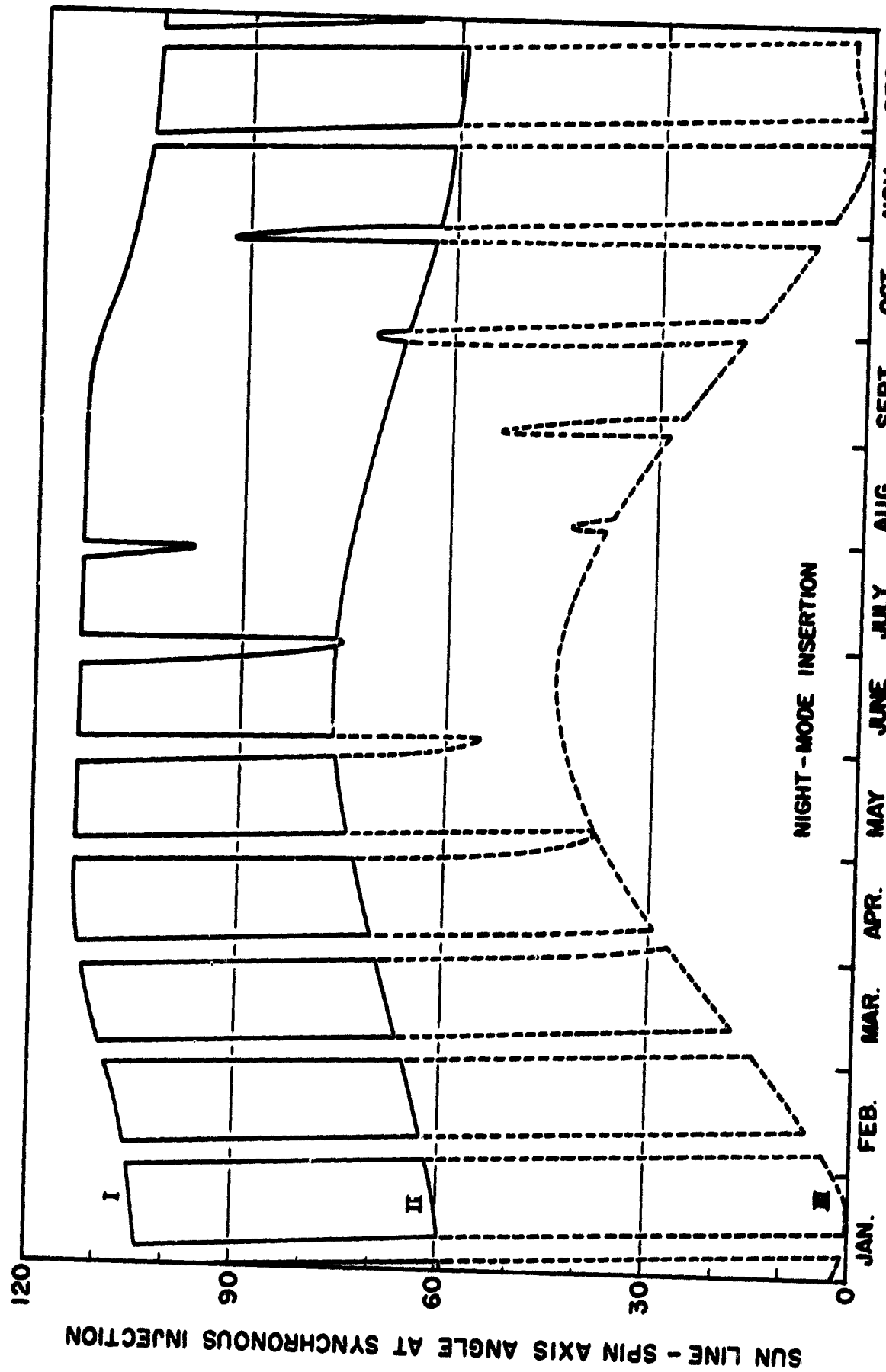


Figure 14: Combined solar-lunar launch window for night-mode insertion; allowed values of ϕ_{SS}. The transfer ellipse orbital inclination is $i = 22^{\circ}.3$, the nominal spin axis declination is $\delta = -20^{\circ}.7$, and the outer radius of the annular field of view is $\theta_e = 30^{\circ}.75$.

combinations of θ_e and δ_{spin} are presented as Table I.

4. Bright Object Interference in the Three-axis Controlled Mode

The analyses above apply principally to the spin stabilized portion of the mission. Thus, the constraints developed there must be met by both the spin mode sensor and the dual mode sensor; these constraints will dominate the design of each sensor and the selection of its location on the spacecraft.

In the case of a sensor which is required to operate only in the three-axis controlled mode, a different set of conditions may be applied. In this mode, the median direction of the spacecraft Y or pitch axis points along the line between the north and south celestial poles. Since the Z axis can be directed at any point on the earth, the Y axis has an uncertainty, ϵ_u, of approximately $8^\circ.7$ relative to this nominal line ($\delta_Y = \pm 90^\circ$).

From synchronous altitude, the earth's limb satisfies the condition

$$|\delta_{EARTH}| \leq 8^\circ.7 \tag{14}$$

Further, the sun and the moon satisfy

$$|\delta_{SUN}| \leq 23^\circ.5 \tag{15}$$

and

$$|\delta_{MOON}| \leq 31^\circ.8 \tag{16}$$

where correction has been made for the moon's parallax as seen from the spacecraft. Thus, if the SCADS axis in the three-axis controlled mode lies close to the Y axis, the earth, sun, and moon will never intrude directly into the field of view.

TABLE I

Dates in 1971 when the moon may enter the SCADS field of view during the transfer ellipse. For each range of dates, the insertion mode--day or night--is also indicated. It is assumed that the insertion in each case is subject to the solar constraint presented by Curves I and II in Figures 11 and 12.

Spin-mode Sensor: $\theta_e = 30^\circ.75$			
$\delta_{scan} = 20^\circ.7$		$\delta_{scan} = 23^\circ$	
Dates of lunar interference	Mode	Dates of lunar interference	Mode
1 - 10	Night	1 - 10	Night
14 - 20	Day	14 - 20	Day
29 - 39	Night	29 - 40	Night
46 - 47	Day	46	Day
58 - 69	Night	59 - 69	Night
88 - 99	Night	88 - 98	Night
109 - 113	Day	109 - 113	Day
117 - 127	Night	117 - 127	Night
136 - 142	Day	137 - 142	Day
146 - 156q	Night	146 - 156	Night
164 - 172	Day	164 - 172	Day
176 - 184	Night	176 - 184	Night
193 - 201	Day	193 - 201	Day
206 - 211	Night	207 - 210	Night
222 - 230	Day	222 - 230	Day
251 - 260	Day	251 - 260	Day
280 - 289	Day	280 - 289	Day
300 - 305	Night	300 - 305	Night
309 - 319	Day	309 - 319	Day
327 - 335	Night	327 - 335	Night
338 - 347	Day	338 - 347	Day
355 - 364	Night	355 - 365	Night

TABLE I
(continued)

Dual-mode Sensor: $\theta_e = 20^\circ$			
$\delta_{scan} = 20^\circ.7$		$\delta_{scan} = 23^\circ$	
Dates of lunar interference	Mode	Dates of lunar interference	Mode
1 - 9	Night	1 - 9	Night
15 - 18	Day	15 - 17	Day
30 - 39	Night	30 - 39	Night
59 - 68	Night	59 - 68	Night
88 - 98	Night	88 - 97	Night
118 - 126	Night	118 - 127	Night
138 - 141	Day	138 - 141	Day
147 - 155	Night	147 - 154	Night
165 - 171	Day	166 - 171	Day
177 - 182	Night	177 - 181	Night
193 - 200	Day	194 - 200	Day
222 - 229	Day	222 - 230	Day
251 - 259	Day	252 - 259	Day
280 - 288	Day	281 - 288	Day
303 - 304	Night	303	Night
310 - 317	Day	310 - 317	Day
329 - 334	Night	329 - 334	Night
339 - 345	Day	339 - 345	Day
356 - 364	Night	357 - 364	Night

Another problem arises however. It is expected that the spacecraft solar panels may also be mounted along the Y axis on long booms. Thus, the SCADS field of view would have to be canted away from the Y axis to exclude these panels and booms. Further, this portion of the spacecraft structure will probably scatter a significant amount of direct and earth-reflected sunlight. Since the design of the spacecraft is likely to evolve further, specific constrains on this shielding problem are difficult to formulate here. However, three general guidelines may be stated.

First, there are a greater number of bright stars near the south celestial pole than near the north pole. Thus, the three-axis controlled mode sensor should point south to maximize target availability.

Second, if the SCADS instrument is to be mounted in the aft equipment module of the spacecraft, it should be located in the Y-Z plane canted away from the Y axis toward the negative Z direction. Note that this has the further advantage of moving the SCADS axis away from the earth.

Finally, if the SCADS instrument is to be mounted in the forward module (at the focus of the parabola), it should again be located in the Y-Z plane but now it should be tilted toward the positive Z axis. In this position, more elaborate shielding from the earth is required but the problem of light reflected from the booms should be reduced. Note that this location places the three-axis controlled mode SCADS in the same package with most of the instruments that require its attitude reference information. Thus, the question of flexure of the truss support between the aft and forward modules does not enter in interpreting and using the attitude determination.

B. SCADS Stellar Target Availability

With a single scanning slit, SCADS requires a minimum of three spatially independent stellar targets to solve the three-axis attitude problem. Thus, if the system is to operate for a random pointing direction on the celestial sphere and if the stars in its field of view are ordered according to decreasing brightness (increasing stellar magnitude), then it must be capable of detecting the faintest third star that it will encounter. As noted earlier, determination of the limiting magnitude of the system requires a "worst case" analysis.

Figure 15 represents the results of a computer simulation using a catalog of the position and photographic magnitude of all stars brighter than fifth magnitude. A field of view in the form of a spherical cap (i.e. the degenerate annulus with $\theta_i = 0$ -- see Figure 7) was "pointed" successively at over 10,000 positions on the celestial sphere. For each pointing direction, the magnitude of the third brightest star was determined. Then, the faintest third-brightest star represents a measure of the limiting magnitude required for that field of view for a random pointing direction.

Note that the effective field of view Θ_{eff} along the abscissa in Figure 15 denotes the full cone angle of the corresponding spherical cap. This field of view covers an area on the celestial sphere given by

$$A_{cap} = 2\pi(1 - \cos \frac{\Theta_{eff}}{2}) \qquad (17)$$

steradians. It is assumed that an annular field of view which covers the same area on the celestial sphere will have the same or brighter limiting magnitude. This is supported by the following argument. The faintest third star occurs for pointing directions which are close to the south galactic pole--i.e. close to a line perpendicular to the plane of the Milky Way. If the spherical-cap field of view is replaced by an annular field of the same area and the pointing directions of both fields are near the sparsely

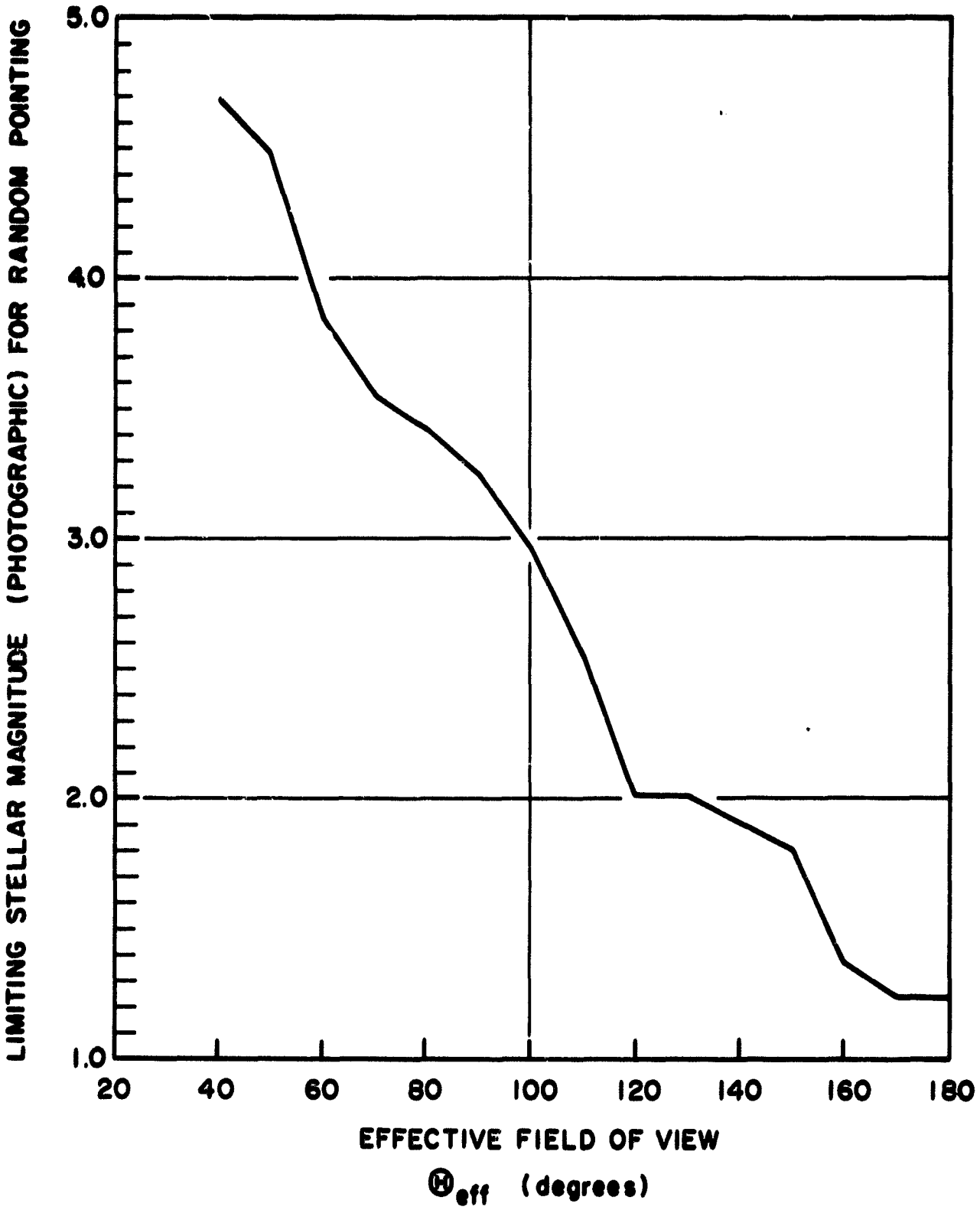


Figure 15: Limiting stellar magnitude required to insure the presence of at least three detectable stars in a given field of view for a random pointing direction on the celestial sphere. The results were obtained from a computer star search over a uniform grid containing in excess of 10,000 "pointing" directions.

populated south galactic pole, then portions of the annular field will be further from the pole and closer to the densely populated Milky Way. Thus, the annulus should contain as many as or more bright stars than the spherical cap.

The area of an annular field of view of interior and exterior radii θ_i and θ_e is given by

$$A_{annulus} = 2\pi(\cos\theta_i - \cos\theta_e) \tag{18}$$

steradians. Then, the effective field of view Θ_{eff} corresponding to a given annulus is found by equating A_{cap} to $A_{annulus}$. Once the Θ_{eff} is known, the curve in Figure 15 can be used to obtain an a priori estimate for the required limiting magnitude, M_l of the system. This is very helpful for preliminary SCADS design considerations before a detailed star availability search has been performed over the actual pointing directions expected in the specific mission. This a priori value of M_l is almost certainly too faint unless the region of the south galactic pole is included in the profile of possible scan axes. Nevertheless, it gives a safe value if no further analysis is performed.

1. Possible Scan Axis Directions: SCADS/ATS F & G

In the discussion of potential interference from the earth (Section IIA1) the scan axis for SCADS in the spinning mode is selected as the negative spin axis (the negative Z axis for the spacecraft). As noted earlier, the profile of the spin stabilized portion of the mission indicates that the nominal scan axis may take on any of five possible directions characterized by

$$(\alpha_{scan}, \delta_{scan}) = (\Omega - 90^\circ, 20.^\circ7 \text{ or } 23^\circ), \tag{19}$$

$$(\alpha_{scan}, \delta_{scan}) = (\Omega \pm 90^\circ, 0^\circ), \tag{20}$$

or $$\delta_{scan} = \pm 90^{o}. \tag{21}$$

Again, Ω is the right ascension of the synchronous orbit insertion point and depends on both the date and time of launch. Further, the actual scan axis may differ from each nominal position--at least for the purposes of this study--by as much as ten degrees in any direction.

Every possible value of Ω is permitted for at least some portion of 1971. Thus, for the nominal positions given in (19), the actual SCADS scan axis can take on any position in the band characterized by $10^{o}.7 \leq \delta_{scan} \leq 30^{o}.7$ or $13^{o} \leq \delta_{scan} \leq 33^{o}$. Similarly, for the positions given in (20), the scan axis can take on any direction in band $-10^{o} \leq \delta_{scan} \leq 10^{o}$. These bands may conveniently be combined into a single band around the celestial sphere given by

$$-10^{o} \leq \delta_{scan} \leq 33^{o}. \tag{22}$$

From (21), any position in the spherical caps

$$|\delta_{scan}| \geq 80^{o} \tag{23}$$

is permitted. The regions of the celestial sphere which are described by relations (22) and (23) are illustrated in Figure 16. It is these regions over which a detailed star availability search must be made.

2. Stellar Target Distributions - Spin Mode SCADS Sensor

The recommended spinning mode SCADS sensor (which is described later) has an annular field of view characterized by $\theta_i = 6^{o}.25$ and $\theta_e = 30^{o}.75$ with respect to the scan axis. The computer was used to "point" this particular field of view at a grid of directions covering the shaded regions in Figure 16. At each grid point, a list of the magnitudes of all stars which are as bright or brighter than fourth magnitude photographic and which lie within

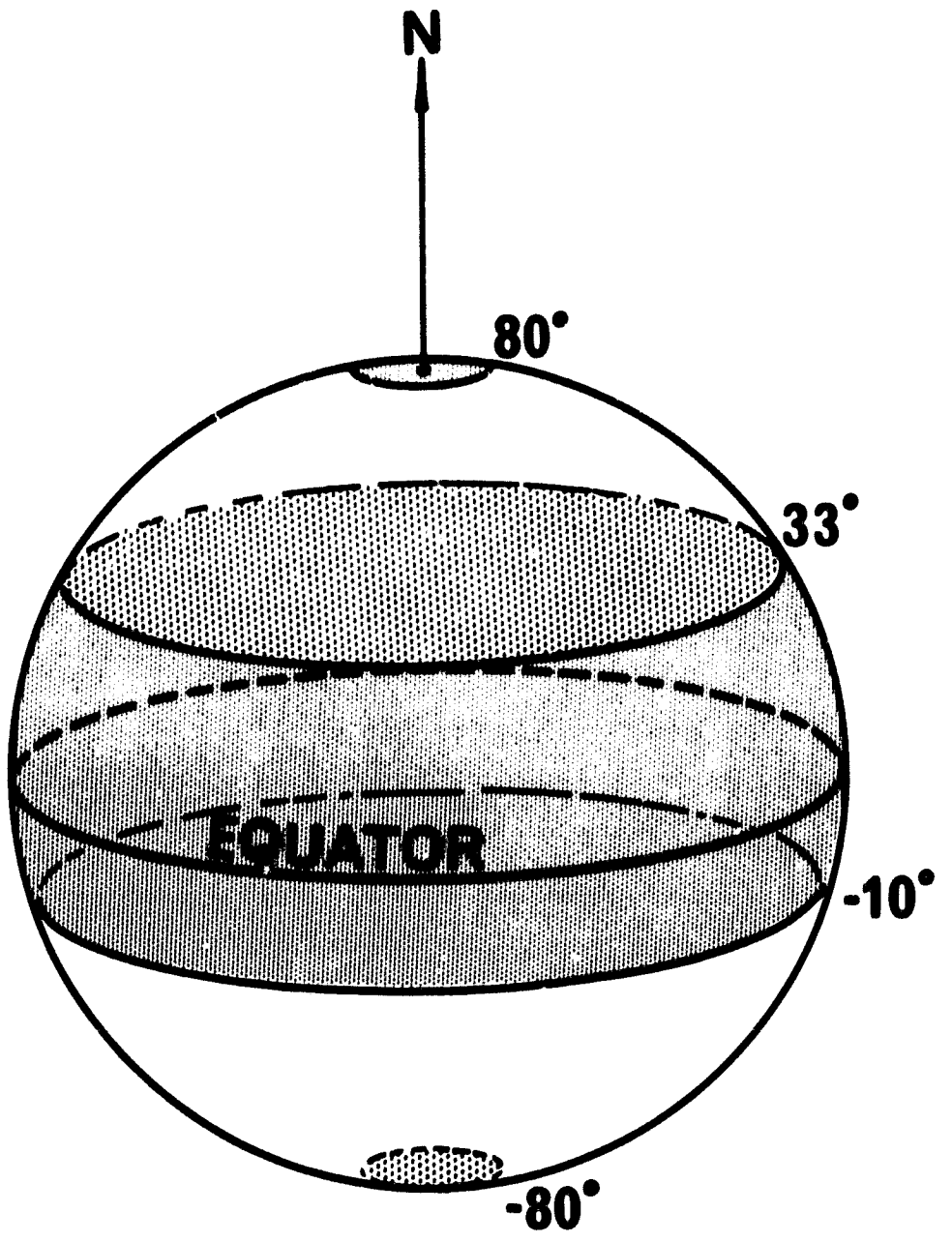


Figure 16: Possible SCADS scan axis pointing directions on the celestial sphere during the spin-stabilized portions of the ATS F&G missions

the annular field was created. The results of this search are presented below in a number of graphical forms.

In the initial series of figures, the stellar magnitudes of the second, third, fourth, and fifth brightest stars in the field are plotted as a function of the scan axis right ascension, α_{scan}, for five fixed values of the scan axis declination: $\delta_{scan} = -10^{o}, 0^{o}, 10^{o}, 20^{o}$, and 30^{o}. These results are covered in Figures 17, 18, 19, 20, and 21. For a particular scan axis direction, this data can be used to determine the approximate detection threshold (in stellar magnitude units) required to acquire two, three, four, or five stars per scan.

The next series of graphs--Figures 22, 23, 24, 25, and 26--presents the number of stars in the field of view which are at least as bright as a given parametric photographic magnitude, P_{lim}. Again, the plots correspond to five different fixed scan axis declinations. Note that the information in these particular figures is very illustrative of the variation in the density of stars over the celestial sphere. The south galactic pole occurs near $\alpha = 10^{o}$, $\delta = -30^{o}$. The closest approach of the scan axis to this region occurs along the curve for $\delta_{scan} = -10^{o}$; as shown in Figure 22, the density of stars near $\alpha_{scan} = 10^{o}$ is very low. The two dense peaks in this same figure correspond to points at which very rich portions of the Milky Way are crossed. It may also be observed from these plots that the density at the north galactic pole--approximately at $\alpha = 190^{o}$, $\delta = +30^{o}$--remains relatively high. Specifically, the graph in Figure 26 passes right through this point.

A third and very useful form in which this star availability data may be cast is presented in Figure 27. Here, lists of the magnitudes of the third and fourth brightest stars corresponding to each grid point are constructed by the computer and the lists are then sorted by increasing stellar magnitude. The position of each entry in the list is reinterpreted as a

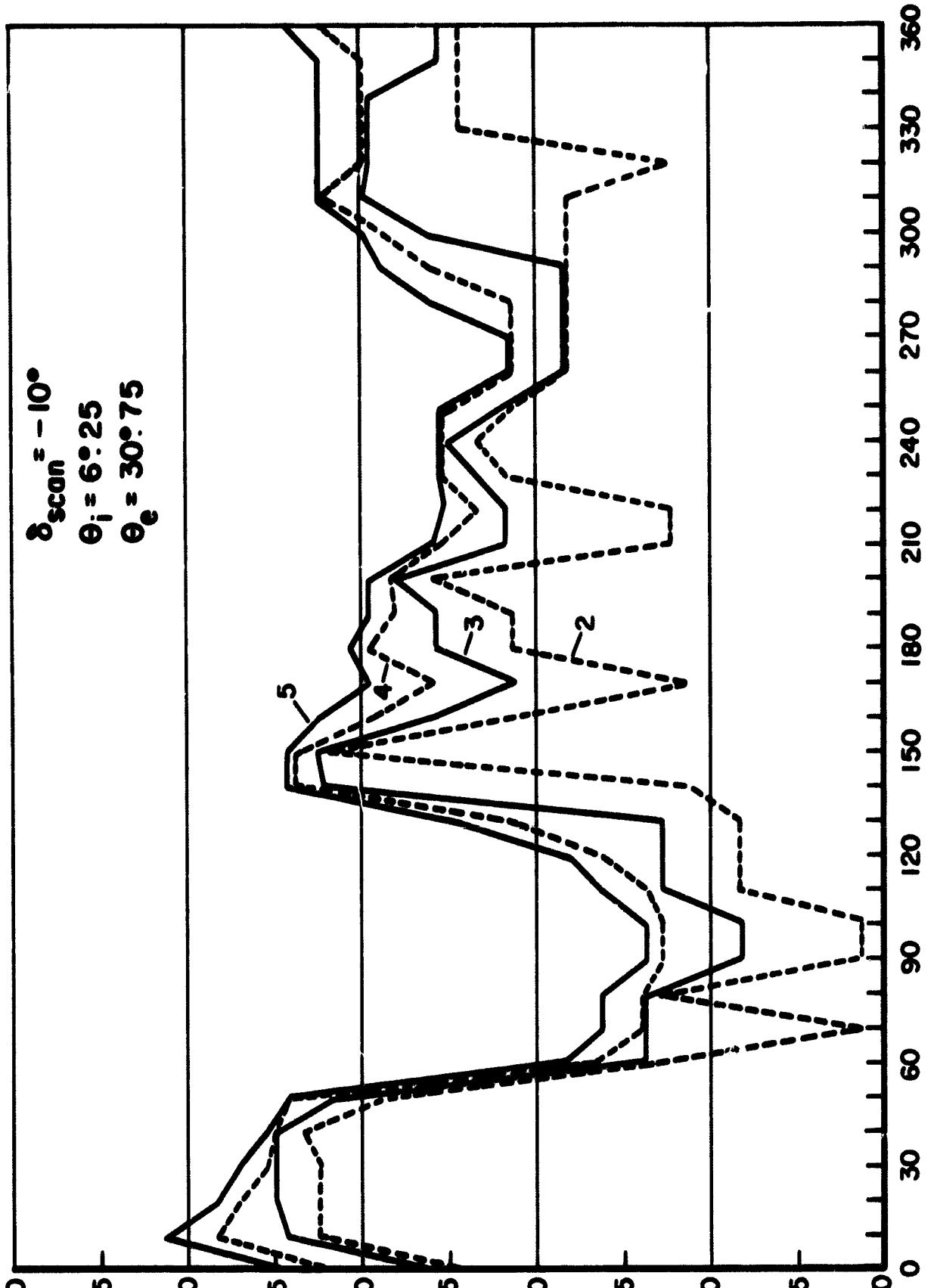


Figure 17: Stellar magnitudes of the second, third, fourth, and fifth brightest stars in the SCADS field of view for the recommended spin mode sensor configuration. The scan axis declination is $\delta_{scan} = -10^{o}$; the annular field of view is characterized by $\theta_i = 6^{o}.25$ and $\theta_e = 30^{o}.75$.

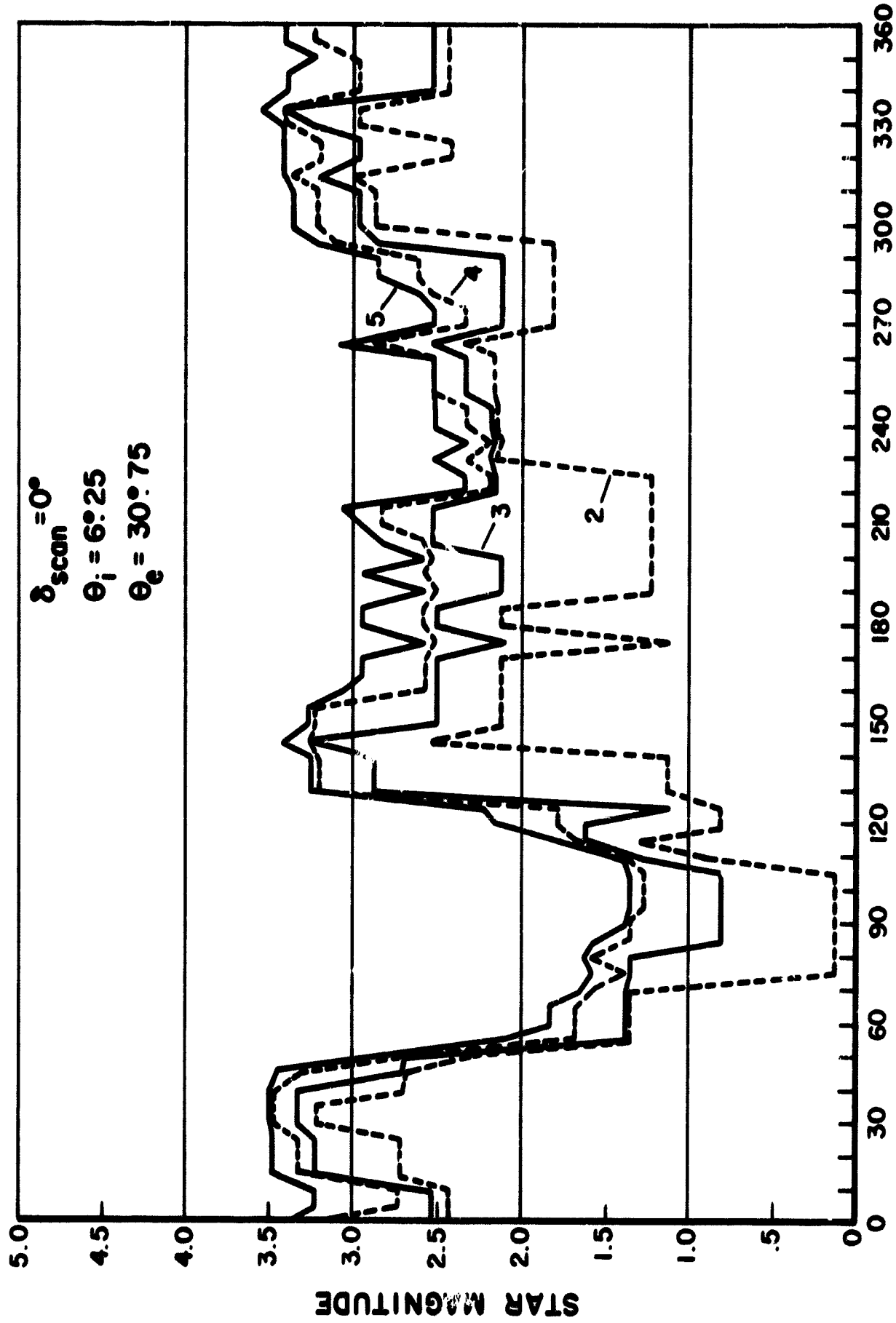


Figure 18: Stellar magnitudes of the second, third, fourth, and fifth brightest stars in the SCADS field of view for the recommended spin mode sensor configuration. The scan axis declination is $\delta_{scan} = 0^{o}$; the annular field of view is characterized by $\theta_i = 6^{o}.25$ and $\theta_e = 30^{o}.75$.

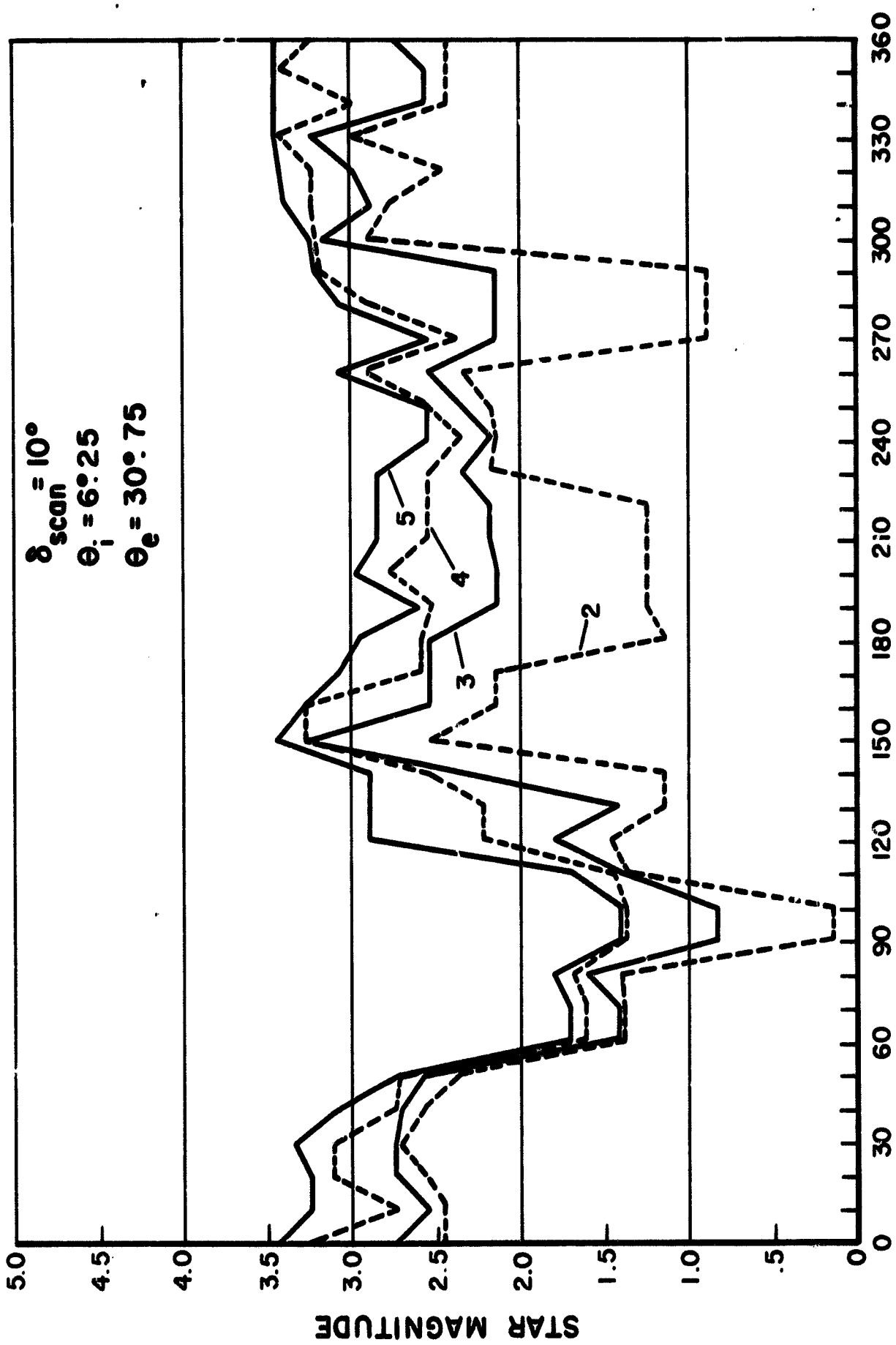


Figure 19: Stellar magnitudes of the second, third, fourth, and fifth brightest stars in the SCADS field of view for the recommended spin mode sensor configuration. The scan axis declination is $\delta_{scan} = 10^{o}$; the annular field of view is characterized by $\theta_i = 6^{o}.25$ and $\theta_e = 30^{o}.75$.

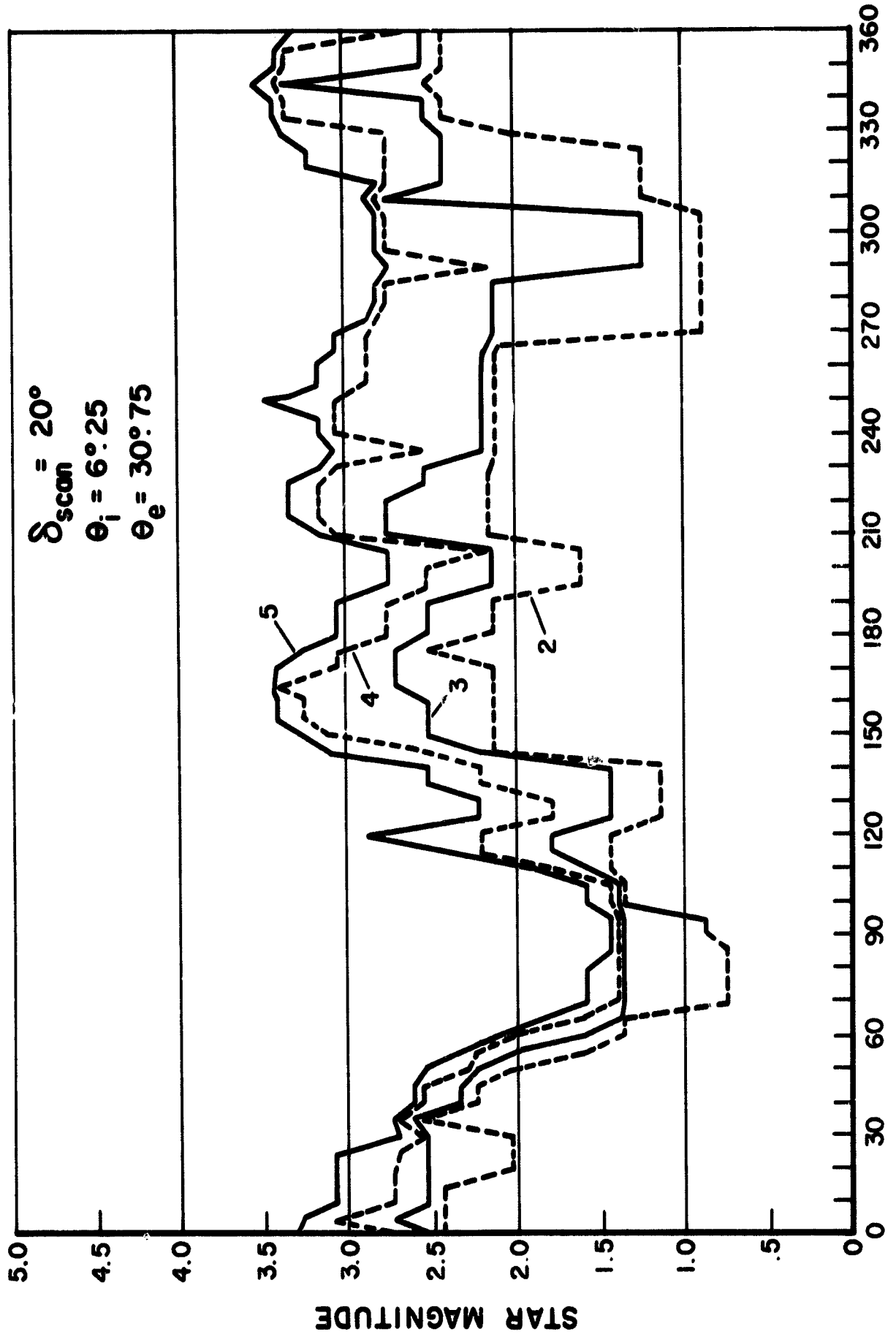


Figure 20: Stellar magnitudes of the second, third, fourth, and fifth brightest stars in the SCADS field of view for the recommended spin mode sensor configuration. The scan axis declination is $\delta_{scan} = 20^{o}$; the annular field of view is characterized by $\theta_i = 6^{o}.25$ and $\theta_e = 30^{o}.75$.

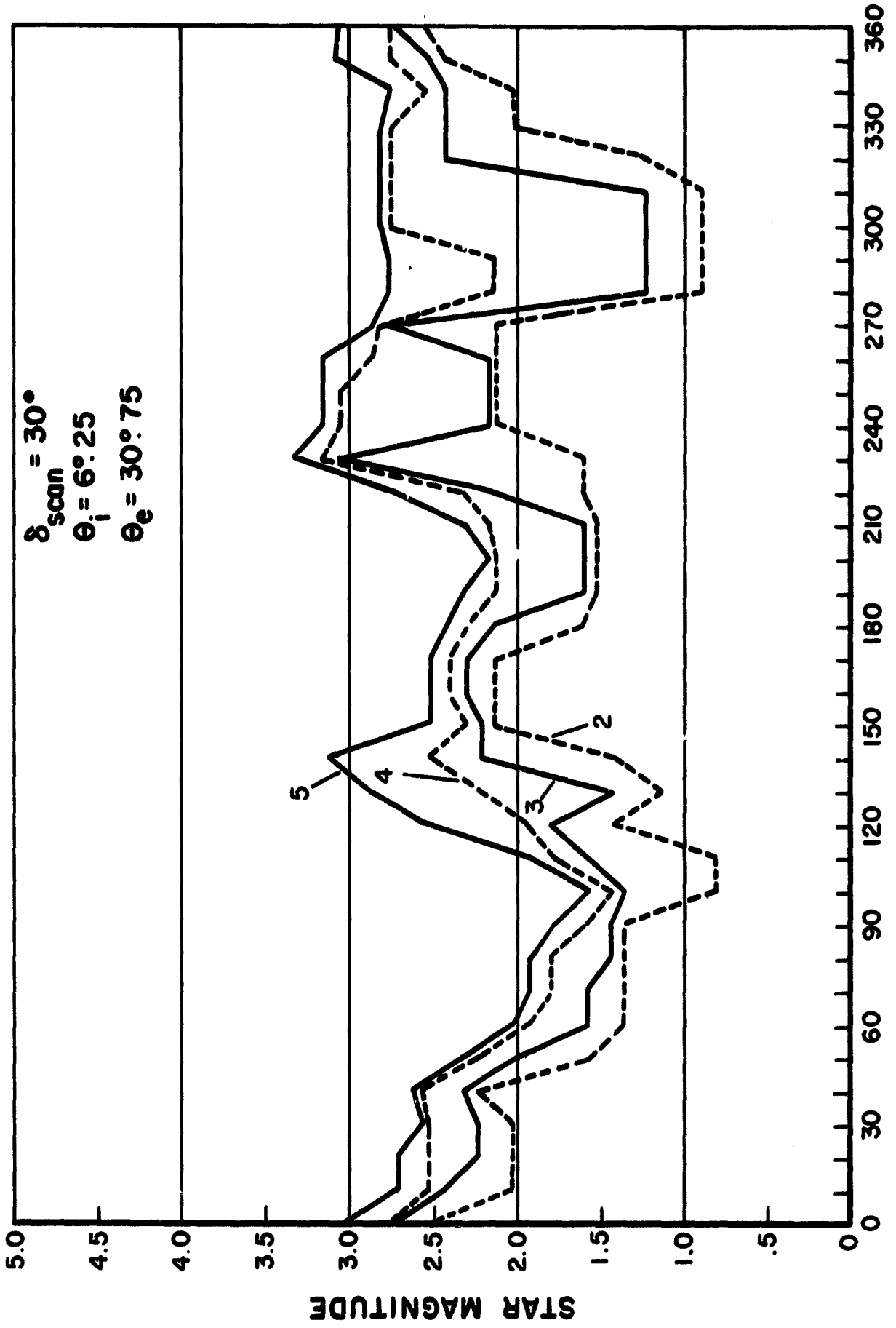


Figure 21: Stellar magnitudes of the second, third, fourth, and fifth brightest stars in the SCADS field of view for the recommended spin mode sensor configuration. The scan axis declination is $\delta_{scan} = 30^{o}$; the annular field of view is characterized by $\theta_i = 6^{o}.25$ $\theta_e = 30^{o}.75$.

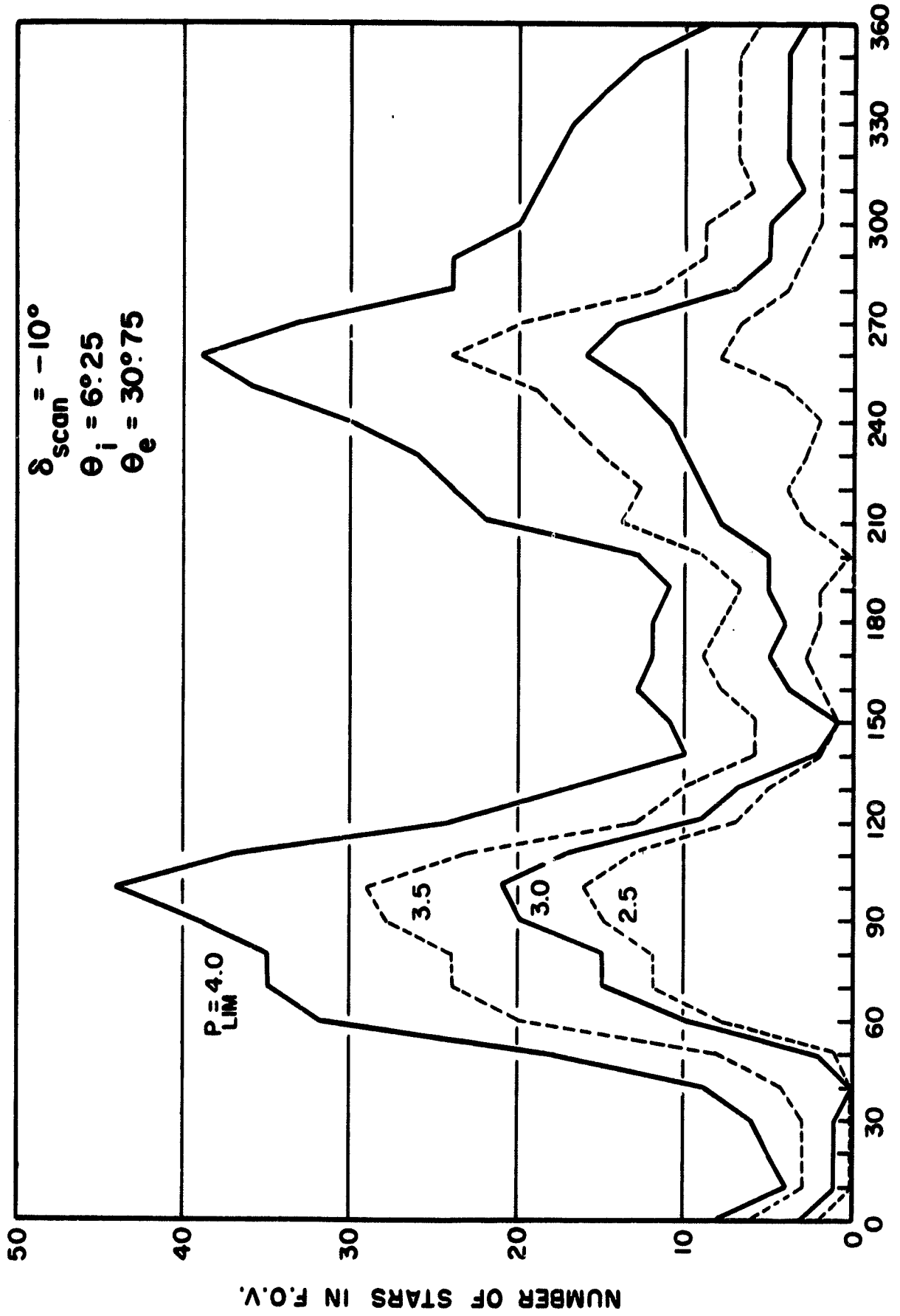


Figure 22: Number of stars in the field of view which are at least as bright as a given parametric limiting magnitude P_{lim}. Results correspond to the recommended SCADS spin mode sensor configuration with annular field $\theta_i = 6°.25$ and $\theta_e = 30°.75$; the scan axis declination is $\delta_{scan} = -10°$.

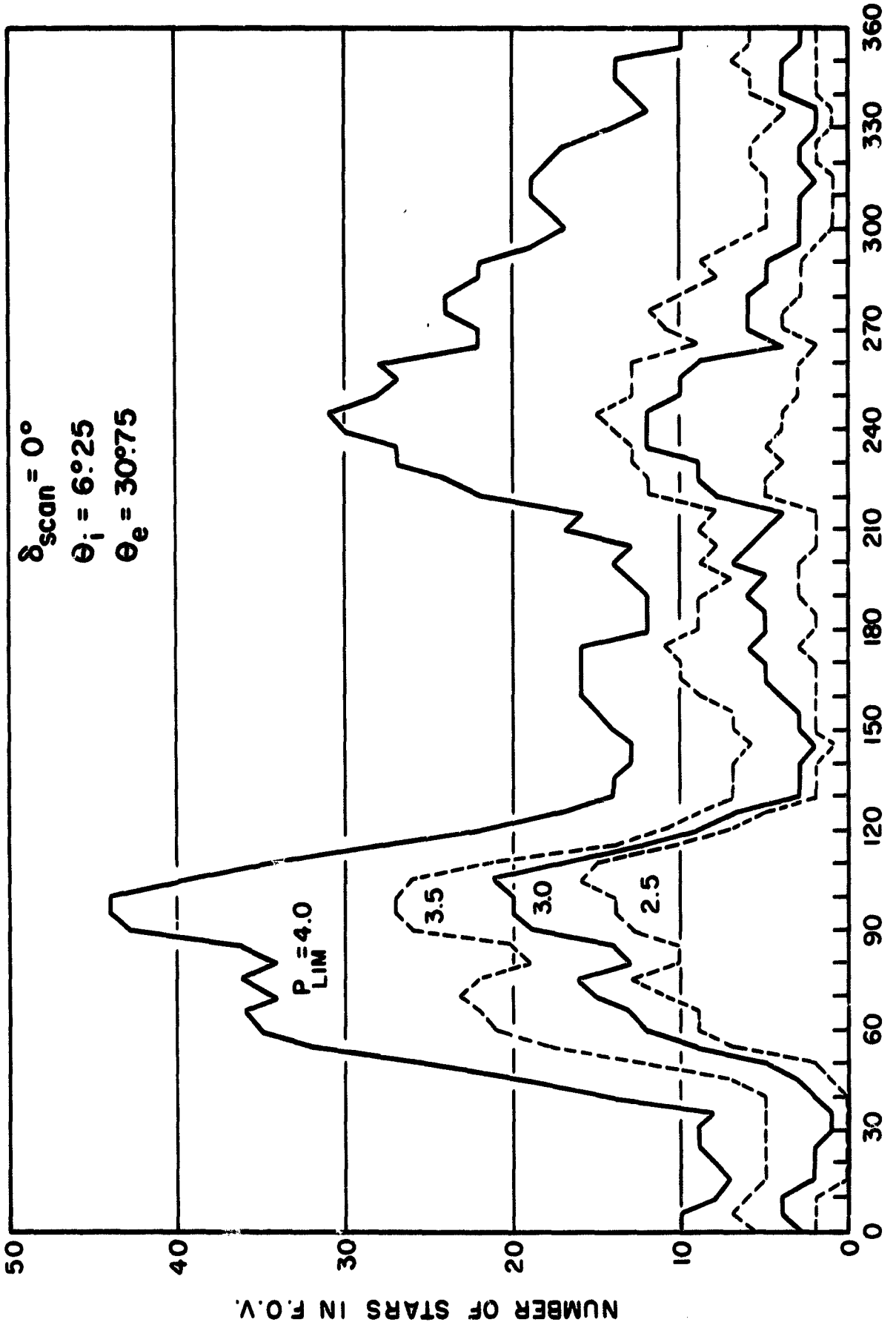


Figure 23: Number of stars in the field of view which are at least as bright as a given parametric limiting magnitude P_{lim}. Results correspond to the recommended SCADS spin mode sensor configuration with annular fields $\theta_i = 6°.25$ and $\theta_e = 30°.75$; the scan axis declination is $\delta_{scan} = 0°$.

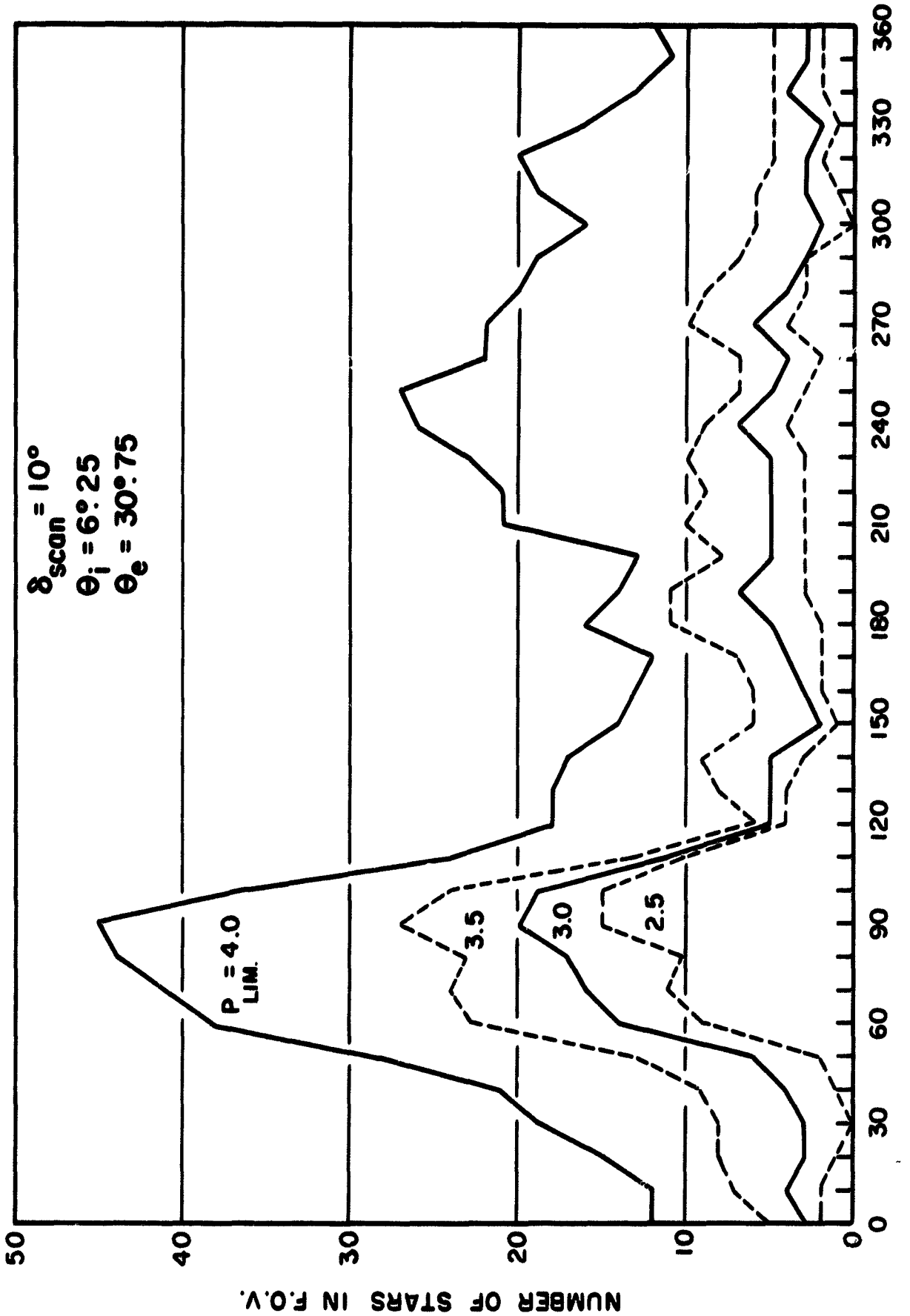


Figure 24: Number of stars in the field of view which are at least as bright as a given parametric limiting magnitude P_{lim}. Results correspond to the recommended SCADS spin mode sensor configuration with annular field $\theta_i = 6.^{o}25$ and $\theta_e = 30.^{o}75$; the scan axis declination is $\delta_{scan} = 10^{o}$.

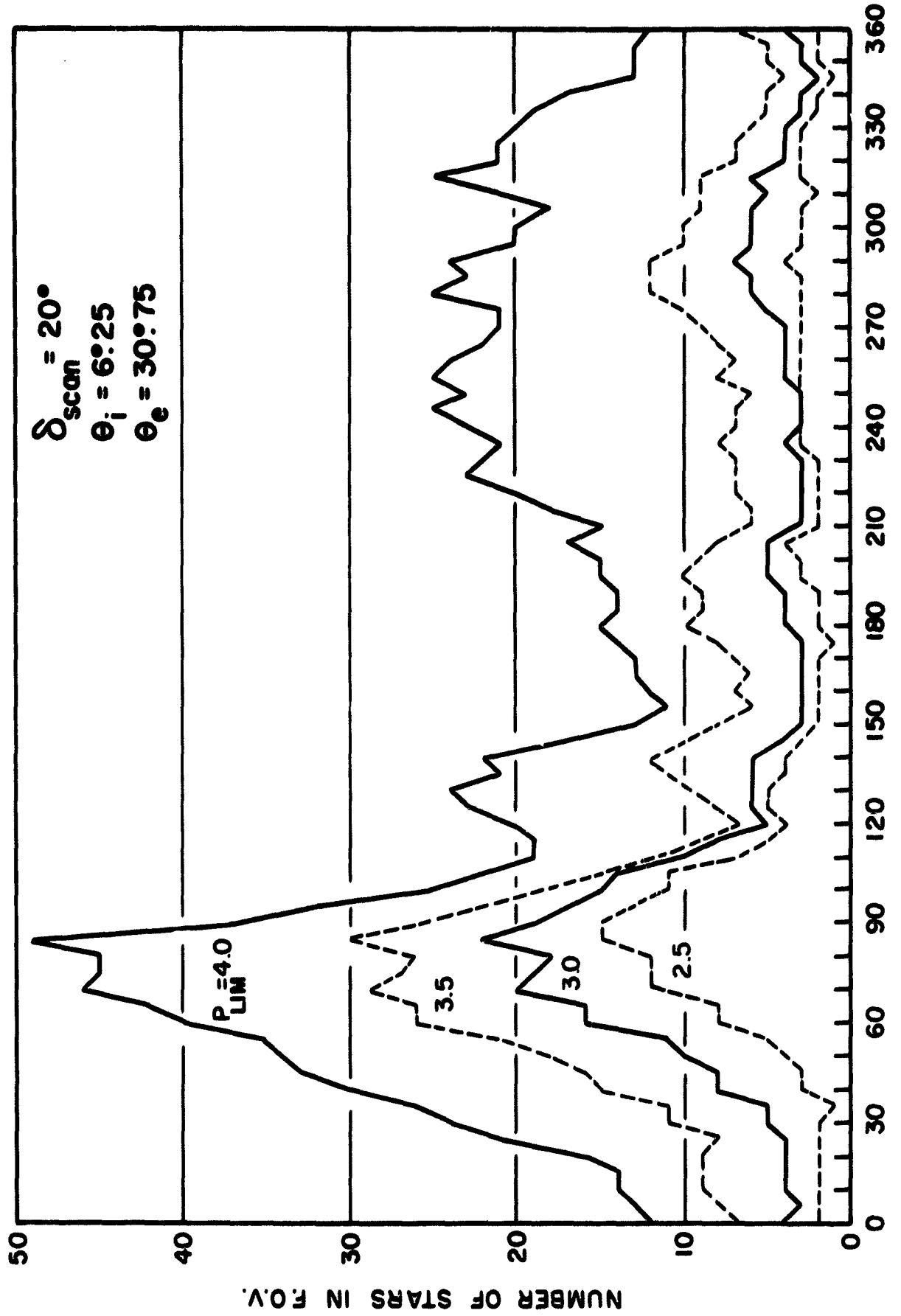


Figure 25: Number of stars in the field of view which are at least as bright as a given parametric limiting magnitude P_{lim}. Results correspond to the recommended SCADS spin mode sensor configuration with annular field $\theta_i = 6^{o}.25$ and $\theta_e = 30^{o}.75$; the scan axis declination is $\delta_{scan} = 20^{o}$.

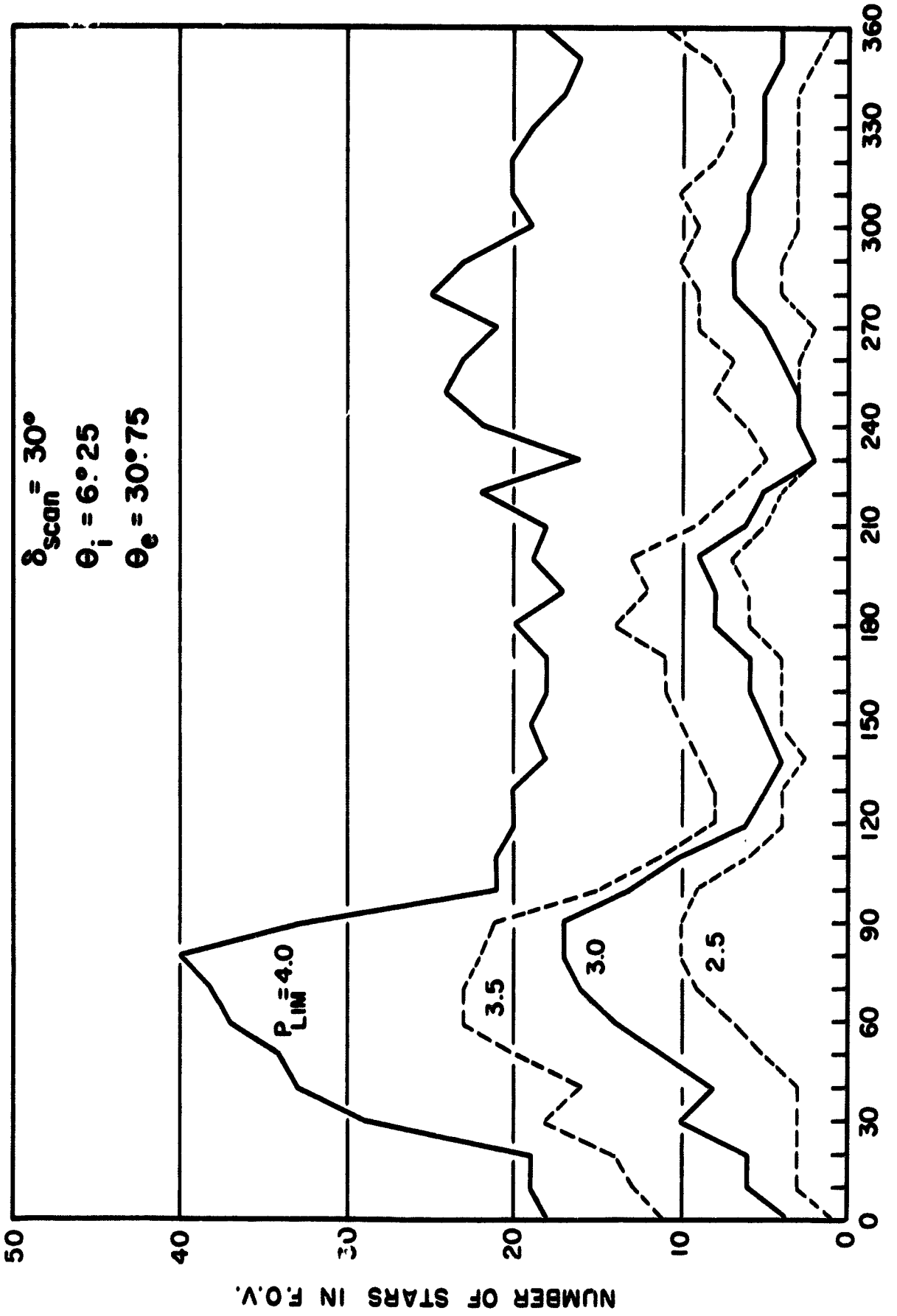


Figure 26: Number of stars in the field of view which are at least as bright as a given parametric limiting magnitude P_{lim}. Results correspond to the recommended SCADS spin mode sensor configuration with annular field $\theta_i = 6^o.25$ and $\theta_e = 30^o.75$; the scan axis declination is $\delta_{scan} = 30^o$.

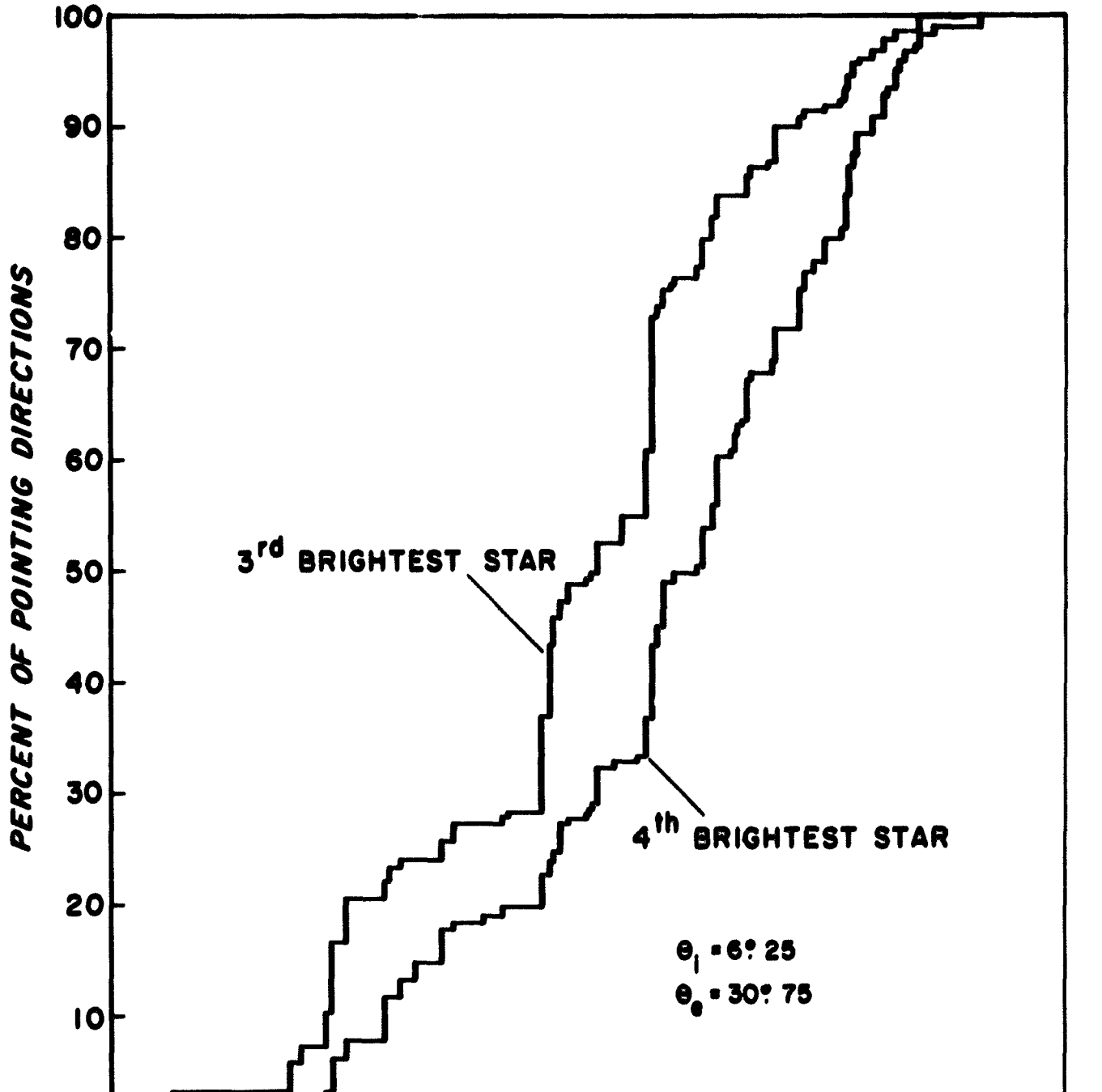
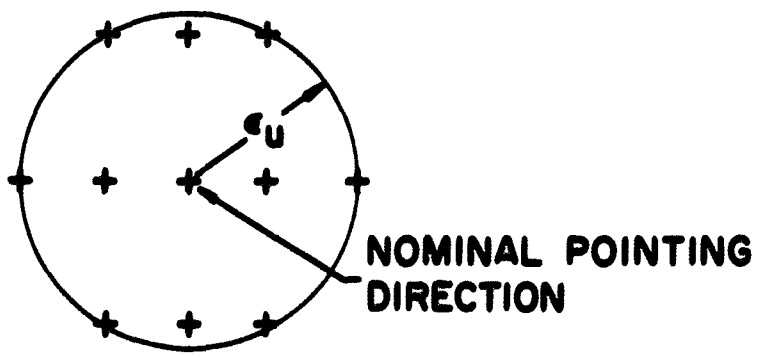


Figure 27: Cumulative probability distribution for the magnitudes of the third and fourth brightest stars in the field of view. The grid of pointing directions covers the possible scan axis orientations in the spin-stabilized portions of the ATS F&G missions. The results correspond to the recommended SCADS spin mode sensor configuration with $\theta_i = 6^{\circ}.25$ and $\theta_e = 30^{\circ}.75$.

percentage of the total number of entries. The resulting relation between this percentage and the corresponding stellar magnitude becomes the cumulative probability estimator plotted in Figure 27. If the system detection threshold is set at a particular magnitude, then the percentage of possible scan axes for which three and four stars can be acquired is given by these distributions.

Figure 27 also presents a convenient means for determining the faintest detection threshold--that is the system limiting magnitude--required for the particular SCADS design. Although the three-axis attitude problem can be solved with transits from three known stars, a pattern of just three transits can be paired with the corresponding stars only if the pointing direction is already known to within a small error. If the initial guess for the pointing direction is somewhat uncertain, an unambiguous identification can usually be made with four stars. In the present application, the uncertainty in the scan axis is ten degrees. Thus, the system should be capable of detecting the faintest fourth brightest star; from Figure 27, the system limiting magnitude, M_ℓ, is then just 3.84 for the recommended spinning mode sensor. Note that for 91% of the possible scan axes, the fourth brightest star is at least one-half magnitude brighter than this limit and for 63% of the cases, it is a full magnitude brighter.

A final format for presenting the star availability data is illustrated by Figures 28, 29, and 30. About each nominal scan axis direction, a pattern of pointing directions of the following form is investigated.



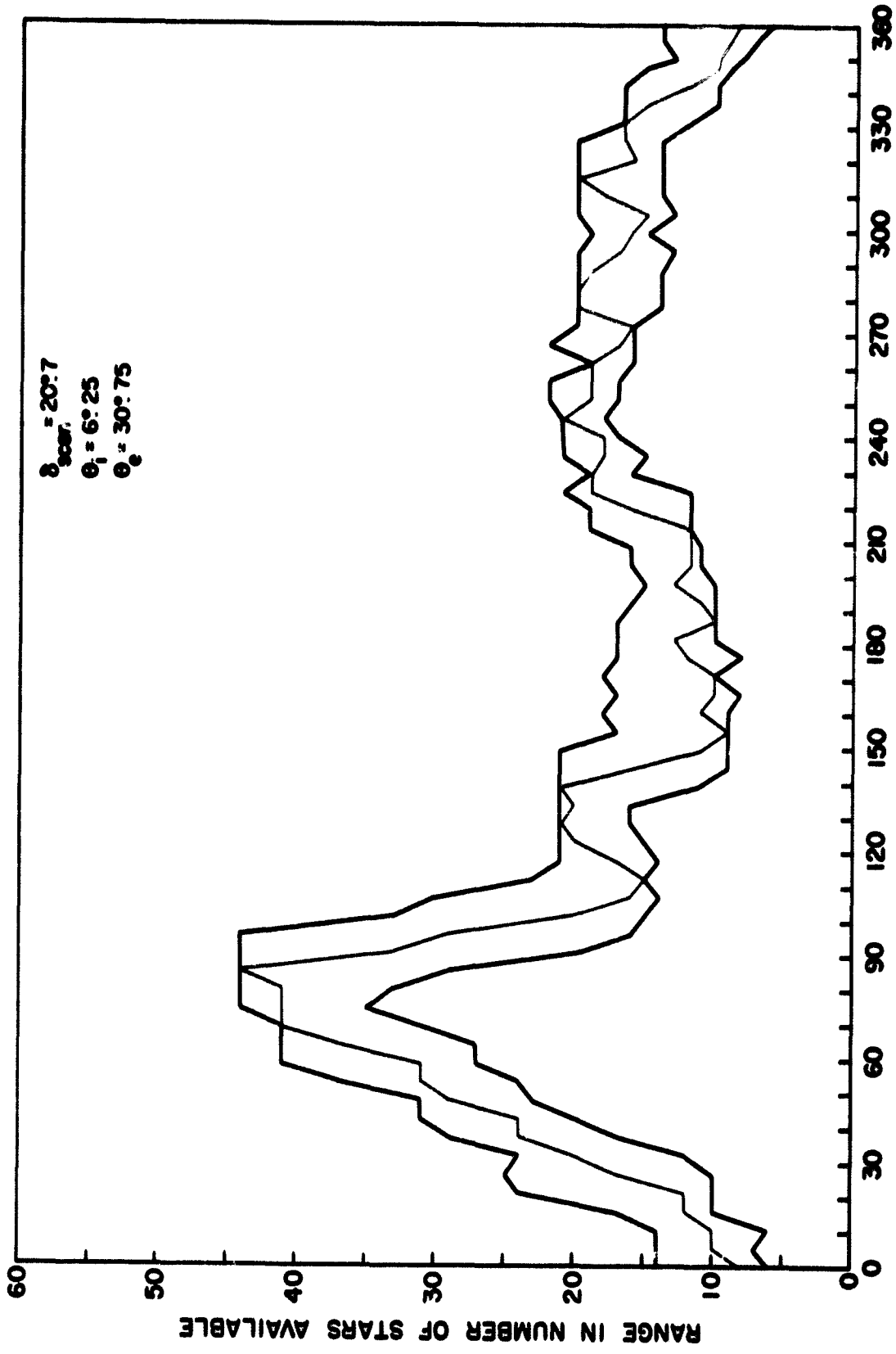


Figure 28: Range in the number of stars available for a ten degree uncertainty about a given nominal scan axis direction (the central curve corresponds to zero uncertainty--i. e., to the nominal direction). The results correspond to the recommended SCADS spin mode sensor configuration with annular fields $\theta_i = 6.25^o$ and $\theta_e = 30.75^o$; the system limiting magnitude is set at $M_\ell = 3.84$. The nominal scan axis declination is $\delta_{scan} = 20.7^o$.

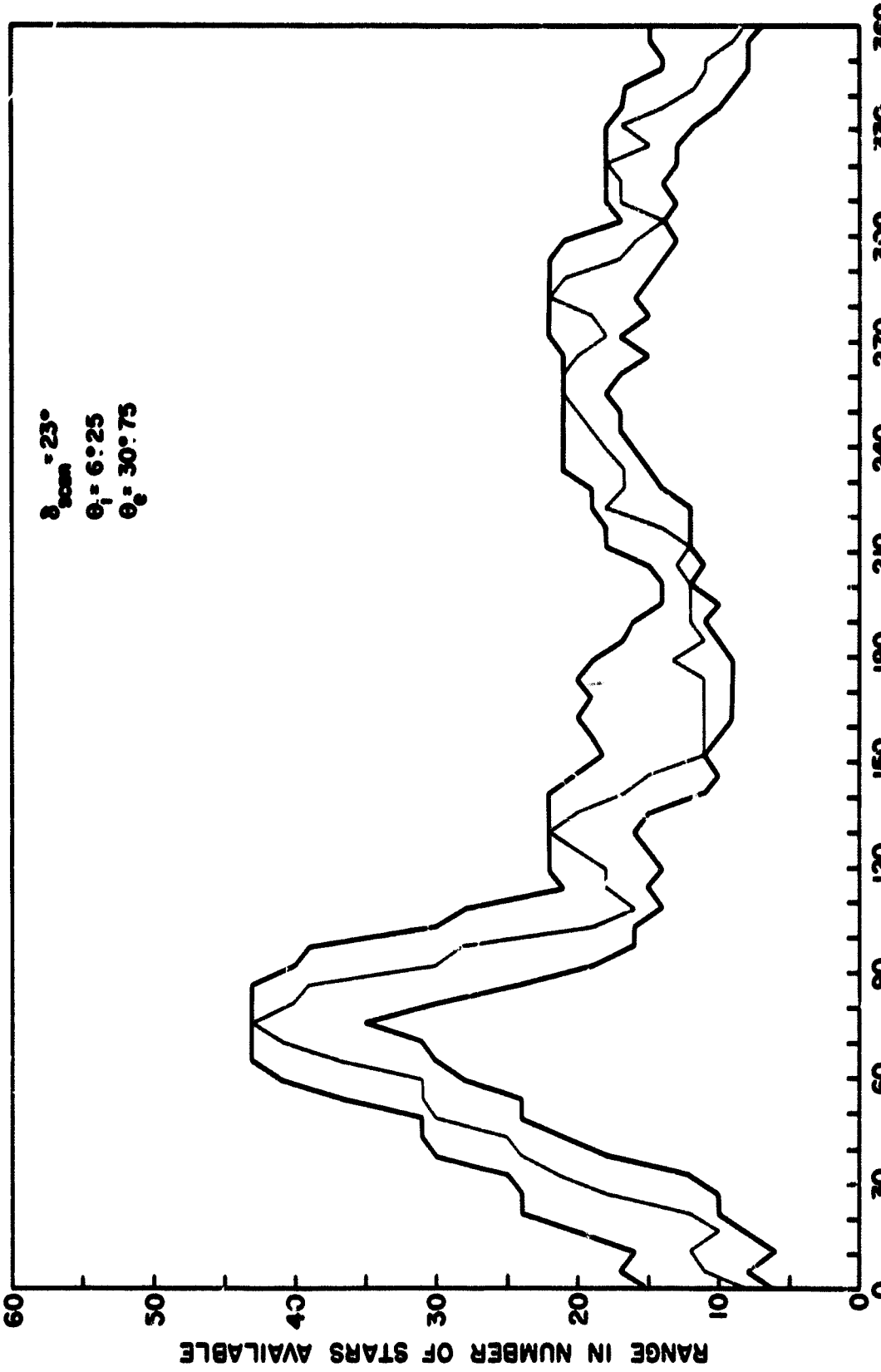


Figure 29: Range in the number of stars available for a ten degree uncertainty about a given nominal scan axis direction (the central curve corresponds to zero uncertainty--i.e., to the nominal direction). The results correspond to the recommended SCADS spin mode sensor configuration with annular field $\theta_i = 6^{o}.25$ and $\theta_e = 30^{o}.75$; the system limiting magnitude is set at $M_{\ell} = 3.84$. The nominal scan axis declination is $\delta_{scan} = 23^{o}$.

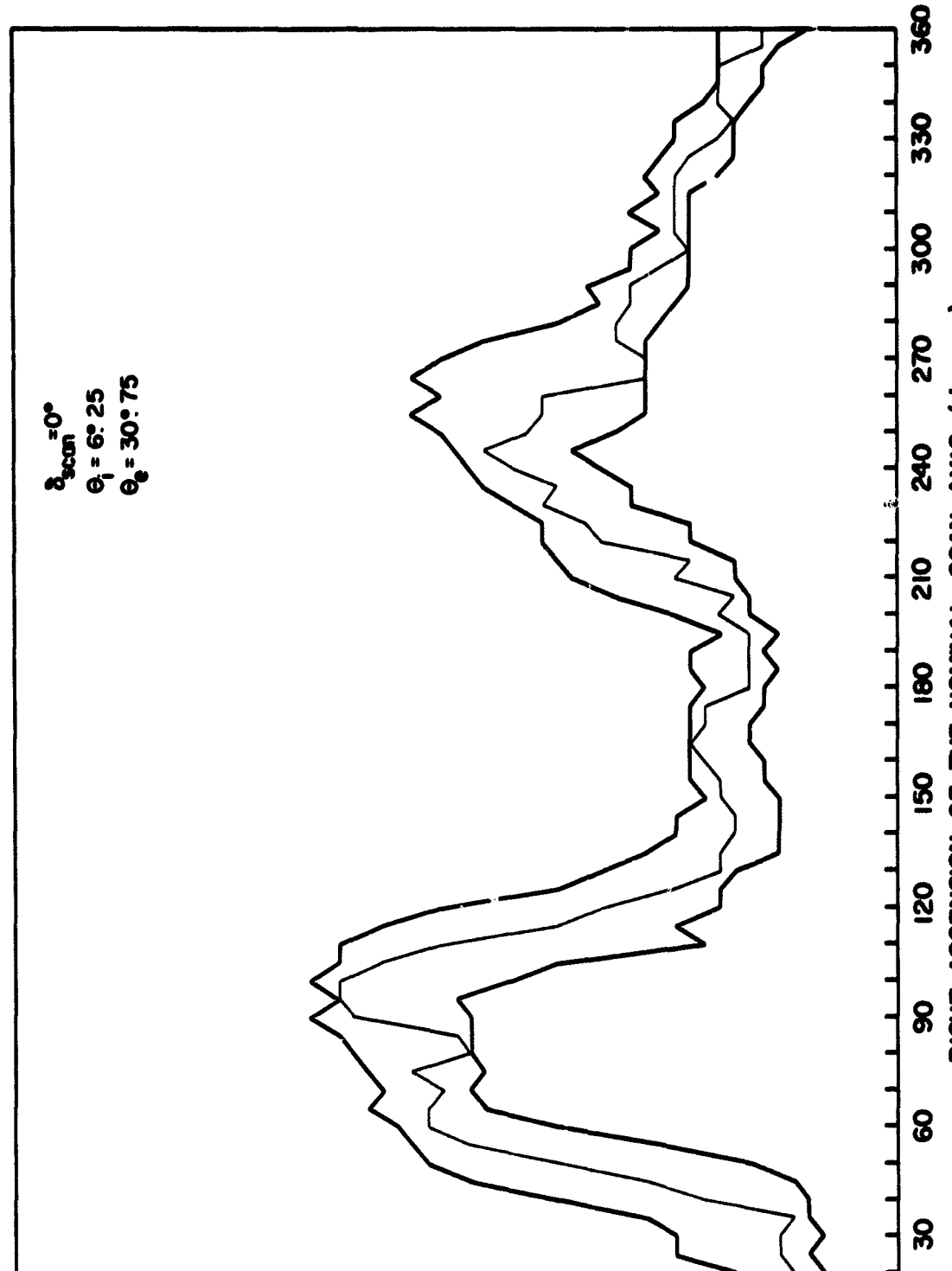


Figure 30: Range in the number of stars available for a ten degree uncertainty about a given nominal scan axis direction (the central curve corresponds to zero uncertainty--i.e., to the nominal direction). The results correspond to the recommended SCADS spin mode sensor configuration with annular fields $\theta_i = 6.^{o}25$ and $\theta_e = 30.^{o}75$; the system limiting magnitude is set at $M_{\ell} = 3.^{o}84$. The nominal scan axis declination is $\delta_{scan} = 0^{o}$.

The exterior points in this pattern lie on a circle of angular radius $\epsilon_u = 10^o$ (the uncertainty in the actual scan axis position). The annular field is centered on each point in the pattern and a count is made of the number of stars which are in this field of view and which satisfy the magnitude condition $M \leq M_\ell = 3.84$. Then, the variation of these counts over the set of points in the pattern is a measure of the range of potential target availability associated with the given nominal scan axis direction and uncertainty. It is these ranges which are plotted as a function of the right ascension of the scan axis for nominal scan axis declinations $\delta_{scan} = 20^o.7$ (Figure 28), $\delta_{scan} = 23^o$ (Figure 29), and $\delta_{scan} = 0^o$ (Figure 30). Note that in only one instance does the potential number of targets drop as low as four--see Figure 30; $\alpha_{scan} = 10^o$, $\delta_{scan} = 0^o$. Thus, a system limiting magnitude $M_\ell = 3.84$ insures adequate star availiability for the recommended spinning mode sensor design.

3. Stellar Target Distributions - Dual Mode SCADS Sensor

The recommended design for the dual mode SCADS sensor has an annular field of view characterized by $\theta_i = 5^o$ and $\theta_e = 20^o$. A complete set of star availability plots for the dual mode case--analogous to those for the spinning mode sensor--is presented below. Figures 31, 32, 33, 34, and 35 show the stellar magnitude of the second, third, fourth, and fifth brightest stars in the field of view as a function of the scan axis right ascension for various scan declinations. Figures 36, 37, 38, 39, and 40 document the number of stars in the field of view in terms of a number of parametric limiting magnitudes.

Figure 41 shows the cumulative probability distributions for the magnitude of the third and fourth brightest stars in the field of view over the set of possible scan axes. Note here that the faintest fourth brightest star has a magnitude of 4.65. This is selected as the system limiting magnitude M_ℓ for the dual mode sensor. Observe further that the fourth brightest star is at least a half magnitude brighter than $M_\ell = 4.65$ for 94% of the potential scan

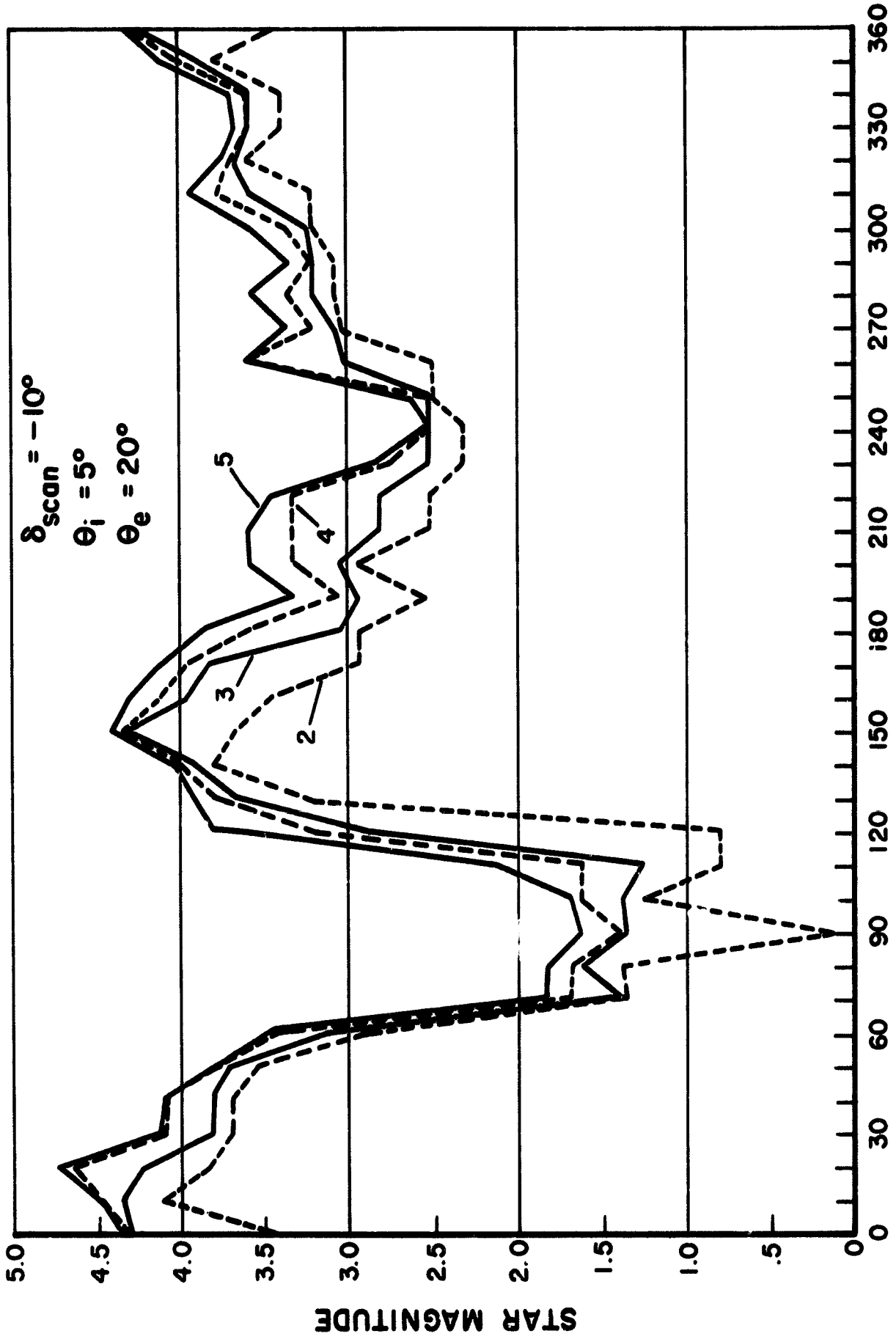


Figure 31: Stellar magnitudes of the second, third, fourth, and fifth brightest stars in the SCADS field of view for the recommended dual mode sensor configuration. The scan axis declination is $\delta_{scan} = -10^{o}$; the annular field of view is characterized by $\theta_i = 5^{o}$ and $\theta_e = 20^{o}$.

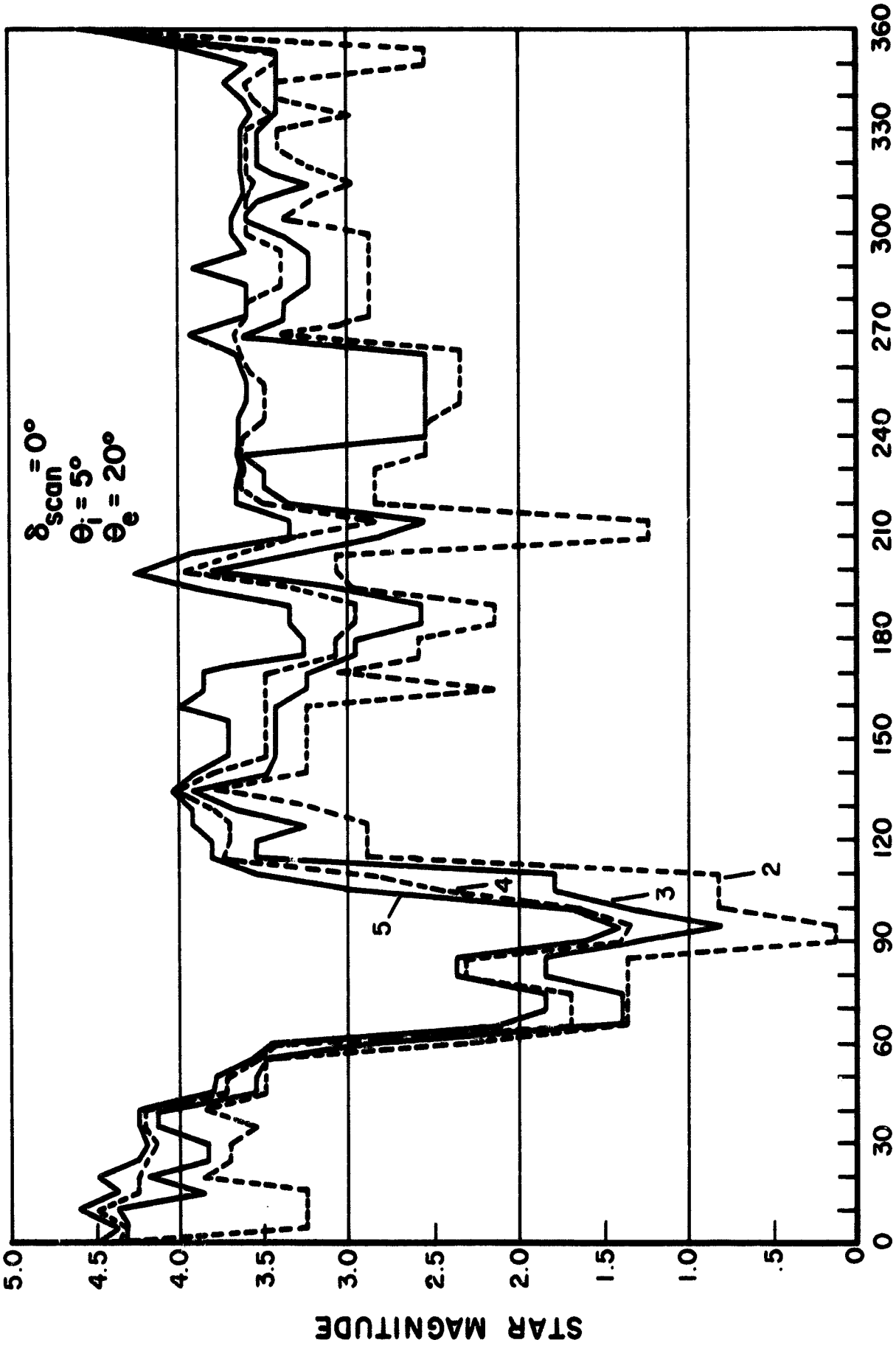


Figure 32: Stellar magnitudes of the second, third, fourth, and fifth brightest stars in the SCADS field of view for the recommended dual mode sensor configuration. The scan axis declination is $\delta_{scan} = 0^o$; the annular field of view is characterized by $\theta_i = 5^o$ and $\theta_e = 20^o$.

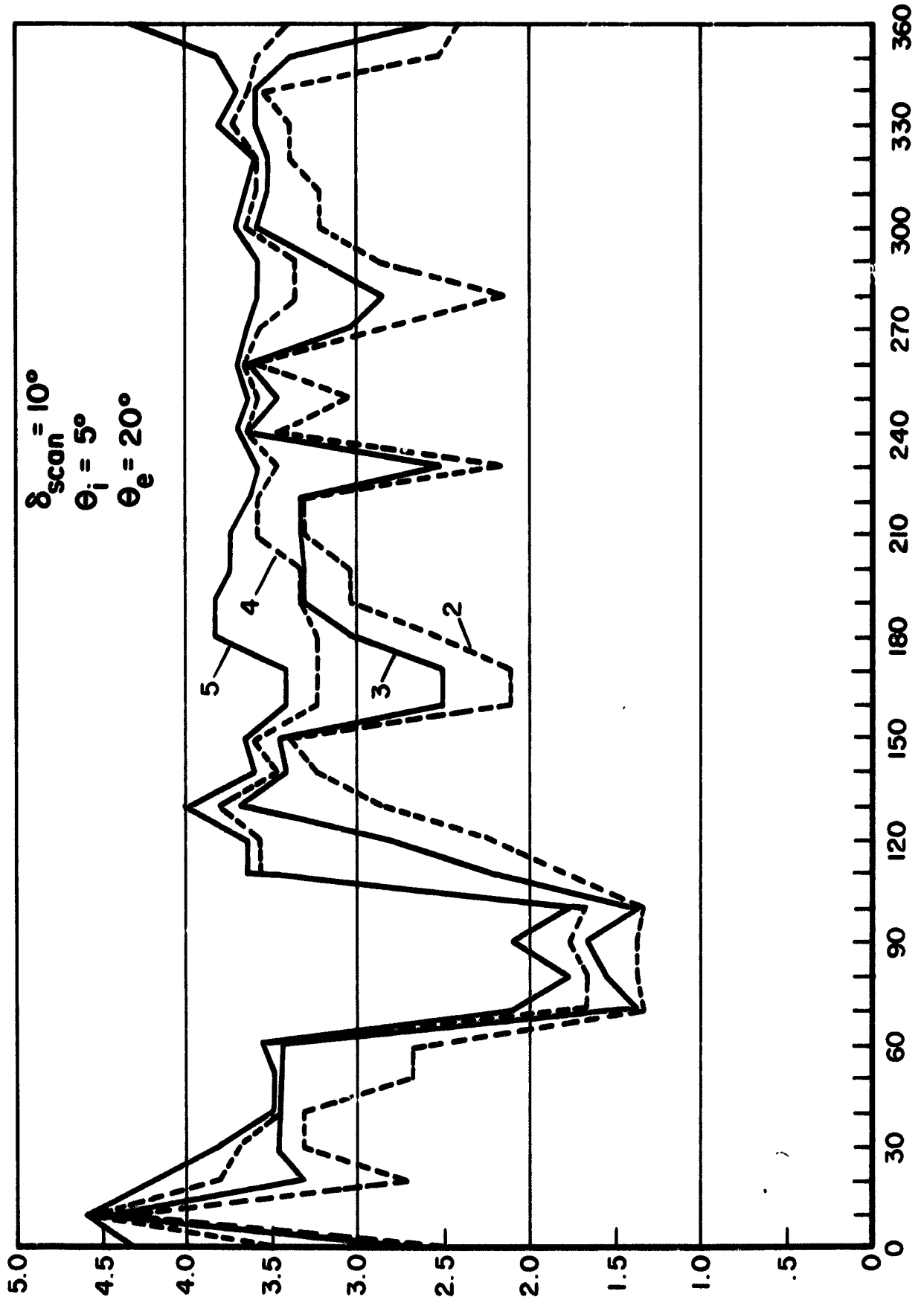


Figure 33: Stellar magnitudes of the second, third, fourth, and fifth brightest stars in the SCADS field of view for the recommended dual mode sensor configuration. The scan axis declination is $\delta_{scan} = 10^{o}$; the annular field of view is characterized by $\theta_i = 5^{o}$ and $\theta_e = 20^{o}$.

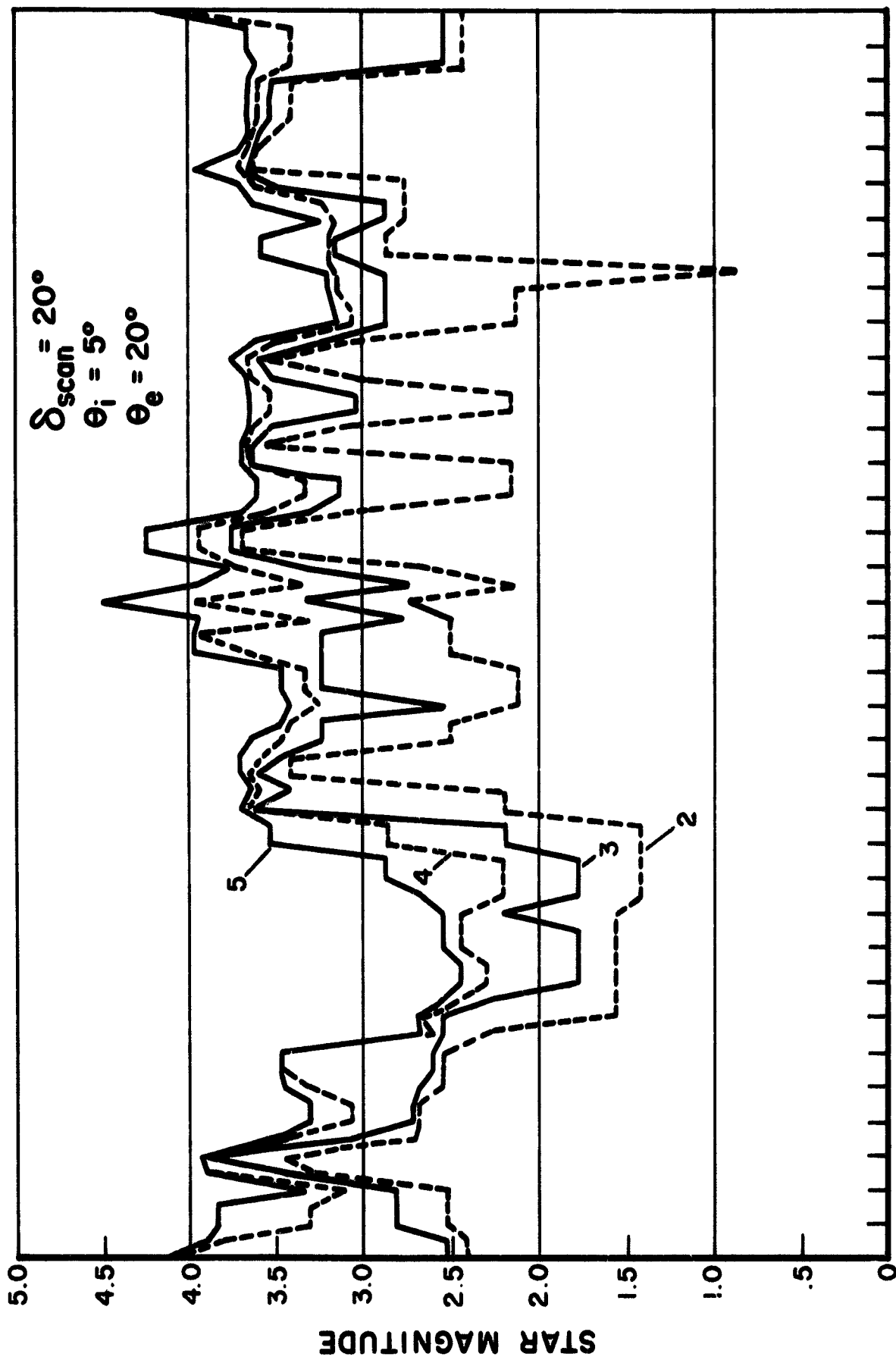


Figure 34: Stellar magnitudes of the second, third, fourth, and fifth brightest stars in the SCADS field of view for the recommended dual mode sensor configuration. The scan axis declination is $\delta_{scan} = 20^o$; the annular field of view is characterized by $\theta_i = 5^o$ and $\theta_e = 20^o$.

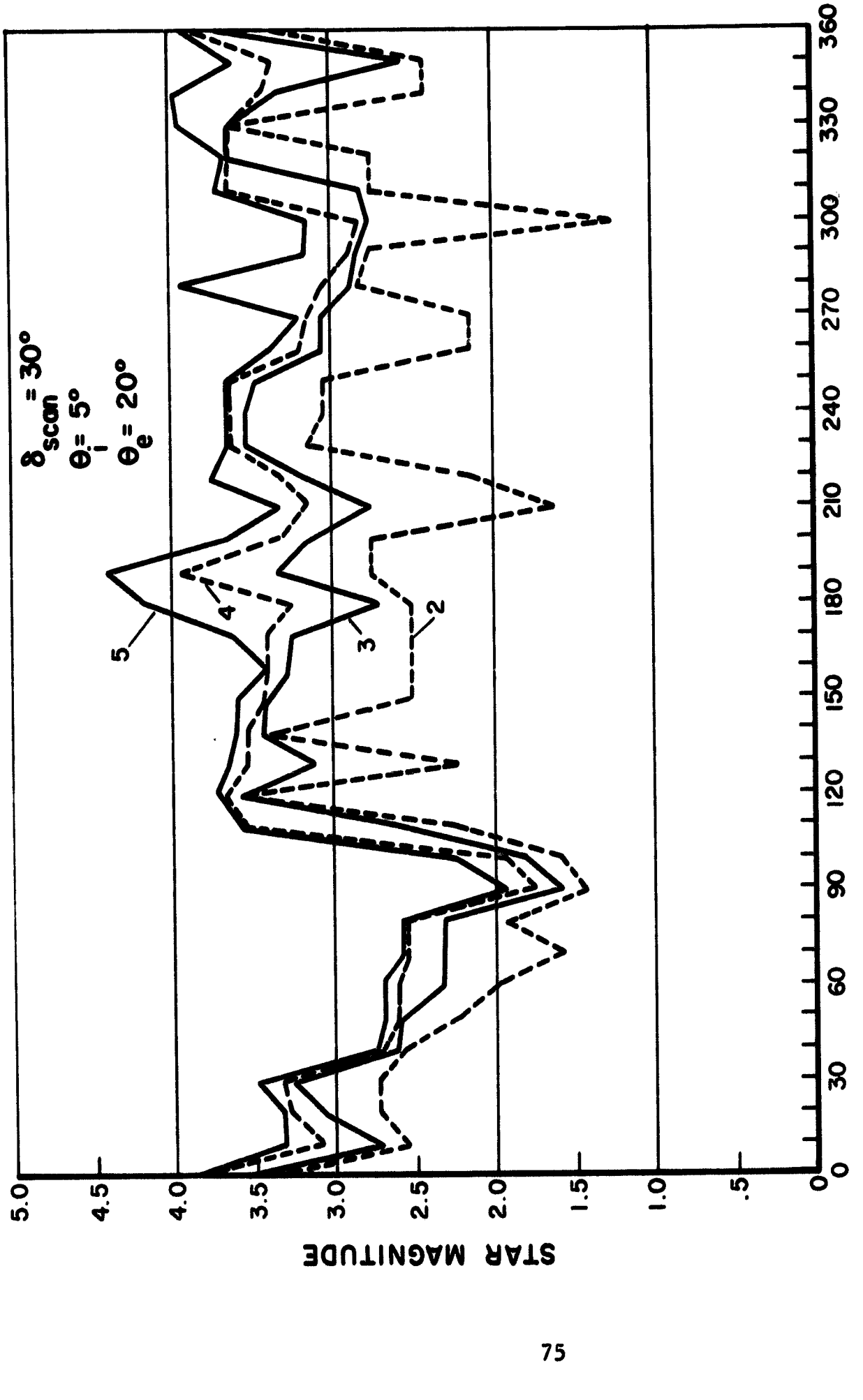


Figure 35: Stellar magnitudes of the second, third, fourth, and fifth brightest stars in the SCADS field of view for the recommended dual mode sensor configuration. The scan axis declination is $\delta_{scan} = 30^o$; the annular field of view is characterized by $\theta_i = 5^o$ and $\theta_e = 20^o$.

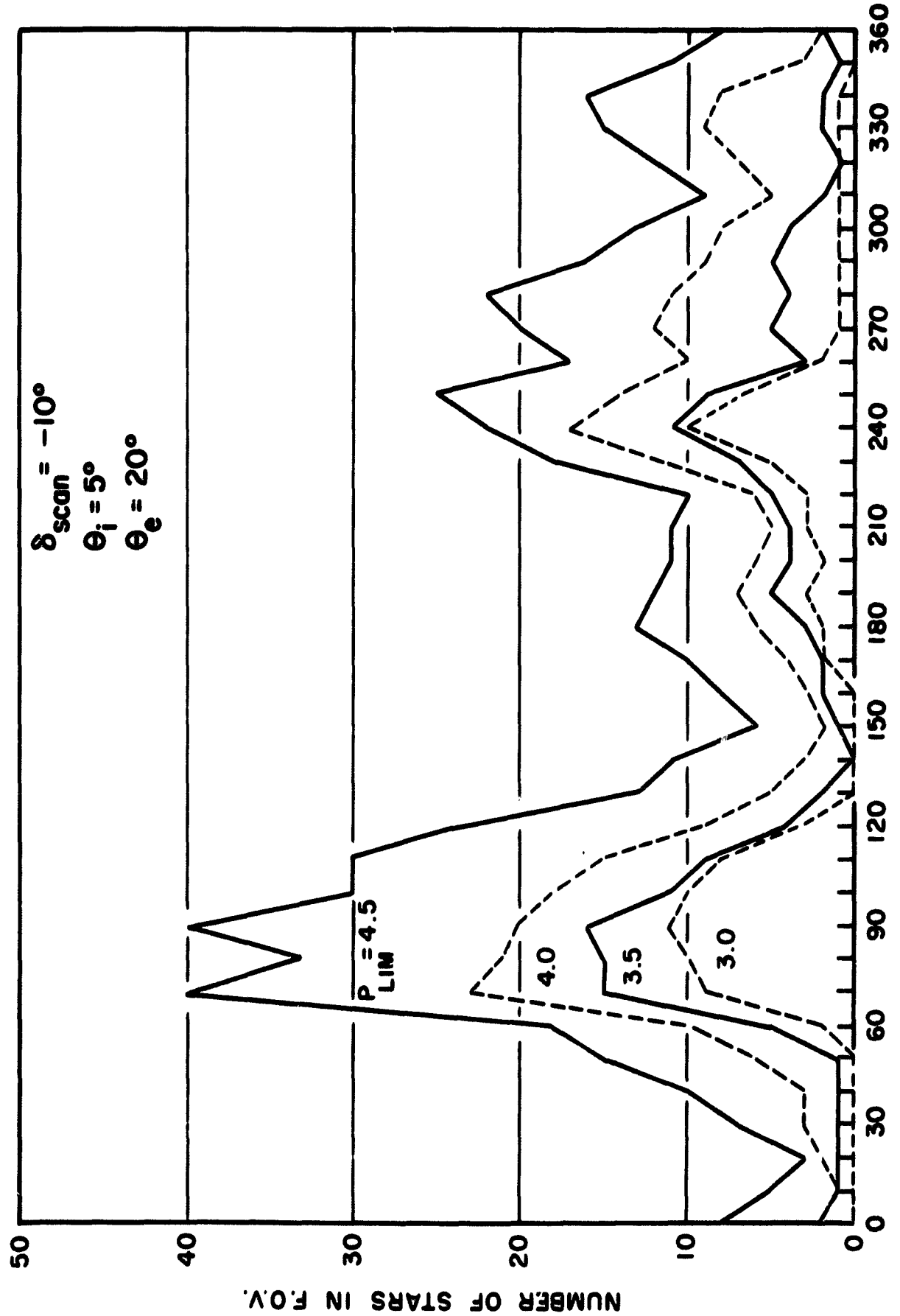


Figure 36: Number of stars in the field of view which are at least as bright as a given parametric limiting magnitude P_{lim}. Results correspond to the recommended SCADS dual mode sensor configuration with annular field $\theta_i = 5^o$ and $\theta_e = 20^o$; the scan axis declination is $\delta_{scan} = -10^o$.

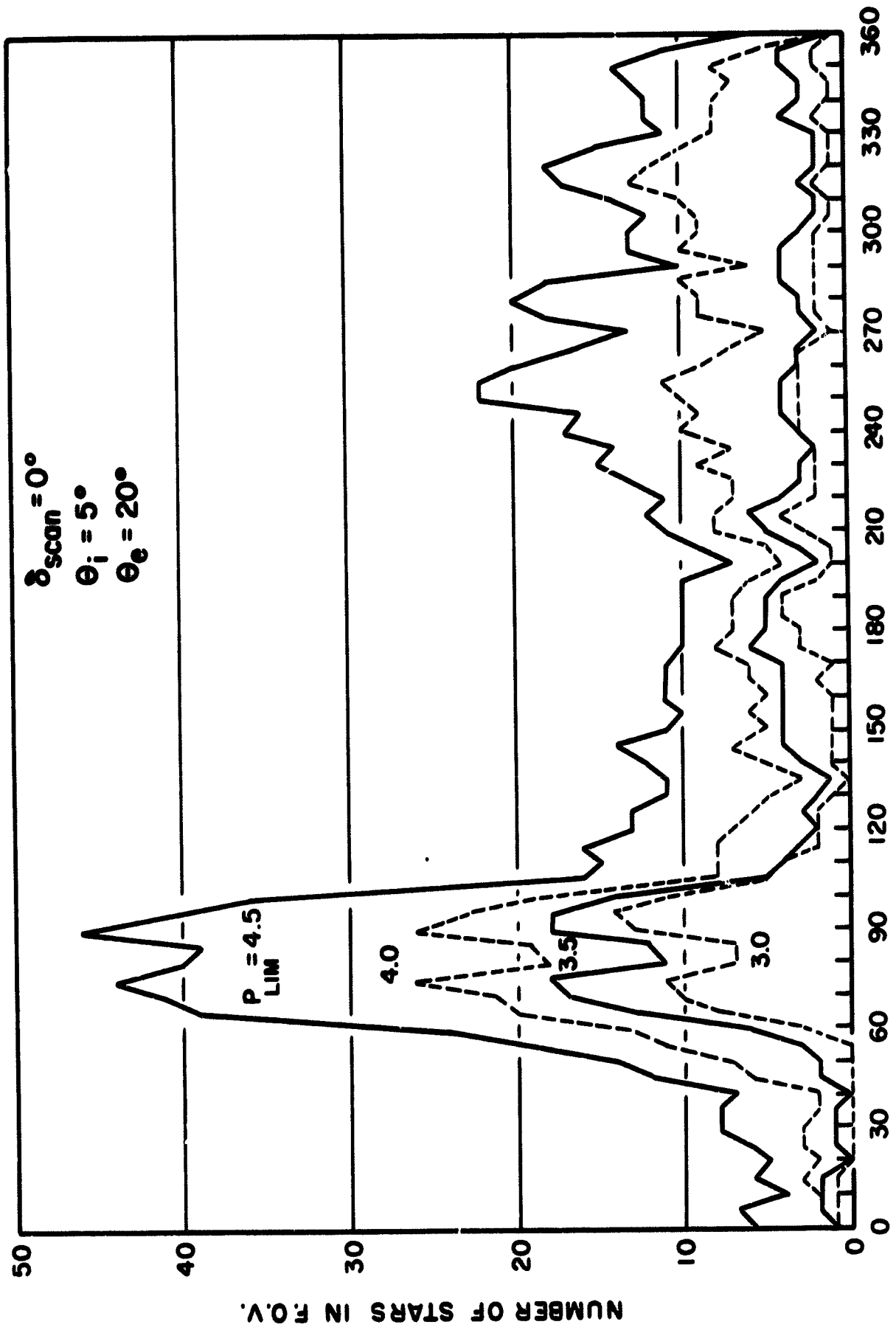


Figure 37: Number of stars in the field of view which are at least as bright as a given parametric limiting magnitude P_{lim}. Results correspond to the recommended SCADS dual mode sensor configuration with annular field $\theta_i = 5^o$ and $\theta_e = 20^o$; the scan axis declination is $\delta_{scan} = 0^o$.

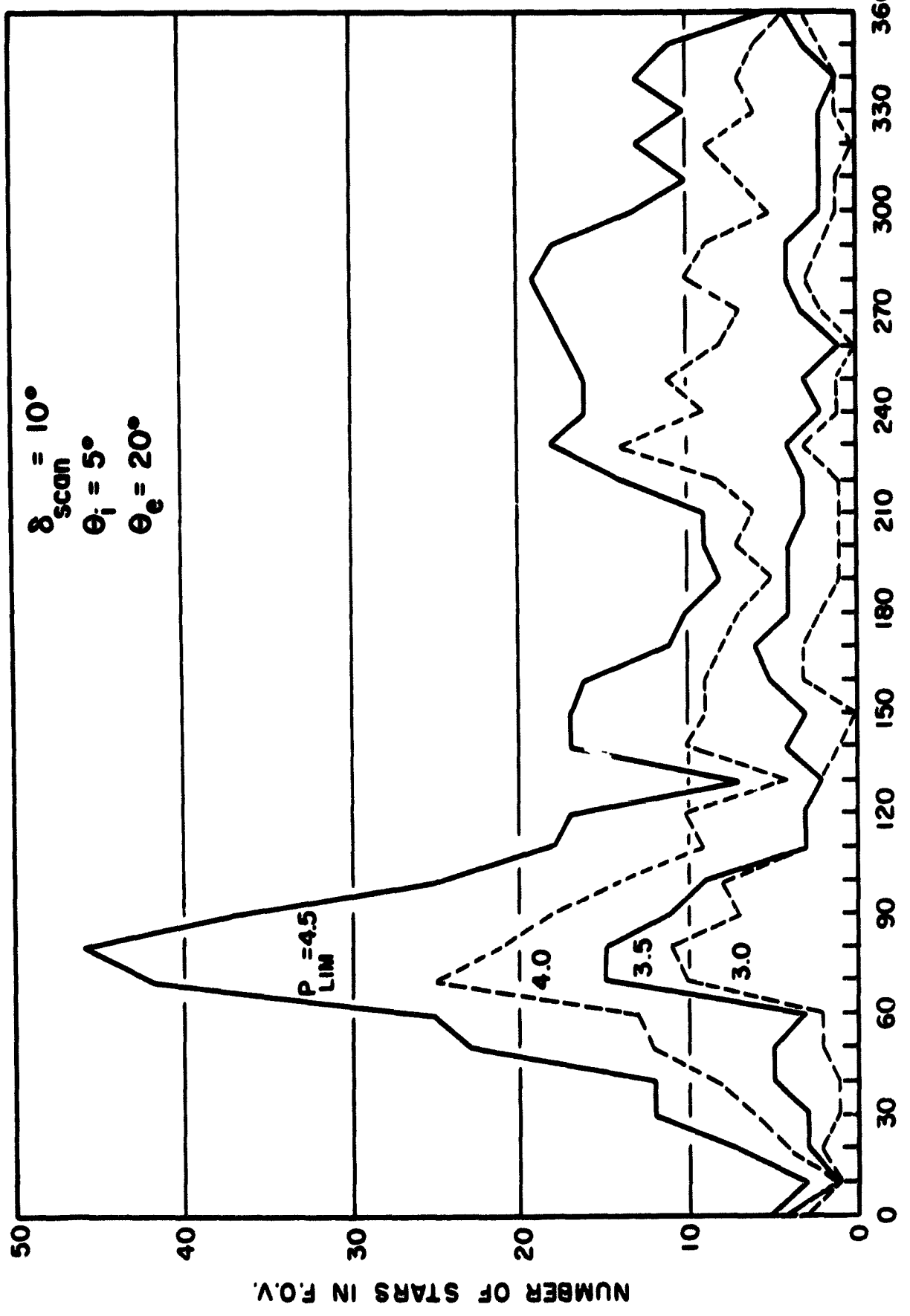


Figure 38: Number of stars in the field of view which are at least as bright as a given parametric limiting magnitude P_{lim}. Results correspond to the recommended SCADS dual mode sensor configuration with annular field $\theta_i = 5^o$ and $\theta_e = 20^o$; the scan axis declination is $\delta_{scan} = 10^o$.

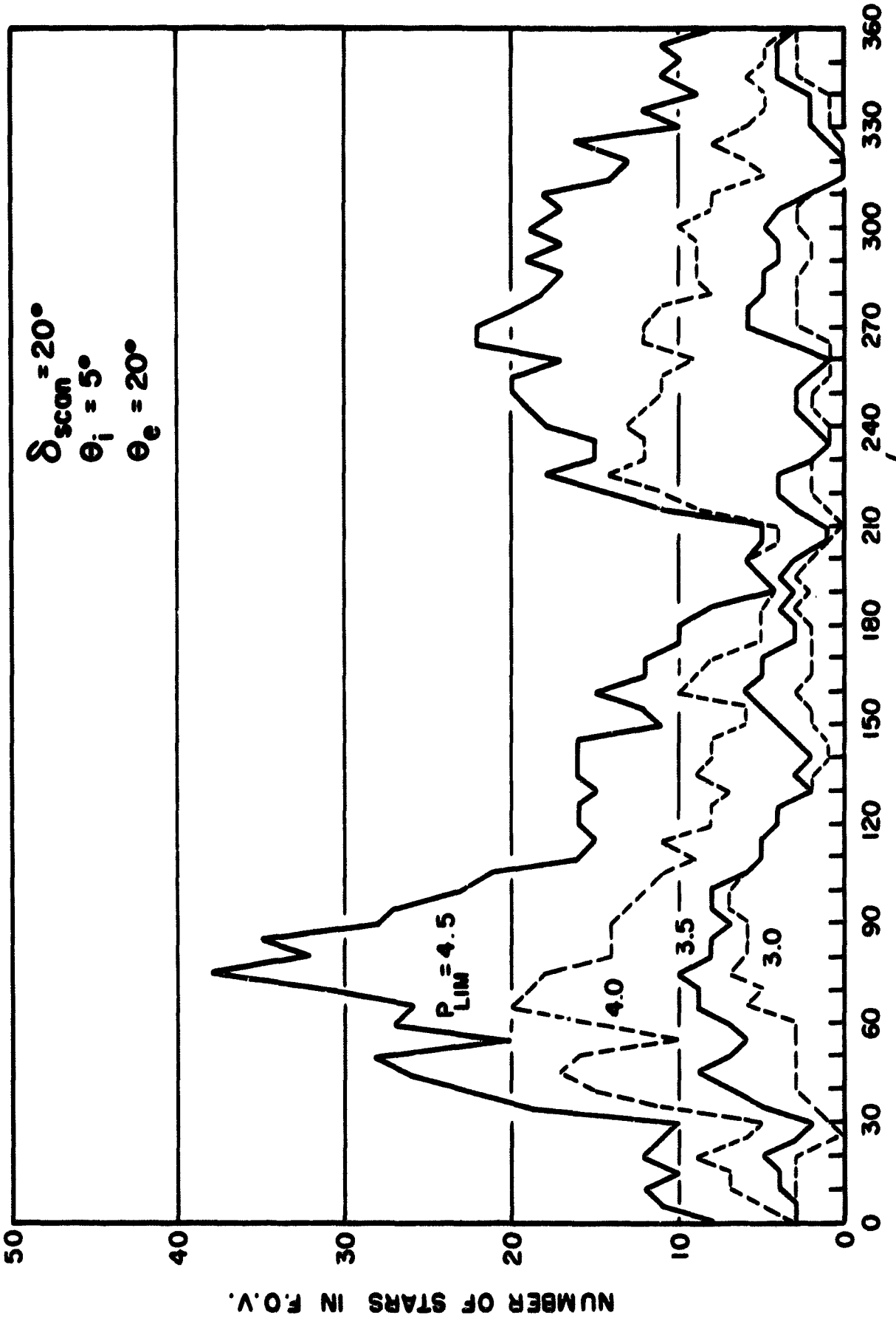


Figure 39: Number of stars in the field of view which are at least as bright as a given parametric limiting magnitude P_{lim}. Results correspond to the recommended SCADS dual mode sensor configuration with annular field $\theta_i = 5^o$ and $\theta_e = 20^o$; the scan axis declination is $\delta_{scan} = 20^o$.

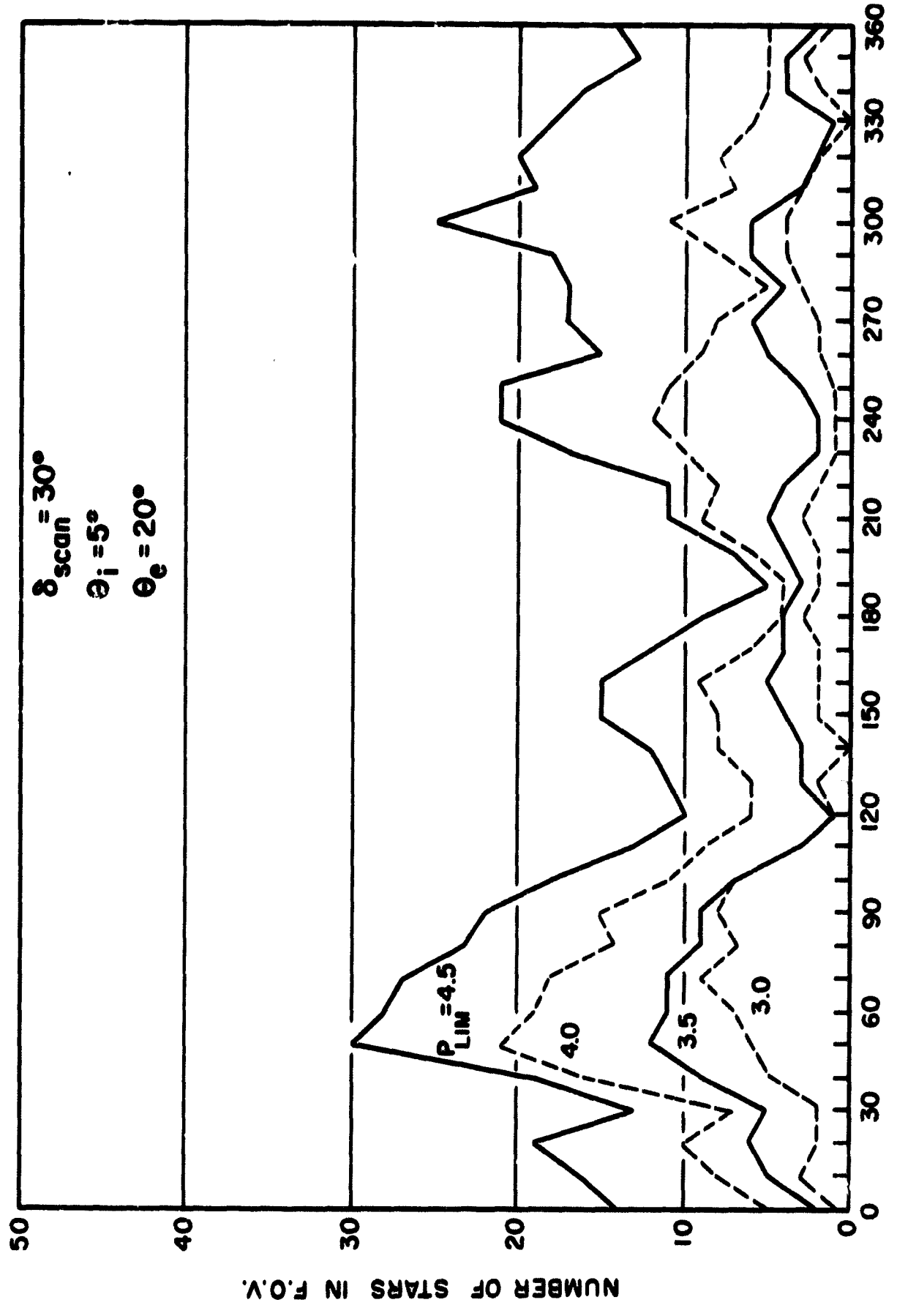


Figure 40: Number of stars in the field of view which are at least as bright as a given parametric limiting magnitude P_{lim}. Results correspond to the recommended SCADS dual mode sensor configuration with annular fields $\theta_i = 5^o$ and $\theta_e = 20^o$; the scan axis declination is $\delta_{scan} = 30^o$.

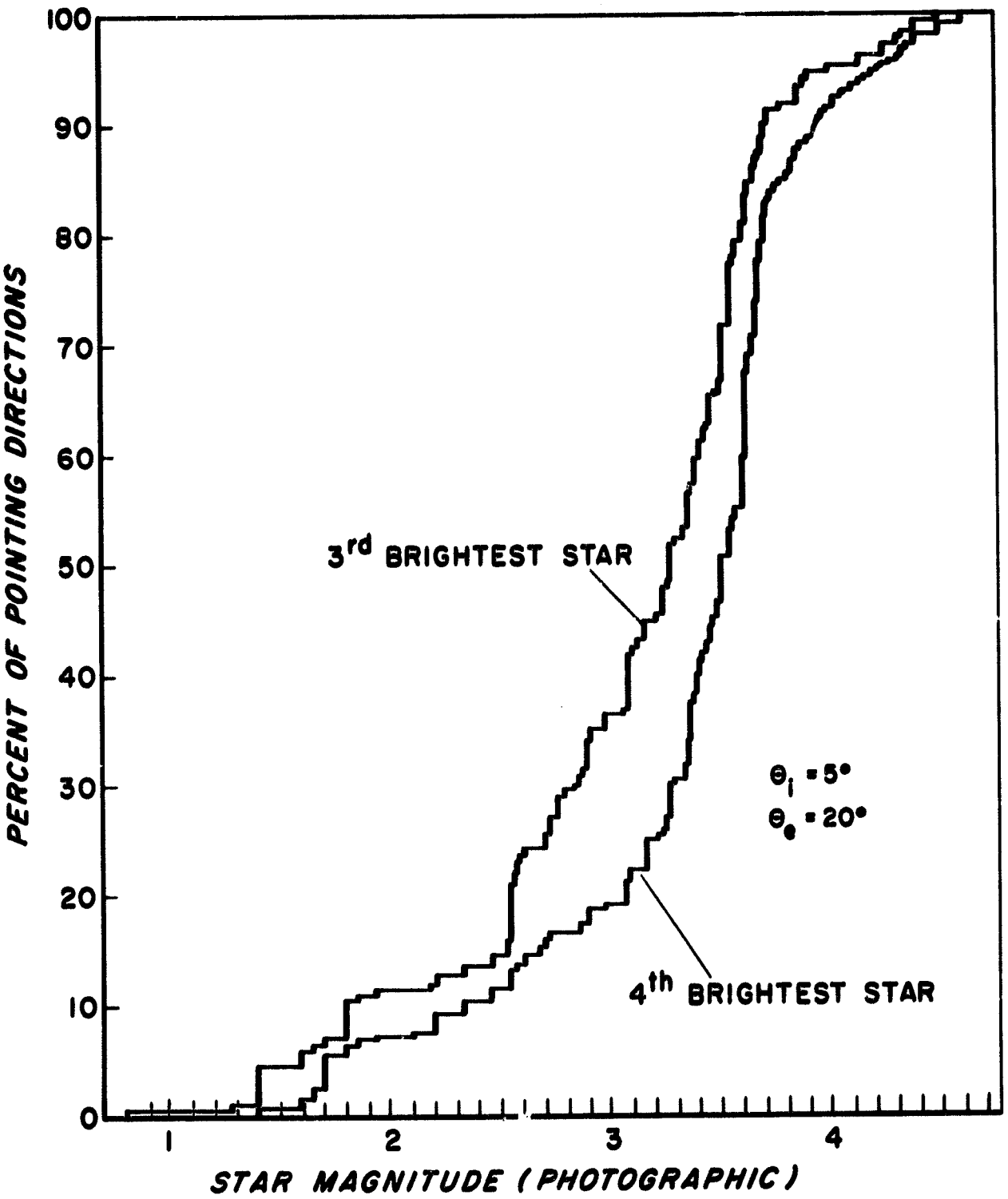


Figure 41: Cumulative probability distribution for the magnitudes of the third and fourth brightest stars in the field of view. The grid of pointing directions covers the possible scan axis orientations in the spin-stabilized portions of the ATS F&G missions. The results correspond to the recommended SCADS dual mode sensor configuration with $\theta_i = 5^\circ$ and $\theta_e = 20^\circ$.

axis directions and more than a full magnitude brighter in over 70% of the cases.

Finally, Figures 42, 43, and 44 present a measure of the range in the number of stars with $M \leq M_{\ell} = 4.65$ for a given nominal scan axis direction and a possible scan axis uncertainty $\epsilon_u = 10^{\circ}$.

The full set of plots in this section characterize the stellar target availability for the dual mode sensor over the spin stabilized portion of the mission. In the three-axis controlled mode, the nominal scan axis for the recommended design of the dual mode sensor will lie in the equatorial plane ($\delta_{scan} = 0$) and will sweep out a full revolution in right ascension once an orbit (i.e. once a day). Thus, Figures 32, 37, and 44 characterize the star availability for this three axis mode.

4. Stellar Target Distribution--Three axis-controlled Mode SCADS Sensor

It was noted in Section IIA4 that a specific location angle for the SCADS design which is required to operate only in the three-axis-controlled portion of the mission will depend strongly on the details of the spacecraft structure. However, it was recommended that this sensor look generally into the southern hemisphere with the scan axis canted away from the Y axis. An annular field of view with $\theta_i = 5^{\circ}$ and $\theta_e = 20^{\circ}$ is postulated. Thus, the cant angle should be at least 20° to avoid inclusion of the solar panel and its boom in the field. At the other extreme, it should be restricted so that the sun will not enter the field of view on any portion of the orbit. Since the Y axis has an uncertainty of $8^{\circ}.7$ (at least for the purposes of this study), the scan axis is limited in declination by

$$\delta_{scan} \leq - |\delta_{SUN}|_{max} - \theta_e = -43^{\circ}.5 \tag{24}$$

and

$$\delta_{scan} \geq - 90^{\circ} - \epsilon_u + \theta_e = -78^{\circ}.7. \tag{25}$$

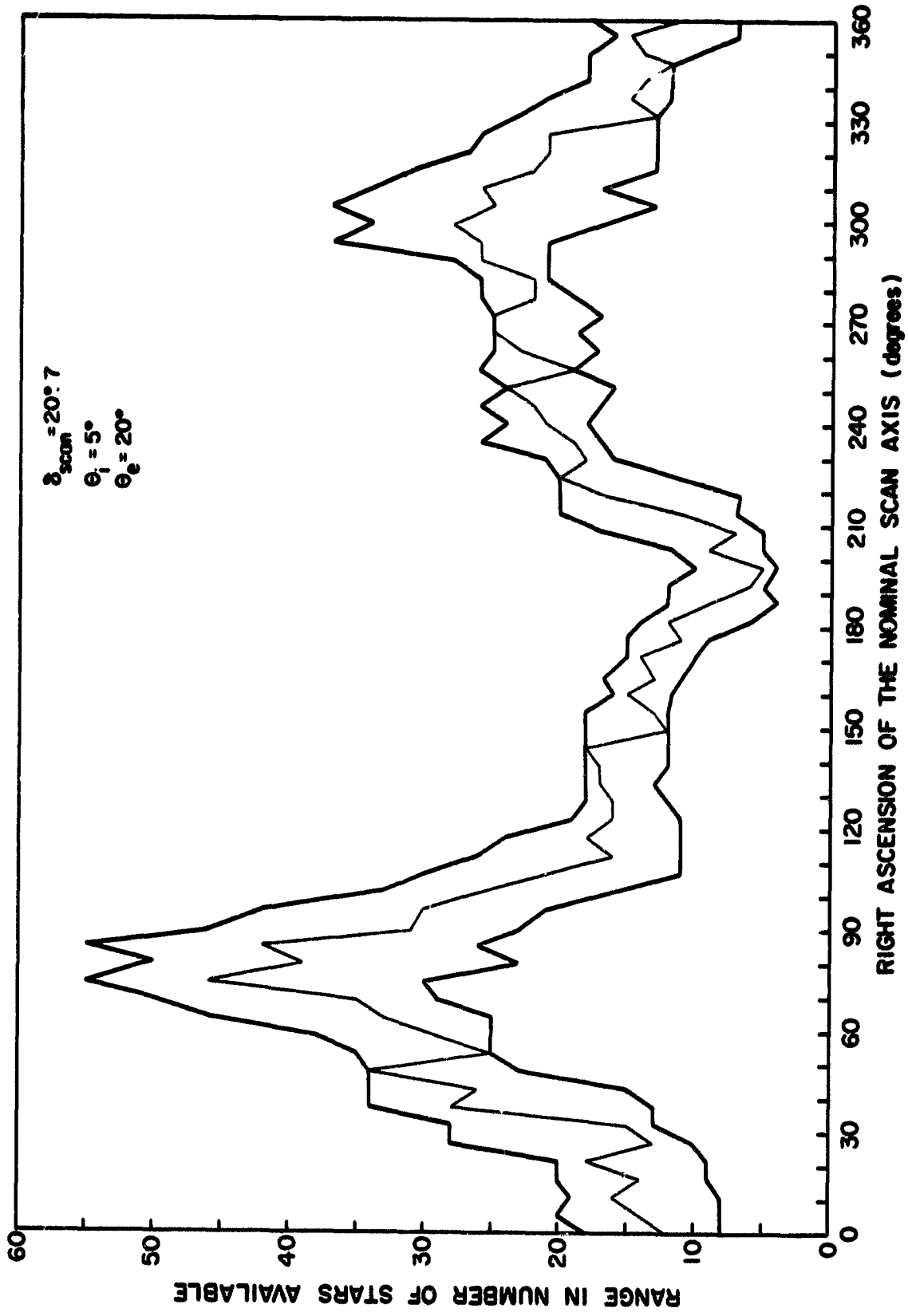


Figure 42: Range in the number of stars available for a ten degree uncertainty about a given nominal scan axis direction (the central curve corresponds to zero uncertainty--i.e., to the nominal direction). The results correspond to the recommended SCADS dual mode sensor configuration with annular field $\theta_i = 5^o$ and $\theta_e = 20^o$; the system limiting magnitude is set at $M_\ell = 4^o.65$. The nominal scan axis declination is $\delta_{scan} = 20^o.7$.

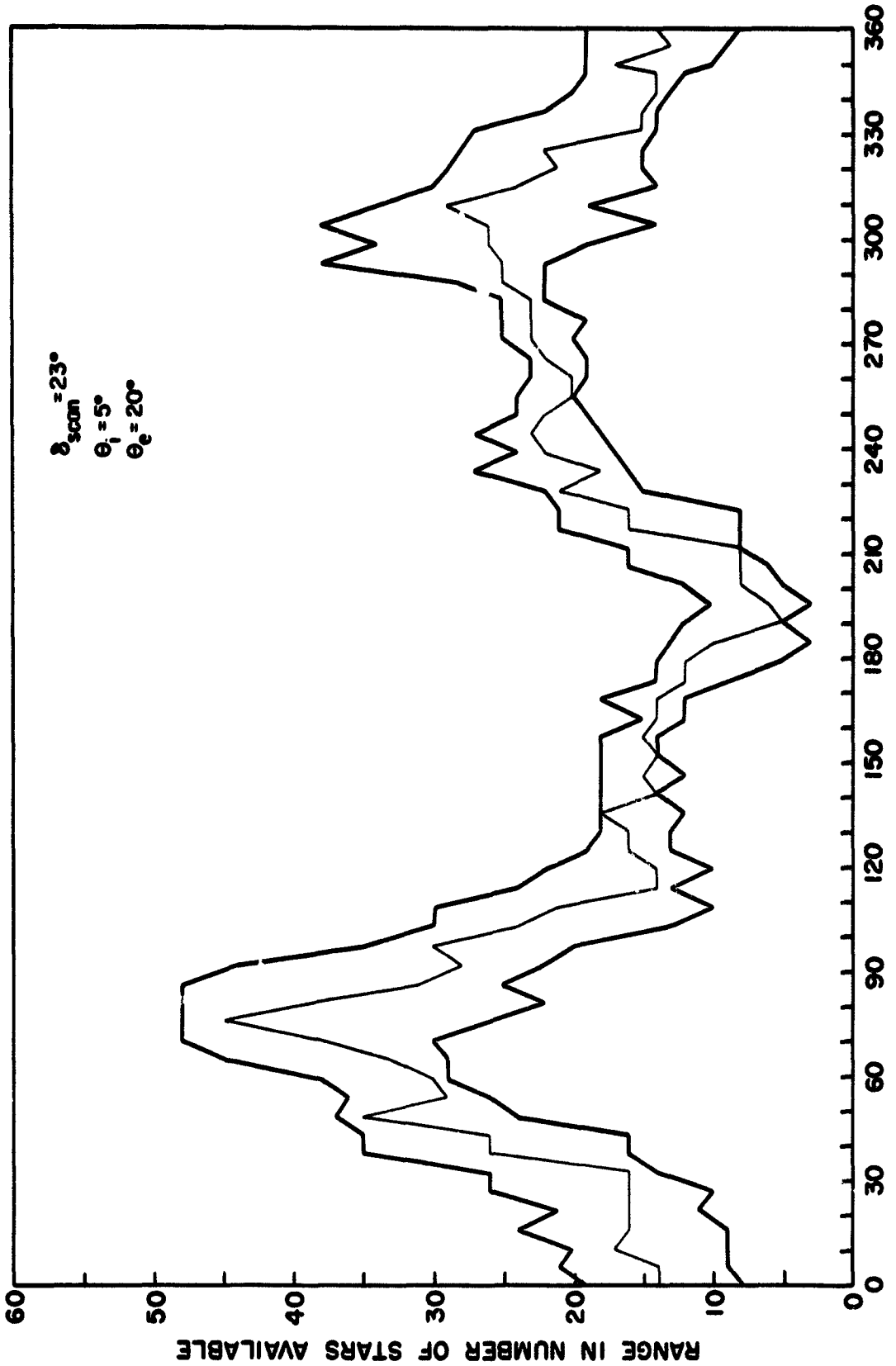


Figure 43: Range in the number of stars available for a ten degree uncertainty about a given nominal scan axis direction (the central curve corresponds to zero uncertainty--i.e., to the nominal direction). The results correspond to the recommended SCADS dual mode sensor configuration with annular fields $\theta_i = 5^o$ and $\theta_e = 20^o$; the system limiting magnitude is set at $M_\ell = 4.^o65$. The nominal scan axis declination is $\delta_{scan} = 23^o$.

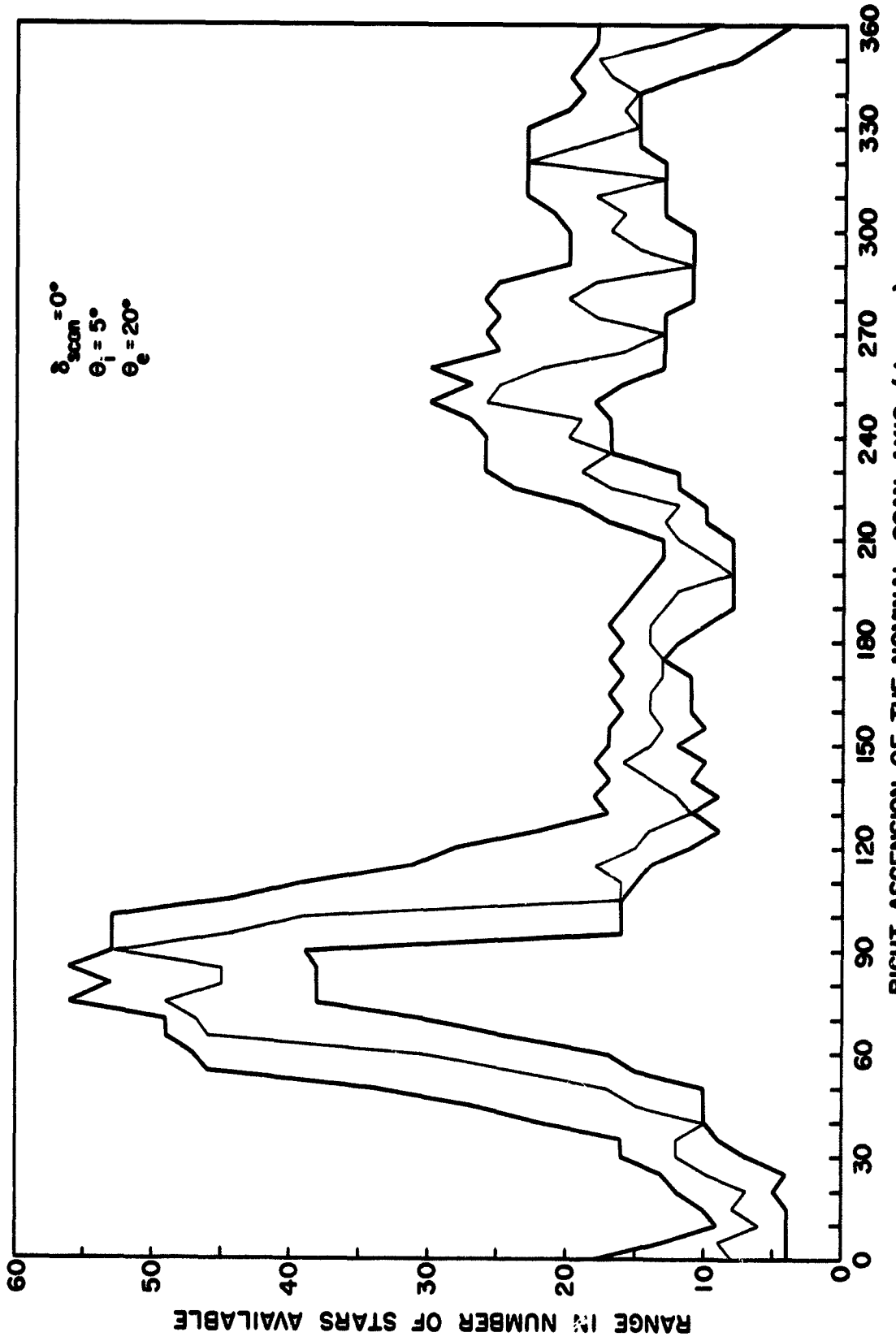


Figure 44: Range in the number of stars available for a ten degree uncertainty about a given nominal scan axis direction (the central curve corresponds to zero uncertainty--i.e., to the nominal direction). The results correspond to the recommended SCADS dual mode sensor configuration with annular fields $\theta_i = 5^o$ and $\theta_e = 20^o$; the system limiting magnitude is set at $M_\ell = 4.^o65$. The nominal scan axis declination is $\delta_{scan} = 0^o$.

All values of right ascension are taken on during each orbit. The annular field was "pointed" at 948 scan axis directions covering the declination band given by (24) and (25). The resulting cumulative probability distributions for the third and fourth brightest stars are shown in Figure 45. The faintest fourth-brightest star has magnitude $M_\ell = 4.21$; this is selected as the system limiting magnitude for the three-axis-controlled mode SCADS sensor. Note that the fourth star is at least a half magnitude brighter than M_ℓ in 88% of the cases and a full magnitude brighter for 54% of the possible scan axis directions.

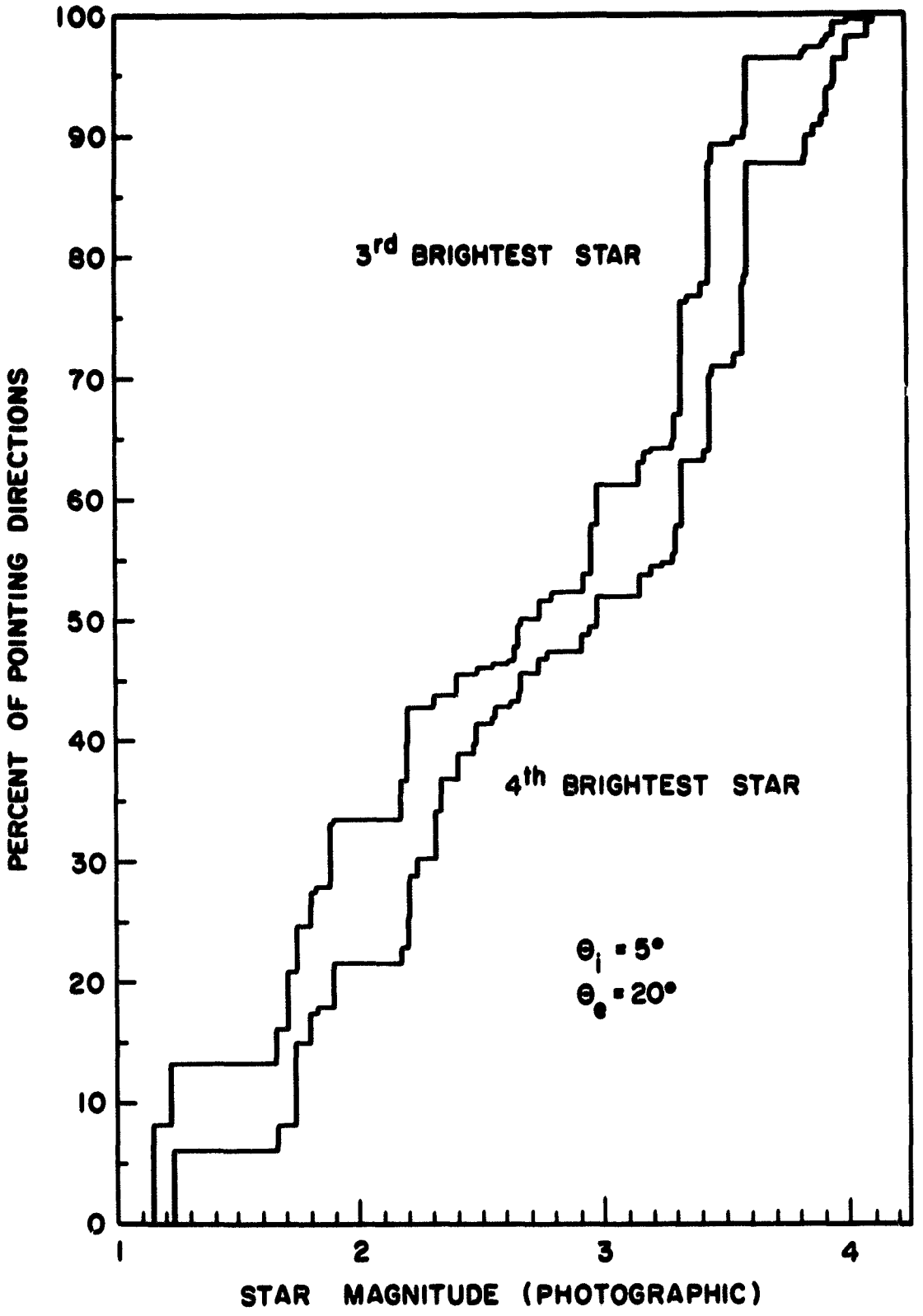


Figure 45: Cumulative probability distribution for the magnitudes of the third and fourth brightest stars in the field of view. The grid of pointing directions covers the declination band $-43^{\circ}.5 < \delta_{scan} < -78^{\circ}.7$. The results correspond to a SCADS three-axis-controlled mode sensor with $\theta_i = 5^{\circ}$ and $\theta_e = 20^{\circ}$.

PRECEDING PAGE BLANK NOT FILMED.

III. SCADS PARAMETER SELECTION

A large number of interacting parameters must be selected in arriving at a suitable SCADS design for a particular application. Three broad categories of parameters may be identified--those related to celestial constraints, those related to star detection and identification, and those related to measurement accuracy. Although the boundaries among these categories are somewhat blurred, they are sufficiently independent so that detailed quantitative design comparisons and selections may be made internal to each category with references only to typical parameter values or ranges from the other categories. This reduces the number of simultaneous variables in the design optimization to a tractable level. The general design considerations for SCADS sensors applicable to synchronous satellite missions (ATS F & G) are developed in the subsections which follow.

A. Parameters Related to Celestial Constraints

The determinations of the geometrical parameters for SCADS--e.g. the size of the optical field of view and the angle at which the optical axis is canted from the scan axis in the spinning mode--are dominated by the celestial constraints described in Section II. The outer edge of the annular scan region is at an angular radius θ_e from the scan axis (the negative Z axis of the spacecraft). Further, the actual scan axis has an uncertainty $\epsilon_u (=10^\circ)$ with respect to the nominal scan axis direction. Finally, SCADS is to be operable for a minimum angle $\psi_S = 66^\circ.557$ between the nominal scan axis and the spacecraft-sun line. Thus, the SCADS geometry is constrained by the relation

$$\theta_e < \min(\psi_S) - \epsilon_u = 56^\circ.557. \qquad (26)$$

However, relation (26) is only a gross constraint which excludes the sun from the direct field of view during the various possible orientations of the scan axis during the spinning mode. The SCADS optical aperture must be shielded from all direct or first-surface-reflected sunlight, including that from angles outside the field. Scattering of the sun's rays in the glass of

the SCADS lens elements is sufficient to override the signals from a stellar target which may be only 10^{-12} times as bright as the full sun. Thus, the geometry of the bright object shield must also be included in optimizing the selection of the basic SCADS parameters. The recommended shield design is described next.

1. Bright Object Shield

The bright object shield requirements are described in terms of three quantities--the optical field of view Θ, the optical aperture a, and the shield angle ξ between the optical axis and the closest approach of the bright source (the sun or the earth in this case). The recommended shield geometry is shown in cross section in Figure 46; the heavy solid lines represent sections in the shield structure.

Observe that the cone of element x-y is generated so that its upper surface cannot be seen from any point within the aperture a. Thus, light which is reflected or scattered from this surface cannot pass directly through a. Further, no light which passes through the surface x-x' at an angle of incidence greater than β with respect to the optical axis can pass directly on through the lower cone aperture y-y'. All such light strikes the upper surface of the cone and can travel deeper into the shield only through a scattering process. Even such scattering can be minimized by making the upper cone surface specularly reflecting. Thus, the angle β becomes a nearly absolute shielding angle.

For light incident at an angle less than β with respect to the optical axis, some rays will pass directly through the bottom of the cone and the lip y-y' of the cone will be directly illuminated. This lip is made in the form of a knife edge to minimize its scattering area. Thus, it approaches a scattering "line" rather than a scattering surface and it is the only directly illuminated shield element which is visible from the aperture.

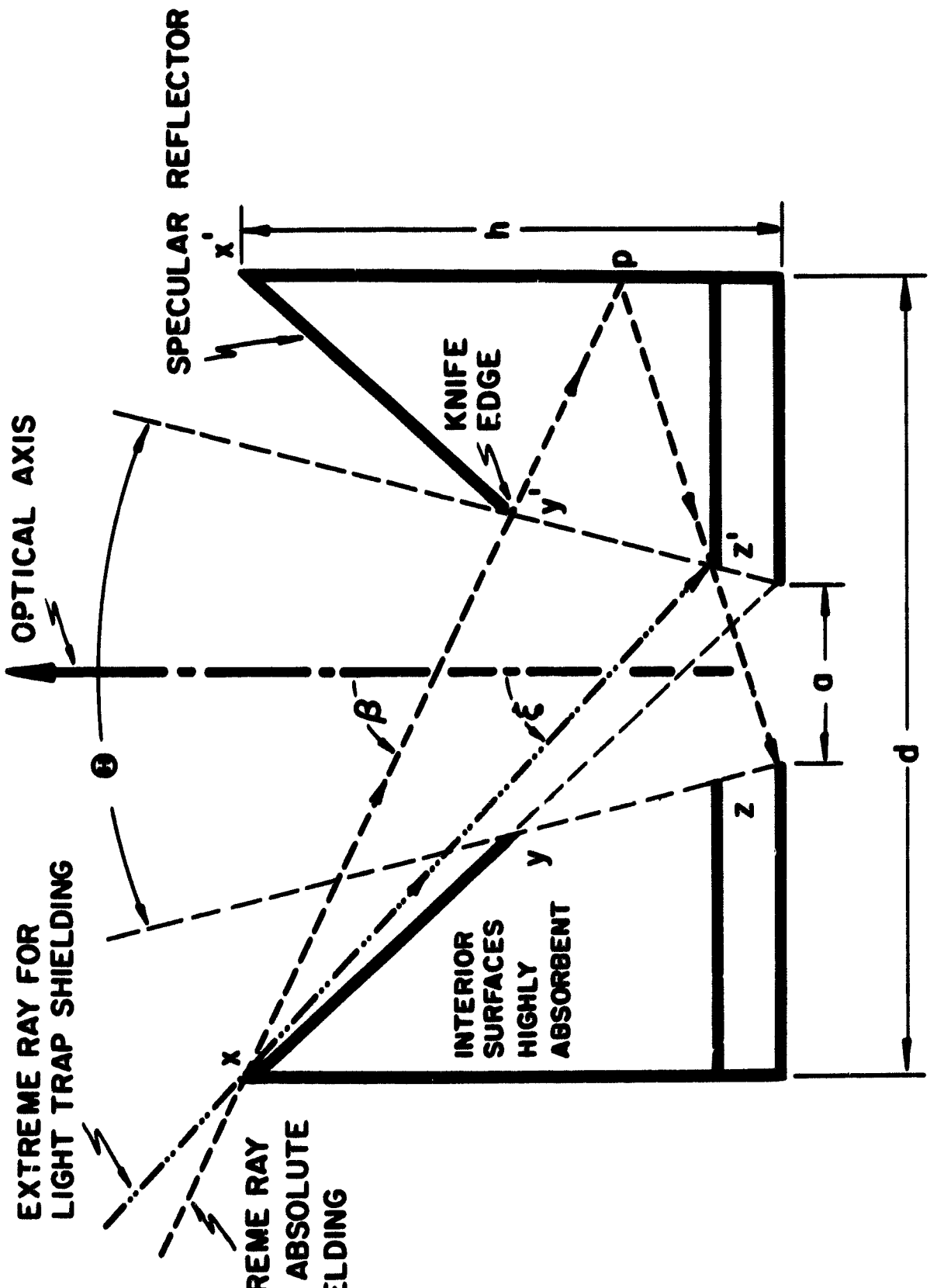


Figure 46: Bright object shield geometry showing shield cross section and principal angles.

For incident rays which pass through the opening y-y', the highest point on the interior of the cylinder which can be directly illuminated is p on the extension of the extreme ray from x through y'. An optical stop is placed at z-z' in a position such that the illuminated interior surface cannot be seen from the aperture a. Then, light which enters this "trap" region must go through a number of reflections before reaching the aperture. The interior surfaces of the trap should, therefore, be coated with a highly absorbent material. Note that light at angles of incidence up to the ray x-z' is accepted by the shield without illuminating any element other than the knife edge y-y'. The angle between x-z' and the optical axis is then identified as the effective shield angle ξ.

The cylinder height h and diameter d are the dependent design variables which characterize the overall volume and form factor for the SCADS bright object shield. This shield volume will represent the dominant portion of the total sensor size. However, a minimum volume sensor design is a goal of this study so the height and diameter of the shield are among the variables which must be included in the detailed parametric investigations.

Note that h and d may be normalized to H = h/a and D = d/a. This normalization is particularly appropriate when shield requirements are to be compared for a given effective field of view Θ_{eff}. For a fixed value of Θ_{eff}, the same total scan area on the celestial sphere is covered independent of the particular values of θ_i and θ_e which yield that effective field. Therefore, the system limiting magnitude should also be nearly invariant. But the optical aperture a depends primarily on this magnitude limit. Hence, a fixed Θ_{eff} implies a nearly constant aperture and the corresponding <u>normalized</u> shield designs are directly comparable.

Elimination of explicit reference to the aperture a leaves only conditions on Θ and ξ which must be met by the normalized shield. But specification of values for these two variables implies only one independent condition

relating Θ, ξ, H, and D. This condition is a rather complex polynomial relation in H, D, and trigonometric functions of Θ and ξ which requires numerical investigation using a digital computer. Observe that any proposed "solution" of this relation can be checked graphically by constructing the shield cross-section in the form shown in Figure 46.

Since only one condition but two dependent variables exist here, there is a family of solutions $\{H(\Theta, \xi), D(\Theta, \xi)\}$ for each pair (Θ, ξ). Thus, an additional requirement may be imposed on the shield design; minimization of the normalized shield volume, $V_{shield} = \pi D^2 H/4$, at fixed (Θ, ξ) is chosen as the added design condition.

2. SCADS Geometric Parameters: Spin Mode Sensor

The principal angles for a SCADS sensor which is required to operate only in the spinning mode are illustrated in Figure 47. These angles are defined as follows:

Θ_{eff} = the effective field of view (equivalent to the full angle of a cone which covers a given solid angle);

Θ = the instantaneous field of view of the SCADS optical system;

Γ = the cant angle of the optical axis with respect to the actual scan axis (the negative z or negative spin axis of the spacecraft);

θ_i = the interior radius of the annular field of view;

θ_e = the exterior radius of the annular field of view;

ϵ_u = the maximum uncertainty in the position of the actual scan axis relative to its nominal direction;

ψ_{min} = the minimum angle between the nominal scan axis and the line from the spacecraft to the sun or the earth;

and ξ = the required shield angle for the system.

The following relations hold among these angles:

$$\theta_i = \Gamma - \frac{\Theta}{2} \tag{27}$$

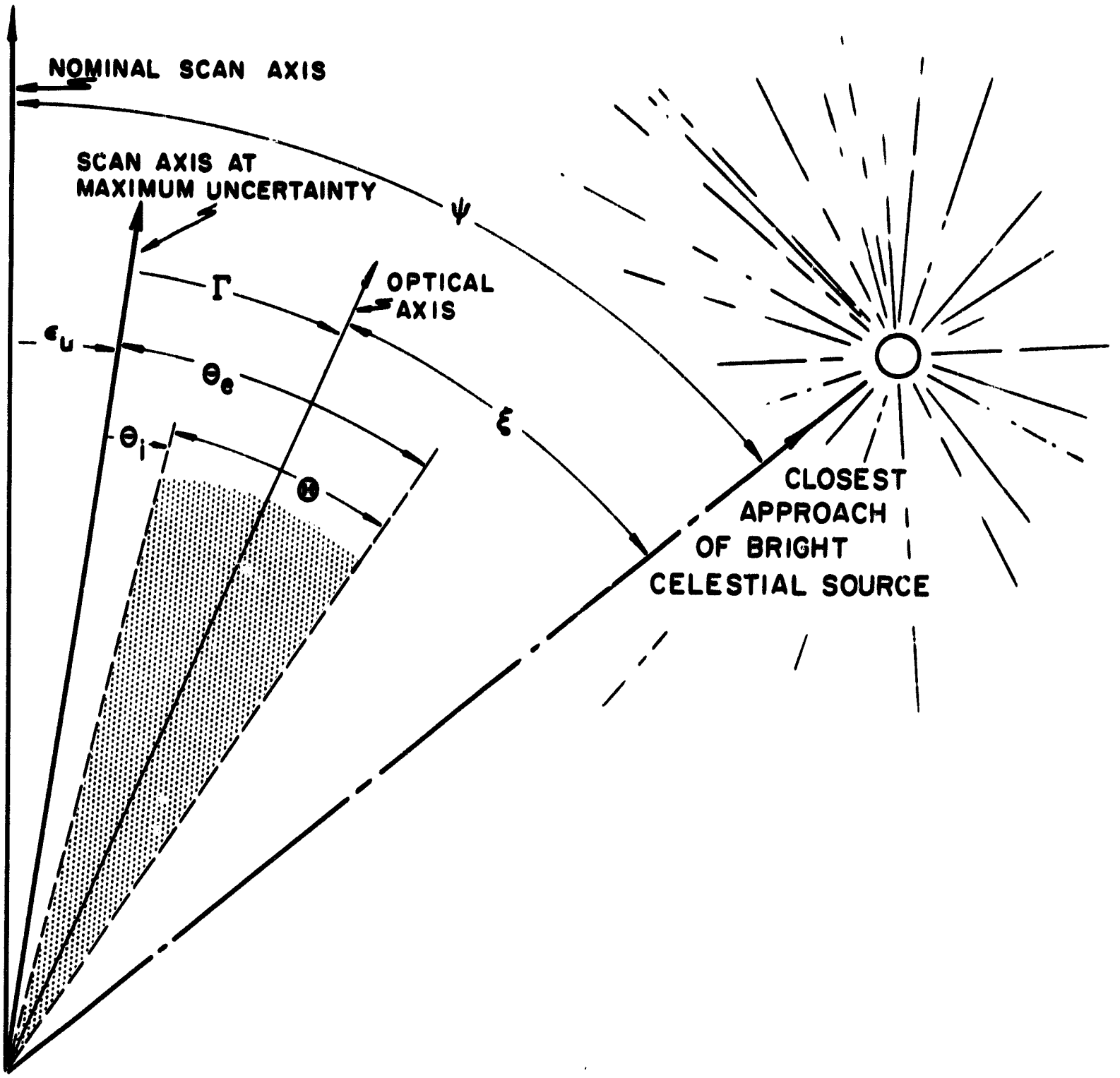


Figure 47: Geometry of the bright object shield problem for the spin mode sensor.

$$\theta_e = \Gamma + \frac{\Theta}{2} \tag{28}$$

$$1 - \cos \frac{\Theta_{eff}}{2} = \cos \theta_i - \cos \theta_e = 2 \sin \Gamma \sin \frac{\Theta}{2} \tag{29}$$

$$\xi = \psi_{min} - \epsilon_u - \Gamma. \tag{30}$$

In addition to these conditions, the inequality from relation (26) above must be satisfied. This latter constraint may be restated as

$$\frac{\Theta}{2} < \xi. \tag{31}$$

Another constraint is imposed by the requirements of the star identification procedure and the desired accuracy of the system; the hole in the annular field must not vanish. This is because the scan axis is essentially stationary in space and attempts to measure the azimuths of stars which lie very close to this axis are subject to large errors. Thus, the condition $\theta_i > 0$ or alternatively,

$$\frac{\Theta}{2} < \Gamma \tag{32}$$

is imposed. The quantity $(2\theta_i)$ is then a measure of the central blocking for the design.

The effective field of view and the cant angle are chosen as the primary independent variables in the parametric design studies reported below. The choice of the effective field of view as a key variable is based on the fact that the system limiting magnitude and optical aperture are nearly invariant at fixed Θ_{eff}. The cant angle is selected as the other key because it characterizes the orientation of SCADS with respect to the spacecraft; the value of Γ is a critical parameter in the SCADS-spacecraft structural interface. Note also that the shield angle ξ is given by equation (30) as a simple linear function of Γ for fixed $(\psi_{min} - \epsilon_u) = 56.^{o}557$.

SCADS PARAMETER SELECTION

Families of SCADS design curves for the spin mode sensor are presented as a function of the cant angle with the effective field of view as the parameter in Figures 48, 49 ,50 , and 51. The curves for the required optical field of view Θ (Figure 48) and the cone angle of the central dead zone (Figure 49) are simply plots of their defining relations. The graphs describing the normalized shield design are more interesting. Each given set of values (Θ_{eff}, Γ) yields a unique pair of values (Θ, ξ). For each such pair considered, the corresponding relationship between H and D was explored using a digital computer and the solution (H, D) which minimizes HD^2 was determined. Thus, all points on the curves in Figures 50 and 51 correspond to minimum volume shield designs. Note that the dimensions of even these optimal shields are many times larger than the aperture which they must shield. Thus, minimization of the bright object shield volume becomes an effective design criterion for obtaining a compact total sensor.

A second level of optimization may be carried out immediately. It was noted earlier that alternative shield designs at the same effective field are directly comparable. Thus, the normalized shield design data presented in Figures 50 and 51 may be searched for minimum volume with respect to the cant angle at fixed Θ_{eff}.

The end product of this search is the specification of the optimum cant angle for a given effective field of view; the resulting relation is presented in Figure 52. Also shown here are the curves of the optical field of view, the required shield angle, and the central blocking corresponding to $\Gamma(\Theta_{eff})$. The normalized shield values may be found from Figures 50 and 51 at the point $[\Theta_{eff}, \Gamma(\Theta_{eff})]$. Figure 52 is the primary design curve for the SCADS geometrical parameters in the spinning mode.

For each Θ_{eff}, a unique optimal pair (Γ, Θ) is found. Equations (27) and (28) may then be used to determine the corresponding pair (θ_i, θ_e). Next, these angular radii which specify the annular field of view may be used

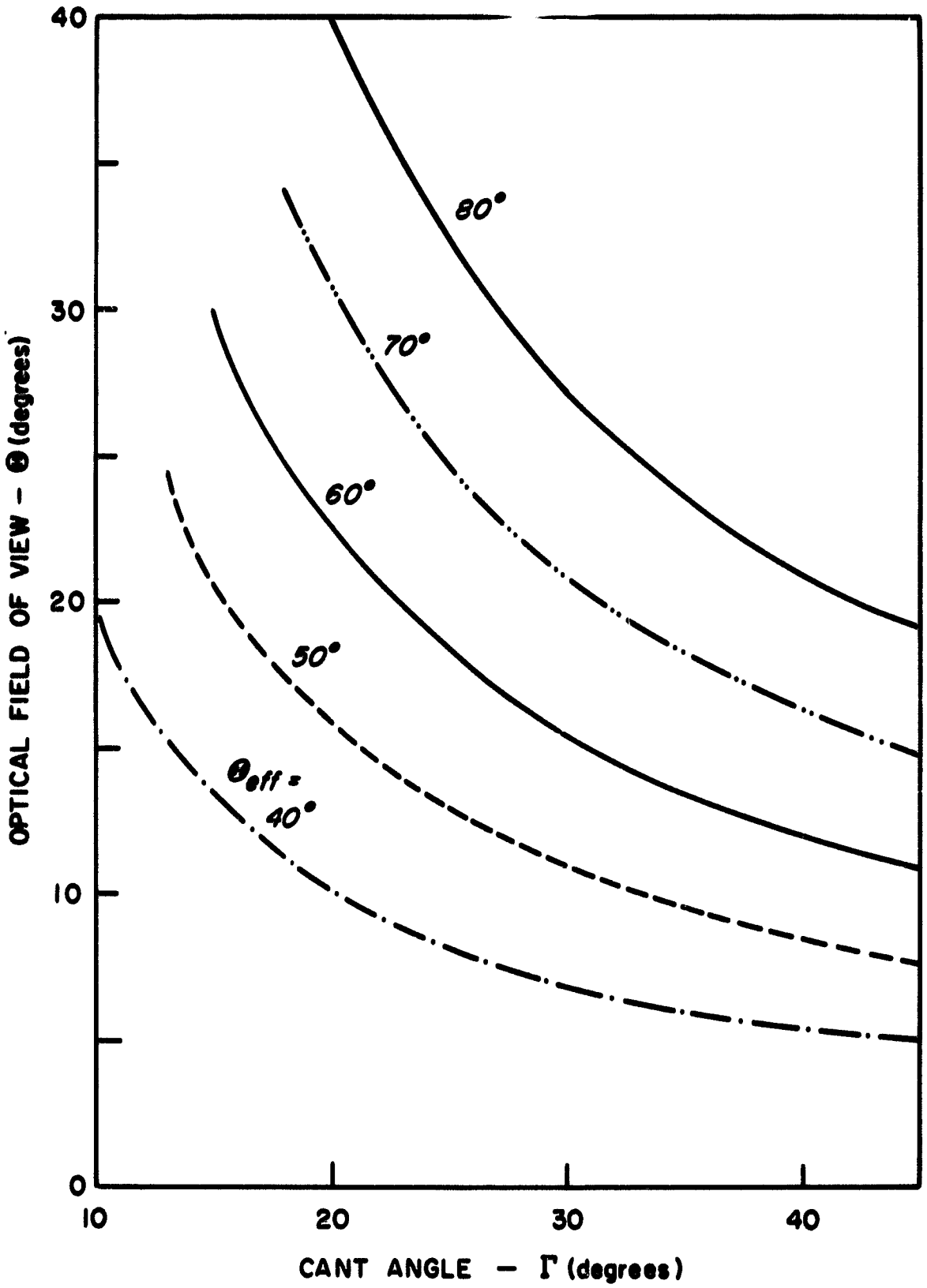


Figure 48: Required optical field of view at a given effective field of view and cant angle for the spin mode sensor.

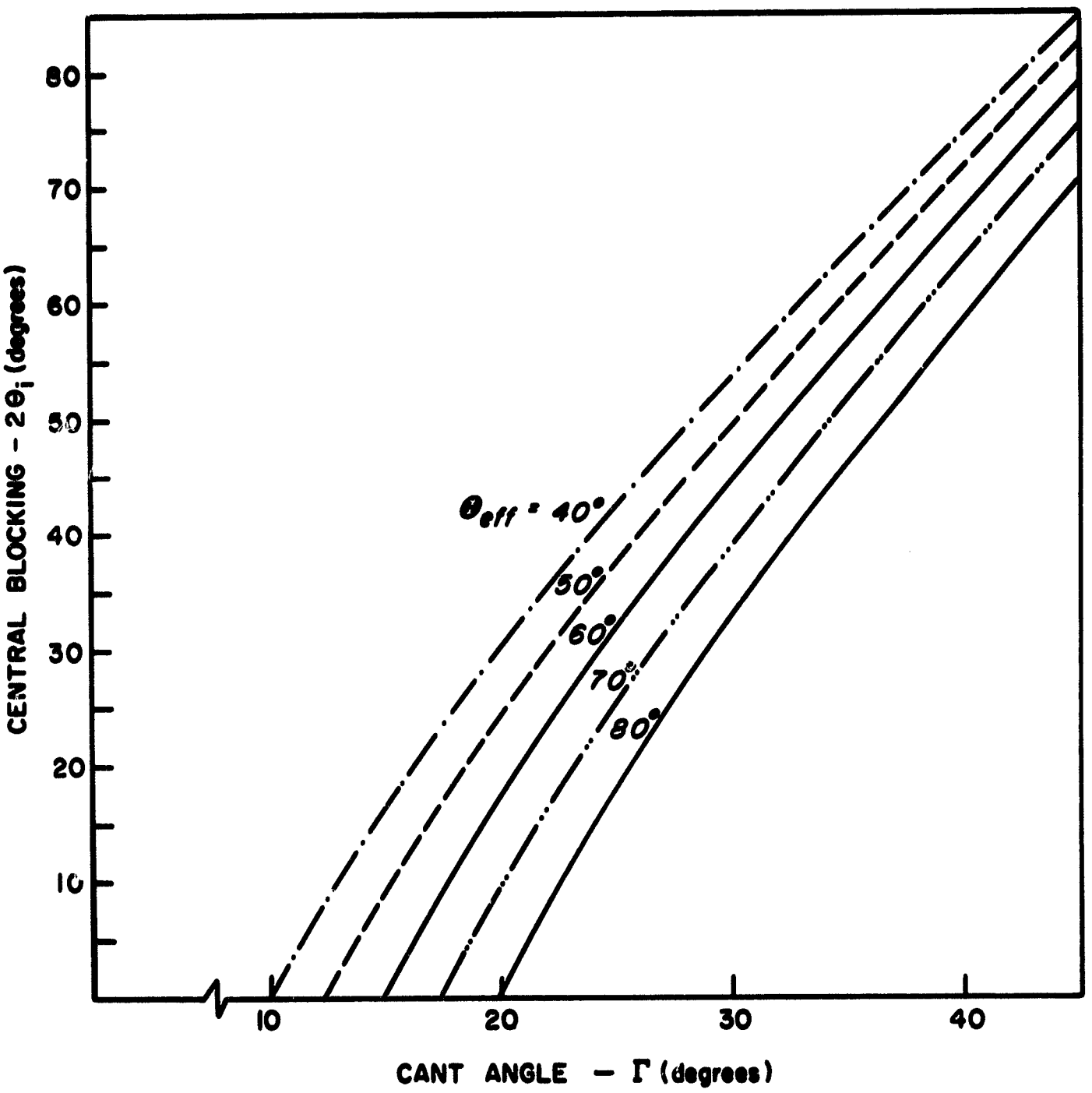


Figure 49: Parametric curves for the central blocking (full cone angle $2\theta_i$) in the annular scan region for the spin mode sensor.

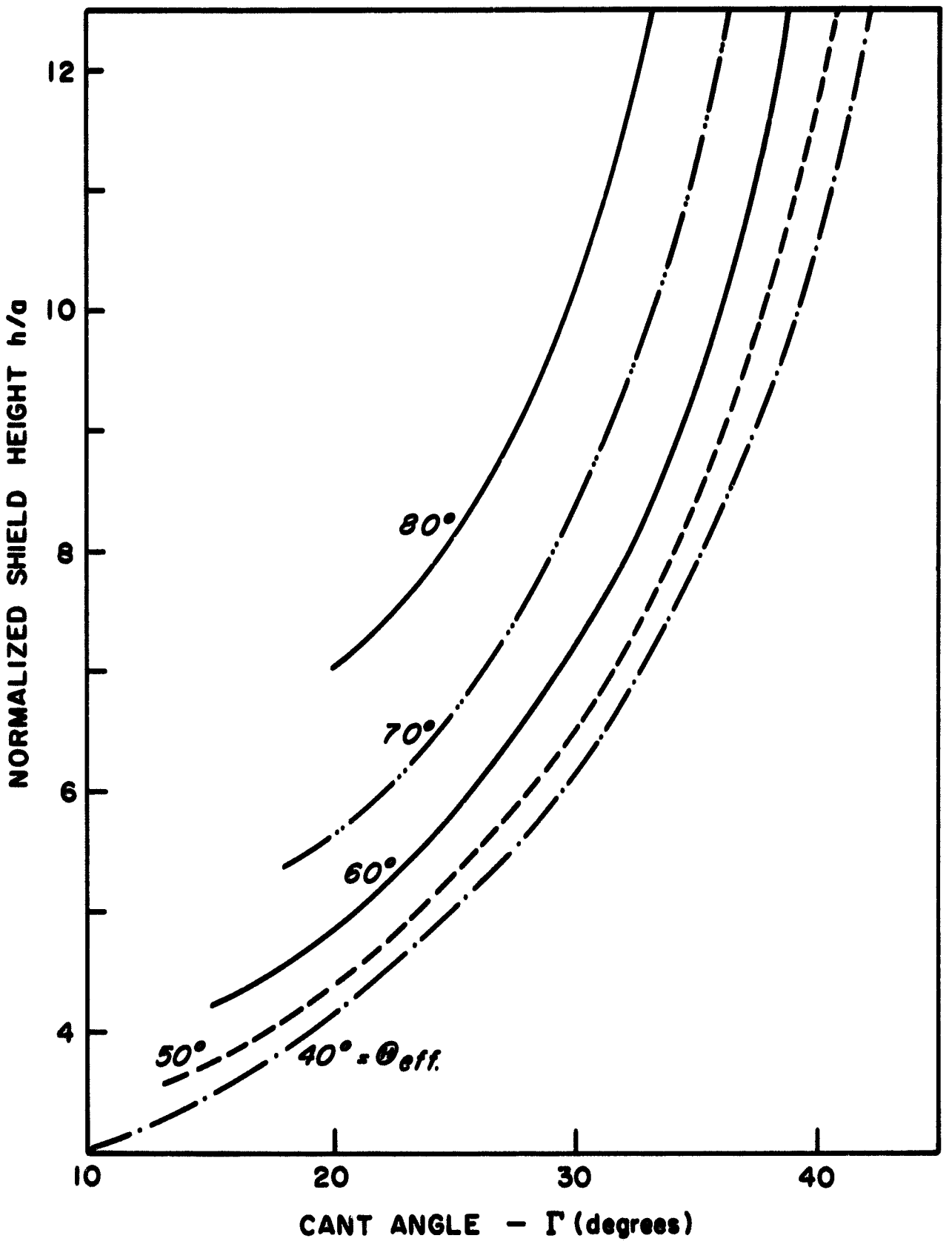


Figure 50: Normalized bright object shield height for the spin mode sensor. Note that the results correspond to a minimum volume shield at given (Θ_{eff}, Γ).

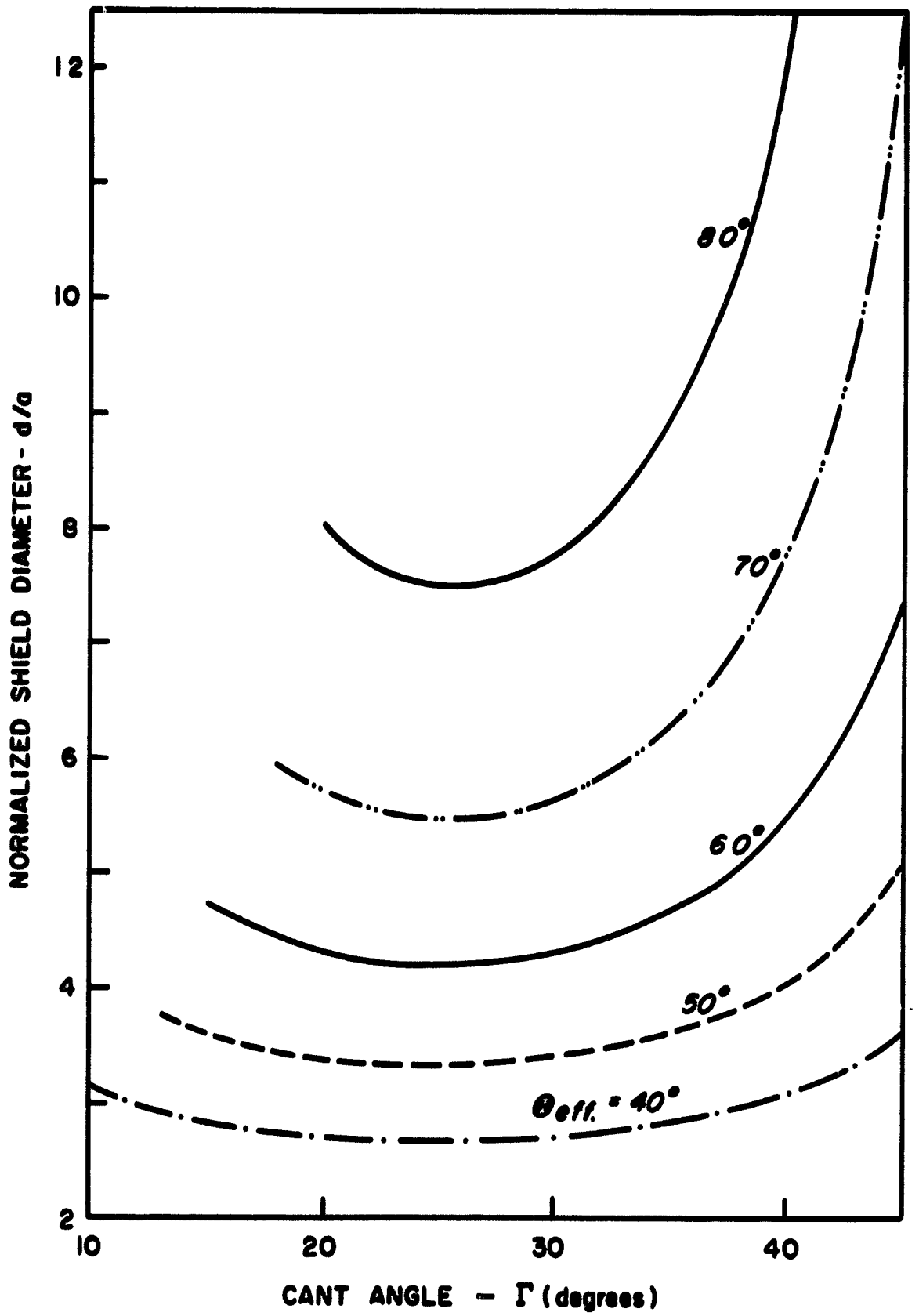


Figure 51: Normalized bright object shield diameter for the spin mode sensor. Note that the results correspond to a minimum volume shield at given (Θ_{eff}, Γ).

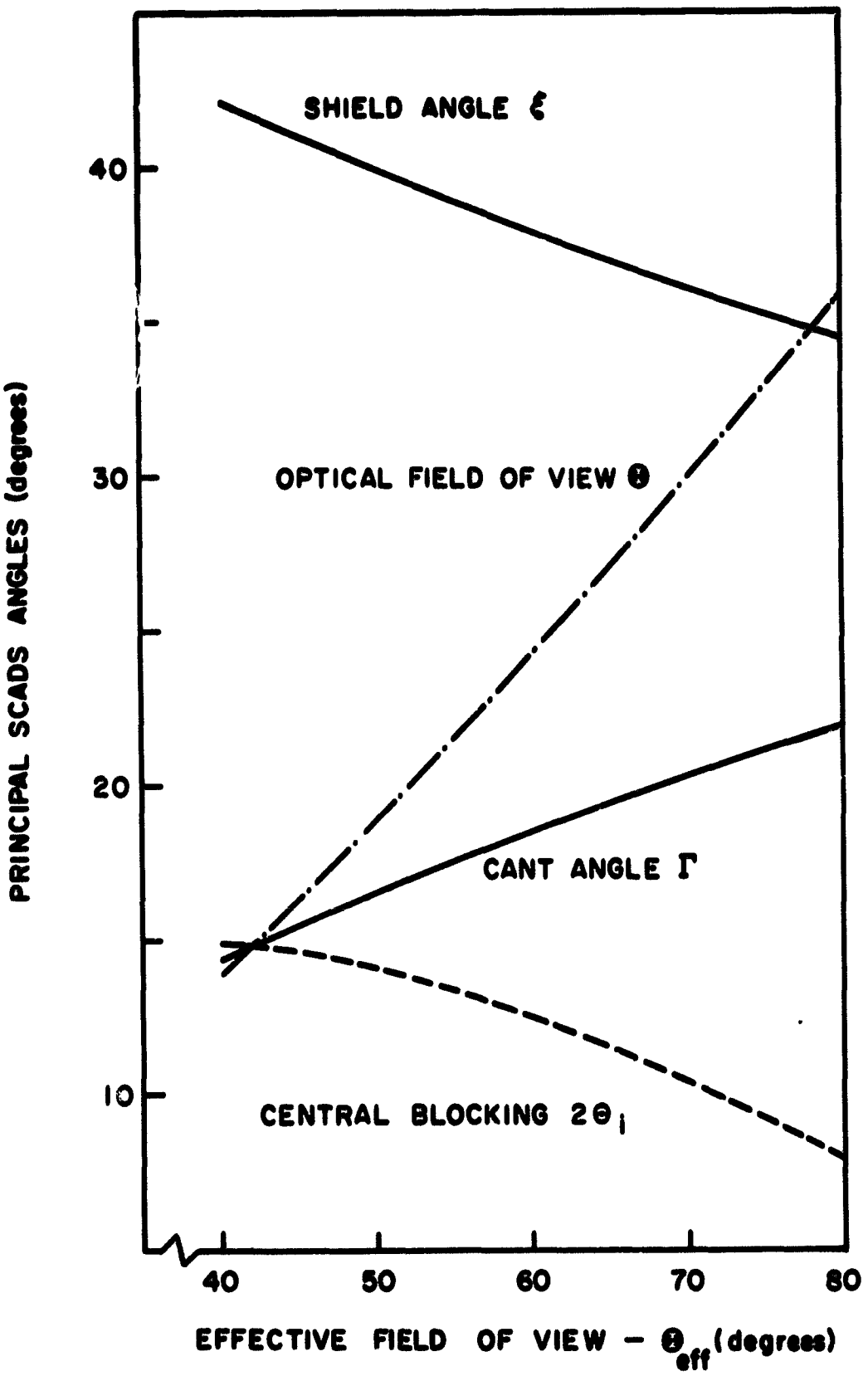


Figure 52: Parametric design curves for the spin mode SCADS sensor after second level optimization. Note that the results correspond to a minimum volume shield at a given effective field Θ_{eff}.

to perform a detailed star availability analysis over the possible scan axis directions in the mission profile. Finally, this stellar target analysis yields a specific system limiting magnitude $M_t(\Theta_{eff})$ for each effective field. Presentation of this function completes the general analysis of spin mode SCADS parameters related to the celestial constraints; it is given in Figure 53.

3. SCADS Geometric Parameters: Dual Mode Sensor

During the spin stabilized portions of the mission, the bright object constraints on the dual mode sensor are the same as those on the spin mode sensor. Since reliable operation of the spinning SCADS is the prime requisite here, these constraints again dominate the design. However, an additional factor must be taken into account for the dual mode instrument. In the three-axis-controlled mode, the motion of the field of view is very slow--about fifteen degrees per hour. Thus, the scanning motion is to be provided by driving the slit reticle and the entire effective field of view must be supplied by the optical system.

The principal angles are defined as before (See IIIB2) but the relations among these angles have changed. The dual mode configuration is illustrated in Figure 54. In the three-axis-controlled or driven mode, the inner radius of the annular field $\theta_{i\ driven}$ is determined by the angle from the optical axis to the closest point in the slit. The outer radius is just

$$\theta_{e\ driven} = \frac{\Theta}{2} . \tag{33}$$

The slit length θ_{slit} in angular measure is

$$\theta_{slit} = \theta_{e\ driven} - \theta_{i\ driven} \tag{34}$$

for both the driven and spinning scans. The driven mode effective field of view is obtained from

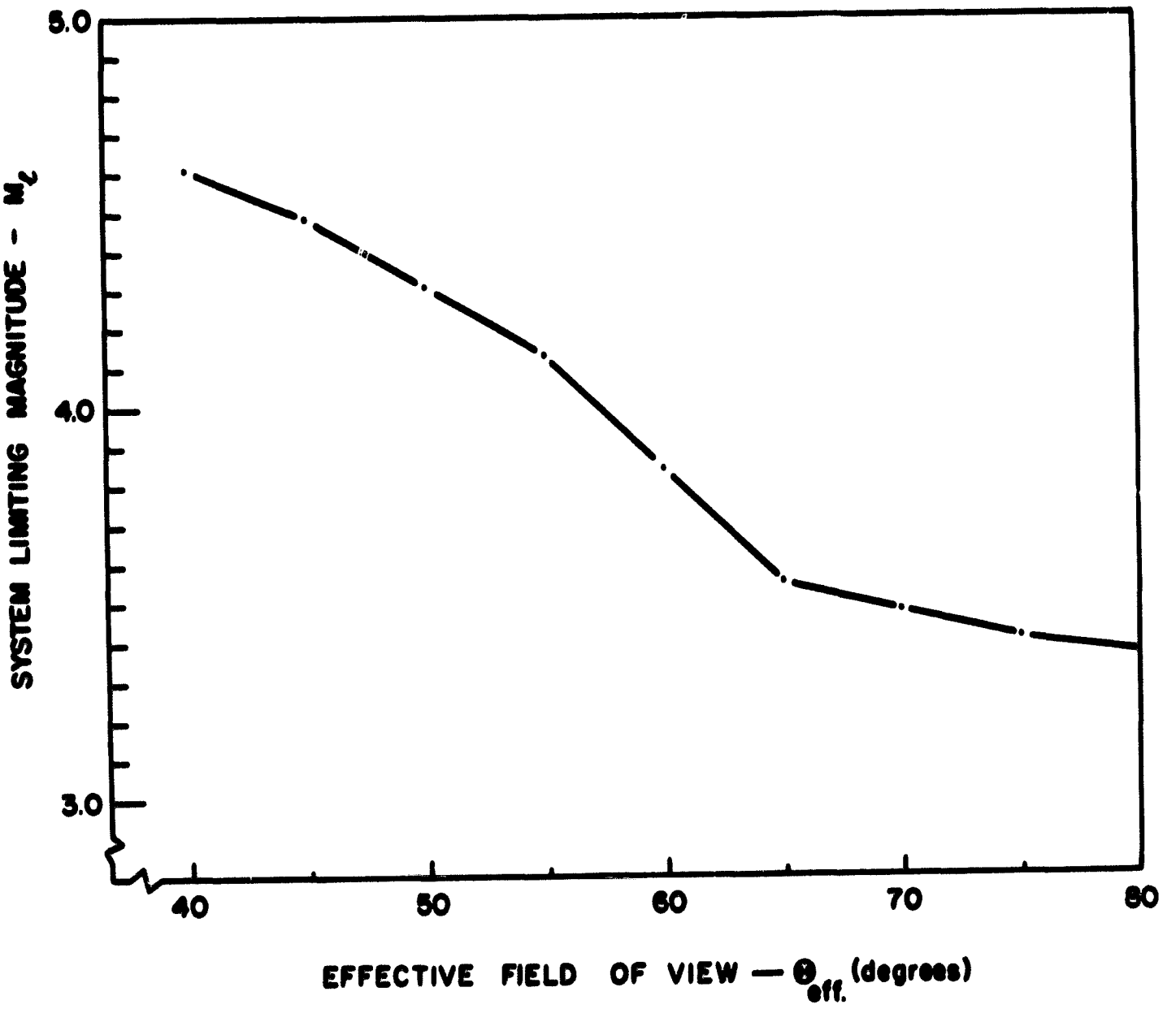


Figure 53: System limiting magnitude M_ℓ as a function of the effective field of view Θ_{eff} for the spin mode sensor. Results based on a detailed star availability search over the possible scan axis directions for the ATS F&G missions.

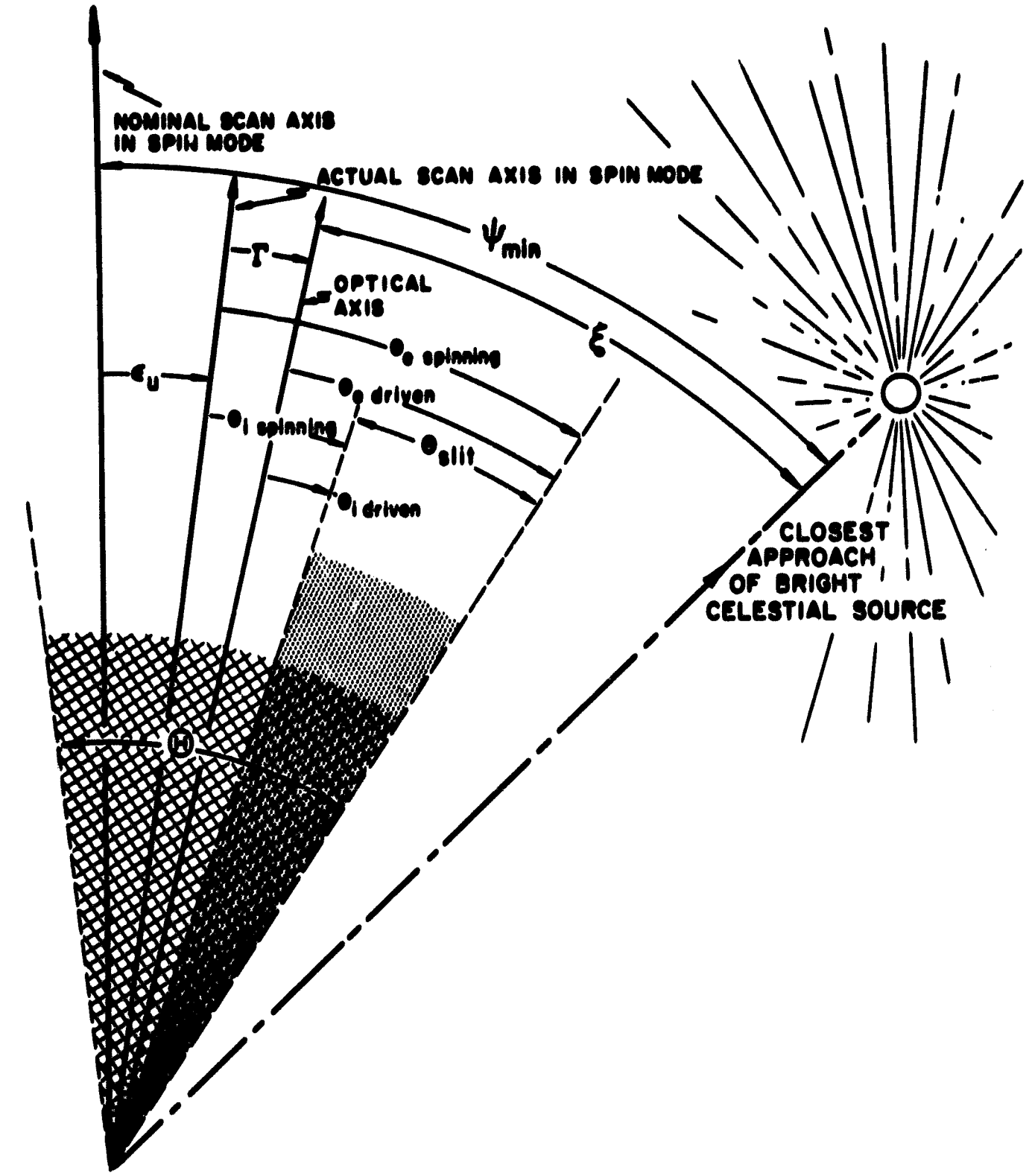


Figure 54: Geometry of the dual mode sensor showing the principal SCADS angles and the related bright object shielding problem.

$$1 - \cos \frac{(\Theta_{eff})_{driven}}{2} = \cos \theta_{i\ driven} - \cos \frac{\Theta}{2} . \tag{35}$$

Thus, the effective field of view $(\Theta_{eff})_{driven}$ is smaller than Θ.

In the spinning mode, the inner and outer radii of the annular field are just

$$\theta_{i\ spinning} = \Gamma + \theta_{i\ driven} \tag{36}$$

and

$$\theta_{e\ spinning} = \Gamma + \frac{\Theta}{2} . \tag{37}$$

Here it is assumed that the slit lies away from the scan axis in the scan axis-optical axis plane. The effective field of view for this mode is obtained from

$$1 - \cos \frac{(\Theta_{eff})_{spinning}}{2} = \cos \theta_{i\ spinning} - \cos \theta_{e\ spinning}. \tag{38}$$

Observe that $(\Theta_{eff})_{spinning}$ may be larger than Θ.

The bright object shield requirements for spinning operation are again given by

$$\xi = \psi_{min} - \epsilon_u - \Gamma \tag{39}$$

subject to the constraint

$$\xi > \frac{\Theta}{2}. \tag{40}$$

Because $\theta_{i\ driven}$ and Γ are selected as positive quantities, the condition analogous to (32) for the simple spinning mode sensor is satisfied automatically.

SCADS PARAMETER SELECTION

For the dual mode sensor, the cant angle and the optical field of view are chosen as the primary independent variables. The choice of Θ as a key variable here is based on its fundamental role in the three-axis-controlled or driven mode. Figure 55 is a family of dual mode SCADS design curves with the spinning mode effective field of view $(\Theta_{eff})_{spinning}$ plotted as a function of the cant angle Γ. The optical field of view Θ and either the inner radius of the slit $\theta_{i\ driven}$ or the slit length θ_{slit} are parametric. Note that the effective field of view in the three-axis-controlled mode $(\Theta_{eff})_{driven}$ corresponds to the condition $\Gamma = 0^{o}$.

Figure 56 presents the normalized dimensions of the minimum volume bright object shield corresponding to each pair (Θ, Γ). These results are again based on the value $(\psi_{min} - \epsilon_{u}) = 56.^{o}557$. Observe that the large optical field of view required for this sensor implies a shield with $d > h$. This is an attractive form factor since the shield does not represent a long thin projection from the satellite; potential interference with the spacecraft shroud or the launch vehicle is thereby minimized.

Further selection criteria for the dual mode sensor geometry are discussed in Section IVC which gives more specific design information. It should also be pointed out before concluding this section that the relations given in (33), (34), and (35) also apply to the three-axis-controlled mode sensor.

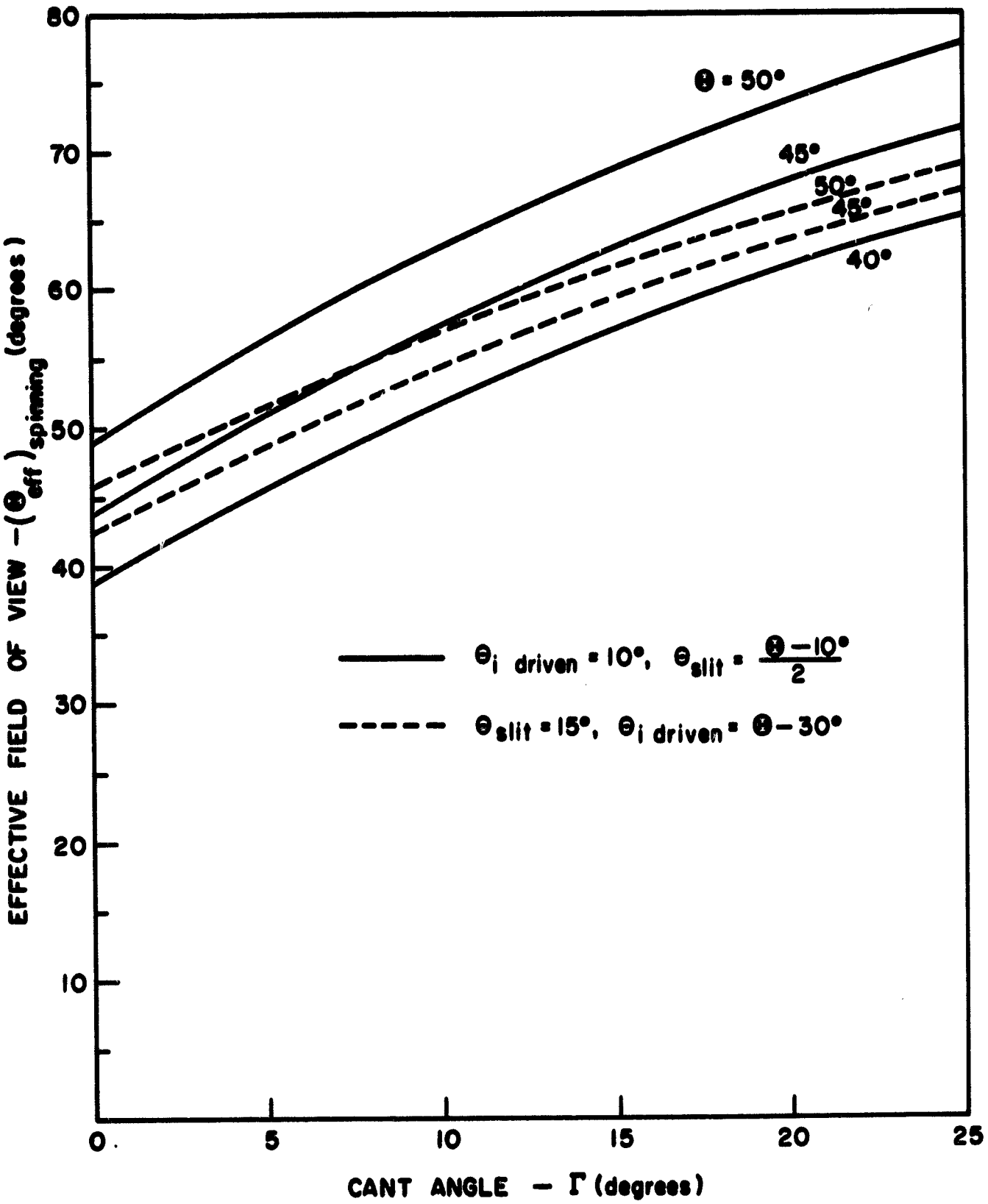


Figure 55: Parametric curves for the dual mode sensor effective field of view in the spinning mode. Note that the effective field of view for the three-axis or driven mode corresponds to $\Gamma = 0$ for each curve.

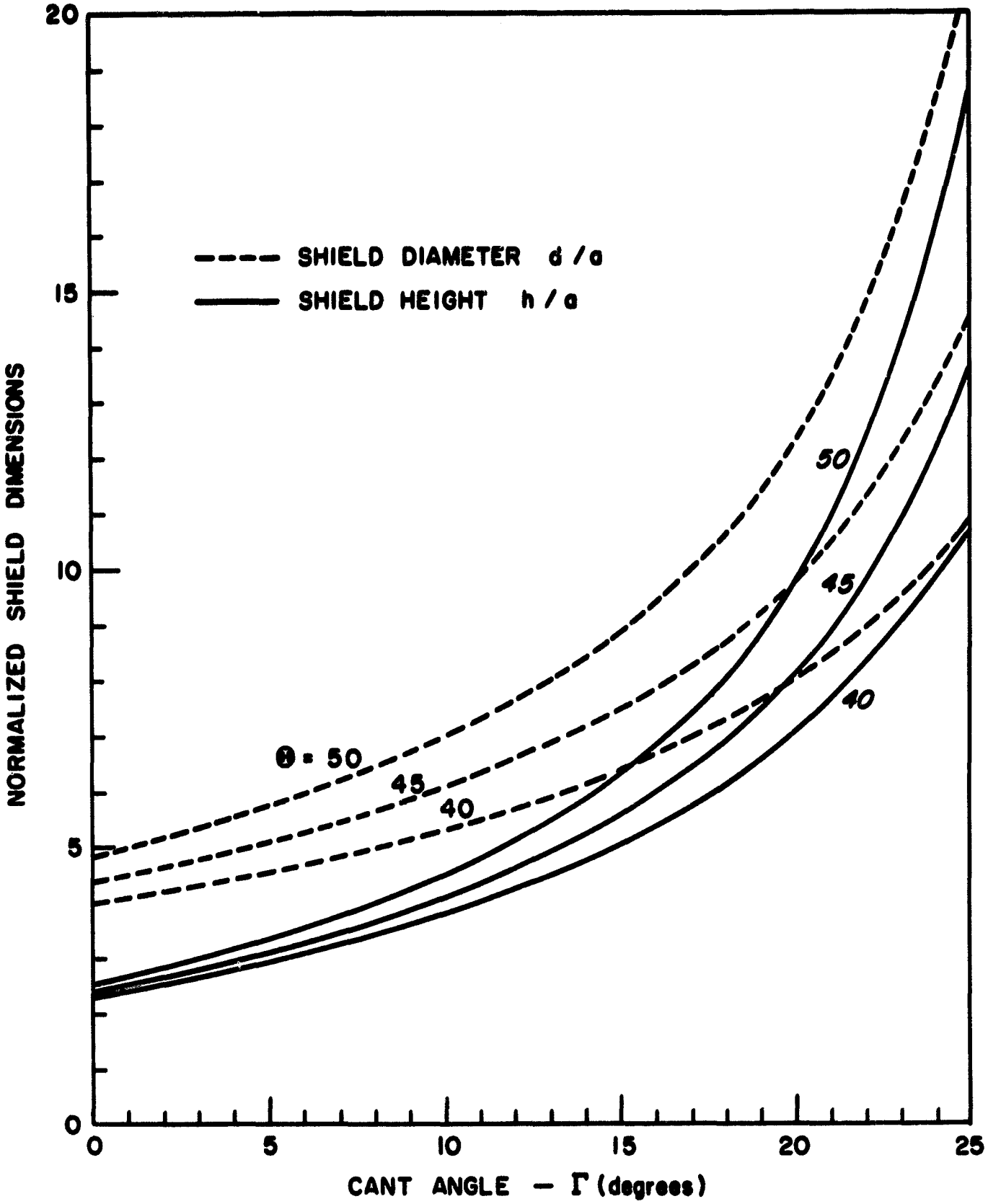


Figure 56: Normalized bright object shield dimensions for the dual mode sensor. Note that the results correspond to a minimum volume shield at given (Θ, Γ).

B. Parameters Related to Star Detection and Identification

The detection of a star within the SCADS field of view depends basically on (1) the number of signal photoevents generated at the detector by photons from the star and (2) the rate at which spurious photoevents are created by other sources. In the subsections which follow, the parameter groups which relate primarily to the detection and identification of stars are discussed.

1. Slit Configuration

The choice as to which slit design should be used is not an easy decision. It seems that there is no ideal design, for each design has its own advantages and disadvantages. Choosing a design thus amounts to deciding what disadvantages are tolerable or most tolerable to the total system.

Figure 57 illustrates what are considered to be the two best slit designs for this SCADS sensor. Of these, the single slit is favored.

First of all, the three slit and single slit designs are favored over other numbers of slits because of the problems of matching star transits. For example, if two slits are utilized, there is some difficulty in pairing the star transit times. That is, given a set of transit times, it is difficult to extract two and be sure they were produced by the same star. Such a pairing is necessary before the stars can be identified. Obviously, no pairing problem exists if a single slit is chosen.

Three slits greatly simplify the matching problem over that presented by other multiple slits. The slits can be so arranged that only triplicates of star transits are obtained such that the transit time difference between the third transit and second transit is equal to the difference between the second and first. When this test is satisfied, it is fairly certain that all three transit times were produced by the same star.

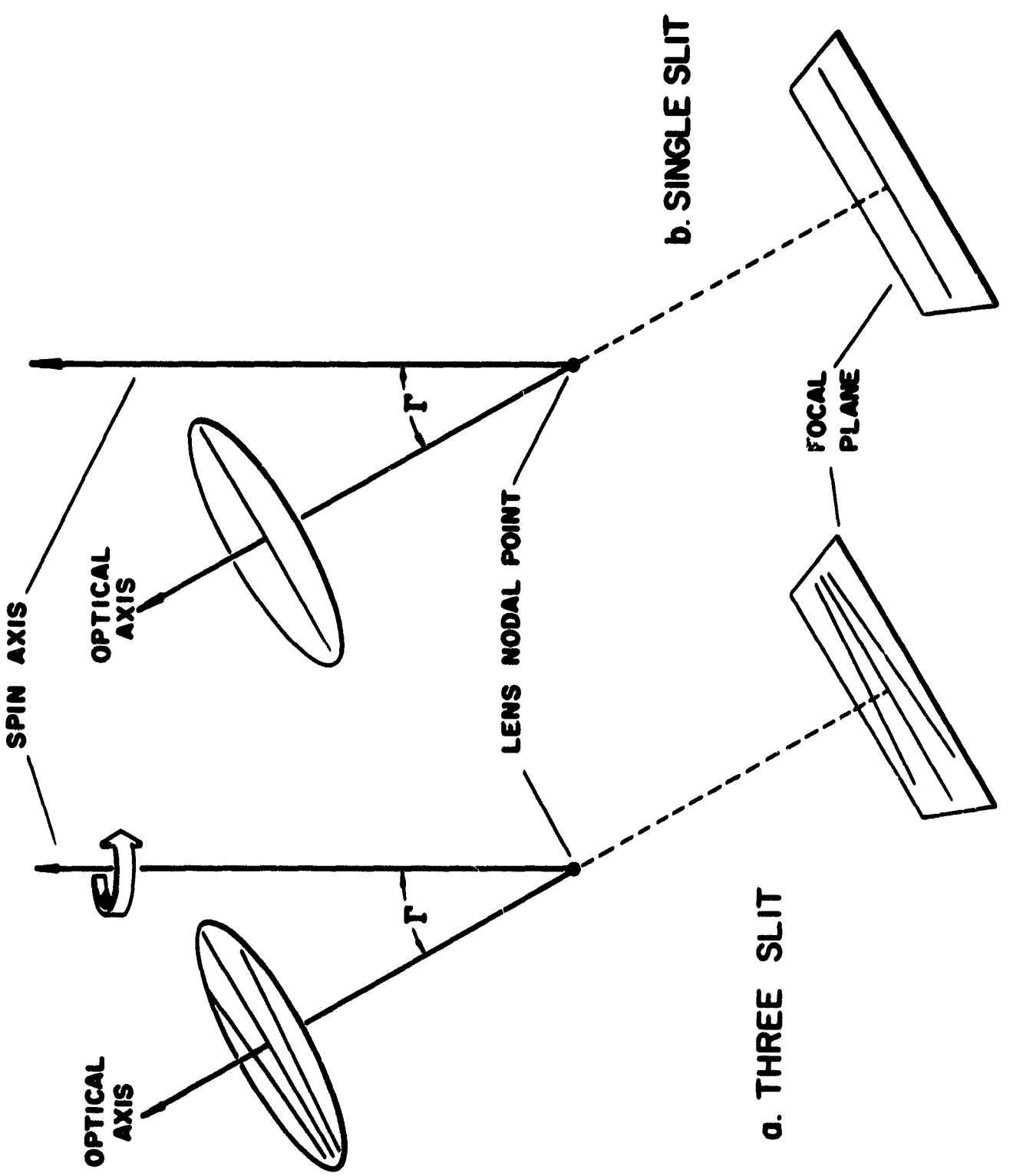


Figure 57: The two most favorable slit configurations for a SCADS-type sensor.

At this point, we have narrowed the choice of slit designs to the two illustrated in Figure 57. Let us now list the advantages and disadvantages of the single radial slit over the three slit design.

The advantages may be listed as follows.

(1) No decision need be made as to which slit the star transits.

(2) The background radiation problem is minimized. This is a strong advantage since the sun and earth's limb are closer than 90° to the spin axis for significant time intervals.

(3) Coma, astigmatism, and other aberrations of optical systems tend to be symmetric about a radial line; thus greater accuracy can be achieved in estimating the center of the blur spot by employing a single radial slit.

(4) A lens system may be chosen which minimizes sagittal (tangent to a radial line) distortions in favor of radial distortions. With a single radial slit, radial distortions cause virtually no error in determining the blur spot center.

(5) Simple to fabricate.

(6) The data gathering, data storage, and telemetry transmission requirements of the single slit system are less than for multiple slit systems.

The disadvantages of the single slit system are listed as follows.

(1) Three stars constitute a minimum set if a single slit is used, while two stars are minimal if multiple slits are used.

(2) Four or more stars are required for positive star identification (excluding magnitude data).

(3) The star identification procedure is much more difficult to implement than with the three slit configuration. This is the strongest disadvantage of a single slit.

(4) Errors in computed attitudes are slightly greater than with the three slit design. This statement, however, is true if both designs produce equal transit time errors; however, the transit time error would be somewhat smaller for the single slit.

After considering the comparative advantages and disadvantages of the two

designs, it appears that the single slit is preferable for the present system, particularly since it is extremely important to minimize the amount of on-board data processing. The single slit is not a single line as pictured in Figure 57, but should be wedge-shaped. The recommended rotational slit width has been selected as 12 arc minutes; this choice is discussed in Section IIIC.

2. Photodetector Performance

In order to achieve adequate signal-to-noise ratios with a minimum aperture optical system for the detection of star signals with the SCADS sensor, it is required that the SCADS photodetector be a photomultiplier. Previous investigations have shown that current solid state detectors are inadequate or at best marginal for a SCADS-type sensor rotating at relatively short scan periods. One of the principal reasons for the superiority of photomultipliers is the relatively noise-free gain achieved by the electron multiplication provided by the secondary emissions of the photomultiplier dynode chain [2]. The dynode chain provides adequate gain to raise the signal levels well above the level of the thermal Johnson noise of the photodetector load resistor.

Extensive investigation has been performed in the applicability of photomultiplier tubes for SCADS systems. The results of these investigations have shown that venetian blind tubes are optimum for several reasons; in particular, the rugged tube structure, the large photocathode area, and the high multiplier gain are some of its outstanding characteristics. Venetian blind photomultipliers have been utilized in two previous SCADS-type experimental systems. For a Breadboard Design of a SCADS System (NAS5-9661), a venetian blind tube designated as the EMR-543A (manufactured by Electro-Mechanical Research, Inc.) was employed. For the ATS Self-Contained Navigation System Experiment, the venetian blind photomultiplier employed was an EMR-541E. Both tubes were ruggedized and capable of withstanding the environment of space vehicle launching. Since both tube types supplied by

EMR performed satisfactorily, this feasibility study will primarily consider EMR photomultipliers.

The cathode type employed by the photomultiplier is particularly important in SCADS sensor applications. It is desirable that the cathode exhibit high quantum efficiency and a low dark emission rate. EMR has given letter designations to indicate different cathode types. For example, the EMR-543A has a cathode designated as an "A" cathode, and its response conforms closely to an S-4 response with a typical peak quantum efficiency of 14 percent and a cathode dark current of $.274 \times 10^{-15}$ ampere per square centimeter of cathode area at $+20^{\circ}C$. Similarly, the EMR-541E has an "E" cathode which conforms closely to an S-20 response with a typical peak quantum efficiency of 25 percent and a cathode dark current of $.407 \times 10^{-16}$ ampere per square centimeter at $+20^{\circ}C$. The "E" cathode has a broad range of spectral response plus its peak sensitivity corresponds closely with the spectral energy distribution of blue stars. More recently EMR has announced the "N" type cathode which has a higher quantum efficiency than the "A" type but is somewhat less efficient than the "E" type. The "N" cathode response conforms closely to the S-11 response. Typical peak quantum efficiency of the "N" cathode is 21.5 percent, however, its dark current is $.51 \times 10^{-17}$ ampere per square centimeter at $+20^{\circ}C$. Hence, its dark current characteristic is much superior to either the "A" or "E" cathodes. In addition, the "N" cathode can withstand a much higher temperature ($+150^{\circ}C$) than either the "A" ($+75^{\circ}C$) or "E" ($+85^{\circ}C$) cathodes. The high temperature characteristic is particularly attractive since some cathode heating is likely to occur whenever the sensor sees either direct sun radiation or earth-reflected sun radiation.

Because of its desirable characteristics of relatively high quantum efficiency, low dark current, and tolerance to high temperatures, the EMR type "N" cathode is recommended for the present SCADS sensor. The type "N" cathode is currently available in two ruggedized EMR photomultipliers, the EMR-541N and the EMR-543N. The active cathode diameter of the EMR-541N is

25 millimeters and the active cathode diameter of the EMR-543N is 43 millimeters. Both photomultipliers will be considered for application to this SCADS sensor.

Data sheets for the EMR-541N and EMR-543N photomultipliers are shown in Appendix B.

For a given photomultiplier it is possible to determine the response of the tube to star radiation. To calculate signal currents at the photomultiplier output, it is necessary to know the absolute spectral energy distribution (ASED) for the star spectral class which contains the greatest percentage of stars. It has been shown that star spectral class A contains the greatest percentage of the 100 brightest stars[7]. Code (1960)[8] has published data from which the ASED of Vega (spectral class AO) can be calculated.

Code gives the monochromatic magnitudes of Vega as a function of wave number (inverse of wavelength). These magnitudes can be converted to monochromatic magnitudes as a function of wavelength by using the transformation[9]

$$M(\lambda) = m(1/\lambda) + 5 \log_{10} \left[\frac{\lambda}{\lambda_o}\right] . \qquad (41)$$

In this case λ_o = .556 micron. The monochromatic intensity of Vega at wavelength λ relative to the intensity at λ_o can be obtained from the expression

$$\frac{f(\lambda)}{f(\lambda_o)} = 10^{-.4[M(\lambda) - M(\lambda_o)]} \qquad (42)$$

where $m(\lambda_o) = 0.0$ at λ_o = .556 micron. The relative spectral energy distribution (RSED) for Vega can be obtained by plotting $f(\lambda)/f(\lambda_o)$ versus λ. By determining f(.556), the absolute spectral energy distribution of Vega can be obtained. Based on measurements, Code has adopted a monochromatic

flux value of 3.8×10^{-12} watt per square centimeter micron at .556 micron from a star of visual magnitude $M_v = 0.0$. Figure 58 shows a plot of the absolute spectral energy distribution for Vega.

The absolute spectral energy distribution for Vega is modified by the spectral response of the photomultiplier cathode, resulting in an effective spectral energy distribution for Vega as shown in Figure 59. The spectral response of the EMR-541N cathode is shown in Figure 58. Numerical integration of the effective spectral energy distribution in Figure 59 yields a cathode current of 7.92×10^{-14} ampere per square centimeter of optical aperture. The visual magnitude of Vega is +0.04. The cathode current for a Vega type star of visual magnitude M_v can be obtained by scaling the cathode current by the factor $10^{-.4(M_v - .04)} = 1.04 \times 10^{-.4M_v}$. So a class AO star of visual magnitude M_v causes a cathode current of $S_K = 8.25 \times 10^{-14} \times 10^{-.4M_v}$ ampere per square centimeter for 100 percent optical efficiency.

Similar calculations have been made for the "E" and "A" cathodes. The results of these calculations are stated as follows for a $0^m.0$ visual magnitude class AO star and 100 percent optical efficiency:

"E" cathode sensitivity - 10.3×10^{-14} ampere per square centimeter.
"A" cathode sensitivity - 5.49×10^{-14} ampere per square centimeter.

It is of interest to determine the type N cathode response to stars of different spectral classification, particularly for those stars whose energy distributions peak at a longer wavelength than do the class A stars. Figure 60 shows the spectral energy distribution for a $0^m.0$ visual magnitude class M2Ia star (Betelgeuse class). The resulting effective spectral energy distribution is shown in Figure 61. Numerical integration of the effective spectral energy distribution of Figure 61 results in a cathode current of

$$S_K = 1.75 \times 10^{-14} \times 10^{-.4M_v} \quad \frac{\text{amp}}{(\text{cm})^2} \qquad (43)$$

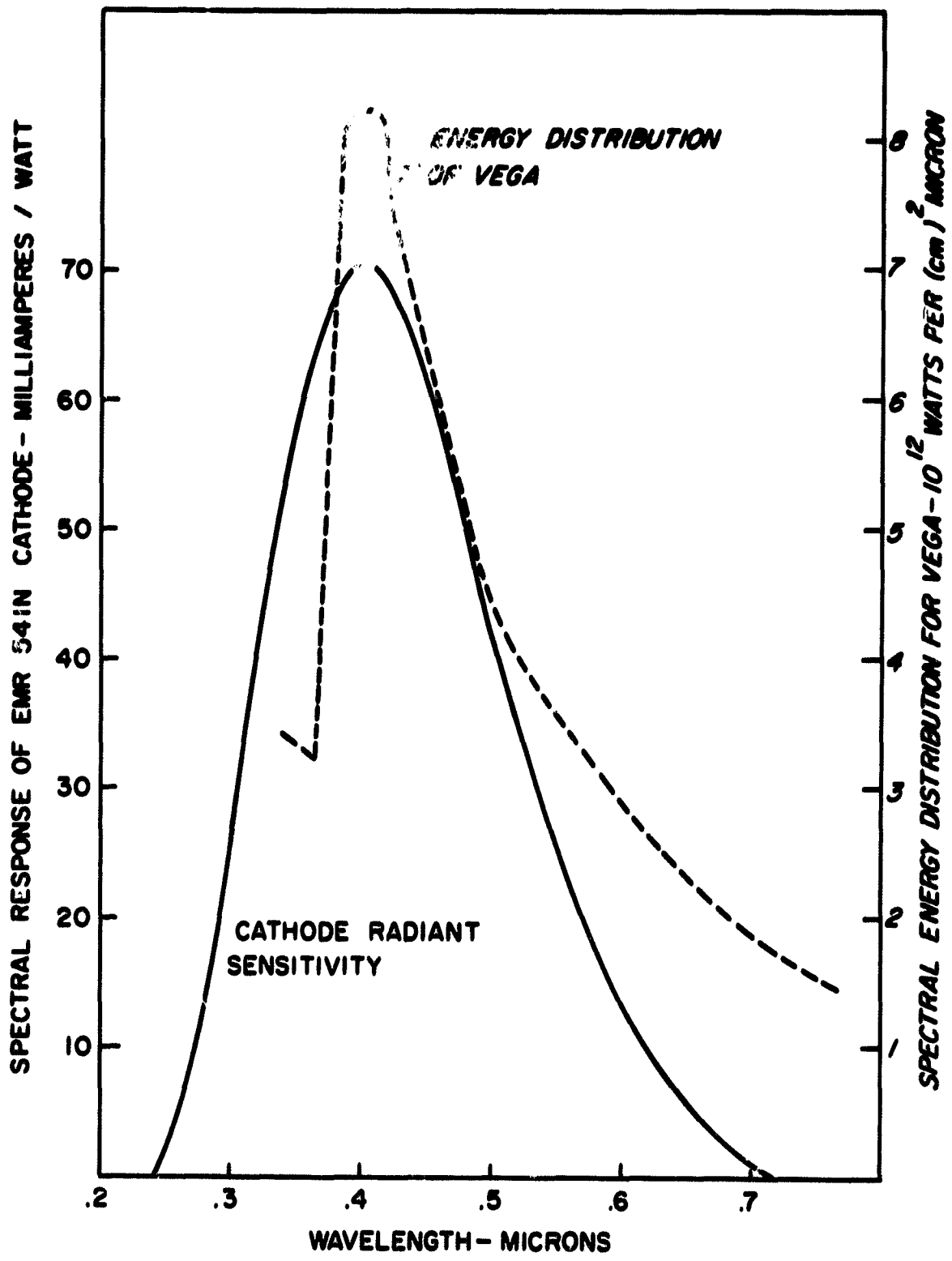


Figure 58: Photocathode radiant sensitivity and spectral energy distribution of Vega.

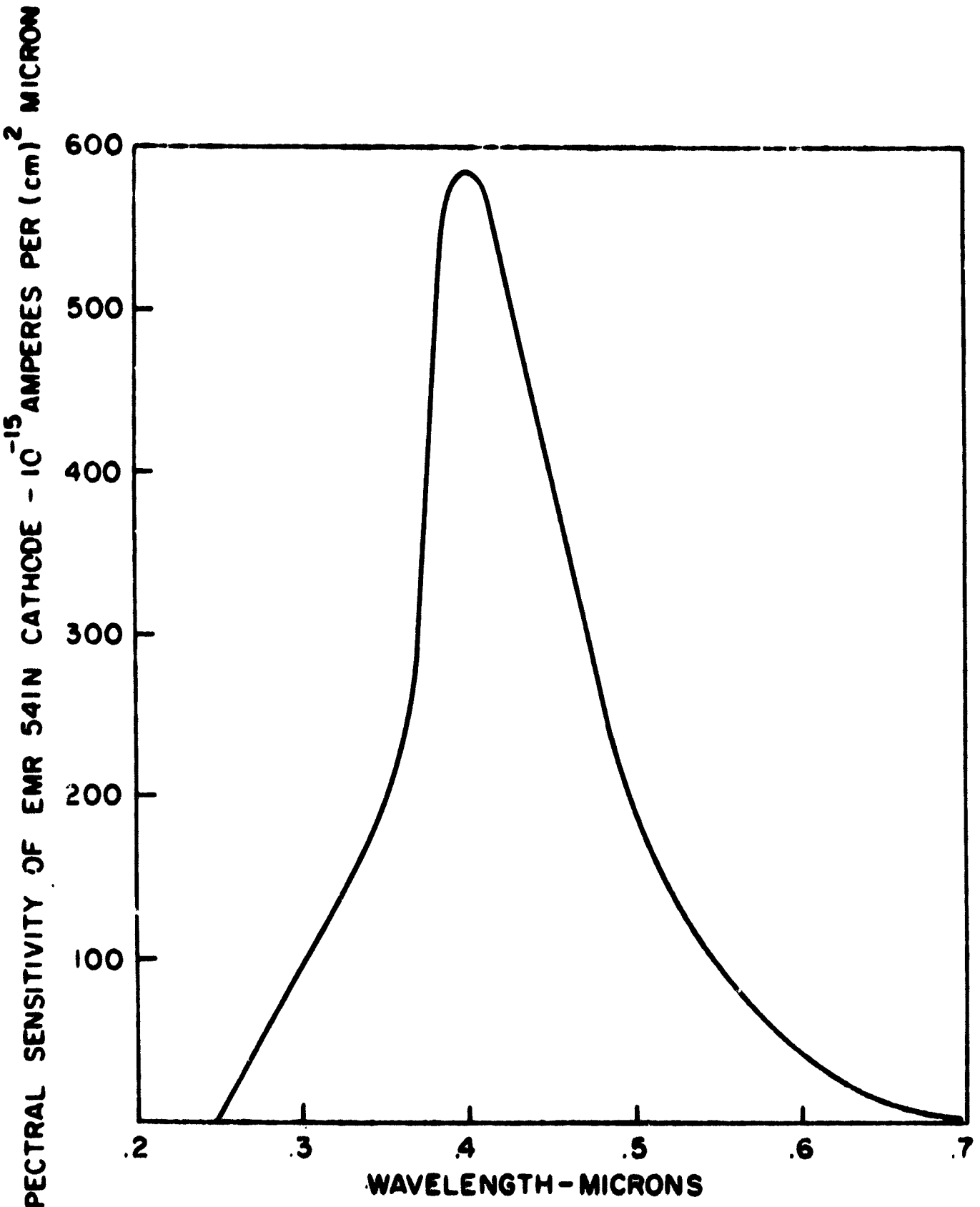


Figure 59: Effective spectral energy distribution for the combination of Vega and the EMR "N"-type cathode

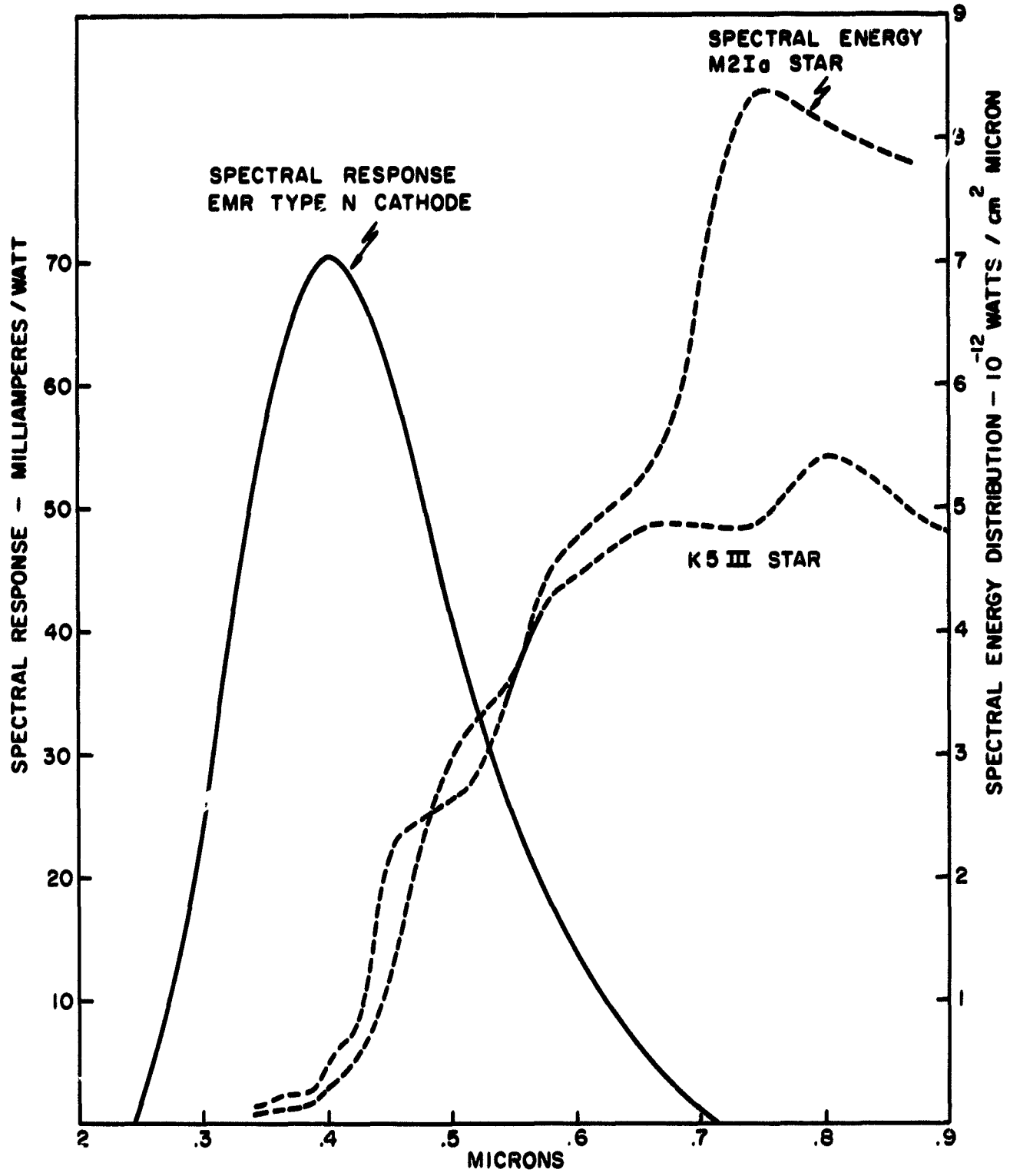


Figure 60: Comparison of photomultiplier spectral response and spectral energy distribution of "red" stars.

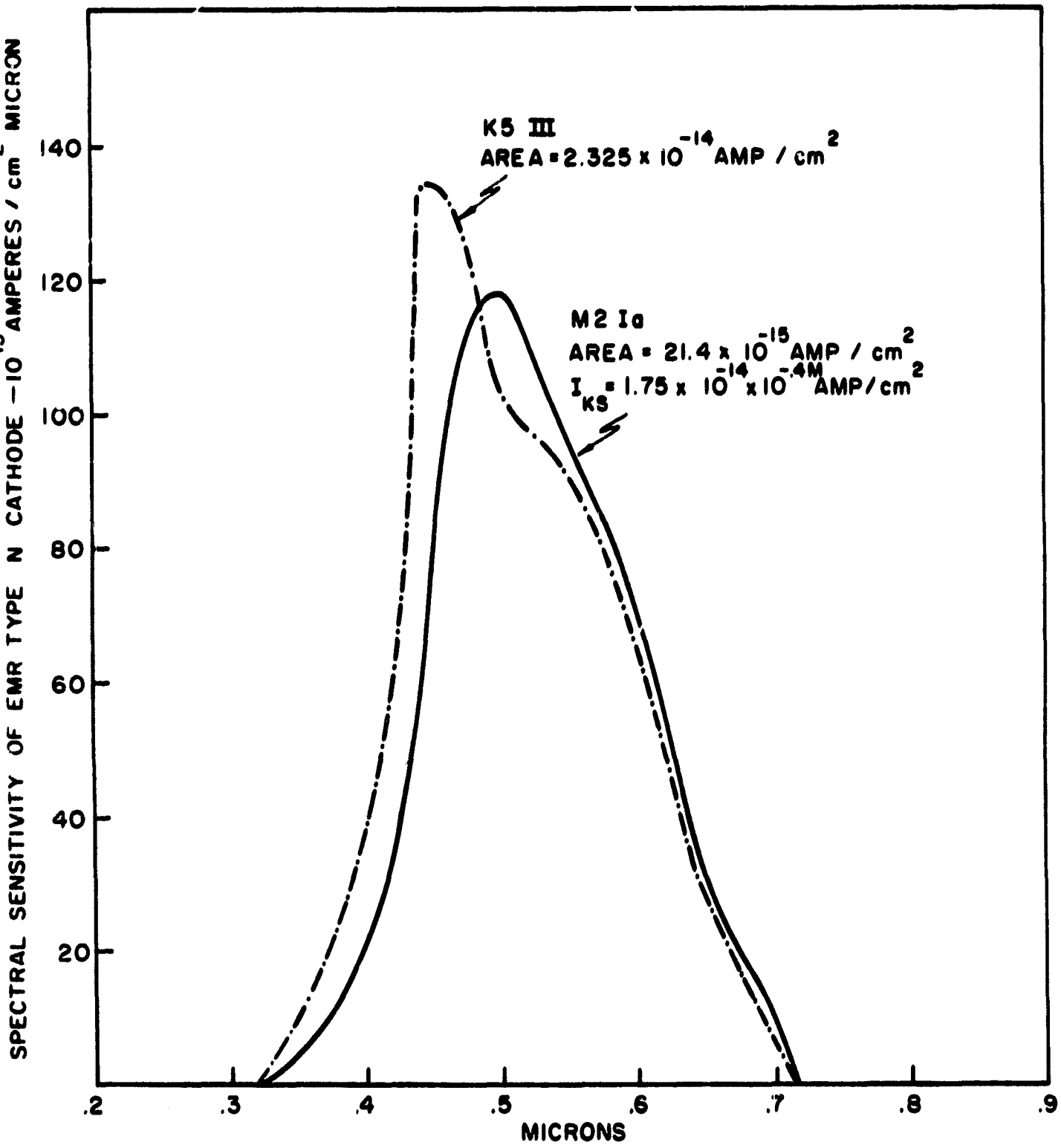


Figure 61: Effective spectral energy distribution for "red" stars.

for 100% optical efficiency. Similarly, Figure 60 shows the spectral energy distribution for a $0^{m}.0$ visual magnitude class K5III star (Aldebaran class). Numerical integration of the effective spectral energy distribution of Figure 61 results in a cathode current of

$$S_K = 2.33 \times 10^{-14} \times 10^{-.4M_V} \frac{amp}{(cm)^2} \qquad (44)$$

for 100% optical efficiency.

The reason that different values of cathode current result from stars of the same visual magnitude but different spectral class can be explained by the fact that the combined spectral response of the visual photometric system (V filter and 1P21 photomultiplier) does not match the spectral response of the EMR-541N photomultiplier. The discrepancy is not particularly troublesome to a SCADS sensor since star intensity data is not essential in solving the attitude determination problem. Even if star intensity were of importance, it would be possible to determine an instrument magnitude for each star class by assigning a correction factor to the visual magnitude. For instance, for a class M2 star the magnitude correction factor can be determined by $\frac{8.25}{1.75} = 10^{+.4M_c}$. Hence, the instrument magnitude for a class M2 star would be

$$M_I = M_V + M_c \qquad (45)$$

In order to more accurately determine the magnitude correction factor, the spectral response of the lens system should be included in the star effective spectral energy distribution.

The actual instrument response as a function of color class and star magnitude is not particularly important except in performing the detailed star availability search. For this task, it is necessary to give some consideration to the instrument response to red stars in order to insure that three or

more stars in the field of view, regardless of color class, exceed the threshold limit. Adequate consideration to this problem is given by working with star magnitudes which more closely match the actual instrument response. As has been shown, visual magnitudes are not suitable since the instrument response from a class M star is down by 1.68 magnitude from the instrument response from a class A star having the same visual magnitude. However, it can be shown that photographic magnitudes are suitable for performing the star availability search.

Although the instrument is calibrated on the absolute spectral energy distribution of the blue star Vega using its visual magnitude, the relative and absolute instrument responses for photographic magnitudes can be readily determined. The photographic star magnitudes can be obtained from the transformation[10]

$$M_p = (M_B - M_V) - .11 + M_V \tag{46}$$

where M_B = the blue magnitude of the star, and
$M_B - M_V$ = star color index.

Two specific stars will now be considered, one blue and the other red. For the blue star Vega (class A0, $M_V = +.04$), its color index $M_B - M_V = 0.0$, so $M_p = -0.07$. For the red star Betelgeuse (class M2, $M_V = 0.7$), its color index is $M_B - M_V = 1.86$, so $M_p = 2.44$. So for photographic magnitudes, red stars appear much dimmer than blue stars which have visual magnitudes comparable to the red stars. This more nearly agrees with the relationship for the instrument responses derived respectively for blue and red stars.

The instrument response to a class A0 star of magnitude M_V has been determined as

$$S_K = 8.25 \times 10^{-14} \times 10^{-.4M_V} . \tag{47}$$

In terms of photographic magnitudes, the instrument response is given by

$$S_K = 8.25 \times 10^{-14} \times 10^{+.4(M_B - M_V)}\ 10^{-.4(M_p + .11)} \quad . \tag{48}$$

Now for stars which are more red than the spectral class AO stars, the color index $M_B - M_V \geq 0$[10], so for a given photographic magnitude the instrument response to red stars is always greater than is the instrument response to class AO stars. Hence by calibrating the instrument on a class AO star (color index $M_B - M_V = 0.0$) and employing photographic magnitudes, it is certain that for the limiting photographic magnitude, adequately detectable signals will be received for almost all star classes since most stars are more red than spectral class AO[7]. Photographic magnitudes were used for the detailed star availability search performed in Section IIB.

3. Signal Filter

The next step in the design procedure requires determination of the optical aperture. This requires analysis of the star signal detection problem which must be preceded by an analysis of the signal filtering problem.

Figure 62 shows the photomultiplier output as a series of impulses where each impulse corresponds to a single randomly emitted electron from the photocathode. For very weak light intensities, the average photocathode emission rate is relatively low so that star detection by electronic counting of the individual emissions during a sliding time interval T_s is practical. However, for a SCADS sensor, the stellar background plus bright star intensities make star detection by counting individual photocathode emissions impractical. Instead, time averaging of the photomultiplier output signal and subsequent threshold level detection is more practical. Time averaging of the star signal is performed with an electronic low pass filter. Because of the random emissions of the photoelectrons from the cathode while the star is in the slit, the time averaged star signal contains a random amplitude noise component superimposed on its true average value. The random noise amplitude component is commonly referred to as shot noise.

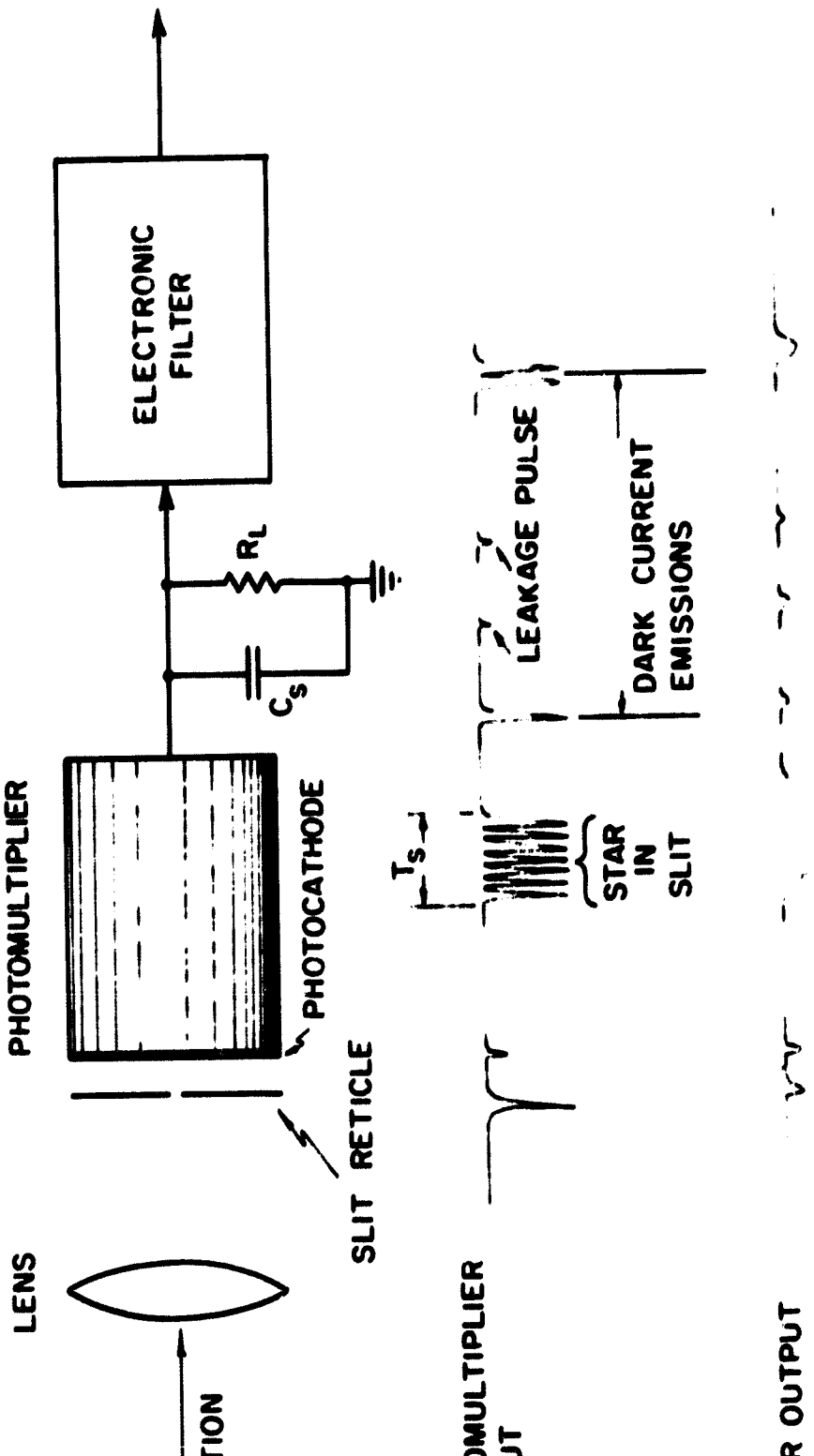


Figure 62: Star Pulse Filtering

The ability to detect star pulses from a photodetector in the presence of shot noise caused by background and star radiation is greatly influenced by the design parameters of the low pass electronic filter shown in Figure 62. Analysis of the filtering problem is complicated by the fact that the RMS noise is dependent on the amplitude of the signal as described by the shot noise equation,

$$i_{RMS} = \left[2e\ (I_S + I_B + I_D)\Delta f\right]^{\frac{1}{2}} \tag{49}$$

where I_S = average current produced by star radiation striking the photodetector,

I_B = average current produced by stellar background radiation striking the photodetector,

I_D = average dark current of the photodetector,

Δf = noise equivalent bandwidth of the electronic filter.

Because the noise is dependent upon the signal, the noise is non-stationary. Consequently, to achieve optimum filtering, it is apparent that the parameters of a linear filter must change with the amplitude of the signal, i.e. the filter parameters must be time variant and be capable of adapting with the magnitude of the pulse being filtered. It is impractical to implement a time variant linear filter, so to simplify matters, it will be assumed that the RMS noise is not dependent upon the signal level, in which case, the noise is considered stationary. Therefore, only linear time invariant filters will be considered.

The objective in filtering star pulses in the presence of shot noise is to minimize the attenuation of the signal while maximizing the attenuation to the RMS noise. This is equivalent to maximizing the ratio of peak signal to RMS noise. If the bandwidth of the filter passband is wide compared with that occupied by the signal energy, extraneous noise is introduced by the excess bandwidth and the output signal-to-noise ratio is lowered. On the other hand, if the filter bandwidth is narrower than the bandwidth occupied

by the signal, the noise energy is reduced along with a considerable part of the signal energy. The net result is again a lower signal-to-noise ratio. Thus, for a given filter transfer function with a given input signal, there is an optimum bandwidth at which the signal-to-noise ratio is a maximum. For a given input signal, different filter transfer functions will yield differing maximum signal-to-noise ratios at the respective optimum bandwidths. The filter transfer function which yields the highest possible output signal-to-noise ratio is called a matched filter. It can be shown that the impulse response of the matched filter is the reverse image of the input signal; that is, it is the same as the input signal run backward in time[11]. Therefore, if the input signal is symmetrical in time, the impulse response of the matched filter must also be symmetrical. The output signal from any filter can be described by the convolution integral of the filter impulse response and the input signal.

$$y(t) = \int f(\tau) \cdot h(t - \tau)\, d\tau \qquad (50)$$

where f(t) = the input signal,

h(t) = the filter impulse response.

So if the input signal is symmetrical, then the output signal from a matched filter is also symmetrical.

A matched filter may not be physically realizable depending upon the form of the input signal it is required to match. If a matched filter is not physically realizable, then the desired filter is a physically realizable filter which has the highest output signal-to-noise ratio for the given input signal. If one filter transfer function has a higher maximum signal-to-noise ratio than another transfer function for a given input signal, then the filter with the higher signal-to-noise ratio is closest to matching the signal. So by calculating and comparing the maximum signal-to-noise ratios for two or more filter transfer functions and a given input signal, the filter most closely matching the input signal may be determined.

The form of the star pulse from the photodetector of a scanning optical system depends upon the energy density profile of the star image blur circle and the relative size of the rotating slit with respect to the blur circle. If the optical system produces a diffraction pattern that is two dimensional Gaussian, the energy density in the focal plane is given by[12]

$$I(x, y) = \frac{\epsilon_o \lambda_s}{2\pi\sigma^2} \exp\left[-\frac{1}{2\sigma^2}(x^2 + y^2)\right] \tag{51}$$

where ϵ_o denotes the optical efficiency,

λ_s = average number of photons received from the star/unit time,

σ = dispersion of the diffraction pattern on the focal plane,

and the slit width is chosen such that 80 percent of the star radiation passes the slit when the blur circle is centered in the slit. If T_s equals the time it takes the center of the star image to cross the slit, then the average photon arrival rate at the photomultiplier is described by[12]

$$f_s(t) = \epsilon_o \lambda_s \, G(t) \tag{52}$$

where

$$G(t) = \Phi\left(\frac{t}{\sigma} + \frac{T_s}{2\sigma}\right) - \Phi\left(\frac{t}{\sigma} - \frac{T_s}{2\sigma}\right) \tag{53}$$

and

$$\Phi(t) = \frac{1}{\sqrt{2\pi}} \int_{-\infty}^{t} e^{-\frac{1}{2}x^2} \, dx. \tag{54}$$

Note that 80 percent of the star radiation passes through the slit when

$$\frac{T_s}{2} = 1.28\,\sigma. \tag{55}$$

The function G(t) is graphed in Figure 63.

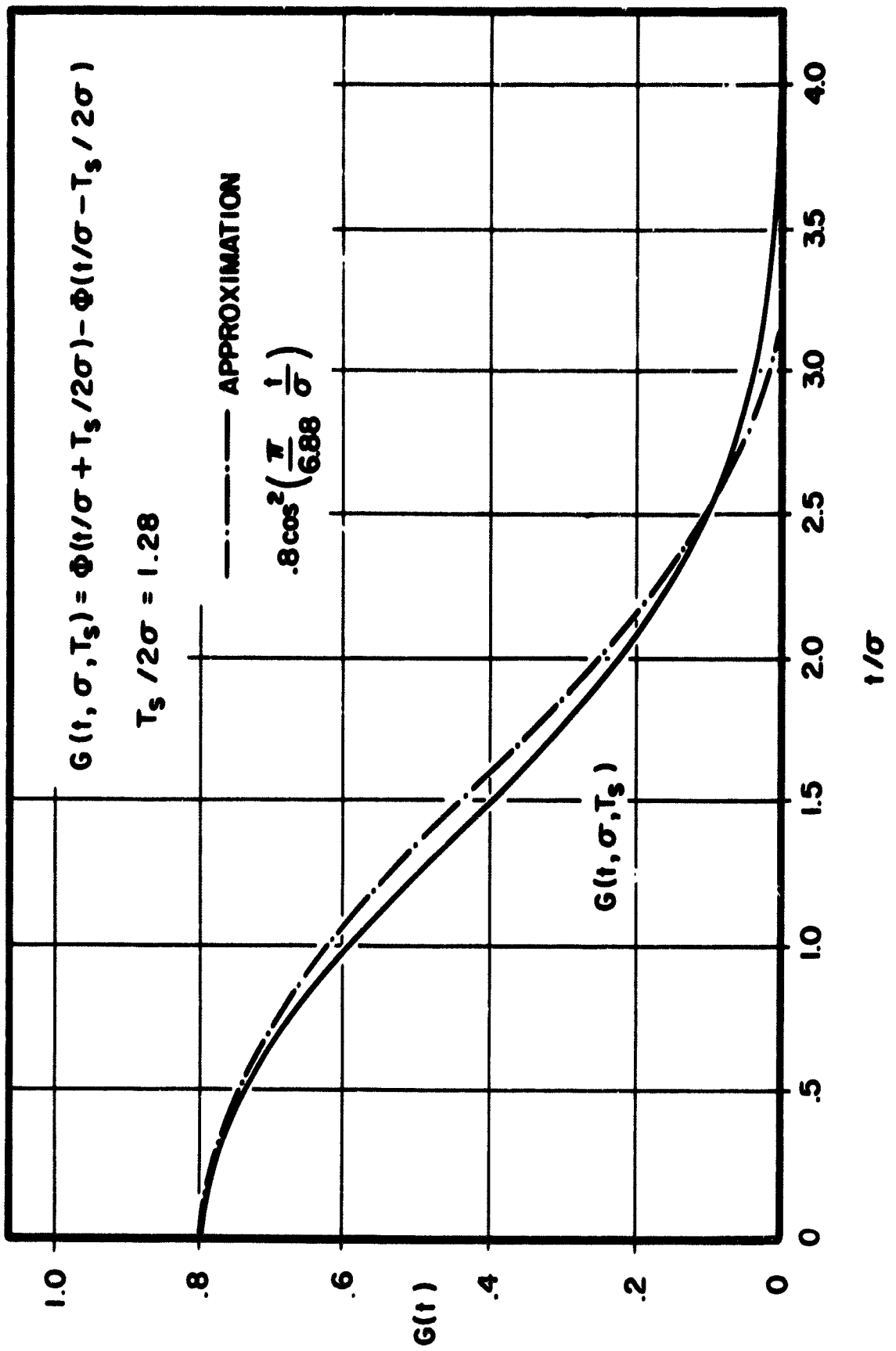


Figure 63: Percent of star radiation passing scanning slit.

The average value (envelope) of the photodetector output signal will be described by

$$f(t) = K\,G(t). \tag{56}$$

The impulse response in Equation (50) can be obtained analytically by finding the inverse Laplace transform of the filter transfer function, H(s). In general, H(s) will contain terms of the form

$$H_i(s) = \frac{2\left[a\left(\frac{s}{\omega} + \alpha\right) + b\beta\right]}{\left(\frac{s}{\omega} + \alpha\right)^2 + \beta^2} \tag{57}$$

whose inverse transform is of the form

$$h_i(t) = 2a\,\omega\, e^{-\alpha\omega t}\cos(\beta\omega t) + 2b\,\omega\, e^{-\alpha\omega t}\sin(\beta\omega t). \tag{58}$$

Equation (50) cannot be integrated in closed form after substitution of Equations (56) and (58). However, G(t) can be approximated by

$$f(t) = (.8)\cos^2\left(\frac{\pi}{2K}\,\frac{t}{\sigma}\right) \text{ for } |t| \le 2K\sigma \tag{59}$$
$$= 0 \qquad \text{elsewhere,}$$

where K is selected to "minimize" the discrepancy between G(t) and f(t). It can be shown that[12]

$$\int_{-\infty}^{t} G(t)\,dt = T_s \quad . \tag{60}$$

Also,

$$\int_{-k\sigma}^{+k\sigma} f(t)\,dt = .8\,K\sigma. \tag{61}$$

Now if $G(t)/T_s$ and $f(t)/.8\ K\sigma$ are considered as probability density functions, their second moments can be equated to determine K. It has been shown that the second moment[12]

$$\int_{-\infty}^{+\infty} t^2 \frac{G(t)}{T_s}\, dt = \sigma^2\left[1 + \frac{1}{3}\left(\frac{T_s}{2\sigma}\right)^2\right]. \tag{62}$$

The second moment for $f(t)/(.8\ K\sigma)$ has been evaluated as

$$(.8)\int_{t=-k\sigma}^{t=+k\sigma} t^2\ \frac{\cos^2 \frac{\pi}{2K}\frac{t}{\sigma}}{(.8\ k\sigma)} = (K\sigma)^2 \frac{2}{\pi^2}\left[\frac{\pi^2}{6} - 1\right] = (K\sigma)^2(.130688). \tag{63}$$

For $T_s/2 = 1.28$, $K = 3.44$. Hence,

$$f(t) = (.8)\cos^2 At \quad \text{for } |t| \leq \frac{\pi}{2A} \tag{64}$$
$$= 0 \qquad\qquad \text{elsewhere}$$

where

$$A = \frac{\pi}{6.88}\ . \tag{65}$$

The function $f(t) = (.8)\cos^2 At$ is shown graphed in Figure 63. By shifting the time axis of Figure 63, G(t) can be approximated by

$$f(t) = (.8)\sin^2 At = (.8)/2\ (1 - \cos^2 At) \quad \text{for } 0 \leq t \leq \pi/A \tag{66}$$
$$f(t) = 0 \qquad\qquad \text{elsewhere.}$$

Now Equation (50) can be integrated analytically after substitution of Equations (58) and (66).

The optimum value for ω_c is that value which maximizes the ratio

$$\frac{S}{N} = \frac{y_{peak}(t, \omega_c)}{I_{RMS}} \tag{67}$$

where

$$I_{RMS}^2 = N_R^2 \int_0^{\infty} |H(f)|^2 \, df = N_R^2 \, \frac{\omega_c}{2\pi} \, \frac{1}{2} \int_{-\infty}^{+\infty} |H(jx)|^2 \, dx \tag{68}$$

= mean noise output power from the filter with white noise input.[13]

$$jx = j \frac{\omega}{\omega_c} = \frac{s}{\omega_c} \tag{69}$$

N_R = input RMS noise per unit bandwidth

$$= [2e(I_S + I_B + I_D)]^{\frac{1}{2}} \tag{70}$$

Comparing Equations (49) and (68) shows that the noise equivalent bandwidth is given by

$$\Delta f = \frac{\omega_c}{4\pi} \int_{-\infty}^{+\infty} |H(jx)|^2 \, dx \tag{71}$$

Since the integral in Equation (68) evaluates to a constant, the value of ω_c which maximizes Equation (67) may be determined from

$$\frac{S}{N} = \frac{y_{peak}(t, \omega_c)}{\sqrt{\omega_c}} \tag{72}$$

If two or more filter transfer functions are to be compared, Equation (68) must be evaluated and used to determine Equation (67) for each case. The transfer function which has the largest maximum value for Equation (67) has the impulse response which most closely matches the given input signal.

By comparing the maximum value of Equation (67) for a two pole transfer

function with the maximum value of Equation (67) for the six pole case, it is possible to compare the effectiveness of each filter.

Since a star transit time is most conveniently determined by averaging the threshold crossing times, it is desirable that the filter output signal, y(t), be symmetrical about its peak value. If the filter output signal is asymmetric, then the transit time is dependent upon the threshold level and the star intensity. With a symmetrical noise-free input signal the noise-free filter output signal, y(t), will be symmetrical if the filter impulse response, h(t), is symmetrical. This can be seen from the convolution integral. But it can be shown that the impulse response is symmetrical if the transfer function $H(j\omega)$ has a linear phase versus frequency characteristic.[14]

The Fourier transform, $H(j\omega)$, of the filter impulse response can always be written as a modulus times its argument, i.e.,

$$H(j\omega) = A(\omega)\ e^{-j\theta(\omega)} \tag{73}$$

But from the inverse Fourier transform

$$h(t) = \frac{1}{2\pi}\int_{-\infty}^{+\infty} A(\omega)\ e^{+j[\omega t-\theta(\omega)]}\ d\omega$$

$$= \frac{1}{2\pi}\int_{-\infty}^{+\infty} A(\omega)\left\{\cos[\omega t - \theta(\omega)]\right\}\ d\omega \tag{74}$$

Now if the phase is linear with frequency, $\theta(\omega) = \omega t_o$, so

$$h_o(t) = \frac{1}{\pi}\int_{0}^{\infty} A(\omega)\ \cos[\omega(t - t_o)]\ d\omega \tag{75}$$

and, therefore, $h_o(t)$ is maximum about $t = t_o$ and is symmetrical about $t = t_o$.

The two pole transfer function of a linear phase shift versus frequency is given by[15]

$$H(s)\ \frac{1}{4\left(\frac{s}{\omega_c}\right)^2 + 3\frac{s}{\omega_c} + 1} = \frac{1}{4}\left\{\frac{2b\beta}{\left(\frac{s}{\omega_c} + \alpha\right)^2 + \beta^2}\right\} \tag{76}$$

where $b = 1.51186$

$\alpha = .375$

$\beta = .331$

The numerator of Equation (67) will be evaluated by writing the analytic expression for y(t) and then numerically determining $y_{peak}(t, \omega_c)$ with a programmed digital computer. In order to determine y(t), the filter impulse response must be known. The filter impulse response is

$$h(t) = \frac{2}{4}\, b\, \omega e^{-\alpha\omega t} \sin(\beta\omega t) \quad \text{for } t \geq 0 \tag{77}$$

$$h(t) = 0 \quad \text{for } t < 0.$$

The expression for y(t) is derived as follows:

$$y(t) = \int f(\tau) \cdot h(t - \tau)\, d\tau \tag{78}$$

where

$$f(\tau) = \sin^2 A\tau = \frac{1}{2} - \frac{\cos 2A\tau}{2} \quad \text{for } 0 \leq \tau \leq \frac{\pi}{A} \tag{79}$$

$f(\tau) = 0$ elsewhere,

and, in general,

$$\frac{h(t-\tau)}{k} = \sum_i \left[2\, a_i\, \omega\, e^{-\alpha_i \omega (t-\tau)} \cos\left\{\beta_i\, \omega (t-\tau)\right\} \right.$$

$$\left. + 2 b_i\, \omega\, e^{-\alpha_i \omega (t-\tau)} \sin\left\{\beta_i\, \omega (t-\tau)\right\} \right] \qquad (80)$$

Since the terms of y(t) are similar for a given value of subscript i, the derivation will proceed for all terms having the same subscript. The terms of y(t) for the remaining subscripts are then summed to give the final result. For the remainder of the derivation let

$$a = a_i\, \omega \qquad b = b_i\, \omega$$

$$\alpha = \alpha_i\, \omega \qquad \beta = \beta_i\, \omega$$

$$\frac{y_i(t)}{k} = (2a \cos \beta t + 2b \sin \beta t)\, \frac{e^{-\alpha t}}{2} \int e^{\alpha \tau} \cos \beta \tau \, d\tau$$

$$+ (2a \sin \beta t - 2b \cos \beta t)\, \frac{e^{-\alpha t}}{2} \int e^{\alpha \tau} \sin \beta \tau \, d\tau$$

$$- (2a \cos \beta t + 2b \sin \beta t) \frac{e^{-\alpha t}}{2} \left\{ \begin{array}{l} \int \frac{e^{\alpha \tau}}{2} \cos[(2A+\beta)\tau] \, d\tau \\ + \int \frac{e^{\alpha \tau}}{2} \cos[(2A-\beta)\tau] \, d\tau \end{array} \right\}$$

$$+ (-2a \sin \beta t + 2b \cos \beta t) \frac{e^{-\alpha t}}{2} \int e^{\alpha \tau} \cos 2A\tau \sin \beta \tau \, d\tau \qquad (81)$$

For $0 \leq t \leq \frac{\pi}{A}$,

$$\frac{y_i(t)}{k} = -\frac{1}{2}(a\cos\beta t + b\sin\beta t)\left\{\begin{array}{l}\dfrac{\alpha\cos[(2A+\beta)t]+(2A+\beta)\sin[(2A+\beta)t]}{\alpha^2+(2A+\beta)^2} \\ \\ +\dfrac{\alpha\cos[(2A-\beta)t]+(2A-\beta)\sin[(2A-\beta)t]}{\alpha^2+(2A-\beta)^2}\end{array}\right\}$$

$$+\frac{1}{2}(a\cos\beta t \quad b\sin\beta t)\,e^{-\alpha t}\left\{\frac{\alpha}{\alpha^2+(2A+\beta)^2}+\frac{\alpha}{\alpha^2+(2A-\beta)^2}\right\}$$

$$+\frac{1}{2}(-a\sin\beta t + b\cos\beta t)\left\{\begin{array}{l}\dfrac{\alpha\sin[(\beta+2A)t]-(\beta+2A)\cos[(\beta+2A)t]}{\alpha^2+(\beta+2A)^2} \\ \\ \dfrac{\alpha\sin[(\beta-2A)t]-(\beta-2A)\cos[(\beta-2A)t]}{\alpha^2+(\beta-2A)^2}\end{array}\right\}$$

$$+\frac{1}{2}(-a\sin\beta t + b\cos\beta t)e^{-\alpha t}\left\{\frac{(\beta+2A)}{\alpha^2+(\beta+2A)^2}+\frac{(\beta-2A)}{\alpha^2+(\beta-2A)^2}\right\}$$

$$+\frac{a\alpha+b\beta}{\alpha^2+\beta^2}-\left[\frac{a\alpha+b\beta}{\alpha^2+\beta^2}\right]e^{-\alpha t}\cos\beta t$$

$$+\left[\frac{a\beta-b\alpha}{\alpha^2+\beta^2}\right]e^{-\alpha t}\sin\beta t \qquad (82)$$

For $t > \frac{\pi}{A} = 6.5 = R$

$$\frac{y_i(t)}{k} = (a\cos\beta t + b\sin\beta t)e^{-\alpha t}\left\{\frac{e^{\alpha R}(\alpha\cos\beta R+\beta\sin\beta R)-\alpha}{\alpha^2+\beta^2}\right\}$$

(equation continued)

$$+ (a \sin \beta t - b \cos \beta t) e^{-\alpha t} \left\{ \frac{e^{\alpha R}(\alpha \sin \beta R - \beta \cos \beta R) + \beta}{\alpha^2 + \beta^2} \right\}$$

$$- \frac{1}{2}(a \cos \beta t + b \sin \beta t) e^{-\alpha t} \left\{ \frac{e^{\alpha R}[\alpha \cos[(2A+B)R] + (2A+\beta) \sin[(2A+\beta)R]]}{\alpha^2 + (2A + \beta)^2} \right.$$

$$+ \frac{e^{\alpha R}[\alpha \cos[(2A-\beta)R] + (2A-\beta) \sin[(2A-\beta)R]]}{\alpha^2 + (2A - \beta)^2}$$

$$\left. + \frac{-\alpha}{\alpha^2 + (2A + \beta)^2} + \frac{-\alpha}{\alpha^2 + (2A - \beta)^2} \right\}$$

$$+ \frac{1}{2}(-a \sin \beta t + b \cos \beta t) e^{-\alpha t} e^{\alpha R} \left\{ \frac{\alpha \sin[(\beta+2A)R] - (\beta+2A) \cos[(\beta+2A)R]}{\alpha^2 + (\beta + 2A)^2} \right.$$

$$\left. + \frac{\alpha \sin[(\beta-2A)R] - (\beta-2A) \cos[(\beta-2A)R]}{\alpha^2 + (\beta - 2A)^2} \right\}$$

$$+ \frac{1}{2}(-a \sin \beta t + b \cos \beta t) e^{-\alpha t} \left\{ \frac{(\beta + 2A)}{\alpha^2 + (\beta+2A)^2} + \frac{(\beta - 2A)}{\alpha^2 + (\beta-2A)^2} \right\} \quad (83)$$

Finally, $y(t) = \sum_i y_i(t)$

The denominator of Equation (67) may be evaluated by finding the partial

fraction expansion of the integrand of Equation (68) and then applying the residue theorem for integrating about a closed contour.[16] The terms of the partial fraction expansion whose poles are in the upper half of the complex plane have been determined to be

$$\frac{(1.51186 - j\ 1.3333)}{(x + .3307 - j\ .375)}, \quad \frac{(-1.51186 - j\ 1.3333)}{(x - .3307 - j\ .375)} \tag{84}$$

The complex number in each numerator is the residue of the integrand at the pole in the denominator. Now, by applying the residue theorem to evaluate the contour integral along a contour enclosing the upper half of the complex plane

$$\int_{-\infty}^{+\infty} |H(jx)|^2\, dx = (.25)^2\, 2\pi\, j[-2j(1.3333)] \tag{85}$$

So the noise equivalent bandwidth is

$$\Delta f = .5236\ f_c \tag{86}$$

and

$$N^2 = N_R^2\, \omega_c (.288675)^2 \tag{87}$$

Equation (67) has been numerically determined versus ω_c for an arbitrarily chosen value of $\sigma = .945$ second in Equation (64). The results are graphed in Figure 64.

The results show that for $\sigma = .945$ second, the maximum output signal-to-noise ratio occurs for $\omega_c = 1.425$. Hence, the product of $\sigma\omega_c$ at the highest signal-to-noise ratio is

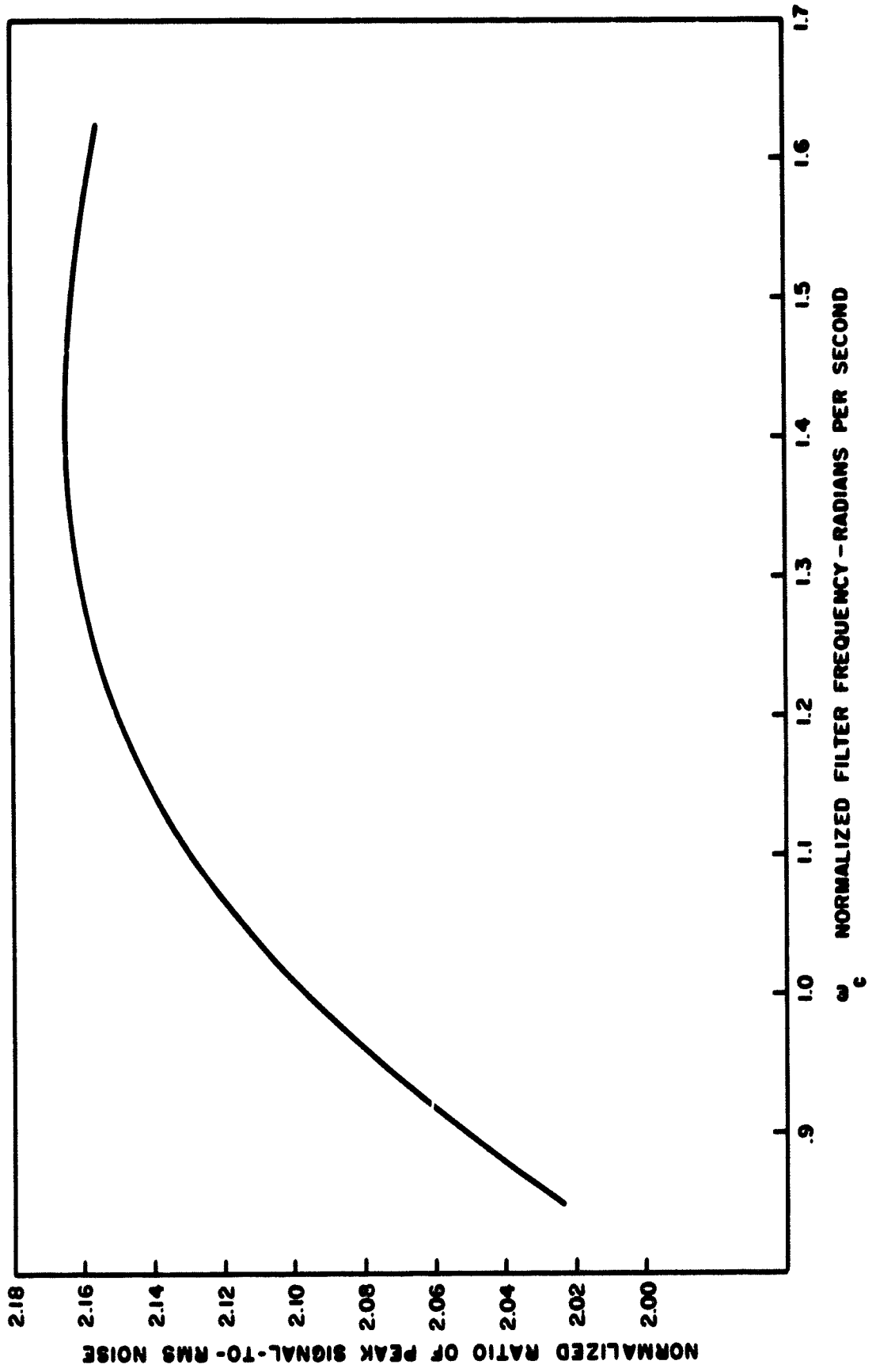


Figure 64: Normalized ratio of peak signal-to-RMS noise for the two pole filter.

$$\sigma\omega_c = (.945)(1.425) = 1.3466 \ . \tag{88}$$

This represents the condition for which the filter impulse response is most closely matched to the input signal,

$$f(t) = \sin^2 \frac{\pi}{6.88} \frac{t}{\sigma} \ , \quad \text{for } 0 \leq t \leq 6.88\,\sigma \ . \tag{89}$$

For the two pole transfer function, the maximum output signal-to-RMS noise ratio corresponding to $\omega_c = 1.425$ is 2.1659. Evaluation of Equation (67) for a six pole linear phase versus frequency filter shows that there is only a loss of 1.8 percent in the ratio of peak signal-to-RMS noise for a two pole filter when compared to its six pole counterpart. This result tends to indicate that a two pole linear phase filter is adequate to smooth star pulses for applications where exceptional system accuracies are not required.

Further analysis shows that Equation (88) may be rewritten in terms of the slit transit time, T_s. Since $T_s = 2.56\sigma$

$$\omega_c = \frac{3.4473}{T_s} \text{ radians per second.} \tag{90}$$

But for a slit radial to the spin axis, T_s is related to the scan period, T, and slit width, $\widehat{SW}$, by

$$T_s = \frac{\widehat{SW}\ T}{21{,}600} \text{ seconds} \tag{91}$$

where

$\widehat{SW}$ = slit width in arc minutes projected onto the celestial sphere, and

T = scan period in seconds.

So,

$$\omega_c = \frac{74,461.68}{\overline{SW} \cdot T} \text{ radians per second .} \qquad (92)$$

Equation (92) gives the value of ω_c which matches the two pole filter impulse response to the signal for a given scan period. A question of particular interest concerns the change in the filter response if the scan period varies while the filter parameter, ω_c, remains fixed. This question may be reasonably answered by observing Figure 64. For this figure, the signal was fixed and ω_c was varied by almost a factor of two causing an approximate change in peak signal-to-noise ratio of only 6.5 percent. Therefore, it can be reasonably concluded that the scan period can change over a relatively broad range without causing intolerable or catastrophic degradation in the performance of a fixed frequency filter.

Figure 65 shows a plot of the noise-free input signal, f(t), and the noise-free output signal, y(t), for $\omega = 1.425$ and $\sigma = .945$. As shown in Figure 65 for $\omega = 1.425$, the noise-free input peak of unity is reduced by the filter to an output peak equal to .7464. The peak of the noise-free input signal corresponds to 80 percent of the star radiation striking the photocathode. Since I_S = the average current produced by 100 percent of the star radiation striking the photodetector, then the input signal peak corresponds to $.8\ I_S$. Hence, the output signal peak corresponds to $(.7464)(.8)\ I_S = .597\ I_S$. Consequently, the peak output signal-to-RMS noise ratio is expressed by

$$\frac{S}{N} = \frac{(.597)\ I_S}{(1.26)[2e(.8\ I_S + I_B + I_D)\ \Delta f]^{\frac{1}{2}}} \qquad (93)$$

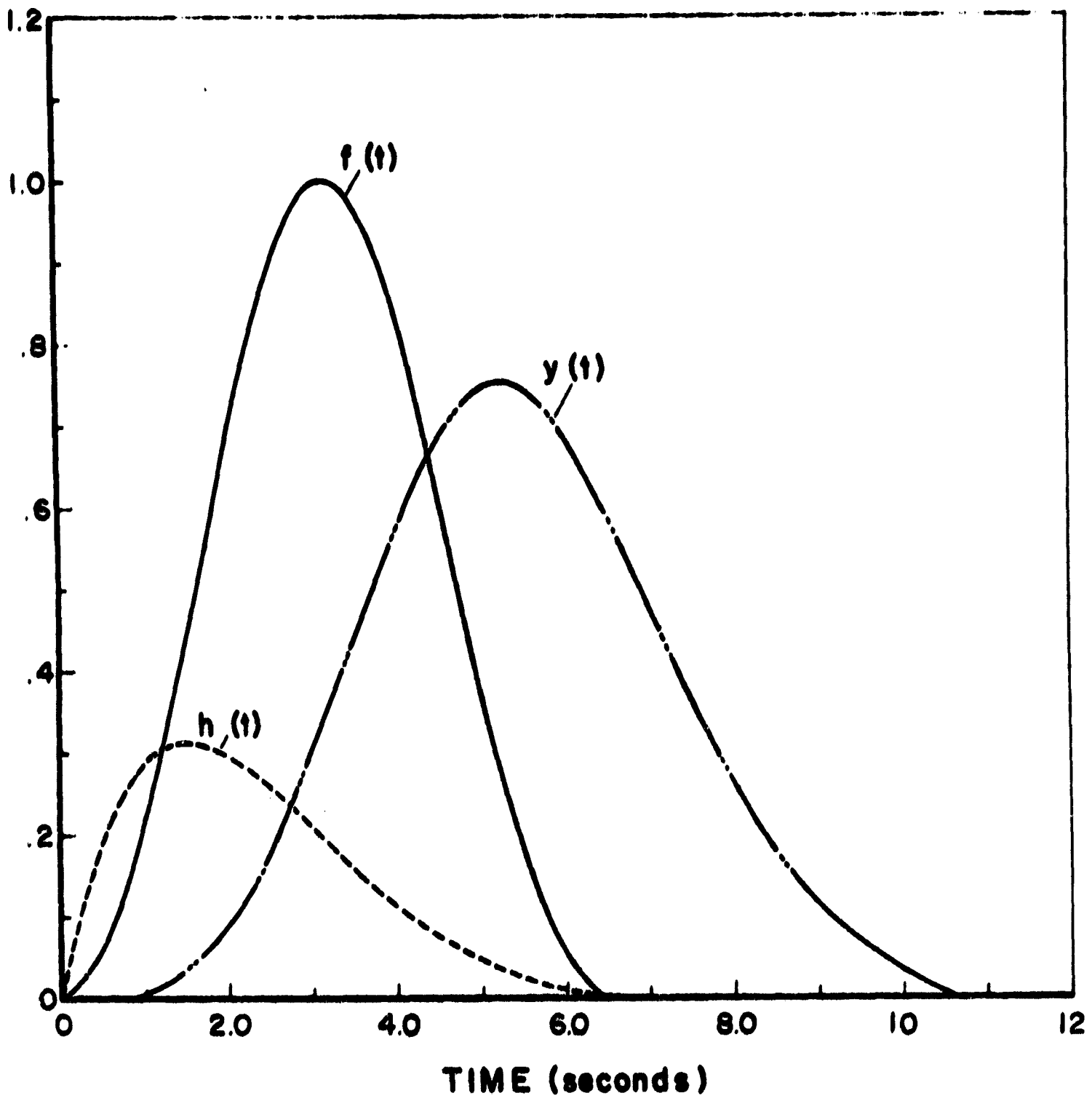


Figure 65: Star pulse input signal to filter, f(t); filter impulse response, h(t); and output signal, y(t).

where

$$\Delta f = \frac{(.524)(11851)}{\widehat{SW} \cdot T} = \frac{6210}{\widehat{SW} \cdot T} \tag{94}$$

and the denominator factor of 1.26 accounts for noise introduced by the photomultiplier dynode chain.[2]

If measurements of the star signal peaks were made at the filter output for a given star, it would be expected that the RMS variation in these measurements would be $N \cdot G_T$, where G_T is the photomultiplier tube gain. If the variation of the intensity measurement, σ_I/I, is defined as the ratio of the RMS variation in the signal peak to the average value of the signal peak, then this ratio must be equivalent to the reciprocal of the peak signal-to-RMS noise ratio. Hence:

$$\frac{\sigma_I}{I} = \frac{N}{S} \quad . \tag{95}$$

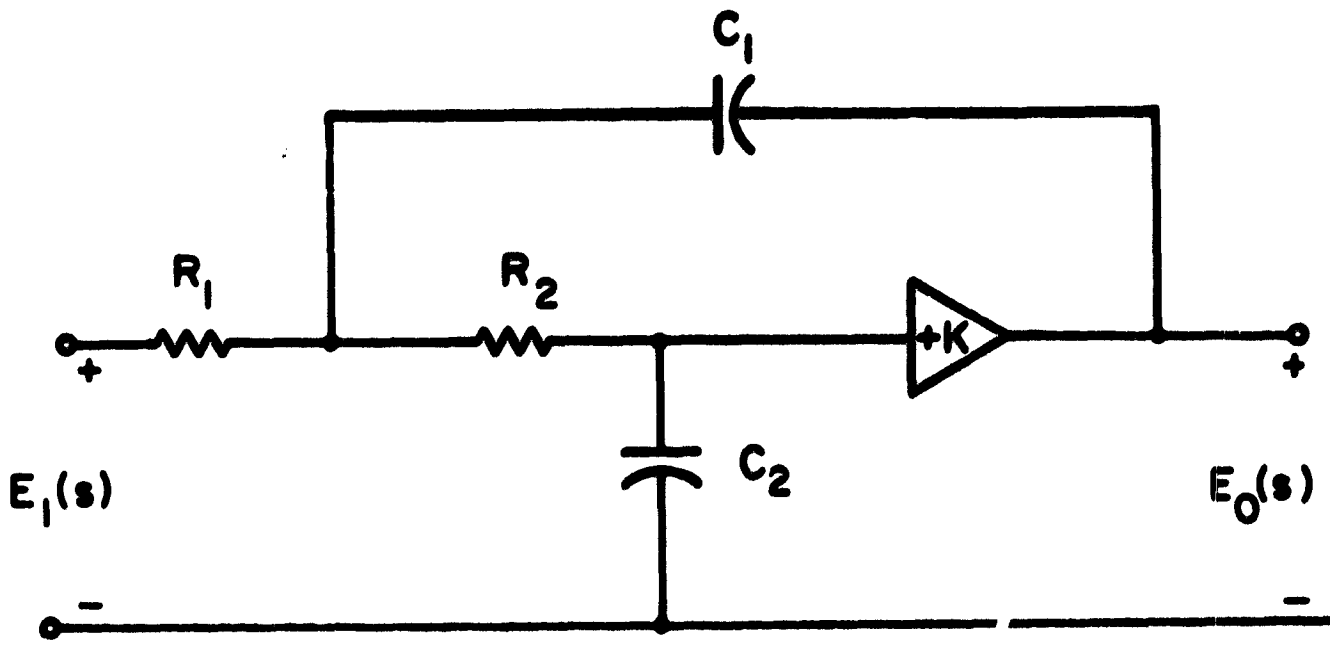
Figure 65 shows the filter impulse response, h(t), plotted for $\omega = 1.425$.

The second order transfer function of Equation (76) may be implemented by the circuit shown in Figure 66. The design procedure for obtaining the values of R and C involves matching the poles of the desired filter transfer function with the poles of the circuit transfer function. If K = 1 in Figure 66, then

$$C_1 C_2 R_1 R_2 = \frac{4}{\omega_c^2} \tag{96}$$

and

$$C_2 (R_2 + R_1) = \frac{3}{\omega_c^2} \tag{97}$$



$$\frac{E_0(s)}{E_1(s)} = \frac{K}{\left[s^2 C_1 C_2 R_1 R_2 + s\left\{C_2 R_2 + C_2 R_1 + (1 - K) C_1 R_1\right\} + 1\right]}$$

Figure 66: Practical circuit configuration with quadratic transfer function for low pass active filter.

Now let $R_2 = R_1 = R$, so that

$$C_2 = \frac{3}{2R\,\omega_c} \quad \text{and} \quad C_1 = \frac{8}{3\,\omega_c R} \tag{98}$$

4. Optical Aperture

In order to determine the required optical aperture, it is first necessary to analyze the problem of star signal detection. For the SCADS sensor, star signal detection will be achieved by threshold detection of the filtered analog signal. In this section, determination of the threshold level for a permissible false detection rate will be based on results derived by S. O. Rice.[17] The required optical aperture diameter will then be determined to detect a given magnitude star with a fixed detection probability.

Rice has shown that a noise signal at the output of a low pass filter having an amplitude probability density function which is normal will pass through the threshold value I_T with a positive slope an average number of times per second equal to

$$N_f = (1.155)\, e^{-\frac{1}{2}\left(\frac{I_T - I_{BD}}{I_{RMS}}\right)^2} f_b \tag{99}$$

where

I_T = threshold value of current
I_{BD} = average value of noise current
I_{RMS} = RMS value of noise current
f_b = noise equivalent bandwidth of low pass filter in cycles per second.

It has been shown above that the noise equivalent bandwidth for a two pole linear phase shift filter is

$$\Delta f = f_b = \frac{6210}{\widehat{SW} \cdot T} \text{ cycles per second} \tag{100}$$

where

$\widehat{SW}$ = rotational slit width in arc minutes,

T = scan period in seconds.

Hence, the average number of threshold crossings per scan period, N_f, equals

$$N_f = \frac{7166.95}{\widehat{SW}} \; e^{-\frac{1}{2}} \left(\frac{I_T - I_{BD}}{I_{RMS}} \right)^2 \tag{101}$$

So

$$\frac{I_T - I_{BD}}{I_{RMS}} = \left[2 \; \ell n \; \frac{7166.95}{N_f \cdot \widehat{SW}} \right]^{\frac{1}{2}} \tag{102}$$

The values of I_T, I_{BD}, and I_{RMS} are taken as current values at the output of the photocathode. The value of I_{RMS} is obtained from the shot noise equation with an additional factor included to account for photomultiplier noise. The current levels at the photomultiplier output can be obtained by multiplying all three values by a noise-free constant equal to the gain of the dynode chain. So at the cathode, the RMS noise equals

$$I_{RMS} = 1.3[2e \; I_{BD} \; \Delta f]^{\frac{1}{2}}, \text{ (e = charge on an electron)} \tag{103}$$

where the factor of 1.3 is included to account for noise introduced by the photomultiplier dynode chain[2]. In the preceding subsection it has been shown that the noise equivalent bandwidth for the two pole filter may be expressed as

$$\Delta f = f_b = \frac{2873}{T_s} \text{ cycles per second} \tag{104}$$

where T_s = time required for the center of the star image blur circle to

cross the slit.

Next, the following quantities may be introduced,

$$n_T = \frac{I_T \, T_s}{e} \tag{105}$$

$$n_{BD} = \frac{I_{BD} \, T_s}{e} \tag{106}$$

where n denotes the average effective number of equally weighted photocathode emissions occurring during a transit interval, T_s. After substitution of Equations (103), (104) , and (105), Equation (102) may be rewritten as

$$n_T = (1.3936) \left[n_{BD} \, \ell n \, \frac{7166.95}{N_f \cdot \widetilde{SW}} \right]^{\frac{1}{2}} + n_{BD} \tag{107}$$

The limiting detectable star magnitude can be determined by considering the value of I required in order to exceed the detection threshold I_T a specified fraction of the time referred to as the detection probability. Consequently, the detection level must be

$$I_T \leq I_{BD} + I - k \, I_{RMS} \tag{108}$$

where

I = the peak value of the star signal at the filter output,

I_{RMS} = the RMS output noise generated by the average peak signal level at the input to the low pass filter, and

k = constant determined by the required detection probability, P_d.

The constant k is determined from

$$P_d = \frac{1}{\sqrt{2\pi}\, I_{RMS}} \int_{-\infty}^{kI_{RMS}} \exp\left[-\frac{1}{2}\left(\frac{I}{I_{RMS}}\right)^2\right] dI \,. \tag{109}$$

It was shown that the peak value of the star signal at the output of a two pole linear phase filter is

$$I = .597\, I_S \tag{110}$$

where I_S = the average photocathode current produced by 100 percent of the star radiation striking the photocathode. Equation (110) assumes that 80 percent of the star radiation passes the slit when the blur circle is centered in the slit. The RMS current in Equation (108) is given by

$$I_{RMS} = 1.3[2e(.8\, I_S + I_{BD}) f_b]^{\frac{1}{2}} \tag{111}$$

Substitution of Equations (104), (105), and (107) into Equation (108) yields

$$(n_T - n_{BD} - .597\, n_s)^2 = \left\{-k(1.3)[(.5746)(.8\, n_s + n_{BD})]^{\frac{1}{2}}\right\}^2 \tag{112}$$

Equation (112) can be written as a quadratic in n_s

$$(.597\, n_s)^2 - n_s[1.194(n_T - n_{BD}) + (1.3\, k)^2\, (.5746)(.8)]$$

$$+ (n_T - n_{BD})^2 - (1.3\, k)^2\, (.5746)\, n_{BD} = 0 \tag{113}$$

From a table of the error function, k = 1.66 for a detection probability of 0.95. So Equation (113) becomes

$$(.3564)n_s^2 - n_s[1.194(n_T-n_{BD}) + 2.141] + (n_T-n_{BD})^2 - 2.676\, n_{BD} = 0 \quad (114)$$

The stellar magnitude, M, for a solidly detectable star (95 scans out of 100) can now be obtained by equating

$$I_S = \frac{n_s e}{T_s} = \epsilon_o\, S_K\, 10^{-.4M} \frac{\pi}{4} a^2 \quad (115)$$

where

ϵ_o = efficiency of the optical system,

S_K = sensitivity of the cathode to a zero magnitude star per unit area of optical aperture,

a = diameter of the optical aperture.

So

$$M = 2.5 \log_{10}\left[\frac{\pi}{4} a^2 \frac{T_s}{n_s \cdot e} \epsilon_o S_K\right] . \quad (116)$$

If a limiting magnitude is specified, then, Equation (116) may be inverted to find the optical aperture a in terms of this magnitude. However, a detection probability of 0.95 for the system limiting magnitude M_ℓ would result in an "over-designed" system. From the cumulative probability distributions for the third and fourth brightest stars in the field of view--see Figures 27, 41, and 45--it is seen that the fourth brightest star is at least a half-magnitude brighter than M_ℓ for about 90 percent or more of the possible scan axis directions. But, a detection probability of 0.5 (i.e., 50 percent) at $M = M_\ell$ would insure that the fourth star would be detected on at least half of the scans in the worst case. This is adequate

for operation of SCADS; it only lengthens the computer time required for scan-to-scan transit correlation and star pattern identification. Further, it has just been seen that the fourth brightest star will be much brighter than M_ℓ most of the time.

Thus, the optical aperture will be found with an assumed value of $k = 0$ (corresponding to $P_d = 0.5$) in Equation(113). Then,

$$a = \left[\frac{4\ 10^{.4M_\ell}}{\pi\ \epsilon_o\ S_K} \cdot \frac{n_s \cdot e}{T_s}\right]^{\frac{1}{2}} . \qquad (117)$$

The optical aperture, a, can be determined if the following quantities are known or assumed:

(a) S_K = photocathode sensitivity,

(b) θ_e = angle between the field of view outer edge and the scan axis,

(c) θ_i = angle between the field of view inner edge and the scan axis,

(d) $\widehat{SW}$ = rotational slit width,

(e) N_S = number of radial slits,

(f) N_B = equivalent stellar background,

(g) ϵ_o = efficiency of optical system,

(h) I_D = dark current of the photocathode,

(i) M_ℓ = limiting detectable magnitude,

(j) N_f = an average number of false star detections per scan period,

(k) T = scan period,

(l) k = argument of the error function at $P_d = 0.5$ $(k = 0)$.

Items (a) through (h) are required to determine

$$I_{BD} = I_B + I_D \tag{118}$$

where I_B = cathode current generated by stellar background radiation striking the photocathode. The stellar background radiation, N_B, is commonly expressed in terms of tenth magnitude stars per square degree of slit area projected onto the celestial sphere. The total slit area projected onto the celestial sphere is

$$S_A = N_S \frac{\widehat{SW}}{60} (\cos \theta_i - \cos \theta_e) \frac{180}{\pi} (\text{degree})^2 \tag{119}$$

where $\widehat{SW}$ is expressed in arc minutes.

With S_K expressed in terms of amperes per square centimeter and a in centimeters, I_B can be determined for a given a by

$$I_B = \epsilon_o \cdot N_B \cdot S_A \cdot S_K \times 10^{-4} \frac{\pi}{4} a^2 \tag{120}$$

The solution for a must be obtained by an iterative numerical method since a cannot be expressed explicitly from Equations (107), (113), (117), and (120). It is also necessary to assume specific values for ϵ_o, N_B, N_F, and $\widehat{SW}$. These parameters cannot be solved for explicitly; however, realistic values can be assigned for each based on either experience or a worst case condition.

For instance, the true efficiency, ϵ_o, of an optical system is a complex function of multiple variables describing a lens system. Since part of the design problem is to determine a SCADS lens system, it is required that a realistic overall optical efficiency be assumed. Such a realistic value is $\epsilon_o = .5 = 50\%$. In general, this is somewhat below the

efficiency of the actual lens; however, it represents a suitable assumption.

For the case of the stellar background, N_B, a worst case value will be assumed based on total integrated starlight for stars of sixth magnitude and weaker.[10] Over the celestial sphere, the background level varies from 15 to 323 tenth magnitude (photographic) stars per square degree. Hence, the stellar background is taken as N_B = 325 tenth magnitude stars per square degree.

In the case of the false detection rate, N_f, the choice is somewhat arbitrary. False detections are undesirable since they lengthen the computer running time of the star identification procedure and contribute no information in terms of attitude determination. In addition, the useful capacity of data storage and telemetry transmission is reduced. For the SCADS design procedure here, the average false detection rate is taken as N_f = one per five scan periods.

Since the selection of the slit width critically affects the accuracy of the attitude determination as well as the ability of SCADS to detect stars, the choice of $\widehat{SW}$ is discussed in the next section.

C. Parameters Related to Measurement Accuracy

Filtered star pulse signals are most conveniently detected by the signal crossing of a predetermined threshold level. If a star pulse crosses the detection threshold then the transit time, t_s, of the star is determined from

$$t_s = \frac{(t_1 + t_2)}{2} \qquad (121)$$

where t_1 = the threshold crossing of the star pulse leading edge,

t_2 = the threshold crossing of the star pulse trailing edge.

If the cross-section of the star image blur spot is symmetrical in the direction of the slit scan and the filter output signal is noise free then the star image blur spot is centered in the slit at exactly

$$t_m = t_s - t_d \qquad (122)$$

where t_d is some constant known delay introduced by the filter holding time (memory) which can be accurately determined either analytically or measured. However, the filter output signal is distorted by superimposed random noise which causes variations in the successive measurements of t_1 and t_2, hence an uncertainty arises in the value for t_s. This uncertainty is related in a complex way to several factors. Included among these factors are

(i) the signal amplitude (star intensity),
(ii) the background signal level,
(iii) the scan period,
(iv) the slit width,
(v) the blur spot size.

The designer has varying amounts of control over these five factors. We will qualitatively discuss how each of these factors tends to influence the transit time uncertainty. We will assume in this discussion that a large

percentage of the star image blur spot is initially containable in the slit width when the spot is centered in the slit to insure that limiting magnitude stars are detected. In the discussion, we will further assume that the best possible match is realized between the filter impulse response and the signal.

For bright stars the energy density in a given blur spot size is greater than for dimmer stars, consequently as the slit moves across the blur spot the slopes of the star signal leading and trailing edges are greater than for dim stars. Therefore, for a fixed threshold the uncertainties in the threshold crossings for bright stars must be less than for dim stars. The energy received from a particular star per unit area is, of course, fixed by the stellar emission, but the available signal from that star may be increased by enlarging the optical aperture. However, the SCADS lens accounts for a significant portion of the weight of the total sensor and the lens weight goes as the cube of the aperture a. Further, the volume of the bright object shield also goes as (a^3). Thus, there are strong physical limitations imposed by the SCADS/spacecraft interface which dictate the use of a small aperture; the detection criteria developed in the last section will be used for the selection of a.

An increased background level with all other factors fixed will result in greater uncertainties in the threshold crossing times due to the increased RMS noise level. This background signal level can be partially controlled by excluding bright-source radiation with careful shielding. However, the stellar background of faint stars is an invariant characteristic of the particular portion of the sky being scanned. Fortunately, regions with many faint stars (the Milky Way) also tend to have proportionately more bright stars which give strong signals.

1. Scan Period

As the scan period is increased for a given slit width, the filter bandwidth must be decreased in order to realize the best possible match

between the filter impulse response and the signal. This results in a reduced RMS noise level so that the uncertainties in the threshold crossing times should also be decreased.

The scan period for a passive sensor in the spin-stabilized mode is fixed by the spin rate. In the present application, this nominal period is one second.

For the three-axis-controlled mode, however, the slit reticle must be driven so the scan period is subject to choice. Thus, the scan may be slowed down to obtain a longer dwell time T_s on the star image in the slit. This is particularly significant for the dual mode sensor where the scan period is one second and the accuracy requirement is $0^{\circ}.1$ in the spinning state while the accuracy desired in the three-axis-controlled state is $0^{\circ}.01$. This increase in accuracy can be obtained in part through a reduction of the scan rate for the driven case. However, a separate filter is needed for each mode if the transit pulse durations are widely different. Also, if the scan period becomes exceptionally long, the motion of the vehicle may complicate the pattern of transits. In the three-axis-controlled mode here, the vehicle rotates at approximately 15° per hour or 15 arc-minutes per minute of time. A scan period of 10 seconds is recommended for the driven mode. During this period, the vehicle itself rotates through about 2.5 minutes-of-arc. The pattern of transits will therefore be almost periodic and should be readily recognizable with scan-to-scan correlation.

2. Blur Spot Size and Slit Width

The joint selections of the allowed blur spot size and the rotational slit width are probably the most difficult to make since they affect both star detection and overall system accuracy.

The ideal slit is chosen in the form of a pie-shaped sector with its apex on the scan axis. This geometry and its projection on the celestial

sphere are shown in Figure 67. Note that in this configuration, the time required for the slit to sweep by any point on the celestial sphere is a constant independent of the angle ρ from the scan axis to that point. Thus, the integration or dwell time during which a star is in the slit is (at least ideally) the same for all stars in the annular field; a single filter matches all transits equally well.

Although the stars are essentially point sources at infinity, their images in the SCADS image plane are blur spots of finite size. This blurring of the image is caused primarily by the aberrations associated with geometric optics--coma, astigmatism, etc.--and to a lesser extent by diffraction. The computer print-out of representative blur spot diagrams generated by a very powerful geometrical ray trace program are shown in Figure 68. It might be noted that these diagrams correspond to the Super Farron lens which is used in the SCADS-type instrument onboard ATS-3.

Observe here also that the blur spot distortions are symmetric about a radial line from the optical axis. Since the slit also has radial symmetry, threshold detection at a fixed level on the star pulse will give expected ingress and egress times which lie at the same distance on either side of the time when the star is centered in the slit. All of these times will, of course, contain the constant delay t_d due to the filter. The point, however, is that the optical system should introduce no significant asymmetry error in the measured transit times. This would not be the case if non-radial slits were used.

As the blur spot size decreases for a given star, the focused light energy becomes more concentrated, so it seems reasonable that the slopes of both the leading and trailing edge of the star pulse should become steeper. A steeper slope in the vicinity of the threshold crossing should then result in reduced uncertainties in the threshold crossing times for a given noise level; i.e. for fixed slit width, scan period, and background signal level.

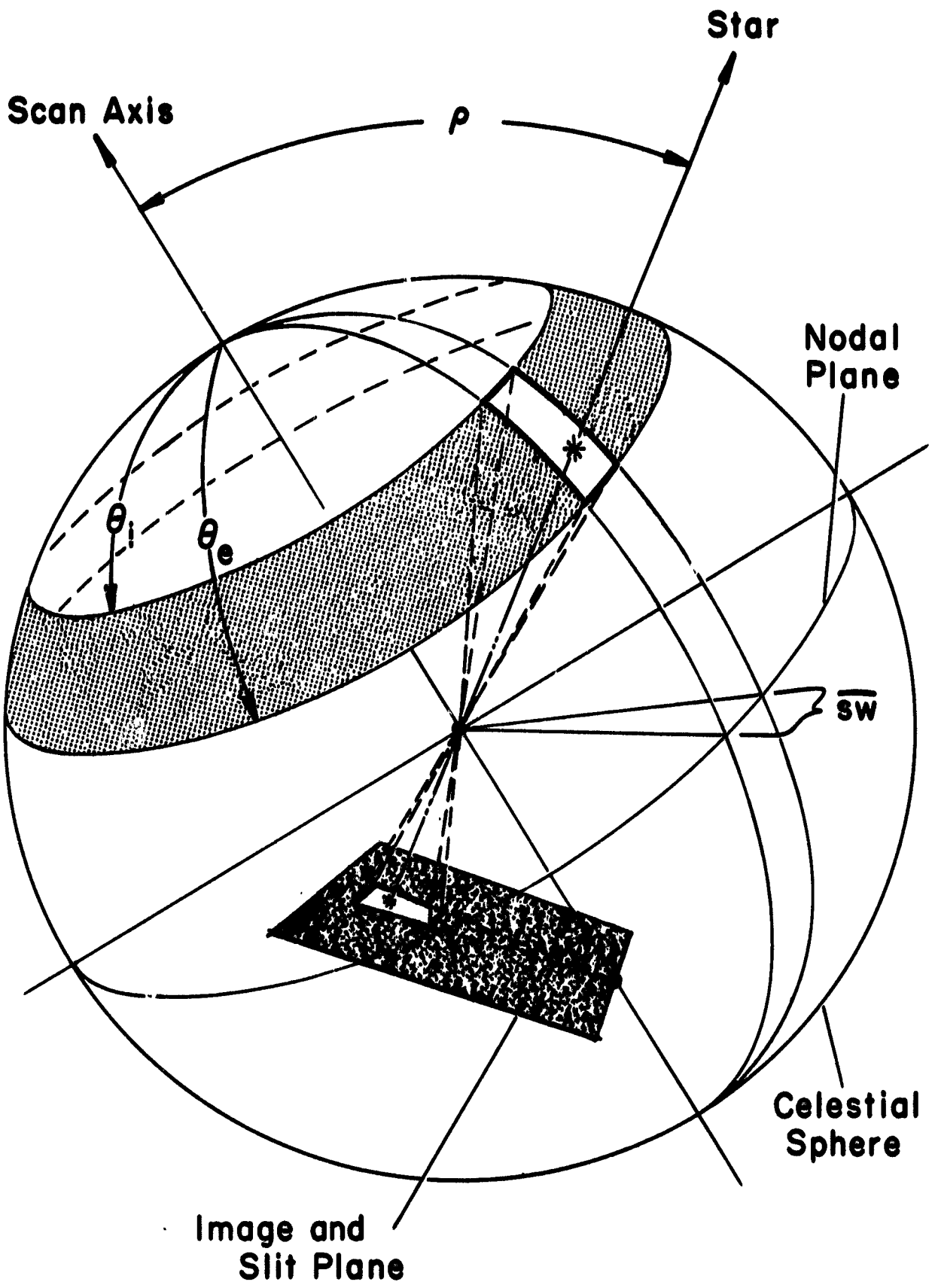


Figure 67: Schematic representation of the rotational slit width $\widetilde{SW}$ projected onto the celestial sphere.

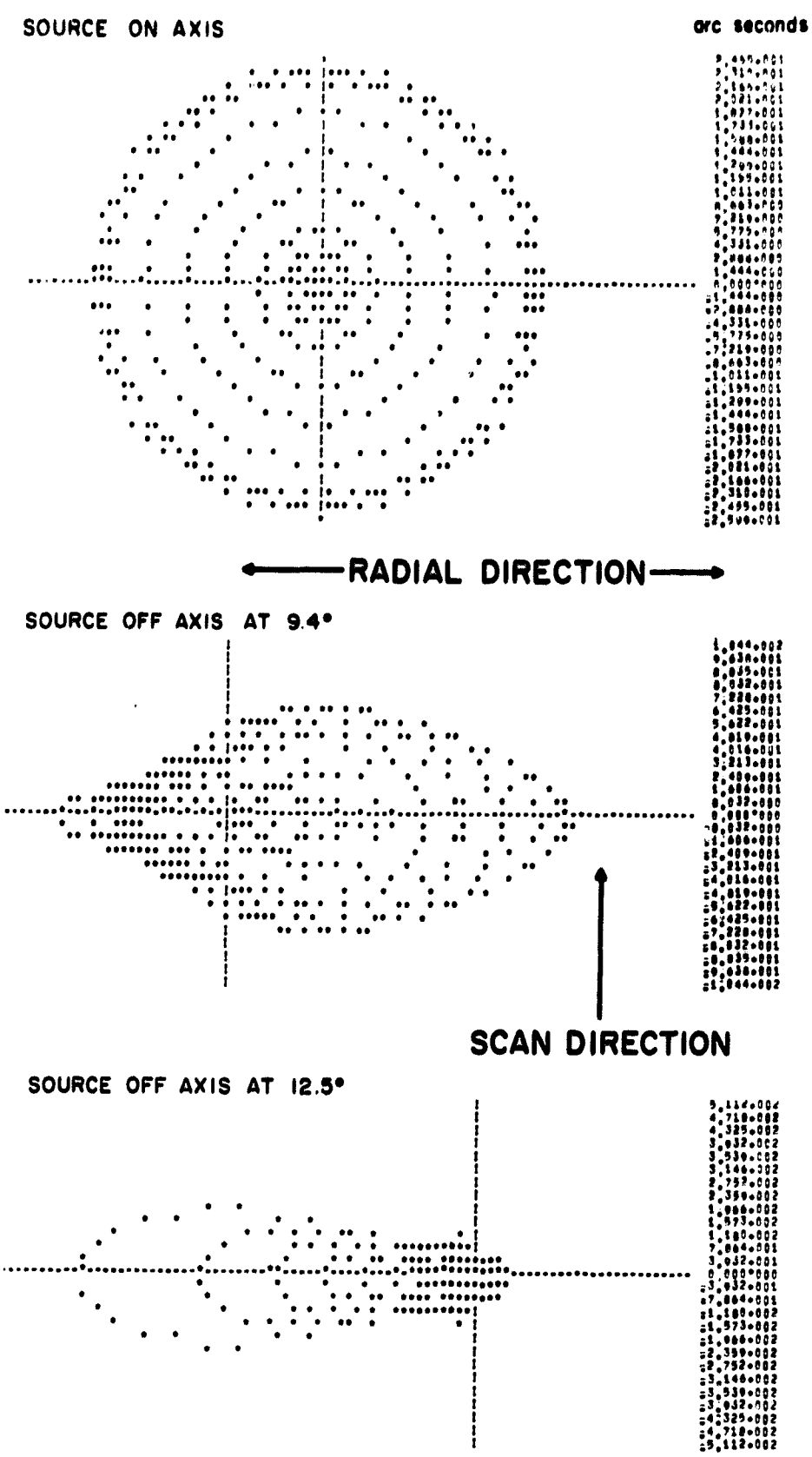


Figure 68: Blur Spot Diagrams generated by a digital computer ray trace program. Lens: Super Farron optically stopped to f/1.3. (Note: the three digits following the + in the "arc seconds" column represent a multiplicative power of ten; thus 2.455+001 is read $2.455 \times 10^1 = 24.55$.)

Little is gained, however, by making the blur spot much smaller than the slit width. In practice, even the problem of reducing the blur spot to approximately the same size as the desired slit width taxes the optical state-of-the-art for wide angle short focal length lenses. Thus, the requirement that the blur spot match the size of the slit is a suitable but sometimes difficult-to-achieve criterion.

The remaining parameter to be discussed in this section is the rotational slit width $\widehat{SW}$. It is desirable to make the slit as wide as possible since for a given scan period this causes a star to be in the slit longer and therefore allows a longer integration (time averaging) of the star pulse. It can be shown that for a given false detection rate and detection probability, a wider slit allows a smaller optical aperture. However, widening the slit reduces the accuracy with which the star can be located. So the slit should be selected to be as wide as possible and still meet the system accuracy requirement.

Experience in performing error analyses on the SCADS system of constraint equations indicates that the accuracy goals specified for this study can be met if individual transit measurements have a total RMS time error corresponding to an azimuth measurement error of about one arc-minute. Further, experience in operating experimental SCADS sensors from the earth (looking through the atmosphere with the corresponding astronomical "seeing" problems) suggests that the azimuth of a solidly detectable star may be located to accuracy of one-tenth to one-twentieth of the matched blur spot-slit width for satellite-borne measurements. On this basis, a rotational slit width $\widehat{SW}$ = 12 arc-minutes is selected for the present application; interpolation of the resulting star pulses to better than one part in twelve relative to this slit width should present no major problems.

3. Time Measurement Resolution and Clock Stability

Encoding of the star transit time must be performed with sufficient

precision so that the required system accuracy can be realized. In order to achieve the required system accuracy, all sources of error must be considered, with one of the sources being the transit time uncertainty introduced by the encoding process. The encoding error contribution can be derived by consideration of the uniform probability density function. The threshold crossing for a star pulse is equally likely to occur at any instant during a clock period resolution interval. So the probability density for the threshold crossing time is a uniformly distributed random variable whose RMS value is $\frac{L}{\sqrt{12}}$ where L is the length of the time interval. It will be assumed that the trailing edge threshold crossing time is independent of the leading edge threshold crossing. Since the star transit time is the average of the leading edge and trailing edge threshold crossings, then the RMS transit time uncertainty must be approximately $\frac{\sqrt{2}}{\sqrt{12}}$ L. This quantity should correspond to an azimuth uncertainty of less than one arc minute; that is, to a relative uncertainty of less than one part in 21600 per scan. Thus $L/T < \sqrt{6}/21600 = 1.134 \times 10^{-4}$ where T is the scan period. The closest simple binary power which satisfies this inequality is 2^{-14}. Hence, the clock should operate with a resolution just sufficient to encode one scan with fourteen bits. For a one second scan period the basic clock oscillator frequency must be 1.08×10^{4} cps.

It is important that the clock used for encoding SCADS star transit data be synchronized with Universal Time, or some equivalent, in order to determine spacecraft attitude as a function of time. Almost any synchronization method should be sufficient. One reasonable method would be to have the period of the clock be slightly greater than the orbital period and then to count the number of orbits. The number of stages required by the binary clock used for SCADS transit time encoding may be determined in order for the clock period to be greater than the orbital period. The number of stages required depends upon the clock resolution interval and the orbital period. For an earth synchronous orbit, the clock must have thirty binary stages for a 24 hour period with a 1.08×10^{4} cps clock frequency.

The clock resolution interval used for star transit time encoding requires stability for only a relatively short time interval. For SCADS the clock stability is most important for statistical averaging of attitude data from successive scan periods in order to improve the accuracy of the attitude estimate. It has been demonstrated that the accuracy of the attitude determination can be significantly improved if averaging is performed over 10 or 15 successive scan periods. So in order to neglect the error contributions due to the clock instability, the clock resolution interval should not change (drift) by more than a small fraction of the nominal resolution interval. Consequently, the clock resolution interval should not change by more than 1/10 the nominal resolution interval over fifteen scan periods. Since fifteen scan periods are comprised of approximately 1.6×10^5 resolution intervals, the clock stability should be better than 1.6 parts in 10^6.

PRECEDING PAGE BLANK NOT FILMED.

IV. SCADS SENSOR DESIGNS

This section will discuss the optical and electronic design configurations required to implement each of three operational modes for the SCADS sensor. The first configuration to be considered is for attitude determination of the ATS vehicle only when the vehicle is spin stabilized. A second sensor configuration is considered for attitude determination of the ATS vehicle only when the vehicle attitude is three axis controlled. The third sensor configuration must be capable of determining the vehicle attitude for either the spin stabilized mode or the three axis controlled mode. A fourth configuration to be considered is the modification of the ATS-C SCADS design for the spin stabilized mode.

A. Spin Stabilized Mode

The specific sensor configuration for the spin mode SCADS sensor is based on the general parameter criteria presented in Section III and particularly on the parametric design curves of Section IIIA2.

1. Optical Sensor Head

The principal design curves for the spin mode sensor are presented above in Figures 50, 51, 52, and 53. The plots in these figures correspond to configurations in which the volume of the bright object shield has been minimized first with respect to the shield shape factor (shield height versus shield diameter) at fixed effective field of view Θ_{eff} and cant angle Γ. Then, a second level of optimization is performed by minimizing the shield volume with respect to Γ at fixed Θ_{eff}. Figure 52 represents the results of this second minimization. Finally, for each of these doubly minimum configurations, the system limiting magnitude was determined by a detailed star availability search over the range of possible pointing directions for ATS F&G in the spin stabilized mode (see Figure 16). Note that this range of potential scan axes was searched over a very fine grid containing in excess of 9500 points; the relationship $M_{\ell}(\Theta_{eff})$ is presented in Figure 53.

Once the limiting magnitude and the annular field angles are known, the optical aperture required for the system may be determined from the equations developed in Section IIIB4. The remaining parameters required in these equations are also obtained in Section III. The optical aperture a and the corresponding actual shield height h and shield diameter d are given as a function of the effective field of view in Figure 69.

A third level of optimization may be achieved with proper selection of Θ_{eff}. A number of factors in addition to the volume of the bright object shield enter at this point. The objective lens represents an appreciable fraction of the total weight of the sensor and the lens weight is proportional to a^3. Thus, it is desirable to make the optical aperture small which in turn suggests a large effective field of view Θ_{eff}. On the other hand, however, the optical field of view Θ should be made small to ease the lens fabrication problem; this indicates a small value of Θ_{eff} (see Figure 52). Also, a large amount of central blocking, $2\theta_i$, is advantageous in the star identification process; this too suggests a small effective field of view.

From observations on Figures 52 and 69, it appears that $\Theta_{eff} = 60^\circ$ is a suitable compromise. Note particularly that this point corresponds to a local minimum of the shield volume; thus, the minimum volume criterion is carried over, at least partially, to the third level of design selection. Also, the shield height and shield diameter at $\Theta_{eff} = 60^\circ$ are nearly equal; this shape factor contributes to the structural rigidity of the shield. The choice of a sixty degree effective field of view is therefore recommended for the spin mode SCADS sensor. The corresponding values of other SCADS parameters are listed in Table II.

The annular field of view for this design is then characterized by $\theta_i = 6^\circ.25$ and $\theta_e = 30^\circ.75$; these are the values which are used in the lunar interference and target availability studies of Section II.

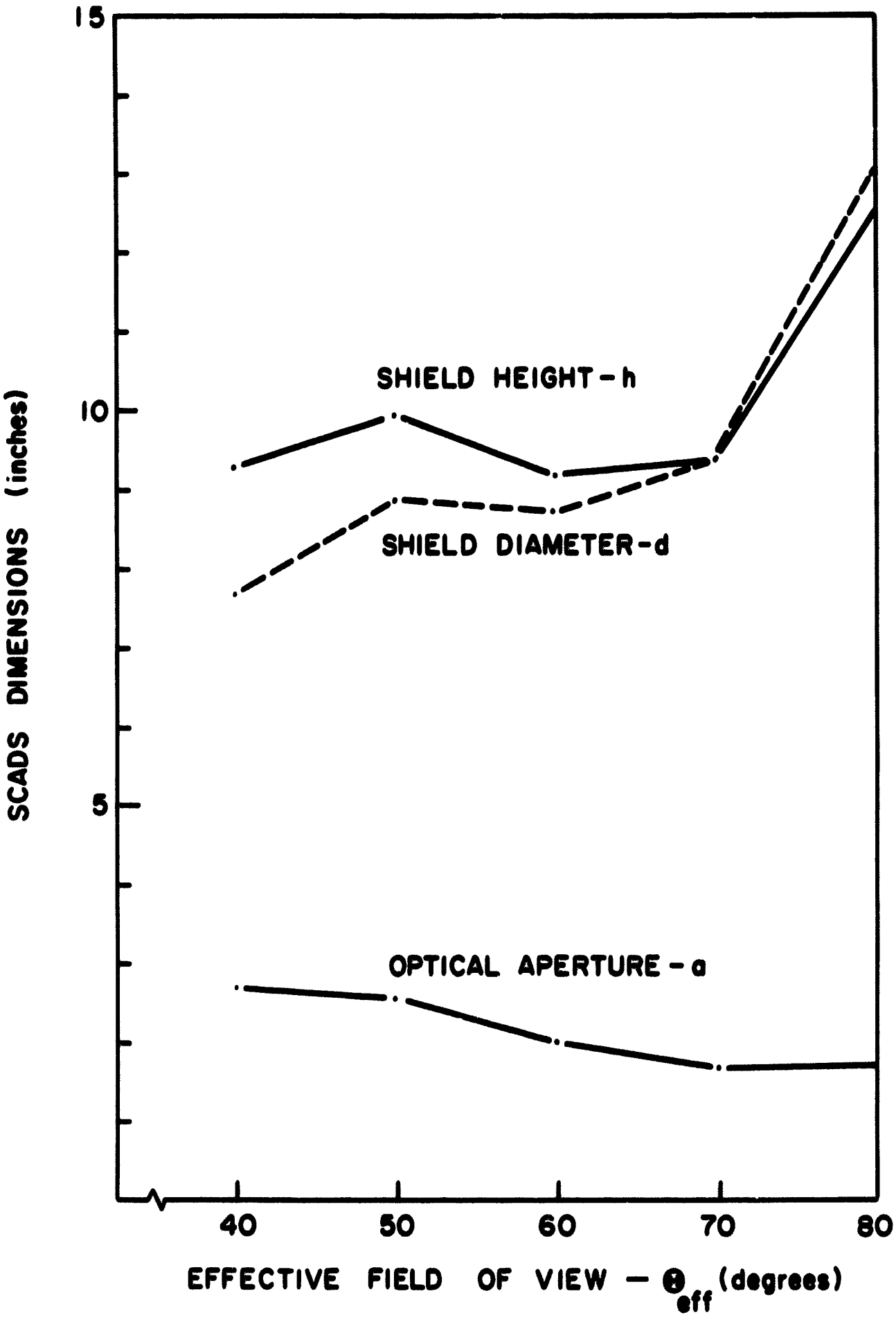


Figure 69: SCADS dimensions for optimal spin mode sensor designs.

TABLE II

PARAMETERS FOR RECOMMENDED SPIN MODE SCADS SENSOR CONFIGURATION

Effective field of view:	$\Theta_{eff} = 60^{\circ}$
Optical field of view:	$\Theta = 24^{\circ}.5$
Cant Angle:	$\Gamma = 18^{\circ}.5$
Central blocking:	$2\theta_i = 12^{\circ}.5$
Shield angle:	$\xi = 38^{\circ}.0$
Rotational slit width:	$\widehat{SW}$ = 12 arc minutes
Optical aperture:	a = 2 inches
Shield height:	h = 9.2 inches
Shield diameter:	d = 8.7 inches
Limiting stellar magnitude:	$M_{\ell} = 3.84$

If possible, the focal length, FL, of the objective lens should be selected so that (i) the radial size of the blur spot can be matched to the slit width and (ii) the image of the full length of the slit will fall within the sensitive area of the cathode of the photomultiplier. The maximum off-axis angle for this system is $\Theta/2 = 12^{\circ}.25$ so the length of the slit in the focal plane will be 2(FL) tan $(12^{\circ}.25)$ = 0.434(FL). The sensitive region of the photocathode for the EMR 541 type photomultiplier tube has a diameter of 25 mm. or about one inch. The focal length matched to this diameter would then be about 2.3 inches; this, in turn, gives a required f/number of approximately 1.15 for the two inch optical aperture.

For the EMR 543 type PMT, the photocathode diameter is 1.7 inches. The matched focal length is then about four inches and the required f/number increases to 2.0. At this latter value for the f/number, design of a lens to meet the blur spot requirements is well within the optical state-of-the-art.

2. Electronic Signal Processor

For a spin stabilized vehicle, the slit reticle is fixed with respect to the vehicle and the slit scanning motion is obtained as the vehicle rotates about its spin axis. The SCADS electronics for the spin stabilized vehicle must include a photomultiplier, a signal filter, a threshold level detector, and power supplies along with their associated voltage regulation circuits. Also, digital circuits are required for data transmission and control. The basic electronic functions which the electronics must perform may be stated as follows:

(a) filter the star signals from the photomultiplier output,

(b) digitally encode the slit transit time of each star whose intensity exceeds the threshold level using as a time base a binary digital clock,

(c) provide overload protection for the photomultiplier.

The basic electronic block diagram required to provide the above electronic functions is shown in Figure 70.

In order to achieve the required system accuracy, it is necessary to design the analog electronics with special care. Since the uniform movement of the slit past a symmetrical cross section of the star image blur spot causes a symmetrical input signal (assuming it is noise-free), the analog electronics must filter and process the signal so that no significant transit time errors are introduced by threshold crossings of an asymmetrical signal. Consequently, the combined signal asymmetry caused by any electronic energy storage elements and the low pass filter must cause negligible errors in the transit time.

The analog electronics are shown in Figure 70 where two capacitive elements are shown in addition to the low pass filter. One element results from stray capacity, C_s, at the output of the photomultiplier tube.

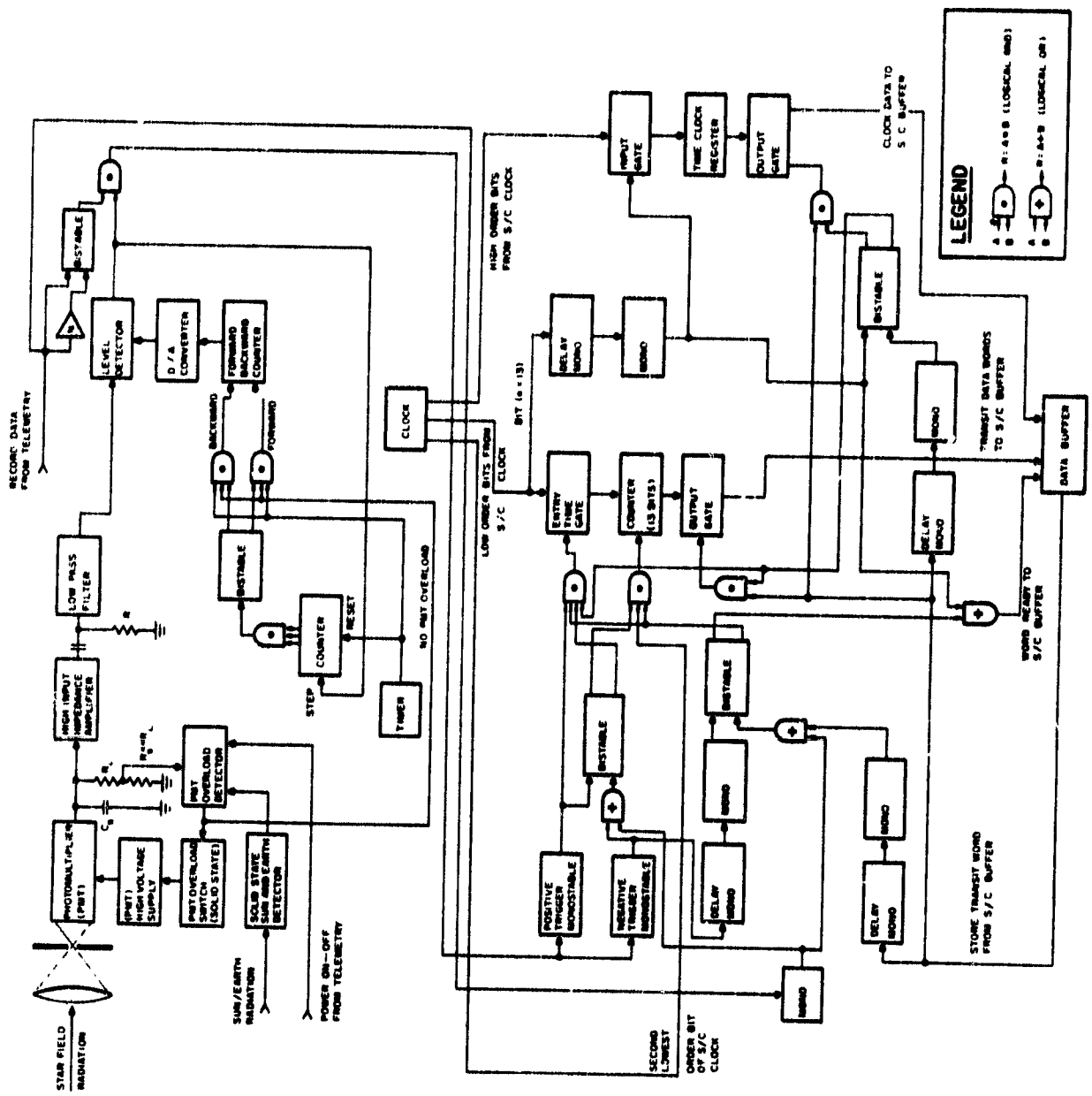


Figure 70: SCADS electronics block diagram

A realistic approximate value for the stray capacitance is 20×10^{-12} farads. The second capacitive element is necessary to remove (filter) the slowly varying (almost DC) background signal from the total signal, which includes the star signals. The slow variation in the background level is caused by the continuous scanning of portions of the celestial sphere having different background intensities. For example, the Milky Way background intensity is greater than for areas outside the Milky Way.

The PMT anode terminal is a very high impedance current source shunted by the stray capacity C_s. It is convenient to convert the current signal to a voltage signal by connecting a load resistor, R_L, to the anode terminal. The maximum value of the load resistor for a given input signal duration is limited by the stray capacitance and the degree of signal symmetry required to achieve system accuracy. A quantitative assessment of the maximum value for R_L can be obtained. The transfer function for the current to voltage conversion is given by

$$\frac{V_{1(s)}}{I_{(s)}} = \frac{1}{C_s\left(S + \frac{1}{R_L C_s}\right)} \tag{123}$$

and the impulse response is given by

$$h(t) - \frac{1}{C_s} \; e^{-\frac{t}{R_L C_S}} \tag{124}$$

Now, if $f(t) = .8 \sin^{-2} At$, $0 \leq t \leq \tau/A$

$= 0$, elsewhere

$$A = \frac{2.5248 \times 10^4}{\widehat{SW} \; T} \tag{125}$$

Then for $0 \leq t \leq \pi/A$,

$$v_1(t) = \int_0^t f(\tau)\, h(t-\tau)\, d\tau$$

$$= .4 \left\{ e^{-\frac{t}{R_L C_s}} R_L \left(e^{\frac{t}{R_L C_s}} - 1\right) - \frac{\cos 2At}{\frac{1}{R_L} + 4A^2 R_L C_s} - \frac{2A \sin 2At}{C_s \frac{1}{R_L^2 C_s^2} + 4A^2} \right.$$

$$\left. + \frac{e^{-\frac{t}{R_L C_\varepsilon}}}{\frac{1}{R_L} + R_L C_s^2\, 4A^2} \right\} \qquad (126)$$

For $t \geq \pi/A$

$$v_1(t) = \frac{.8}{2} \left\{ e^{\frac{-t}{R_L C_s}} R_L \; e^{\frac{\pi}{AR_L C_s}} - 1 - \frac{e^{-\frac{t}{R_L C_S}} e^{\frac{\pi}{AR_L C_s}}}{\frac{1}{R_L} + 4A^2 R_L C_s} \right.$$

$$\left. + \frac{e^{-\frac{t}{R_L C_s}}}{\frac{1}{R_L} + R_L C_s{}^2 4A^2} \right\} \qquad (127)$$

If R_L is made sufficiently small, then $v_1(t) = .8R_1/2\ (1-\cos 2At)$ + negligible error terms. By numerical evaluation of the above equations for $\widehat{SW}$ = 12 arc-minutes and T = 1 second, it was determined that transit time errors due to asymmetry are less than 10 arc-seconds if

$$R_L C_s \leq \frac{T_s}{10} = \frac{1}{10} \frac{\widehat{SW}\ T}{2.16 \times 10^4} \quad . \tag{128}$$

In Figure 71 waveforms illustrate why removal of the slowly varying background is desirable. The top waveform shows how the filter output waveform would appear if the slowly varying background level is not removed. The bottom waveform shows the filter output waveform if the slowly varying background level is removed. Setting the threshold level for the top waveform having unfiltered background can result in missed star transit pulses; this, in turn, can result in the failure to compute the attitude.

Removal of the slowly varying background level can be accomplished with a simple RC high pass filter as shown in Figure 70. However, it is important that the RC time constant be sufficiently large so that the signal asymmetry introduced is negligible. Analysis similar to that used to determine the limit for the product of $R_L C_s$ can be used to determine the restriction on the product of RC. For the simple RC high pass filter, the transfer function is given by

$$\frac{V_2(s)}{V(s)} = \frac{sT}{1 + sT} \tag{129}$$

where the time constant is $T = RC$. Hence the impulse response for the simple high pass RC filter is given by

$$h(t) = \delta(t) - \frac{1}{T} e^{-t/T} \quad . \tag{130}$$

Now if the input signal is f(t) as before, then from the convolution integral, the output signal is given by

$$v_2(t) = f(t) + \text{error terms} \quad . \tag{131}$$

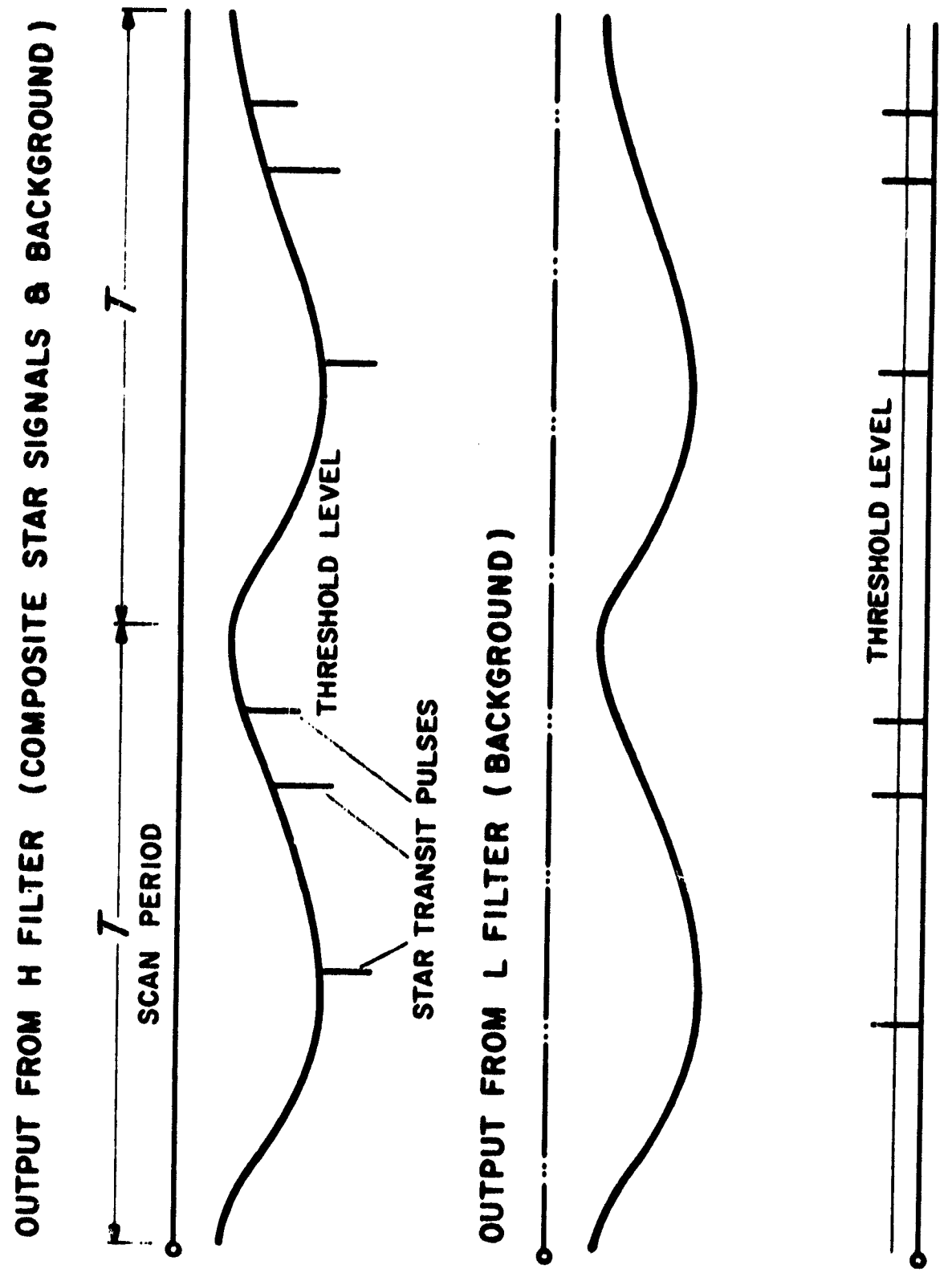


Figure 71: Waveforms illustrating background filtering

For $0 \leq t \leq \pi/A$,

$$v_2(t) = .8 \sin^2 At - .4(1 - e^{-t/T}) + \frac{.4}{T\,\frac{1}{T^2} + 4A^2}\left\{\frac{\cos 2At}{T} + 2A \sin 2At\right\}$$

$$- \frac{\frac{1}{T^2}\, e^{-t/T}}{\frac{1}{T^2} + 4A^2} \quad . \qquad (132)$$

For $t \geq \pi/A$,

$$v_2(t) = - .4\, e^{-t/T}\,(e^{\pi/AT} - 1) + \frac{.4\, e^{-t/T}\, e^{\pi/AT}}{[1 + 4(AT)^2]} - \frac{.4\, e^{-t/T}}{[1 + 4(AT)^2]} . \qquad (133)$$

Note as T becomes large, the error terms tend to zero. By numerical evaluation of the above equations for $\widehat{SW}$ = 12 arc-minutes and T = 1 second, it was determined that transit time errors less than 5 arc-seconds are introduced by pulse asymmetry for threshold settings which range through four magnitudes if $T = RC \leq 500\ T_s$. Figure 72 shows a plot of $v_2(t)$ for $RC = 500\ T_s$.

As described in Section IIIB, the low pass filter transfer function must have a linear phase shift characteristic in order for the filter impulse response to be symmetrical. With a symmetrical impulse response, the filter output signal will be symmetrical if the input signal is symmetrical. A filter with the ideal linear phase shift characteristic is not physically realizable; however, this characteristic can be approximated as close as desired. Section IIIB described a two pole linear phase shift filter. However, as seen in Figure 65 , the impulse response for a two pole filter

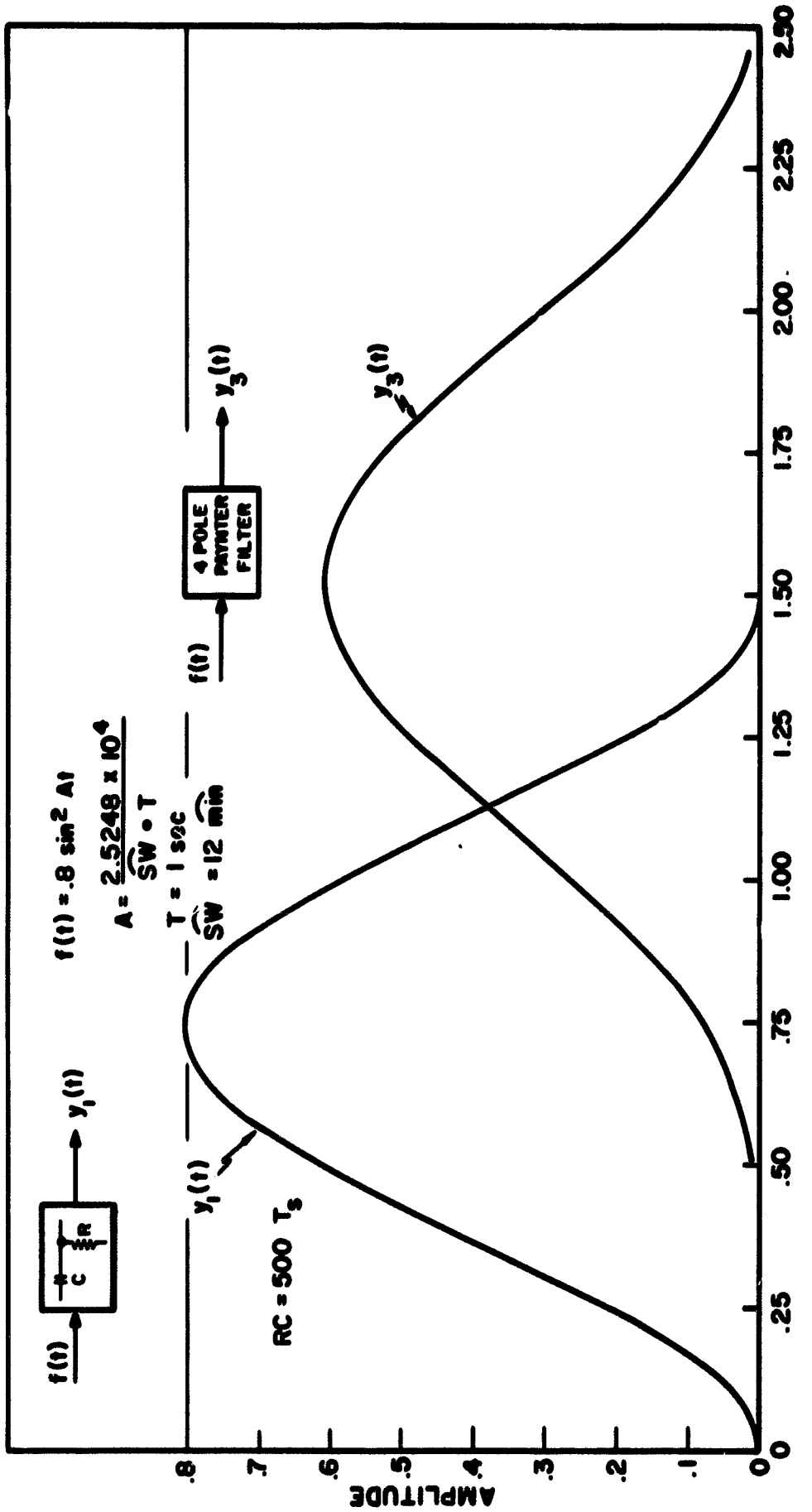


Figure 72: Output signals from the simple high pass RC filter and the four-pole low-pass filter

is not highly symmetrical. A closer approximation to the ideal linear phase shift filter is given by the four pole transfer function [15]

$$H(s) = \frac{1}{\left[2.42\left(\frac{s}{\omega_c}\right)^2 + 2.62\ \frac{s}{\omega_c} + 1\right]\left[.734\left(\frac{s}{\omega_c}\right)^2 + .49\ \frac{s}{\omega_c} + 1\right]} \quad (134)$$

Analysis similar to that performed for the two pole case in Section IIIC shows that the filter is matched to the input signal

$$f(t) = .8 \sin^2 At \text{ for } 0 \leq t \leq \pi/a \quad (135)$$

$$= 0 \quad \text{elsewhere}$$

when

$$\omega_c = \frac{4.8323 \times 10^4}{\widehat{SW} \cdot T} . \quad (136)$$

With the value of ω_c given for $\widehat{SW}$ = 12 arc-minutes and T = 1 second, the filter output signal $y_3(t)$, is shown in Figure 72. The output signal (noise-free $y_3(t)$) is symmetrical to within 30 arc-seconds for threshold settings which vary by 3.6 magnitudes.

It should be noted here that although the optical aperture was determined assuming a two pole filter transfer function, almost identical apertures would have been obtained if the above four pole transfer function had been assumed. Consequently, the analysis leading to the determination of the optical aperture using a two pole transfer function is not invalidated if a four pole filter is implemented to improve pulse symmetry.

After the star pulse has been filtered, the star transit time must be

encoded by the digital logic circuits. The filtered star pulse drives one of the two inputs of a level detector. The other level detector input is driven by a voltage level supplied by a D/A converter which determines the detection threshold. As the filtered star pulse rises above the threshold level, the level detector output switches rapidly from a "0" voltage level to a binary "1" voltage level. This instant of switching is referred to as the star entry time. Similarly, when the star pulse falls below the detection level, the level detector output rapidly switches from the "1" voltage level to the "0" voltage level. The latter instant of switching is referred to as the star exit time. The star transit time will be defined as the average of the star entry time and the star exit time. The primary purpose of the digital logic is to encode the transit time for each star whose signal amplitude crosses the threshold level.

If the on-board spacecraft electronics exclusive of the SCADS system does not include an accessible binary clock with sufficient stability and resolution for encoding of star transit time data, then the binary clock must be included within the SCADS electronics. Also, if the on-board spacecraft electronics exclusive of the SCADS system does not include an accessible data buffer, then a buffer memory must be supplied by the SCADS electronics. The memory size required for the storage of SCADS transit time data depends upon telemetry channel transmission data rate capacity available. However, since these rates are not specified for the purposes of this study, the memory size cannot be presently determined.

Assuming the availability of a spacecraft clock and buffer memory, a reasonable method of encoding the star transit time is presented in Figure 70. The method is briefly described below.

At the leading edge (star entry time) of the level detector output, the low order bits of the clock are gated into the transit time counter and register. Also at this time a clock signal is gated into the transit

time counter. This clock signal should be the second low order bit from the clock so that the transit time counter is stepped at one-half the rate of the clock's lowest order bit. This counting is continued until the trailing edge (star exit time) of the level detector output occurs at which time the counting is stopped. Counting at one-half the basic clock frequency has the effect of arithmetically averaging star entry and star exit times.

Immediately after the star exit time, a signal is sent to the buffer memory informing it that star transit data is available for storage. As soon as the buffer memory is ready to receive data, it sends a Store Data signal to the control logic which gates the contents of the transit time counter to the buffer memory. Immediately after the transit data has been stored in the buffer, the logic is reset to encode the next star transit. While a star transit word is awaiting storage in the buffer, the logic is inhibited from encoding and storing any star transits that occur during the wait interval.

The highest order, or n^{th}, bit from the clock that is gated into the transit time counter should have a period which is somewhat greater than the vehicle scan period to insure that two different star transits in a single scan period do not have similar transit times. To further avoid transit time ambiguity and also to allow determination of vehicle attitude as a function of spacecraft time (or spacecraft orbital position), the remaining upper order bits (above the n^{th}) of the clock should be stored in the buffer at the beginning of each period of the n^{th} bit. This is shown in Figure 70 for n = 13 where the n^{th} bit clear detector detects the beginning of a new period for the n^{th} bit. At this instant, the high order bits of the clock are stored in the time clock register. After a short delay, a ready signal is sent to the buffer memory to inform it that a word is ready for storage. When the buffer is ready, a store signal is received from the buffer which gates the time clock register contents into the buffer. Star

transit data is inhibited from being encoded while the upper order bits of the clock are being stored.

The number of stars scanned per spin period which are brighter than the limiting detectable magnitude varies over a very broad range, typically from about 4 to more than 40. Since detection of only four star per scan period is required for star identification and attitude determination, it is desirable to limit the number of transit detections to some intermediate number. This can be accomplished by automatically raising and lowering the detection threshold depending upon the number of starsdetected per period. The logic implementation shown in Figure 70 counts the number of star detections per scan period. If the number of detections per scan period is greater than eight, then another counter is stepped forward causing the D/A converter output to raise the threshold voltage at the level detector input. If the number of detections per scan period is less than four, then the counter is stepped backward which lowers the threshold voltage to the level detector. A preset timer having the same approximate time period as the scan period will reset the star transit counter.

It is required that the photomultiplier high voltage power supply be capable of turning OFF and ON within a small fraction of the scan period in order to prevent the formation of high current densities within the tube when bright radiation sources are scanned. The EMR photomultipliers can be purchased from the manufacturer with an integrated high voltage power supply wrapped around the tube envelope. However, the design of this supply does not permit sufficiently rapid turn ON and turn OFF capability, especially for relatively short scan periods. Consequently, it is necessary to consider a specially designed high voltage supply which is capable of switching OFF and ON in tens of milliseconds.

A block diagram for a high voltage power supply design which permits fast switching is shown in Figure 73. The input voltage to a DC-AC inverter

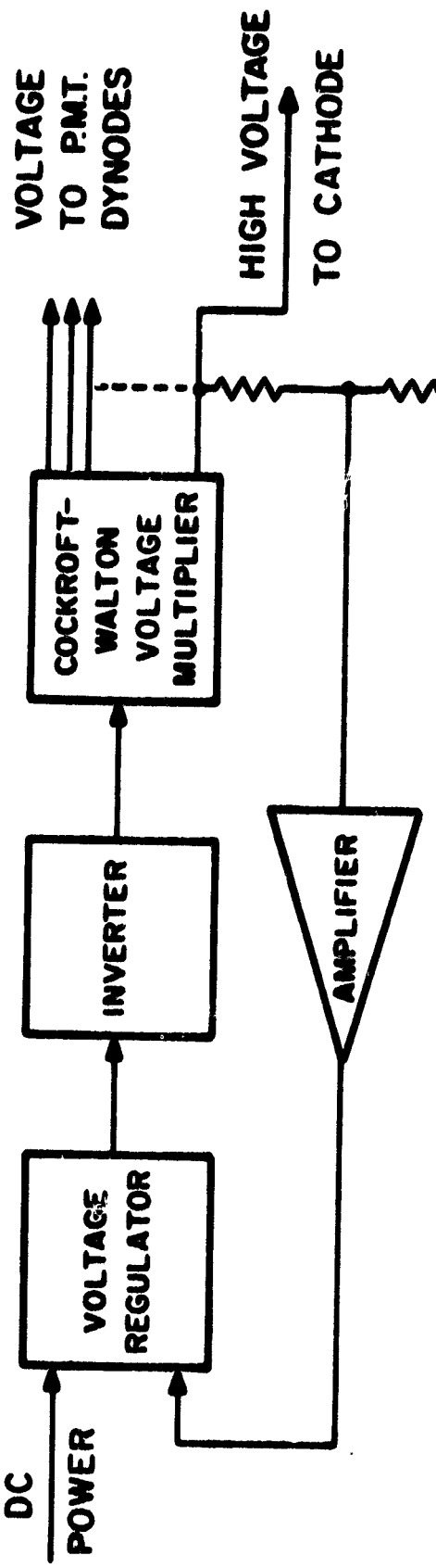


Figure 73: Block diagram for high voltage power supply.

is regulated up or down inversely proportional to the voltage change at the high voltage output from the Cockroft-Walton voltage multiplier. A high gain feedback loop senses changes in the output voltage and causes the voltage regulator to provide correcting input voltage changes to the inverter. The following paragraphs discuss voltage multiplication and the achievable charging and decay time of the output voltage.

A common method of producing low current high voltage DC power from low voltage AC sources is the voltage doubler shown in Figure 74. One-half of the AC cycle is used to charge capacitor C_1 to the peak of the input and this capacitor charge in series with the other half cycle charges C_2 to twice the input peak voltage. This principle can be extended indefinitely at least theoretically to provide a very high voltage which is conveniently divided into equal steps. While this multi-step multiplier was originally developed for powering charged particle accelerators with requirements in the megavolt range; with the proper input voltage, it has voltage and current capabilities closely matching photomultiplier requirements. In Figure 74 it would be a simple matter to add a half wave rectifier to provide the missing first step E_p, but then difficulty ensues when an arrangement for $3E_p$ is wanted. A system for tripling is shown in Figure 75. It is the same as Figure 74 with an added capacitor and diode and a different ground reference point. From the characteristics of these two circuits it is easy to deduce that a single multiplier will only produce odd or even multiples of the transformer voltage but not both. Of course, the transformer secondary could be designed for half the required voltage step, but this does not produce the lowest possible supply output impedance, especially for the first two stages which ideally could be positive and negative half wave rectifiers. Multiple transformer windings produce unequal loading effects which are not desirable with high frequency saturable core inverters.

It would be possible to connect both of these networks, mutually extended to provide 14 voltage steps, to a single transformer for a

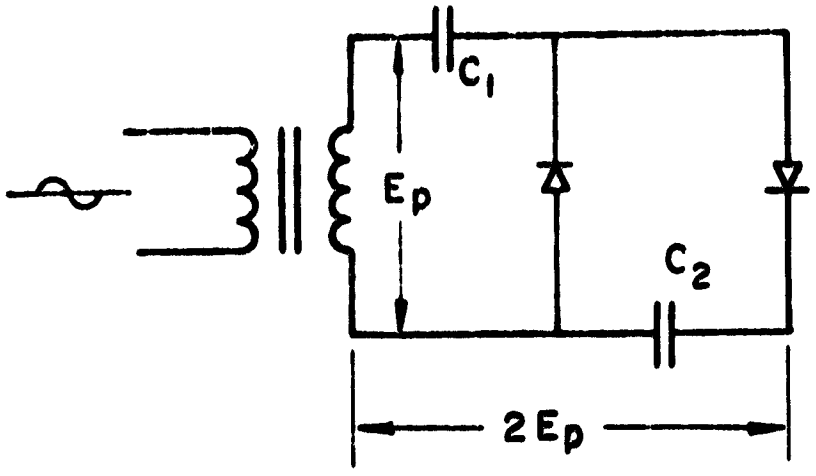


Figure 74: Voltage Doubler Circuit

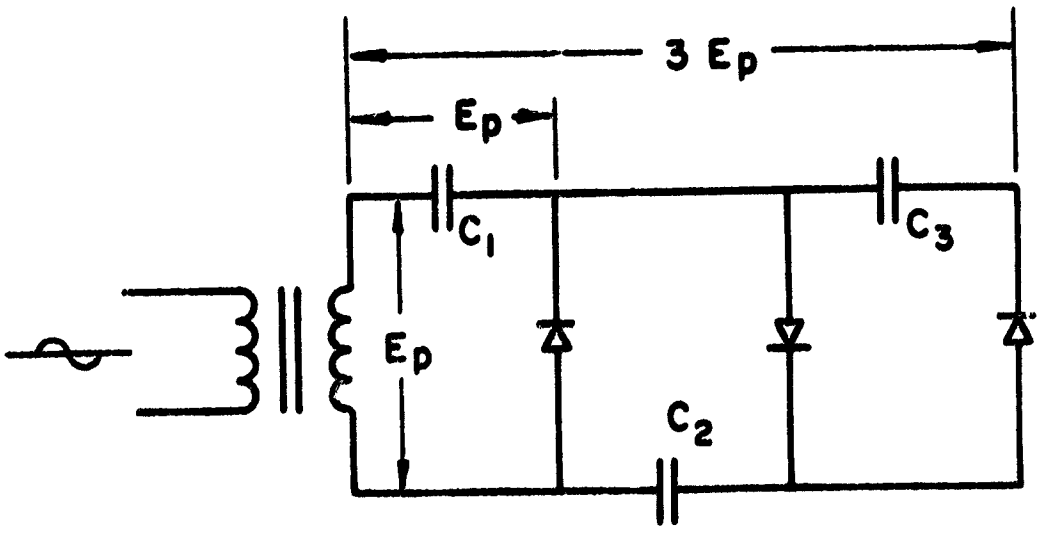


Figure 75: Voltage Tripler Circuit

photomultiplier tube power supply. A reduction in capacitor voltage requirement and thus size is achieved by an interlacing or series connection of the capacitor strings as shown in Figure 76. While the schematics in Figures 74 and 75 are for positive output, the one in Figure 76 is reversed to show the actual negative output required for grounded photomultiplier output operation. A positive half wave rectifier is added to the lower end of the multiplier with the output grounded to provide two low impedance stages.

In a saturable transformer inverter, leakage reactance spikes of various amplitudes can exist depending on loading. With this multiplier where separate sections supply even and odd dynodes, it is possible for a spike on one set to contribute enough voltage to seriously upset interdynode voltages under very light load conditions. It is thus necessary to load both sections to insure the voltage is determined by actual square wave amplitude. A voltage sensing divider across the supply for feedback regulator control will only load one section, and it is most economical to connect a load between the next highest even and odd voltages to load the other section.

For a given load and ripple tolerance, supply frequency and capacitor size can be chosen. For a photomultiplier in a scanning system which must be turned OFF during Sun, Earth, or Moon scan, charge and discharge times are also important. Discharge time is simply related to load and capacitor size by the equivalent exponential RC time constant. Charging time is more difficult to determine but has been obtained for a 14 stage multiplier (Figure 77) by computer simulation. For each half cycle it is possible to write equations at each stage for the voltage on each capacitor as a function of the voltage on the two capacitors at the end of the previous half cycle. The overall multiplication factor as a function of elapsed cycles is shown in Figure 78. With a 50 kilocycle input square wave, the charging times are as follows:

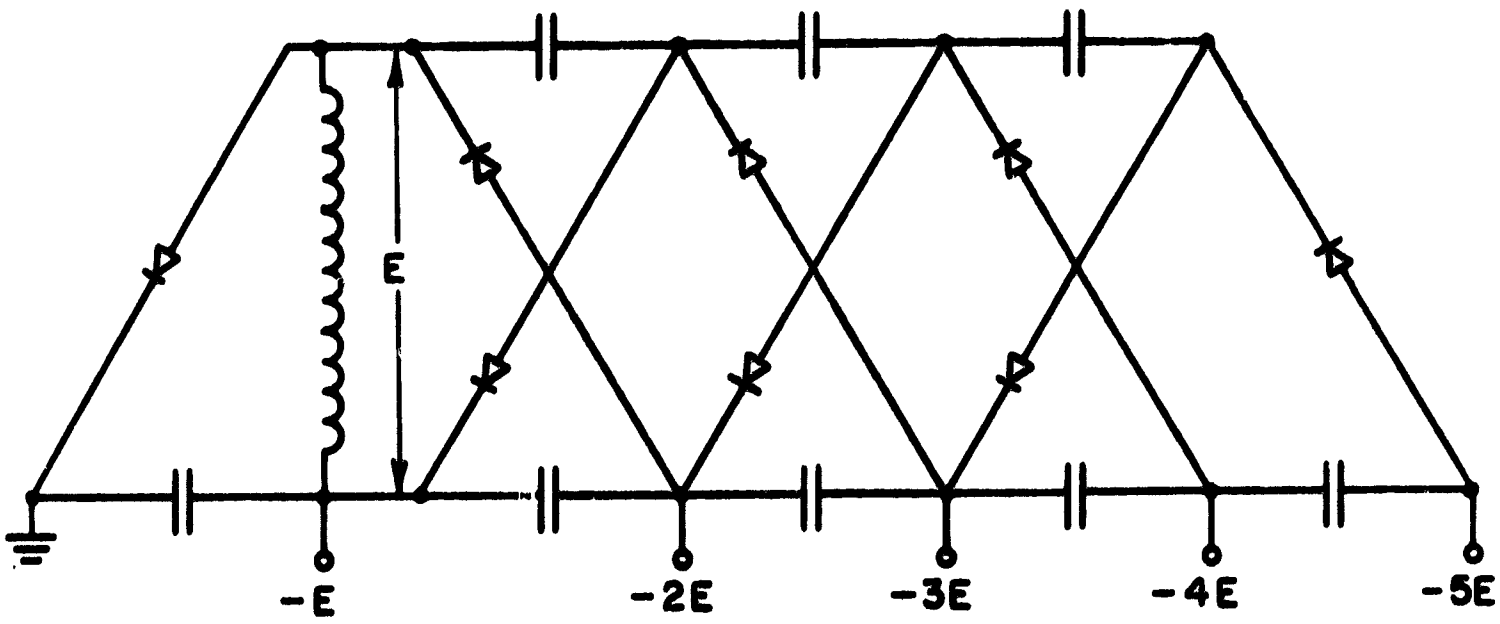


Figure 76: Interlaced dual even-odd multiplier

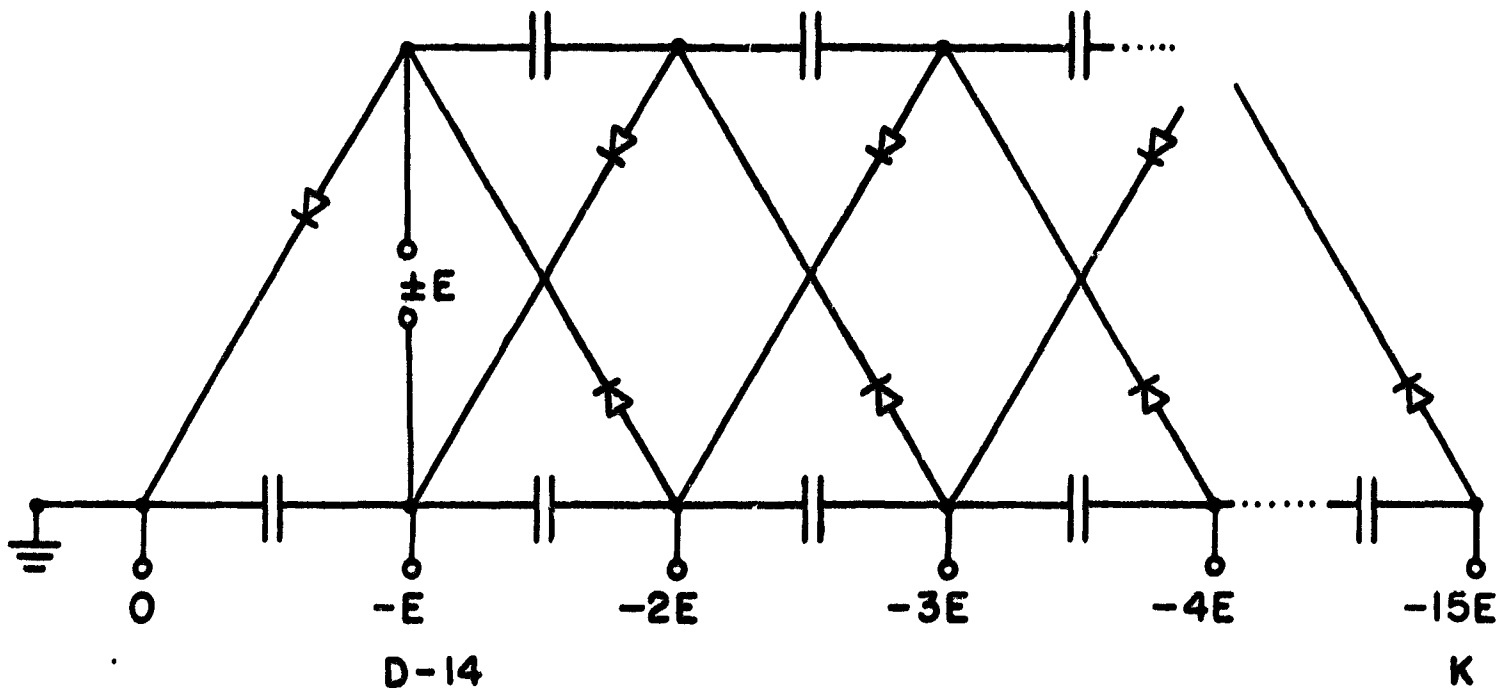


Figure 77: Cockroft-Walton multiplier for EMR 14 stage photomultiplier tube.

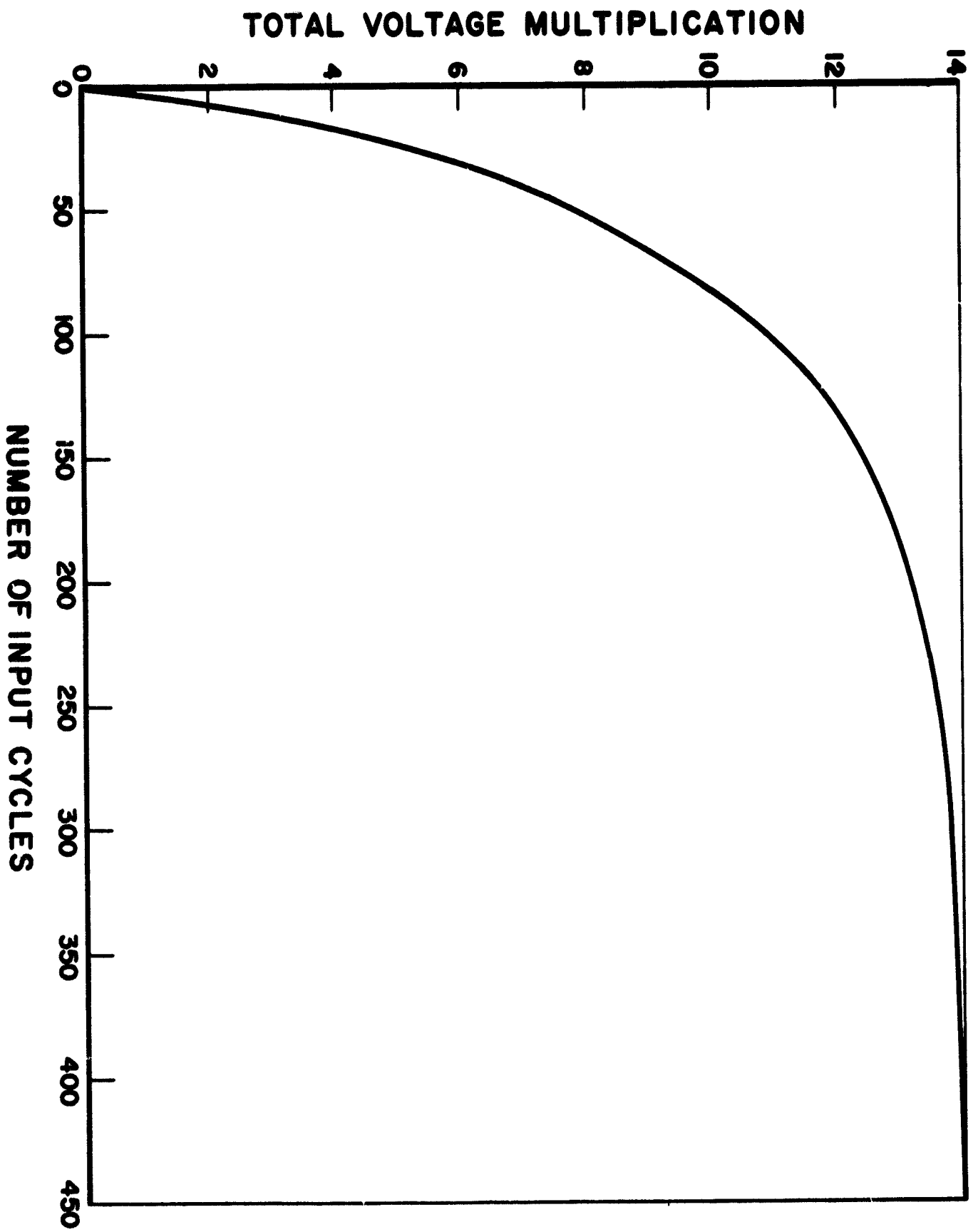


Figure 78: Charging time of a 14 stage Cockroft-Walton multiplier

99 percent full output requires 6.61 milliseconds,

99.9 percent full output requires 10.2 milliseconds.

B. Three Axis Controlled Mode

In the three-axis controlled mode, the spacecraft Z axis is directed toward the earth and the vehicle rotates slowly about its Y or pitch axis as the orbit is traversed. The rate of this rotation is approximately 15 degrees per hour so that the spacecraft orientation is very nearly fixed in celestial space over short time intervals. As a consequence, a suitable natural scan is not provided by the vehicle motion; the SCADS scan capability must therefore be supplied as an integral portion of the instrument. New design considerations are therefore implied for the operation of SCADS in the three axis mode; these requirements are described in the subsections which follow.

1. Optical Sensor Head

Since the vehicle provides essentially no scan motion, the star field available to SCADS is identical with the optical field of view. However, not even this full field is available; a region of central blocking must be provided to assist the star identification procedure and assure adequate precision for the transit azimuth measurements. The size of the optical field of view, Θ, becomes the dominant factor in this mode. To insure adequate target availability, Θ should be large (see Figure 15). However, the practical problems of designing and making an objective lens with both a very wide field of view and a small blur spot size over this entire field are severe. Forty degrees is close to the limit of the optical state-of-the-art; for angles beyond this, image quality deteriorates rapidly near the edge of the field and the blur spot can no longer be matched to the required slit width. Thus, $\Theta = 40^{\circ}$ is chosen here.

For this field, the central blocking is chosen as 10°. Thus, the slit is 15° long and the annular scan pattern has $\theta_i = 5^{\circ}$ and $\theta_e = 20^{\circ}$. Although the central blocking represents a cone of fairly large angle--sufficient to allow accurate transit measurements--it subtracts relatively little from the area of the celestial sphere available to the scan. The effective

field of view for this configuration is $\Theta_{eff} = 38.^{\circ}7$.

From the star availability results presented in Section IIB4, it is found that $M_{\ell} = 4.21$ is the system limiting magnitude required for this configuration. Since a relatively high accuracy ($0.^{\circ}01$ error in each axis) is required for the three axis mode, it is advantageous to reduce the slit width over that used in the spin mode. This is possible for a SCADS sensor which is required to operate only in the three axis controlled mode because the designer may choose the scan period--it is not fixed by the vehicle motion. For this sensor, a rotational slit width $\widetilde{SW}$ of six arc minutes is selected. From Section III, the scan period for the three axis or driven mode is taken as ten seconds.

The optical aperture implied by these parameters is found from the equations developed in Section IIIB4 to be a = 0.6 inches. Closer examination of the results, however, reveals that a limiting magnitude star would produce only 25 photoevents at this small aperture. Such a small number of discrete events in the signal invalidates the statistical smoothing used in the analysis and detection becomes very uncertain. Thus, an aperture a=1 inch is chosen; the detection probability at $M_{\ell} = 4.21$ is then found to be 0.96. The parameters for this design are summarized in Table III.

TABLE III

PARAMETERS FOR RECOMMENDED THREE AXIS CONTROLLED MODE SENSOR CONFIGURATION

Effective field of view:	$\Theta_{eff} = 38.^{\circ}7$
Optical field of view:	$\Theta = 40^{\circ}$
Central blocking:	$2\theta_i = 10^{\circ}$
Rotational slit width:	$\widetilde{SW}$ = 6 arc minutes
Scan period:	T = 10 seconds
Optical aperture:	a = 1.0 inches
Limiting stellar magnitude:	$M_{\ell} = 4.21$

For a three-axis controlled vehicle, the scanning motion must be electromechanically supplied by a synchronous motor which rotates the slit reticle. In order to eliminate the need for a gear drive mechanism, it is recommended that the synchronous motor be a Scanning Angle Sequential Incrementer (SASI) motor which consists of a rotating disk that carries the reticle slit and is supported by a jeweled bearing assembly. The disk rotates at a constant RPM in synchronism with the clock pulses used for encoding star transit times. Motor drive circuits provide a properly timed sequence of pulses to the motor mechanism. The motor torque is generated by magnetic field forces between teeth positioned on the disk periphery and stationary electromagnets positioned adjacent to the disk teeth.

An exploded schematic view of the motor is shown in Figure 79 . The rotor disk shaft ends contain sapphire jewel bearings for low friction and no metal-to-metal contact. Adjustable conical pivots in bushings bonded to the optical glass wibs in the top and bottom plates support the rotor. The stator assembly contains 32 (2^5) electromagnetic poles with a specific placement that will be discussed later. A flange on the rotor fits into the gap of the stator poles to complete the magnetic circuit. This rotor flange contains 256 (2^8) narrow, equally spaced slots which provide discrete poles with a width approximately equal to that of the stator poles.

The poles are positioned around the stator and energized in a sequence such that each successive pulse rotates the rotor 1/32 of a rotor tooth width. Thus it requires each of the 32 stator poles to be energized once for the rotor to advance one tooth, and since there are 256 rotor teeth, a total of 8,192 (2^{13}) pulses are required for one revolution, or a rotation of 2.637 arc minutes from each pulse. The sequence of pulsing is back and forth across the stator which minimizes the effects of machining tolerances. The "wrap-around" design of the individual stator poles also is beneficial since it maintains a constant total air gap in spite of rotor eccentricity

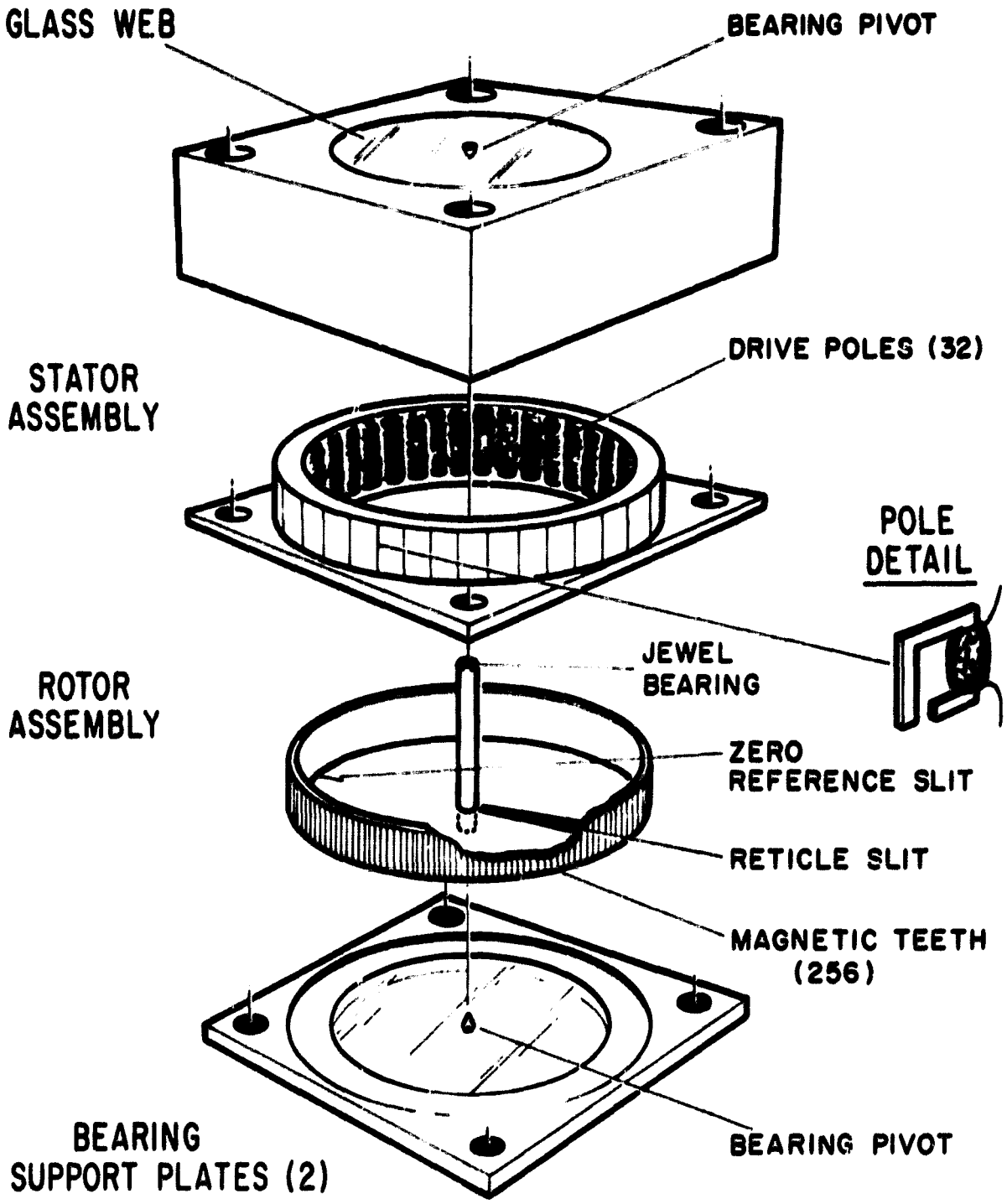


Figure 79: Exploded view of the Scanning Angle Sequential Incrementer (SASI) motor.

The only power required from the motor is the small amount to overcome the jewel bearing friction. The relatively large inertia of the rotor will sustain the rotation with only a small amount of speed variation or cogging between pulses.

2. Electronic Signal Processor

The SCADS electronics for the three-axis controlled application must include motor drive circuits in addition to the electronics required for the spin stabilized mode (see Figure 70).

The logic required to drive the SASI motor is relatively simple as shown in Figure 80. The basic clock resolution interval is first divided into 32 time intervals. The subdivided clock frequency is then used to drive sequencing logic which sequentially provides drive pulses to each of the 32 magnet poles. The sequencing logic consists of a five stage binary counter and a decoding matrix whose 32 outputs each drive one pole winding.

In order to orient the position of the slit with respect to the vehicle axis it is necessary to provide a zero reference indication. When the zero reference signal occurs for each revolution, the contents of the clock must be stored in the buffer memory as part of the SCADS data.

The zero reference signal is generated by the passage of the zero reference slit in the reticle, which may be narrower than the star detection slit. A solid state gallium arsenide light source is located above the reticle disk, and a solid state silicon diode detector is located in the base plate. Both these units consume low power and are extremely reliable. In addition, the GaAs source emits a very narrow bandwidth of light in the infrared region that cannot be detected by the photomultiplier; it might otherwise produce spurious pulses. The detector output is fed to a low gain amplifier and then to a Schmitt trigger circuit to shape the signal.

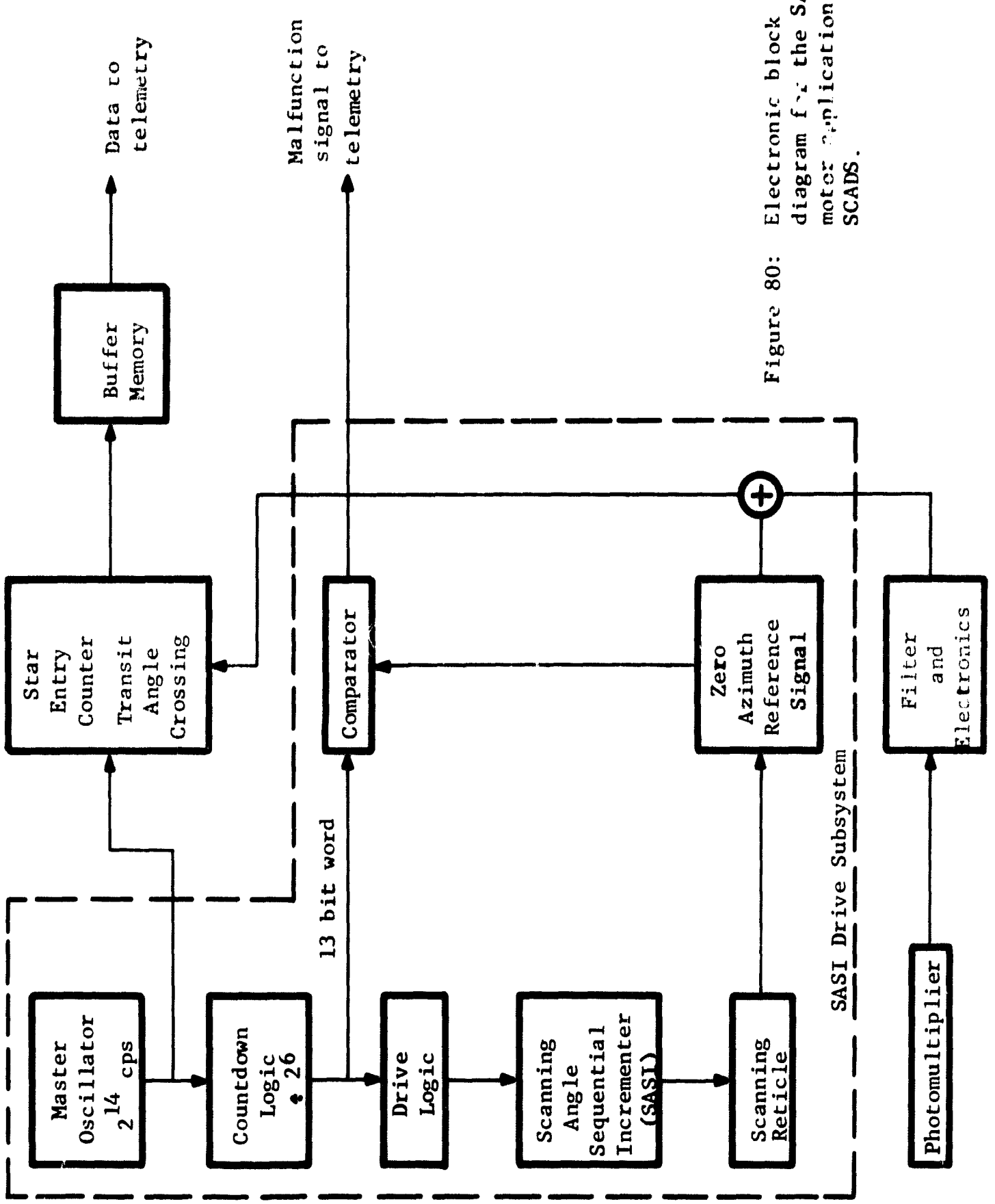


Figure 80: Electronic block diagram for the SASI motor application to SCADS.

Finally, the Schmitt trigger output is used to gate the clock output into the buffer, an operation analogous to the encoding of star transit data.

C. Dual Mode

The dual mode SCADS sensor must operate during both the spin stabilized and three axis controlled portions of the ATS F&G missions with emphasis on reliability in the spinning mode. Thus, this twin-purpose sensor must meet both the bright source constraints imposed during spin stabilized operation and the optical field of view requirements of three axis controlled operation.

1. Optical Sensor Head

The geometry of the key SCADS angles for the dual mode sensor is shown above in Figure 54. The instantaneous field of view is just the slit length θ_{slit}. If the entire optical system were canted away from the scan (negative spin) axis and the slit were positioned in the resultant scan axis-optical axis plane, then an annulus with $\theta_{1\ spinning} = \Gamma + \Theta/2 - \theta_{slit}$ and $\theta_{e\ spinning} = \Gamma + \Theta/2$ would be swept out due to the spin of the vehicle. This would increase the effective field of view for the spinning mode over that for the case in which the optical and scan axes coincide. However, from Figure 55 in Section IIIA3 it is seen that the increase in $(\Theta_{eff})_{spinning}$ with increasing Γ is rather slow.

An increase in Γ also brings the optical axis of the wide field Θ somewhat closer to the bright sources over a portion of the spinning scan; the shielding problem is made more difficult. From Figure 56 it is seen that the normalized shield dimensions grow rather rapidly. For example, an increase in Γ from 0° to 18° increases $(\Theta_{eff})_{spinning}$ only from $38.^\circ7$ to 60° while d/a increases from 4.0 to 7.4 and h/a increases from 2.3 to 6.2. Thus it appears that canting of the optical axis of the dual mode sensor away from the negative spin axis is not advantageous; $\Gamma = 0^\circ$ is recommended.

It may be observed at this point that the cant angle $\Gamma = 0^\circ$, which is imposed by performance requirements in the spinning mode, will place the

nominal scan axis in the equatorial plane during three axis controlled mode operation. As a consequence, the sun will sweep very close to or through the optical field of view on each synchronous orbit. However, the bright object shielding needed for the spin mode will permit the angle between the (actual) scan axis and the sun line to be at least as small as $56.^{\circ}6$ before solar interference forces shut-down of SCADS. Therefore, SCADS should be operable (in the presence of the sun) over at least 68% of each synchronous orbit. Since SCADS is to be used in the three axis mode to evaluate the control system and to provide reference attitude data to calibrate other sensors aboard the spacecraft, continuous operation is not required. The limitation imposed here by the sun, then, appears to be acceptable for the dual mode sensor concept.

The optical field of view Θ is again determined primarily by the practical limitations of lens design and fabrication. Although results are given above in Figures 55 and 56 for parametric Θ values of 40°, 45°, and 50°, the expected improvement in limiting magnitude in going from 40° to 50° is quite small (see Figures 15 and 53). Thus, the optical complications of going to the wider fields are not justified by the modest increase in target availability. An optical field of view $\Theta = 40^{\circ}$ is selected as before. The choice of 10° of central blocking is also repeated.

The star availability results for the dual mode sensor with this configuration ($\theta_i = 5^{\circ}$, $\theta_e = 20^{\circ}$) are presented in Section IIIB3. From Figure 41 of that section it is seen that the system limiting magnitude required to insure the presence of four detectable stars in the spinning mode is $M_{\ell} = 4.65$. A rotational slit width $\widetilde{SW} = 12$ arc-minutes is selected as with the previous sensor design to operate only in the spinning mode. Also, the scan period is again fixed at T = 1 second by the spin motion.

The optical aperture implied by these parameters is then found to be a = 2.7 inches. The recommended dual mode sensor design is then summarized

in Table IV . The shield dimensions listed here are obtained from the normalized shield data given in Figure 56 and the specific value for the optical aperture.

Note that with the exception of the selection of the optical field Θ, the design of this dual mode sensor is determined primarily by the requirements for reliable operation in the spin stabilized application. In particular, the rotational slit width $\widehat{SW}$ was chosen to meet the target detection problem in the spin mode rather than the accuracy problem in the three axis controlled mode. The error problem introduced by the comparatively wide slit is partially compensated by the selection of T_{driven} = 10 seconds

TABLE IV

PARAMETERS FOR THE RECOMMENDED DUAL MODE SENSOR CONFIGURATION

Effective field of view:	$\Theta_{eff} = 38.^{\circ}7$
Optical field of view:	$\Theta = 40^{\circ}$
Cant angle:	$\Gamma = 0^{\circ}$
Central blocking:	$2\theta_i = 10^{\circ}$
Shield angle:	$\xi = 56.^{\circ}6$
Rotational slit width:	$\widehat{SW}$ = 12 arc minutes
Scan period:	T_{spin} = 1 second T_{driven} = 10 seconds
Optical aperture:	a = 2.7 inches
Shield height:	h = 6.2 inches
Shield diameter:	d = 10.7 inches
Limiting stellar magnitude:	$M_{\ell} = 4.65$

for the scan period in the three axis mode. Lengthening the scan period has two effects which tend to improve the accuracy. First, the signal at the filter output for any given star transit is stronger for the slower scan while the background remains essentially constant--i.e., the slit is always open to the sky whether the scan is rapid or slow. Thus the signal-to-noise ratio for the star pulse becomes larger and the threshold crossing points become relatively less noise sensitive; star entry and exit points are determined with less uncertainty. Second, the slower scan allows more stars to be detected which in turn provides greater overdetermination in the set of constraint equations from which attitude is determined. Since these equations are solved with a least squares approach, additional redundancy in the data will reduce the RMS errors. Further, if a sufficient number of measurements is available, those few entries which contribute large residuals in the least squares solution can simply be discarded. It will be seen from the detailed error analysis below that the required three-axis mode accuracy can be achieved with a 12 arc minute slit width if these added factors are taken into account.

2. Electronic Signal Processor

The electronics for the dual mode sensor is almost identical to the electronics required for the three-axis controlled mode sensor (see Figures 70 and 80) with the exception of some additional control circuits. During the transfer orbit the ATS vehicle is spin stabilized until it is injected into the Earth synchronous orbit after which the vehicle stabilization is three axis controlled. During the spin stabilized mode, the slit is fixed with respect to the vehicle and the scanning motion is obtained as the vehicle rotates about its spin axis. After injection into the synchronous orbit and the vehicle is three axis controlled, the reticle must be rotated by a synchronous motor. To achieve this dual operation mode with a single sensor, the synchronous motor and slit reticle must be initially latched into a fixed position in such a manner that both may be automatically unlatched by telemetry command after the vehicle is injected

into the synchronous orbit. So in addition to the electronics required for the three-axis-controlled mode sensor, control circuits must be provided to unlatch the slit reticle and to actuate the motor drive circuits after three-axis-controlled vehicle stabilization has begun.

The latch mechanism could be a simple mechanical stop which holds the slit reticle and motor drive shaft in a precisely known position and which can be released by actuation of a solenoid. After its release by the solenoid, the stop should mechanically latch itself in the non-stopped position so that power dissipation in the solenoid is not required to maintain the non-stopped position. The latch release mechanism is required to operate only once, hence it should prove to be reliable.

Note finally that two filters corresponding to the two recommended scan periods should be provided. Proper filter matching is required if the potential benefits of the longer scan period in the three-axis mode are to be fully realized.

D. Spinning Mode; Possible Modifications of the ATS-C Design

A SCADS-type system has been built and is currently in orbit aboard the ATS-3 spacecraft (formerly the ATS-C program). At this writing, the sensor has not yet been turned on so unfortunately no preliminary results are available. However, data received from this sensor should be of considerable assistance to arriving at a final detailed design for SCADS/ATS F&G. In this section, the possibility of directly modifying the ATS-C SCADS design for the present application is considered.

1. Optical Sensor Head

In order to assess the applicability of the SCADS/ATS-C design, its goals must be compared and contrasted with those of SCADS/ATS F&G. The SCADS-type equipment aboard ATS-3 is actually a composite instrument designed to serve as the first step toward a self-contained navigation system (SCNS). In addition to the sensor head for acquiring star transit pulses, the instrument package contains a set of three white spherical projectiles about the size of tennis balls and the means of ejecting them one at a time from the satellite. If a ball is released with a velocity which is small with respect to the spacecraft, then the ball and the spacecraft will traverse orbits which have only slightly different parameters. Thus, the ball will remain relatively close to the satellite and since it is coated with a white diffusely-reflecting material, the ball will be visible from the spacecraft due to the sun and earthlight it reflects. Each time it falls within the scanning field of the ATS-C SCADS-type sensor, it will be detected as though it were a star. By singling out the apparent motion of the ball against the background of fixed stars and by taking a sufficient number of measurements, a solution for the orbital motions of both the ball and the observing satellite in the earth's central force field can be found. Thus, navigational capability in addition to attitude determination is supplied.

For the work here, the important point is that the balls and their

associated ejection mechanisms occupy a significant and integral part of the instrument package. Thus, extensive structural redesign would be required if the sensor is to be used only for star transit detection. Further, the SCNS instrument is designed to be used only as an experiment and only under optimal viewing conditions. Since the system is to be operated only in the shadow of the earth, very minimal sun shielding has been supplied. Modification for the present application where operation is required in many different orientations and orbital positions would therefore require the development of a carefully designed bright object shield.

In the SCNS/ATS-C optical head itself, a three-slit reticle configuration is used (see Figure 57). Since it has been concluded that a single slit is appropriate for the systems under discussion here, the SCNS reticle is not deemed suitable. However, the objective lens in the ATS-C system might find use in the present application. This lens is a ruggedized and space-qualified version of the Super Farron which is purported to have a 30° field of view at approximately f/0.9 and an aperture of 3.5 inches. However, the image quality is found to deteriorate rather rapidly for off-axis angles greater than about $12^{\circ}.5$; the fully useful field is then closer to 25°. But this is just the field required for the recommended spin mode sensor described in Section IVA. Further, the lens can be stopped down from 3.5 inches to the suggested 2.0 inches (or slightly larger) with additional gain in the image quality. The principal drawback of this approach is the added weight from the unused portions of the lens. This is, however, offset considerably by the reduced cost and reliability from an item which is essentially off-the-shelf. Note finally that the spot diagrams in Figure 68 correspond to geometrical ray traces on the Super Farron.

2. Electronic Signal Processor

The on-board SCADS electronics for ATS-C performs only limited data

processing of the star transit signals. The ATS-C SCADS electronics provides no on-board data storage or binary clock. Star transit data is sent directly to a wide band telemetry link and transit times are encoded at the ground station. In addition to a level detector output, a redundant amplifier-filter combination is provided whose output is also transmitted via telemetry to the ground station. If the signals from this second signal channel are used for attitude determination both level detection and transit time encoding must be performed at the ground station. The ATS-C on-board electronics also provides the capability to control via telemetry the voltage (PMT gain) of the photomultiplier power supply and the analog signal gain.

Clearly, the SCADS ATS-C electronics are not adequate for direct application to ATS F&G since no on-board data processing is included. However, part of the ATS-C SCADS electronics could be modified for ATS F&G application. It would be possible to retain the ATS-C high voltage (photomultiplier) power supply and the associated gain control circuits. Similarly, the analog signal amplifiers/attenuators and the associated gain control circuits could be retained along with the level detector (signal comparator). It is recommended, however, that the ATS-C star signal filter be modified for application to SCADS/ATS F&G.

The present ATS-C filter consists of two identical cascaded stages with the transfer function for each stage having a second order Butterworth polynomial in the denominator. Hence, the signal filter for ATS-C has a transfer function

$$H(s) = \frac{1}{\left(\left(\frac{s}{\omega_c}\right)^2 + \frac{s}{\omega_c}\sqrt{2} + 1\right)^2} \qquad (137)$$

This filter transfer function does not approximate the linear phase versus frequency characteristic as discussed in Section IIIB; hence, it is recommended that the ATS-C filter transfer function be modified to a linear phase transfer function which is matched to the input signal. With a four pole linear phase transfer function, the filter output signal will have adequate symmetry as described in Section IIIB.

In summary, the nature and requirements of the SCADS applications for the ATS-C program and the ATS F&G program are sufficiently different so that separate designs are recommended. As stated above, however, the experience which will be gained from ATS-C should provide valuable insights for the detailed final design of SCADS/ATS F&G.

E. Sensor Volume, Weight, and Power Estimates

The sensor volume, weight, and power estimates are somewhat dependent upon the vehicle stabilization mode for which the SCADS instrument is required to determine attitude. If the SCADS instrument is required to determine attitude for a three axis controlled vehicle, a synchronous motor is required to rotate the slit reticle. This, of course, adds weight and requires more power than an equivalent sensor in which the slit motion is provided by the vehicle spin. However, the scan period can be increased in a three-axis-controlled mode sensor and the optical aperture can be reduced correspondingly. Since the weight of the objective lens is proportional to the aperture cubed, the added weight of the motor may be partly or completely compensated by a reduction in the lens size. The dual mode sensor which requires both a large aperture and the motor may be significantly larger and heavier than either of the single mode sensors.

The volume of the SCADS sensor can be approximately estimated from manufacturer's data sheets of components and by extrapolating from previous studies[1,2] relating to a SCADS-type sensor.

In the tables which follow the volume estimates have been based on the dimensions of individual components. For example, the volume of a lens system can be approximately determined from

$$V = \text{aperture area} \times \text{focal length}$$

$$= \frac{\pi}{4} a^2 (af) = \frac{\pi}{4} a^3 f \qquad (138)$$

where f is the f/number of the lens. A value f = 2.0 has been assumed here; reduction of f beyond this level while maintaining adequate blur spot quality will require a major investment in optical design time.

The EMR-543 photomultiplier is approximately 7 inches long and 2 inches

in diameter in its housing. For the remaining electronics it is assumed that the circuits require approximately 0.03 $(inch)^3$ per integrated circuit package including the printed circuit boards on which they are mounted. Since the bright object shield is external to the remainder of the SCADS sensor head, its volume is listed separately in the tables.

The weight estimates in the tables below have been based on individual component weights and weights of similar existing subassemblies. For example, the lens weights have been scaled from an existing lens assembly by multiplying its weight by the cube of the ratios of optical apertures. The reference lens used was a Canon lens[2] whose optical aperture is 2.1 inches and whose measured weight is 605 grams = 1.34 pounds. So the weight of a lens with optical aperture a inches can be estimated by

$$w = 1.34 \left(\frac{a}{2.1} \right)^3 \quad \text{pounds.} \tag{139}$$

The manufacturer lists the potted weight for the EMR-543 photomultiplier as 385 grams. The cathode particle shield is assumed to be aluminum whose density is 2.7 $grams/cm^3$. The weight of the electronics is estimated from the volume where the density is taken as 1/16 pound per $(inch)^3$. This latter figure is based on the weight of the CDC 449 computer whose volume is $4 \times 4 \times 4 = 64$ $(inch)^3$ and whose weight is four pounds.

The power consumption for the SCADS sensor has been estimated for both the spin stabilized mode and the three-axis controlled mode. The power estimate for the photomultiplier power supply was based on the design employed in the occultation photometer experiment successfully flown on the Gemini 10 flight.[18] The idle current (dynode load resistors disconnected) from 12 volts was measured as 7 milliamperes. This power was largely consumed by the tape wound core. With the dynode load resistors connected, the power consumption was approximately 300 milliwatts from a 12 volt supply. The digital circuits were assumed to be complementary "N"

and "P" channel MOS transistor gates whose power consumption per gate is 10^{-6} watt when switching at 1000 cycles per second.

1. Spinning Mode Sensor Estimates

TABLE V

ESTIMATED VOLUME OF SCADS SENSOR
SPIN STABILIZED MODE
(Excluding On-Board Data Buffer)

Subsystem	Volume $(Inch)^3$
Lens System (a = 2.0 inches)	12.6
Photomultiplier (EMR-543)	28.0
Electronics	
Analog Circuits	3.0
Digital Circuits including Clock	4.5
Overload Circuits	.5
Power Supplies	2.0
TOTAL	50.6
Bright Object Shield (8.7 inch diameter, 9.2 inches high)	548

TABLE VI

ESTIMATED WEIGHT OF SCADS SENSOR
SPIN STABILIZED MODE

Subsystem	Weight (Pounds)
Sun Shield	.5
Lens System (D = 2 inches)	1.2
Photomultiplier (EMR-543, potted)	.85
Electronics	
Analog	.19
Digital	.40
Overload Circuits	.03
Power Supplies	.13
Sensor Housing	.75
TOTAL	4.05

TABLE VII

ESTIMATED POWER REQUIRED FOR SCADS SENSOR
SPIN STABILIZED MODE

Subsystem		Watts
PMT Power Supply		.300
Analog Circuits	.400	
Digital Circuits	.300	
PMT Overload Circuits	.100	
	.800	
Low Voltage Power Supply (80% efficient)		1.00
TOTAL		1.30

2. Three Axis Controlled Mode Estimates

TABLE VIII

ESTIMATED VOLUME OF SCADS SENSOR
THREE AXIS CONTROLLED MODE

(Excluding On-Board Data Buffer)

Subsystem	Volume $(Inch)^3$
Lens System (a = 1.00 inches)	1.6
SASI Motor	5.0
Photomultiplier (EMR-543)	28.0
Electronics	
Analog Circuits	3.0
Digital Circuits Including Clock	4.5
Overload Circuits	.5
Motor Drive Circuits	1.0
Power Supplies	2.0
TOTAL	44.6
Bright Object Shield (specific dimensions dependent on final spacecraft boom and solar panel configuration)	29*

* Estimate based on $\left(\frac{a_{3axis}}{a_{dual}}\right)^3 V_{dual}$ where the "dual" subscript refers to the dual mode sensor estimates below.

TABLE IX

ESTIMATED WEIGHT OF SCADS SENSOR
THREE AXIS CONTROLLED MODE

Subsystem	Weight (Pounds)
Sun Shield	.2
Lens System	.15
Photomultiplier (EMR-543)	.85
SASI Motor	.4
Electronics	
Analog Circuits	.19
Digital Circuits	.40
Overload Circuits	.03
Motor Drive Circuits	.10
Power Supplies	.13
Sensor Housing	.75
TOTAL	3.20

TABLE X

ESTIMATED POWER REQUIRED FOR SCADS SENSOR
THREE AXIS CONTROLLED MODE

Subsystem		Watts
PMT Power Supply		.300
Analog Circuits	.400	
Digital Circuits	.300	
PMT Overload Circuits	.100	
SASI Motor and Drive Circuits	1.00	
	1.80	
Low Voltage Power Supply (80% efficient)		2.25
TOTAL		2.55

3. Dual Mode Estimates

TABLE XI

ESTIMATED VOLUME OF SCADS SENSOR
DUAL MODE

(Excluding On-Board Data Buffer)

Subsystem	Volume $(Inch)^3$
Lens System (a = 2.7 inches)	39.4
SASI Motor	15.0
Photomultiplier (EMR-543)	28.0
Electronics	
Analog Circuits	5.0
Digital Circuits including Clock	4.5
Overload Circuits	0.5
Motor Drive Circuits	1.0
Power Supplies	2.0
TOTAL	95.4
Bright Object Shield (10.7 inch diameter, 6.2 inches high)	557.5

TABLE XII

ESTIMATED WEIGHT OF SCADS SENSOR
DUAL MODE

Subsystem	Weight (Pounds)
Sun Shield	.5
Lens System	2.9
Photomultiplier (EMR 543)	0.85
SASI Motor	0.8
Electronics	
Analog Circuits	.26
Digital Circuits	.40
Overload Circuits	.03
Motor Drive Circuits	.10
Power Supplies	.13
Sensor Housing	1.4
TOTAL	7.37

TABLE XIII

ESTIMATED POWER REQUIRED FOR SCADS SENSOR
DUAL MODE

Subsystem		Power (watts)
PMT Power Supply		.30
Analog Circuits	.40	
Digital Circuits	.30	
PMT Overload Circuits	.10	
SASI Motor and Drive Circuits	1.00	
	1.80	
Low Voltage Power Supply (80% efficient)		2.25
TOTAL		2.55

V. SCADS PERFORMANCE ANALYSES

In this section, the specific SCADS designs developed above are analyzed in terms of their expected performance in obtaining the star transit data required for attitude determination. These analyses characterize (1) the ability of SCADS to detect an adequate number of star transits, (2) the distribution of attitude errors expected with SCADS, and (3) the precaution required for the operation of SCADS in a radiation environment. The section concludes with a brief commentary on the general reliability of the instrumentation.

A. Star Transit Detection

Each of the SCADS designs presented here is based on a particular system limiting magnitude M_ℓ. The value of M_ℓ for each case is determined by first selecting the field of view configuration and then applying this field specification in a detailed star availability search. The magnitude of the faintest fourth-brightest star in the field of view for all possible viewing directions over the mission profile is then chosen as the system limit. An optical aperture is then chosen so that the SCADS instrument can detect a star of magnitude M_ℓ with some given detection probability $P_d(M_\ell)$; here $P_d(M_\ell) = 0.5$ for the spin stabilized case.

Once the optical aperture and the other parameters of the SCADS design have been fixed, however, the equations in Section IIIB4 can be inverted to find the detection probability associated with any stellar magnitude M. The principal relations are given in Equations (112)and (115)above. Equation (112)may be solved for k, the argument of the cumulative normal probability distribution. Thus

$$k = \frac{.597\, n_s - (n_T - n_{BD})}{[.9711(.8n_s + n_{BD})]^{\frac{1}{2}}} \qquad (140)$$

where the number of signal photo-events n_s, the number of events characterizing the threshold n_T, and the number of combined background and dark current emissions n_{BD} remain as defined in Section IIIB4. Note that the stellar magnitude M enters Equation (140) through Equation (115) in the form $n_s = C(10^{-.4M})$. Once k has been evaluated for a particular set of sensor parameters, the corresponding probability P_d can be found from a table of the error function.

The detection probability is plotted as a function of the stellar magnitude M for the recommended spin mode SCADS sensor in Figure 81. Similar plots are given for the dual mode sensor in Figure 82 and for the three-axis controlled mode sensor in Figure 83. Note that the curves given for the dual mode sensor characterize both spinning operation (scan period $T_{spinning}$ = 1 second) and three-axis controlled operation (scan period T_{driven} = 10 seconds). It is clear from Figure 82 that if the scan period is lengthened and the filter is modified accordingly but all other sensor parameters are held fixed, then the detection capability of the sensor is significantly enhanced.

It will be seen in the next section on attitude error analysis that the ability to detect a large number of stars is an important requisite for obtaining the desired accuracy with the dual mode sensor in the three-axis controlled state.

From Figure 81 it is seen that the spin mode sensor has a detection probability of 0.5 at the system limiting magnitude $M_\ell = 3.84$ and that the probability rises rapidly to 0.95 at M = 3.38. But, from the distribution in Figure 27 of Section IIB it is seen that the fourth brightest star is at least as bright as M = 3.38 in 93 percent of the possible scan axis directions.

Similarly, from Figure 82 one observes that the dual mode sensor attains

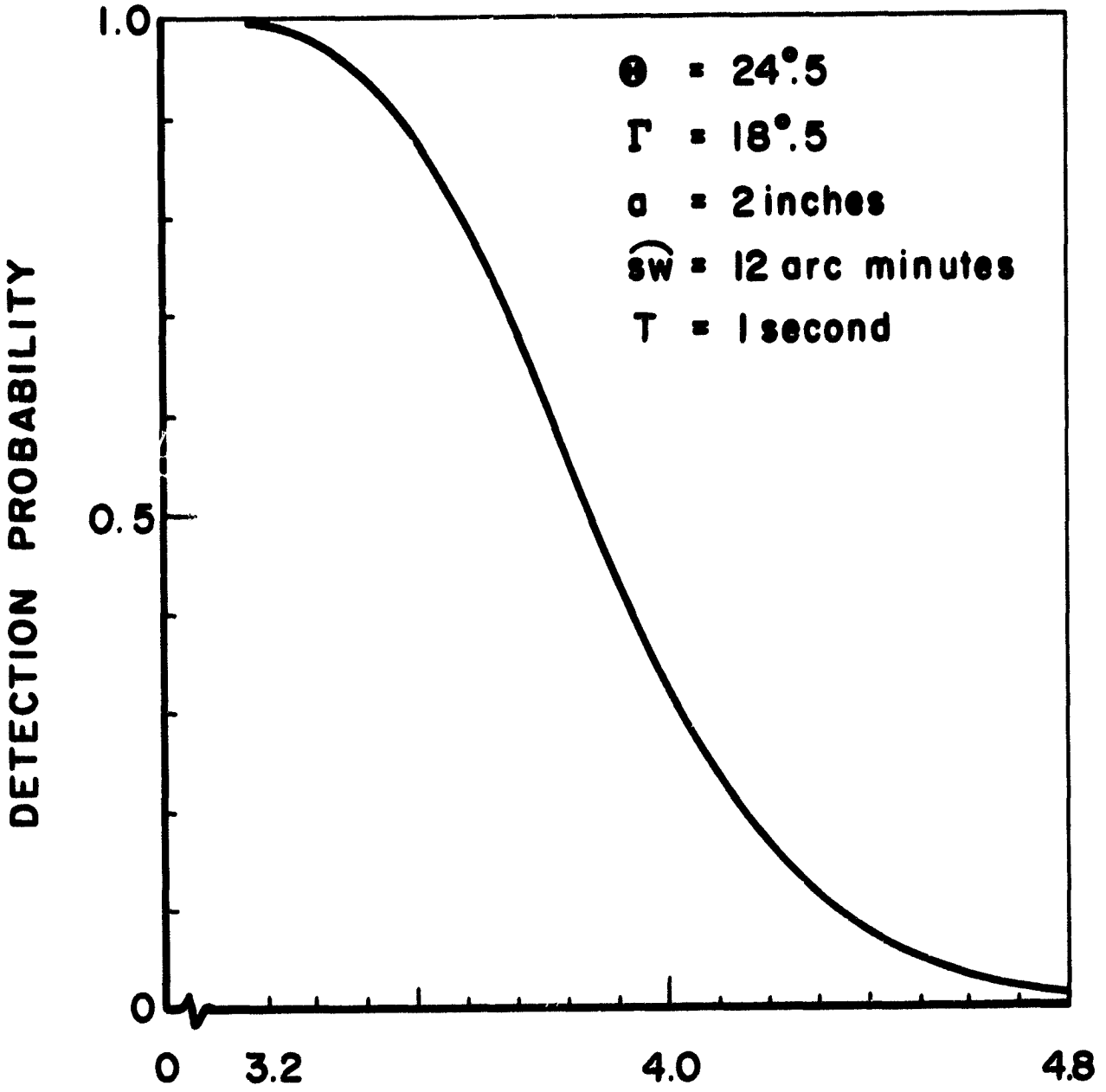


Figure 81: Detection probability as a function of stellar magnitude for the recommended spin mode SCADS sensor. Note: required limiting magnitude $M_\ell = 3.84$.

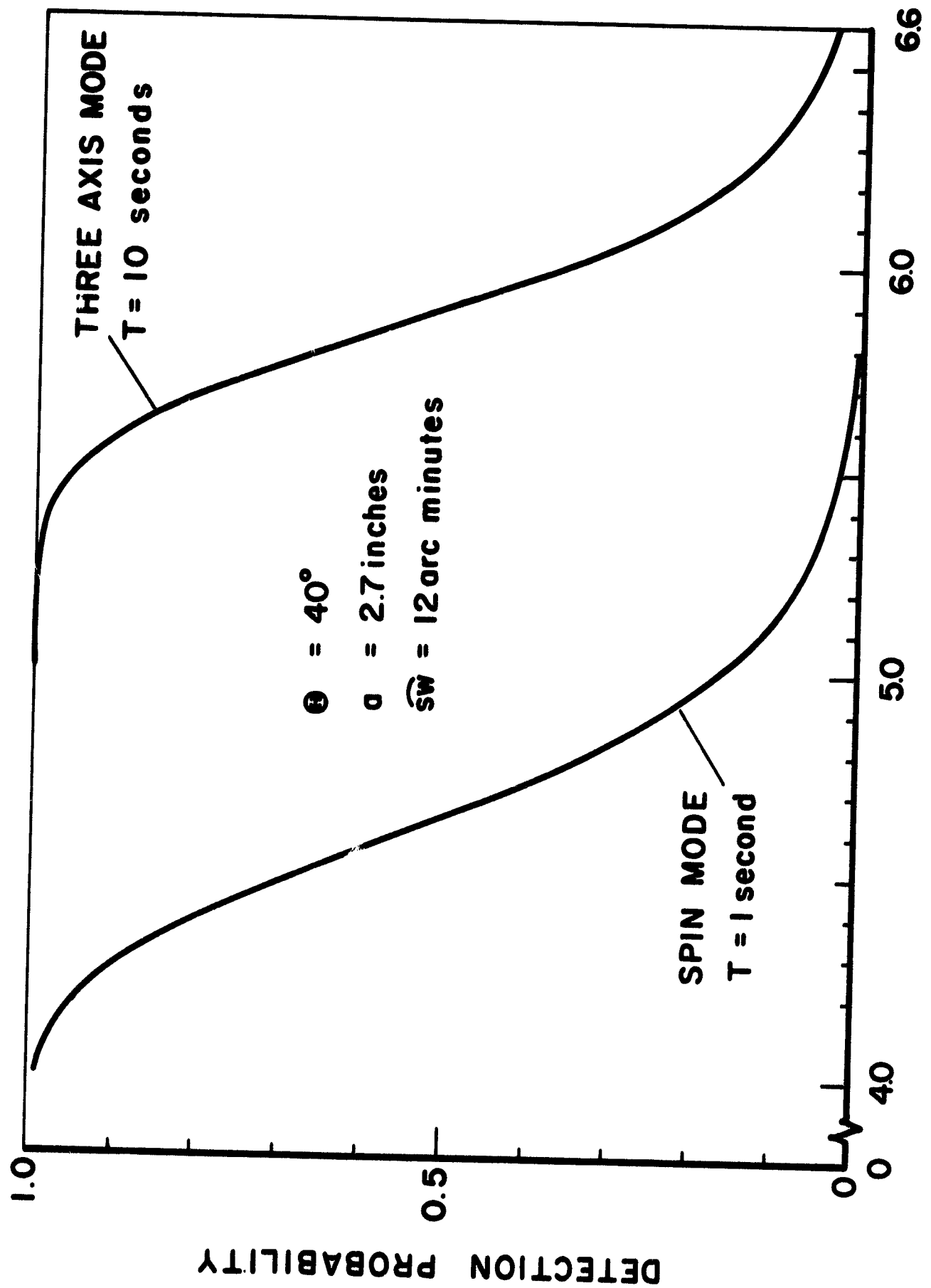


Figure 82: Detection probability as a function of stellar magnitude for the recommended dual mode SCADS sensor. Note: required limiting magnitude $M_{\ell} = 4.65$.

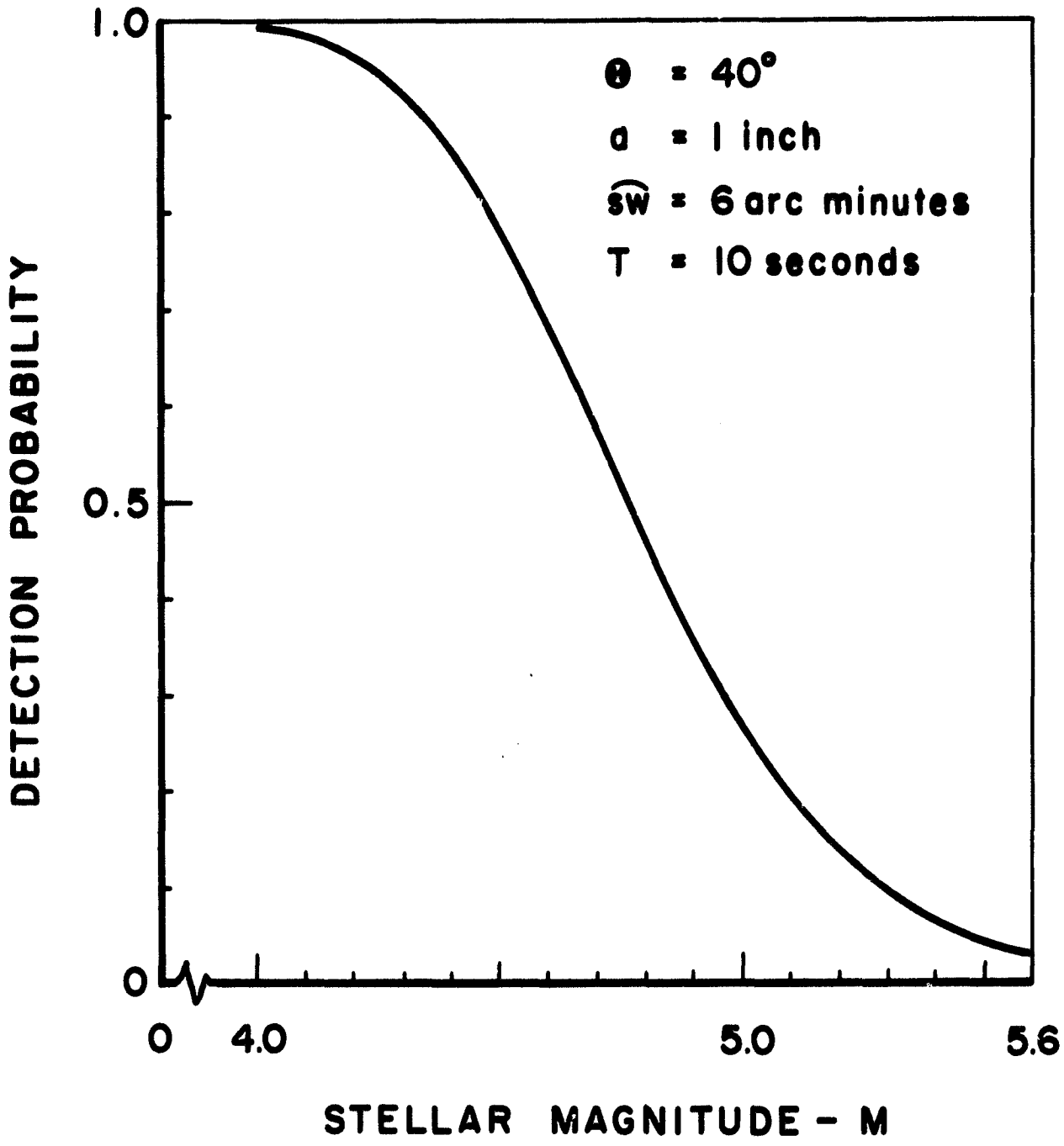


Figure 83: Detection probability as a function of stellar magnitude for the recommended three-axis-controlled mode SCADS sensor. Note: required limiting magnitude M_l = 4.21.

a detection probability of at least 0.95 in the spin stabilized state for stars brighter than M = 4.16. From Figure 41 it is seen that the fourth brightest star is at least as bright as M = 4.16 in 94 percent of the possible scan axis directions.

Thus the target availability and detection probability for the spinning mode are distributed such that there are at least four solidly detectable stars (95 scans or more out of 100) for 93% of the possible fields of view in the ATS F&G mission. The SCADS configurations presented here, then, do indeed solve the star transit detection problem. Further, the criterion of a 0.5 detection probability for a true limiting magnitude star appears to represent a sound design approach.

B. Attitude Determination Error Analysis

To gain some insight into the accuracy of the system, a somewhat simplified error analysis was performed. For this analysis we assume the slit is spinning with a known rate about a fixed axis. Hence, this simplified problem contains only three unknowns: the right ascension and declination of the spin axis, and the direction of the reference zero azimuth. In addition to the assumption of motion about a fixed axis, the following series of conditions is assumed. First, for both modes, the effective instrument field of view is an annularly-shaped region of the celestial sphere. The scan axis is the axis of the annulus. The outer and inner radii for the spin mode sensor are $30^{\circ}.75$ and $6^{\circ}.25$, respectively. The corresponding radii for both the dual mode and the controlled mode sensors are 20° and 5°.

Second, the instrument field of view limits the available stars. Moreover, only the brightest (in photographic magnitude) three, four, five, or six (four cases) stars in any given effective field of view are utilized. Then in no case are any stars dimmer than 3.84 photographic magnitude used for the spin mode sensor, while the corresponding magnitude for both operational phases of the dual mode sensor is 4.65.

Finally, the only input errors of the system are errors in the measurement of the transit time. These errors can be easily converted to an error in measurement of the angle from the zero reference to the slit at the instant of a star transit. Thus,

$$\sigma(\theta) = \frac{\sigma(t)}{T} \tag{141}$$

where $\sigma(\theta)$ = standard deviation of rotation error,

$\sigma(t)$ = standard deviation of transit time error,

T = scan period.

1. Method of Determination of Errors

It may be shown that each transit of a star across a slit yields one equation of the form

$$0 = f(\alpha, \delta, \beta + \dot{\beta}\, t_i, \hat{s}_i) \tag{142}$$

where α = right ascension of spin axis,
δ = declination of spin axis,
β = angle from north to reference direction,
$\dot{\beta}$ = spin rate,
t_i = transit time of i^{th} star,
$\hat{s}_i$ = unit vector to transitted star.

Hence, for small errors in the time of transit

$$0 = f_1\, \delta\alpha + f_2\, \delta\delta + f_3(\delta\beta + \dot{\beta}\delta\, t_i) \tag{143}$$

where f_j = the partial of f with respect to its j^{th} argument. So, $\delta t_i = \bar{a}'\, \bar{X}$ where $\bar{a}' = -(f_1, f_2, f_3)/\dot{\beta}\, f_3$

$$\bar{X} = \begin{pmatrix} \delta\alpha \\ \delta\delta \\ \delta\beta \end{pmatrix} . \tag{144}$$

Hence, after many measurements are taken, we obtain a system of linear equations for $\bar{X}$ which is of the form

$$\delta\bar{t} = A\, \bar{X} . \tag{145}$$

If the columns of A are linearly independent vectors, then the choice of $\bar{X}$ which renders $\delta\bar{t}'\, \overline{\delta t}$ a minimum is

$$\bar{X}_m = (A' A)^{-1} A' \overline{\delta t} \quad . \tag{146}$$

Let us now assume each component of $\overline{\delta t}$ is a random variable whose distribution has mean zero and standard deviation $\sigma(t)$. Also, assume each of the distributions are independent. Hence, the covariance matrix of $\bar{X}_m$ is

$$E(\bar{X}_m \bar{X}_m') = \delta^2(t)(A' A)^{-1} = \frac{\sigma^2(\theta)}{T^2} (A' A)^{-1} \quad . \tag{147}$$

Hence, even though the input errors are independent, errors in the output quantities may be highly correlated. In any event, we will take as a measure of the output error

$$\Sigma = \sqrt{\sigma^2(\delta\alpha) + \sigma^2(\delta\delta) + \sigma^2(\delta\beta)} \quad . \tag{148}$$

We will call Σ the total attitude error. Note that Σ is a linear function of $\sigma(t)$ or $\sigma(\theta)$.

2, Spin Mode Sensor Errors

For the spin mode, the results presented will be those obtained from data collected over one rotational period. However, if n rotational periods of data are collected then the total attitude error will be divided by $\sqrt{n}$.

In Figure 84, we plot the total attitude error for the spin mode as a function of the right ascension of the spin axis. For this figure, the declination of the spin axis was set equal to zero. Results are shown for the brightest three, four, five, and six stars in the field of view. Note that generally, there is a substantial reduction in the output error if four instead of three stars are utilized. In this and all succeeding graphs pertinent to the spinning mode we assume for input error $\sigma(\theta)$ = 1 minute

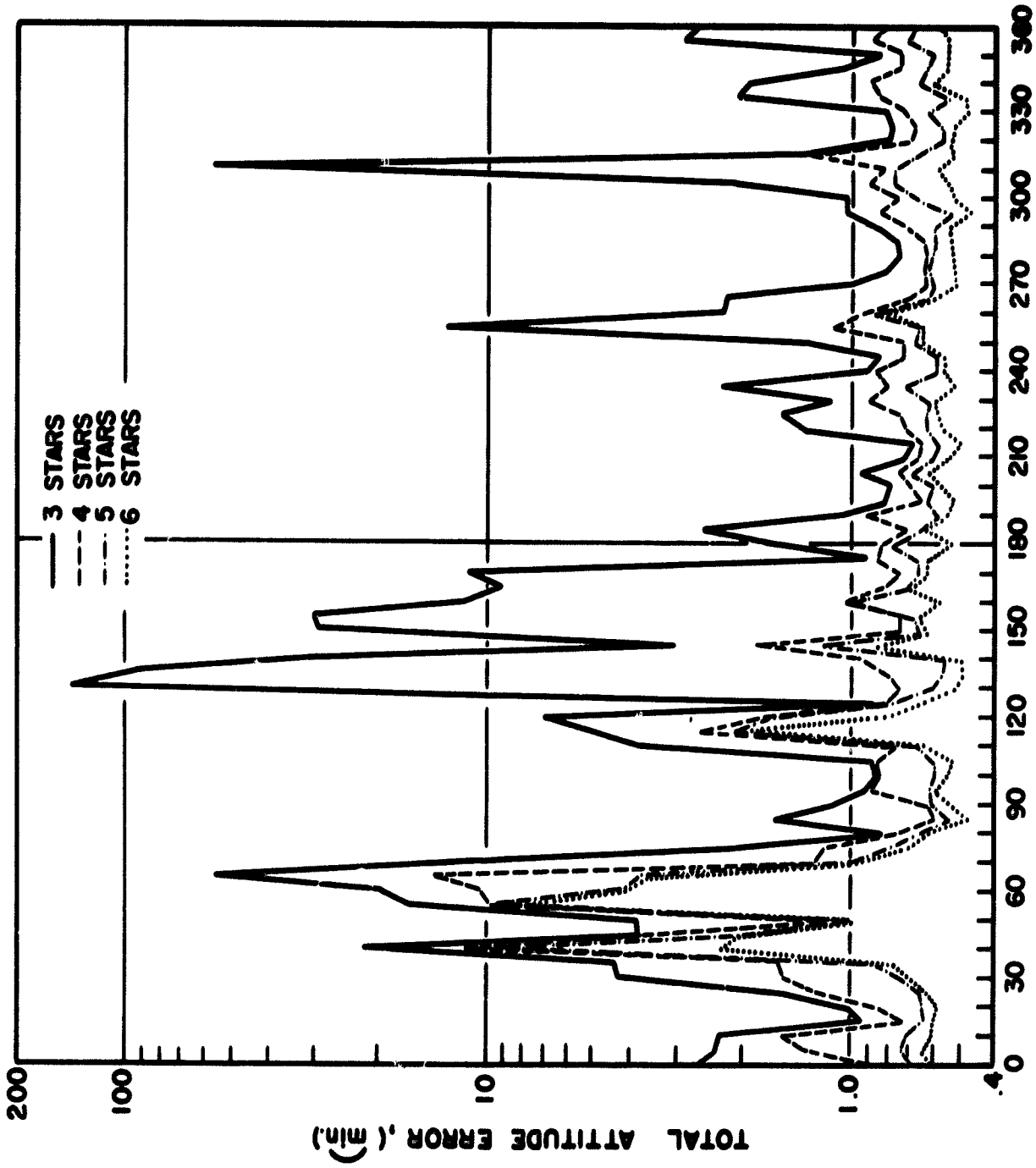


Figure 84: Total attitude error for the spin mode as a function of the right ascension of the scan axis at $\delta_{scan} = 0^{o}$. Results employing the brightest three, four, five, and six stars in the field of view are presented.

of arc. This error is consistent with the proposed instrument design. (See Section IIIC.) However, if $\sigma(\theta)$ were ½ minute of arc, then the output errors should simply be one-half those shown.

Instead of plotting the total attitude error as a function of the position of the spin axis, in Figure 85 we plot the cumulative probability distribution of the total attitude error. Recall that the declination of the scan axis was such that $-10^{\circ} \leq \delta \leq 30^{\circ}$, while the right ascension was not confined. In order to obtain Figure 85, a larger number (648) of points in the region to which the scan axis is confined were investigated. Again, note the significant difference between the results produced by four instead of three stars. Note also that the desired system accuracy for the spin mode is $0^{\circ}.1$ or six arc minutes. Thus it is seen in Figure 85 that accuracy requirements are met with the three brightest stars in 85% of the cases and with the four brightest stars in 97% of the cases.

3. Dual Mode Sensor Errors

In Figure 86, we plot the cumulative probability distribution for the brightest three, four, five, and six stars in the field of view for the dual mode sensor. These results apply to both the spinning mode and the three-axis controlled mode. Again it is seen that the spin mode accuracy requirements are adequately met. Note that $\Sigma \leq 0^{\circ}.1$ in 84% of the instances where the three brightest stars are employed and in 97% of the four star cases.

The performance of the dual mode sensor does not meet the goal of $0^{\circ}.01$ in each axis (or $0^{\circ}.017$ in Σ if equal errors are assigned to each axis) on a single scan basis if only three or four stars are used. However, the detection capability of the dual mode sensor extends to much fainter stars when the reticle is driven at a ten second scan period (see Figure 83). Thus, solid detection of six or more stars on each scan should present little difficulty. From Figure 86 it is seen that $\Sigma \leq 0^{\circ}.01$ for 50%

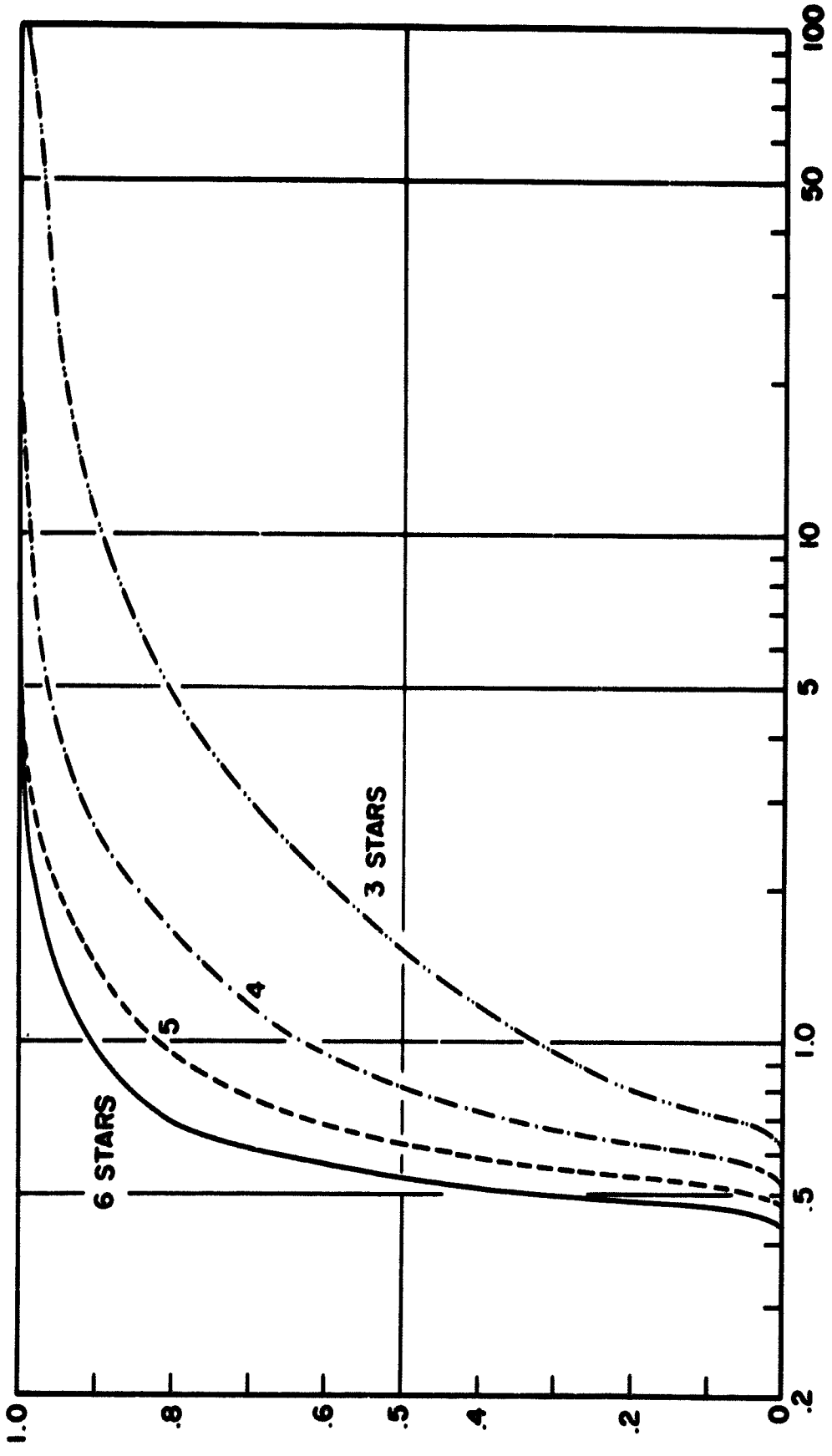


Figure 85: Cumulative distribution of the total attitude error for three, four, five, and six stars detected in the field of view. Results presented for the spin mode sensor.

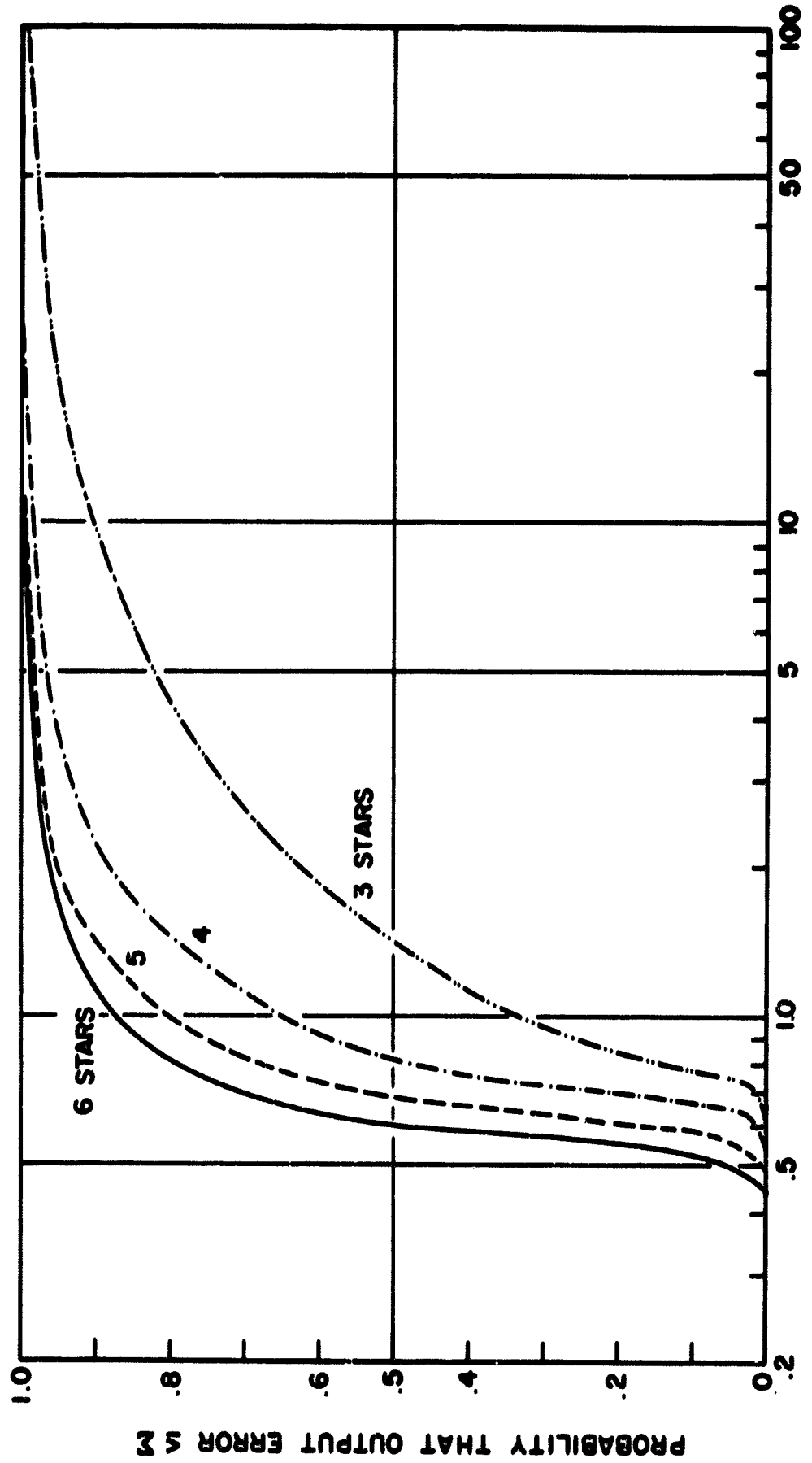


Figure 86: Cumulative distribution of the total attitude error for three, four, five, and six stars detected in the field of view. Results presented for the dual mode sensor.

of the cases when six stars are used. Further, these error distributions are based on a single scan of data. By using transits from the same stars but from multiple scans, the errors can be reduced significantly. As was noted above, complete data from n scans should reduce the single scan errors by a factor of $1/\sqrt{n}$; thus, use of information from four scans should approximately halve the errors. On this basis, it is seen that four-scan data would yield $\sigma \leq 0.01$ in 70% of the four-star cases and in 94% of those in which six stars are used.

It should also be noted here that continuous attitude determination is not required in the three-axis controlled mode. Thus, for any particular pointing direction, star transits may be encoded and processed through the star identification and attitude determination computer programs. An error analysis of the type described here may then be carried out for the actual pointing direction and with the actual stars obtained. If the resulting error estimates appear excessive, data can be acquired again when the field of view encounters a more suitable configuration of stellar targets. Observe further that in addition to this a priori error analysis, the residuals from the least squares attitude solution also represent a measure of the errors.

4. Three-Axis Mode Sensor Errors

The error distributions of Figure 85 and 86 are nearly identical even though the geometry of the respective fields of view were quite different. It appears then that these curves may represent a form of "universal" error plot for this SCADS application and this interpretation is used to estimate the errors for the three-axis controlled or driven mode sensor.

The driven mode sensor is required to operate only in the mission phase during which the vehicle is three-axis stabilized. Thus, the scan is slowed down and star transit detection is much less of a problem than in the rapidly spinning mode. Easing of the detection problem, in turn, allows

the slit to be narrowed to half the width used in the spin sensors. As a consequence, the input errors $\sigma(\theta)$ should also be approximately halved. In Figure 86, the values of Σ along the abscissa should then also be halved. The single scan error for the three axis mode is then $\Sigma \leq 0.01$ for 70% of the cases in which four stars are used and in 94% when six stars are employed. The comments above about multiple scan data are also applicable here. Thus, the three-axis attitude accuracy goals can be met.

A final form of presenting the error analysis results is given in Figure 87. Here we plot the points at which it was found that the total attitude error is excessive for the spin mode. If the brightest six stars in the field of view are utilized, at no point is the error excessive.

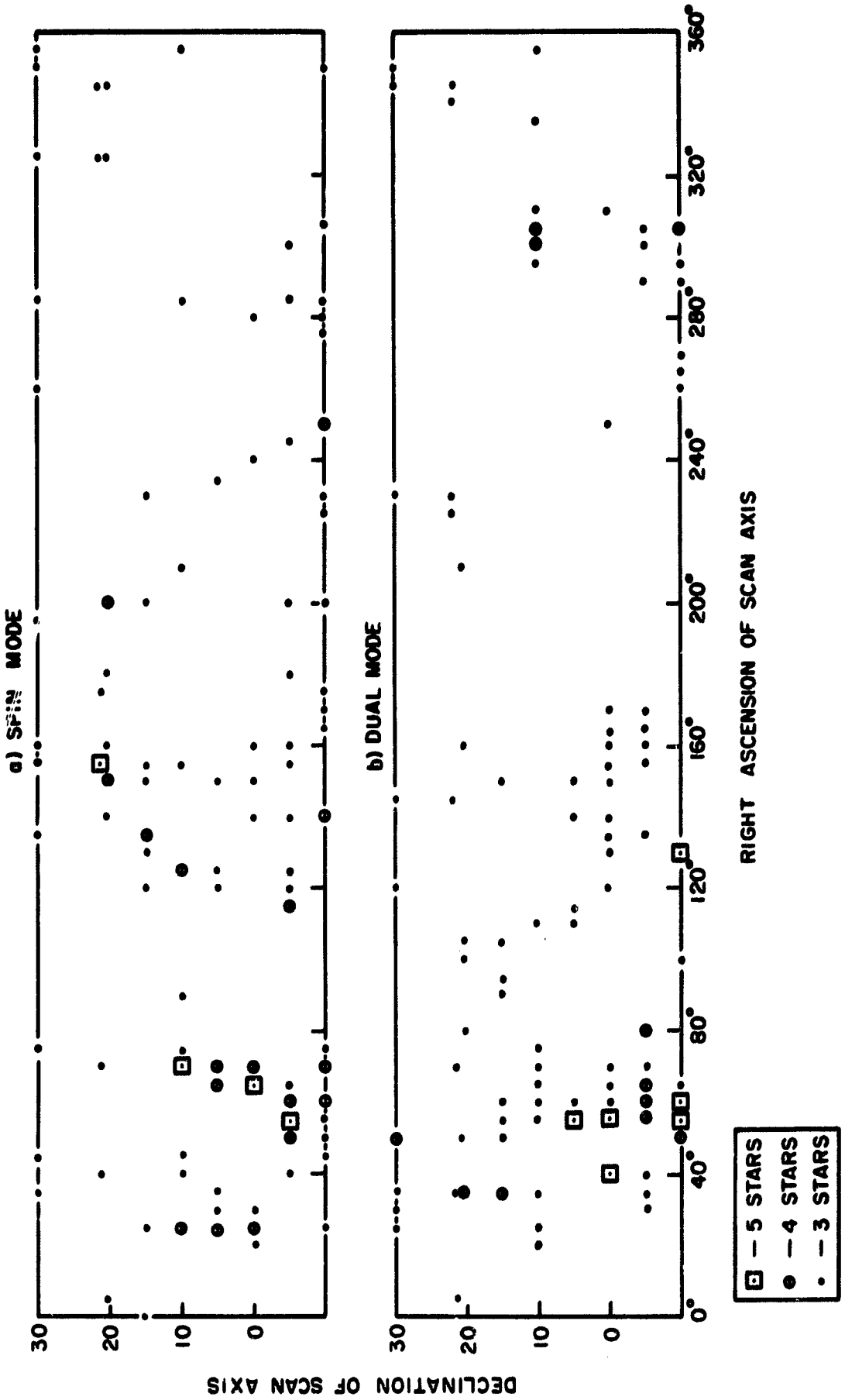


Figure 87: Points at which the computed total attitude error is excessive for three, four, and five stars detected in the field of view.

C. Radiation Susceptibility

Since the SCADS instrument is a photosensitive system designed to detect very weak sources of light, it can be overloaded and made inoperable or it may even be damaged if it is subjected to strong sources of visible or higher energy radiation.

1. Optically Bright Objects

The operation of SCADS in the presence of the sun, the earth, and the moon was discussed in detail in Section IIA. Care was taken in the SCADS design co insure that these bright celestial sources would be well out of the scanned field of view during the portions of the mission over which SCADS operation is required. These investigations resulted in the choice of appropriate launch conditions, selection of the angular relations of SCADS to the spacecraft coordinate system, and consideration of the shielding problem to avoid interference when the sun or earth come closer than 90° to the optical axis. Over some portions of the mission, however, SCADS operation is not required and the bright celestial sources may fall directly within the field of view. The implications of this condition are discussed in the remainder of this subsection.

a. Photomultiplier Overload Protection

In order to prevent degradation of the photomultiplier cathode and dynodes, it is necessary to limit the current emitted by these surfaces when bright sources such as the sun, earth, or moon get into the optical system field of view. Since current flow does not occur when high voltage is removed from the photomultiplier cathode and dynode chain, an obvious way of limiting the emission currents is to reduce or remove the electron acceleration voltages to the cathode-dynode chain whenever bright sources of radiation enter the field of view.

In the spin stabilized phase, the sunlit earth will get into the field of view for segments of each orbit (both on the transfer ellipse and on the spinning orbit-correction phase of the synchronous orbit). Further, the

sun will enter the field of view of the dual mode sensor over a sector of every orbit in the three-axis controlled mode. For these cases, it is certain that the photomultiplier emission current limits will be exceeded if the photomultiplier voltage is not reduced or removed when the bright source enters the field of view. The full moon intensity can also cause excessive emission currents, so it too must be considered as a bright source. However, the moon is less of a problem than the earth or the sun because it is a factor of only 10^{-6} times as bright.

The logic block diagram in Figure 70 indicates ways of detecting an overload or a potential overload condition. Both of these conditions must provide logic signals which can temporarily reduce or remove the photomultiplier high voltage.

An actual overload condition can be detected at the photomultiplier output by sensing when the output signal across R_s exceeds a threshold level determined from the maximum average anode current rating. The output of a level detector will automatically switch OFF the photomultiplier high voltage. The photomultiplier high voltage must then be turned back ON by a telemetry command from the ground station, provided no bright source is in the field of view.

Alternatively, a potential overload condition could be detected with a simple auxiliary sensor. This sensor might take the form of a subminiature solid state photocell and a very simple lens. The optical field of view of this auxiliary system would be slightly larger than the field of the SCADS instrument itself and the two systems would have parallel optical axes. Then, as a bright celestial source approached the SCADS field from any direction, it would be detected first by the auxiliary sensor and the resulting signal would automatically switch OFF the photomultiplier high voltage. The photomultiplier voltage would remain OFF until the photocell output fell below the threshold level at which time the photomultiplier voltage is automatically turned back ON.

Because of the vast difference in the strength of the local bright sources and the stars, there is no problem in selecting a photocell which will respond only to the sun, earth, and moon. Note that the entire auxiliary sensor system should require only a fraction of a cubic inch of volume.

b. Radiation Heating Protection

Removal of the photomultiplier high voltage will provide adequate protection for most bright source encounters. However, when the sun or earth falls directly in the field of view, the SCADS optical system takes on the role of an excellent "burning glass" and damage to the photocathode or slit reticle could result. This is not expected to be a problem in the spinning mode where the rapid motion of the vehicle sweeps the slit across the source very quickly; the dwell time is thus quite short.

However, the dual mode sensor presents a particular problem in the three-axis controlled mode. The sun will gradually pass across the field once in each orbit and its transit may take as long as two and one-half hours. There are two factors which assist in meeting the resulting problem of direct solar radiation. First, the SASI motor prevents the positioning of the photomultiplier up against the slit reticle; that is, against the focal plane. Thus, the sun's image is "bloomed" after passing through the slit and a concentrated point is not formed on the photocathode. Second, the SASI motor may be left on while the sun is in the field of view. Thus, the slit will sweep across the sun's image in a short time in a manner analogous to that found in the spinning mode. Note that the upper surface of the slit reticle should be highly specularly reflecting to reduce spot heating of this element.

One additional note should be made here. For the spinning mode, an alternative approach is to employ a reticle shutter as shown in Figure 88. The shutter can consist of a spring leaf reed which is pulled over the slit opening when the solenoid is energized by either a photomultiplier overload

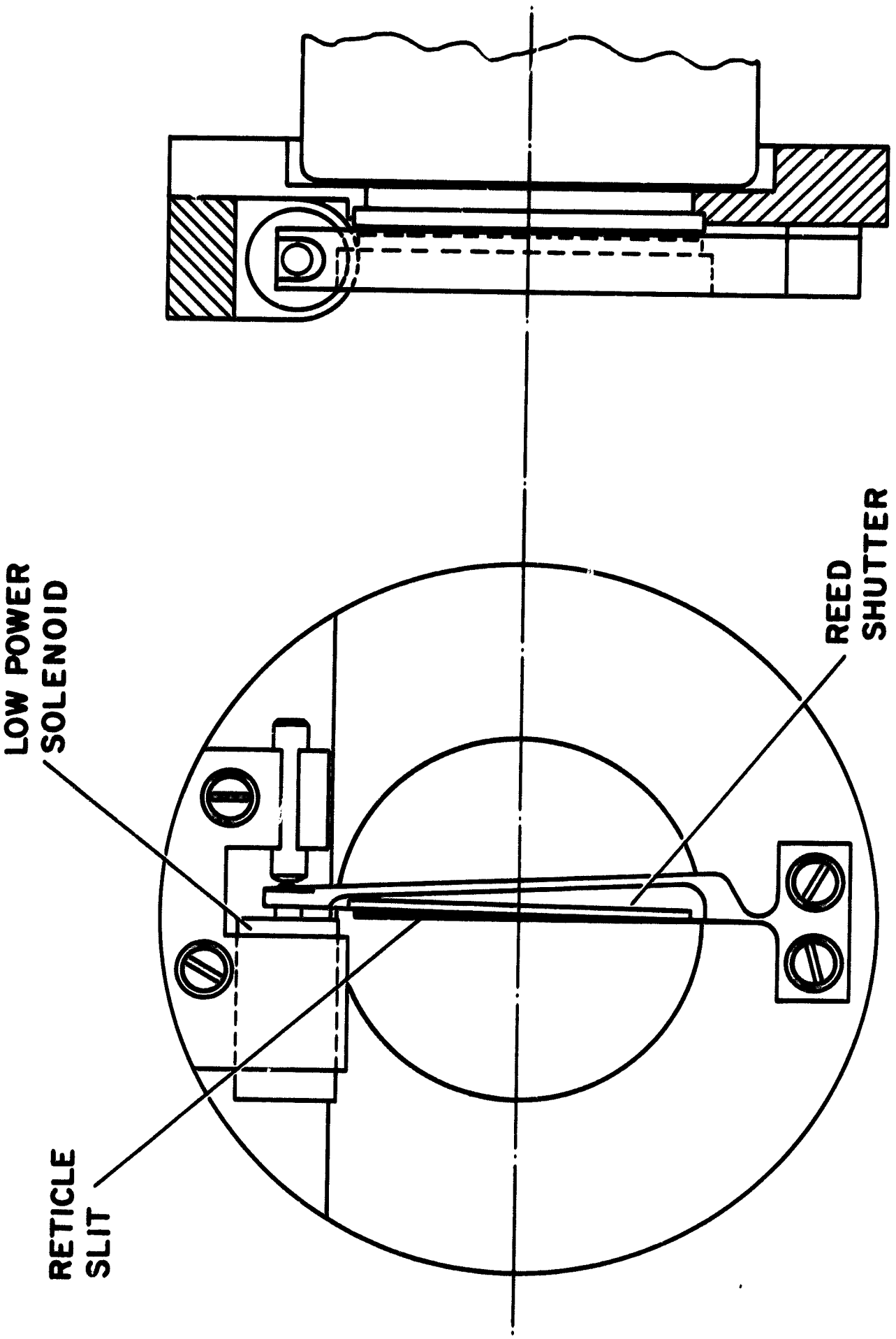


Figure 88: Reticle slit reed shutter mechanism.

WEIGHT : 2 ounces
POWER CONSUMPTION : 0.5 watt (est.)
SHUTTER CLOSURE TIME : 6-8 msec.

protector circuit or a small solid-state detector. The shutter may be closed or opened in six to eight milliseconds. Less than .5 watt of power is required to hold the shutter closed. Average power dissipation depends upon the duty cycle determined by the presence of the sun and sunlit earth in the field of view. Hence, average power dissipation is much less than .5 watt. The shutter weight is approximately two ounces. Although the device does utilize a moving part, it can be demonstrated that such a device could withstand several hundred million operations at operation rates between 25 to 100 per second without failing.

The shutter mechanism shown in Figure 88 is mounted on a thin cylindrical ring. The mechanism and mounting ring would then be sandwiched between two additional rings which would comprise a one centimeter thick cathode particle radiation shield. Particle radiation shielding requirements are discussed in Part 2 of this section.

With a shutter mechanism such as this, the sensor could remain operational even if the field sweeps through a bright source on each scan. However, a sector of the scan annulus would be removed and the instrument itself would be made more complex. Since a satisfactory solution appears to have been found without this complication, the shutter is not recommended here. However, should subsequent spacecraft constraints eliminate the possibility of looking out close to the negative spin axis (out the back of the vehicle), this approach might be given more consideration.

2. High Energy Radiation

The overall problem of the hard radiation environment to be encountered by SCADS and the general considerations for photomultiplier shielding to cope with this radiation are discussed in Appendix C. Also, the problem of shielding semiconductor circuits is discussed in Appendix D. In the following subsections, these results are specialized to the particular requirements of this application.

a. Photocathode Shielding

If we are satisfied that the photomultiplier can be shielded from the radiation belts, and the work of the NASA group on OGO II[19] indicates that it can be, the amount of shielding necessary to reduce the noise to a tolerable level can be estimated straightforwardly.

We shall wish to detect stars of magnitude $3^m.85$ against the background noise due to all sources.

From the work of Code[8] we can estimate the number, n_o, of photons incident on the earth's atmosphere from Vega. (Type A0, $0^m.0$) This is,

$n_o = 1.66 \times 10^7/cm^2$ sec micron, at the center of the Johnson B filter (4300 Angstroms).

Then the number of resulting photoelectrons from a sensor with optical aperture, a, optical efficiency, ϵ_o, photomultiplier quantum efficiency E_q and band pass $\Delta\lambda$, which views a star of magnitude M_B, is about

$$S = n_o \, 10^{-.4M_B} \frac{\pi}{4} a^2 \, \epsilon_o \, E_q \, \Delta\lambda \ . \tag{149}$$

If the faint star background is N tenth magnitude stars per square degree and A is the slit area in square degrees, the signal due to this source is

$$N_B = n_o \, N \, 10^{-4} \frac{\pi}{4} a^2 \, \epsilon_o \, E_q \, A \, \Delta\lambda \ . \tag{150}$$

A reasonable aperture is about two inces. Choose $\epsilon_o = .5$, $E_q = .2$, $\Delta\lambda = .3$ micron, $M_B = 3.85$, $N = 325$, $A = .3$ square degree.

$$\text{Then } S = 2.91 \times 10^5/\text{sec} \tag{151}$$
$$N_B = 1.24 \times 10^4/\text{sec}.$$

In the absence of radiation noise the faint star background is the major source of noise, even so the d.c. signal due to it is less than the star signal by a factor 17. It appears that we can neglect it altogether and we do.

The NASA group observed a dark current of 2.06×10^{10} electrons per second, and were shielded for about an MeV. Above an MeV at the equator in the inner Van Allen belt are about 10^8 electrons/sec cm^2. If each fast electron incident on the photocathode produced k photoevents,

$$2.06 \times 10^{10} \approx \frac{\pi}{2} R^2 \, k \times 10^8, \tag{152}$$

Since R = 1.27, where R is the radius of the photocathode, $k \approx 80$ for the EMR 541 PMT used in the OGO work.

Consider the situation of Figure 89. Some random process f(t) acting on the sensor causes an output,

$$I(t) = \sum_{k=-\infty}^{\infty} a_k \, p(t-t_k), \tag{153}$$

where p(t) describes the individual pulse shapes at the photomultiplier output and a_k their amplitude. Let a_k be a random variable.

I(t) is fed to the input of a filter with impulse response h(t).

The filter output will be

$$I_o(t) = \sum_{k \equiv -\infty}^{\infty} a_k \int_{-\infty}^{\infty} p(t - \tau - t_k) \, h(\tau) \, d\tau \tag{154}$$

By Campbell's Theorem[17] the variance of I_o will be

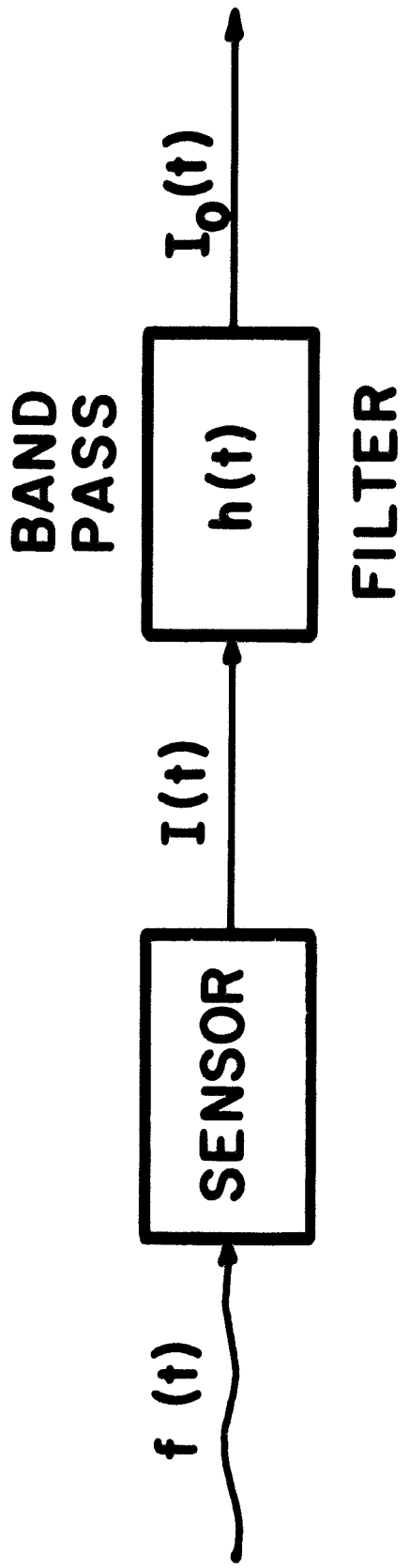


Figure 89: Schematic of the radiation random noise process.

$$\sigma^2 = \nu \overline{a^2} \int_{-\infty}^{\infty} \left[\int_{-\infty}^{\infty} p(\tau' - \tau)\, h(\tau)\ d\tau \right]^2 d\tau', \tag{155}$$

where ν is the rate at which photoevents occur and $\overline{a^2}$ is the second moment of a_k.

Since the filter response will be much slower than the photomultiplier we can as well take p(t) as the delta function. Then on integrating over τ,

$$\sigma^2 = \nu \overline{a^2} \int_{-\infty}^{\infty} h^2(\tau')\, d\tau'$$

$$= \nu \overline{a^2} \int_{-\infty}^{\infty} H^2(f)\, df\ . \tag{156}$$

Finally,

$$\sigma^2 = 2\ \nu \overline{a^2}\ \Delta f, \tag{157}$$

where

$$\Delta f = \int_0^{\infty} |H(f)|^2\, df, \tag{158}$$

is the filter noise bandwidth.

To proceed further knowledge of the distribution of the a_k is needed. Lacking this knowledge, we assume a normal distribution with mean $\overline{a} = k$. Then

$$\overline{a^2} = k + k^2 \approx k^2\ . \tag{159}$$

Then if particle radiation noise dominates and photoevents due to this occur at a rate N per second of mean magnitude k, the peak signal to RMS

noise is

$$\frac{S}{N} = \frac{S}{\sqrt{2(S + k^2 N)\,\Delta f}} \tag{160}$$

(Note that $a^2 = 1$ for signal photoelectrons)

Accurate location of a star position at a signal to noise ratio of five is reasonable. Thus, take $\frac{S}{N} = 5$. A twelve arc-minute slit rotating at 60 rpm transits a star in a time,

$$T_s = \frac{1}{6 \times 360} \quad . \tag{161}$$

The optimum electrical bandwidth is about

$$\Delta f = \frac{1}{3T_s} = 720 \text{ cps}. \tag{162}$$

One can now solve for N from (160) with the result that

$$N_a = 6.25 \times 10^3 \ \frac{\text{fast electrons}}{\text{sec}} \quad . \tag{163}$$

The average projected area of the photocathode being half its total area, the allowable Van Allen belt flux becomes

$$\phi = 3.22 \times 10^3/\text{sec cm}^2. \tag{164}$$

A dotted horizontal line which corresponds to this flux has been drawn in Figure C-7 of Appendix C. We see that unless we shield against at least two MeV, operation with an end-on tri-alkali photocathode is not possible at L = 6.6. Since disturbed Sun conditions may increase the outer belt radiation by factors of about 10^2 shielding the photocathode and first dynode stages for three MeV seems indicated. This would require 1.5 gm/cm^2 about the

neck of the sensor and amounts to a .55 cm. thickness of Al.

b. Protection of the Optics

The usual optical glasses are known to suffer changes in refractive index and transmission on electron and proton irradiation. To prevent this a quartz shield over the objective is necessary or the first element of the lens itself may be of quartz.

The OGO-I Photo-Electric Camera which has the first two elements of its optics of quartz has survived a year in the radiation belts with no measurable change in performance[20]. The interior elements of the lens are of CaF which is quite susceptible to radiation damage.

D. Reliability

It is essential that the SCADS system be operative during the spin stabilized mode. The spin mode sensor represents the simplest and most reliable design and thus provides the fundamental attitude detector when the vehicle is spinning. If the SCADS system for ATS F & G is regarded as an experimental program, then it will serve as a back-up to the sun sensor--rf polarization measurement combination in the spinning mode. Under these conditions, no redundancy in the SCADS system is required and much of the electronics for the spin and three-axis operations may be common; this applies whether the dual mode sensor or two separate sensor heads are selected.

However, if SCADS becomes the primary mode of attitude determination, some redundancy is desirable. Should the power supply or detection electronics fail in the spin mode sensor, a separate set of electronics for each system would permit a remotely actuated switch to transfer the sensor output to the detection electronics and power supply of the three-axis sensor. Note that the filter for the driven mode would not be ideally matched to the spin period but the match would be adequate for contingency use. Should the photomultiplier of the spin mode sensor fail, then the three-axis sensor head might be used with the SASI motor turned off and the slit fixed in the scan axis-optical axis plane. Operation in this condition, however, will depend on the position of the sun relative to the optical axis. In any event, it may be possible to operate the three-axis sensor as a partial back-up for the spinning mode if it is used in the shadow of the earth. It is assumed that the sun sensor--rf polarization combination would also serve as a back-up.

For operation in the three-axis mode, the electronics from the spin sensor may serve as an alternate. However, if the motor drive fails, the probability of obtaining a sufficient number of star transits of the fixed slit in the slowly rotating (earth rate) vehicle is low. But if transits are acquired from the fixed slits in both sensors, then for some star-rich portions of the sky sufficient data may be obtained. Note that very faint targets can

be detected at the slow scan rate involved here. Thus, the target availability problem may be less stringent than it would appear at first glance.

PRECEDING PAGE BLANK NOT FILMED.

VI. CONDITIONS REQUIRED FOR OPTIMAL SCADS OPERATION

In this section, the SCADS operational conditions and constraints are briefly summarized.

A. Spacecraft and Mission Constraints

The only SCADS-imposed restrictions on the mission are represented by the launch window constraints discussed in Section IIA2 and IIA3. These restrictions are imposed primarily by the relative position of the sun; the solar launch window is summarized in Figures 11 and 12 above. In addition, possible lunar interference affects the allowed launch conditions; the moon-imposed limitations are summarized in Table I .

If the launch window or insertion requirements are met, then SCADS will be operable in all of the possible orientations described in Section IB; no spin axis pointing directions need be excluded from the mission profile as presently planned. It should be noted, however, that the earth will impinge on the field of view for a portion of each near-synchronous orbit in the spinning mode. Nevertheless, the bright object shielding recommended here should be sufficient to permit full SCADS operation over 63% of the orbit; this should be more than adequate to perform the required orbit correction maneuvers.

In the three-axis controlled mode, the dual mode sensor will also encounter the sun once per orbit. In this case, the recommended bright object shield will allow full operation over the remaining 68% of the orbit. For the three-axis sensor, no interference from the sun or earth is expected.

B. Suggested Spacecraft Location of SCADS

Possible locations of SCADS on the spacecraft are limited by the required scan geometry. Thus, the $24^{\circ}.5$ optical field of view of the recommended spin mode sensor is to be canted at an angle of $18^{\circ}.5$ with respect to the negative spin or negative Z axis of the vehicle. Thus, if it is possible, it is desirable to mount the spin mode sensor on the back face of the aft equipment module with the bright object shield projecting out beyond the kick motor heat shield plate. Note that the cylinder of the bright object shield should be made of such a material that it also acts as a heat shield for the optical aperture and the SCADS sensor head. Observe also that the specific location of the sensor on the large area at the back of the module can be chosen for structural convenience. It is only necessary that care be exercised to avoid inclusion of the kick motor support structure within the critical angle of the bright object shield.

The location requirements of the dual mode sensor are essentially equivalent to those for the spin mode sensor except that no canting is required. However, a potential problem exists when the kick motor and its support structure are jettisoned after the spin stabilized phase is completed. The possibility of sensor damage during this operation must be guarded against. Note that this is not a problem with the spin mode sensor since its application is completed at the end of the spinning phase.

Finally, the three-axis sensor may be mounted in either the aft or forward modules in the Y-Z plane looking generally south. The optical axis here must be canted away from the boom and solar panel which lie along the spacecraft Y axis. For a forty degree field of view, this cant angle with respect to the Y axis will lie between 20° and 38° to avoid interference from both the sun at $|\delta_{SUN}|_{max} = 23^{\circ}.4$ and the spacecraft structure. The specific angle will depend on the final detailed vehicle configuration. In any event, the three-axis SCADS sensor should look out the side of the module in which it is mounted.

C. SCADS Information Bandwidth Requirements

SCADS transit time data will be digitally encoded on board the satellite. In general each scan in the spinning mode will be resolved into approximately 2^{14} time intervals; since the scan period in the three-axis mode is ten times as long, the corresponding time resolution may be as great as 2^{17} intervals per scan. Note that such additional resolution is advantageous here since higher accuracy is required in the controlled mode.

A suitable scheme for handling time and transit data would proceed as follows. A scan sequence would be initiated from the ground but the start of the data gathering operation would be delayed until the eighteenth bit (2^{17}) in the clock toggles from 0 to 1 or 1 to 0. At this point, the high order clock bits (17 through 30 - see Section IIIC3) would be transmitted as a time reference word. Then, for each star transit following this reference point, only the seventeen low order bits (2^0 through 2^{16}) of the transit time are transmitted. A new time reference is obtained each time the eighteenth bit is toggled. The total time characterization for a star transit is found by forming a single thirty bit word from the seventeen bits in the transit data and the high order bits from its time reference.

In the spin mode, the threshold is to be selected so that eight or fewer stars are detected per scan. Thus, the bit rate for transit detections will be approximately 8 x 17 per scan or 136 bits per second since the scan period is one second. A time reference word will occur only once every 8 to 10 seconds and requires only 14 bits.

Thus, the information rate or "digital bandwidth" required of the data handling system should be no more than 140 bits per second. Note that this should also suffice for the three-axis mode; even though more star transits will be acquired in one scan, the scan period in the driven mode is ten times longer than that for the spinning mode. Observe also that a time reference word will be sent approximately once per scan in the three axis controlled mode.

PRECEDING PAGE BLANK NOT FILMED.

VII. RECOMMENDED SCADS DESIGN

In the work presented above, three basic configurations--a spin mode sensor, a three axis controlled mode sensor, and a dual mode sensor--have been considered to collect the necessary star transit data for vehicle attitude determination during the spinning transfer orbit, the stationary synchronous orbit, or both.

Figure 90 illustrates the operation of the spin mode sensor scanning a portion of the celestial sphere while the ATS F or G vehicle is in the transfer orbit. Note that due to the cant angle of the sensor, the relatively small optical field of view sweeps out an effective field of view of 60^{o} with the spin motion of the satellite. The inset shows the suggested mounting position relationship in the aft section of the spacecraft.

The complementary three axis sensor which is recommended for use when the vehicle is in synchronous orbit is pictorially shown in Figure 91. In this case, as explained in the previous text, a rotating reticle provides the scan of the star field which requires a large optical field of view, but small aperture. The sensor is shown mounted in the aft module, but could also be satisfactorily mounted in the forward module. In either location the optical axis should be canted between 20 and 38 degrees from the southerly end of the spacecraft Y axis toward the Z axis to avoid interference from both the sun and the vehicle structure.

The combination, or dual mode, sensor operation is illustrated in Figure 92. The scan motion is provided by vehicle spin with the slit reticle fixed during the transfer orbit, and then in synchronous orbit the reticle is rotated to provide the scan. For these conditions, the optical system requires both a large field of view and a large aperture. Note that this system is aligned parallel to the Z, or spin axis (0^{o} cant angle), and must operate both before and after kick rocket firing and stage separation.

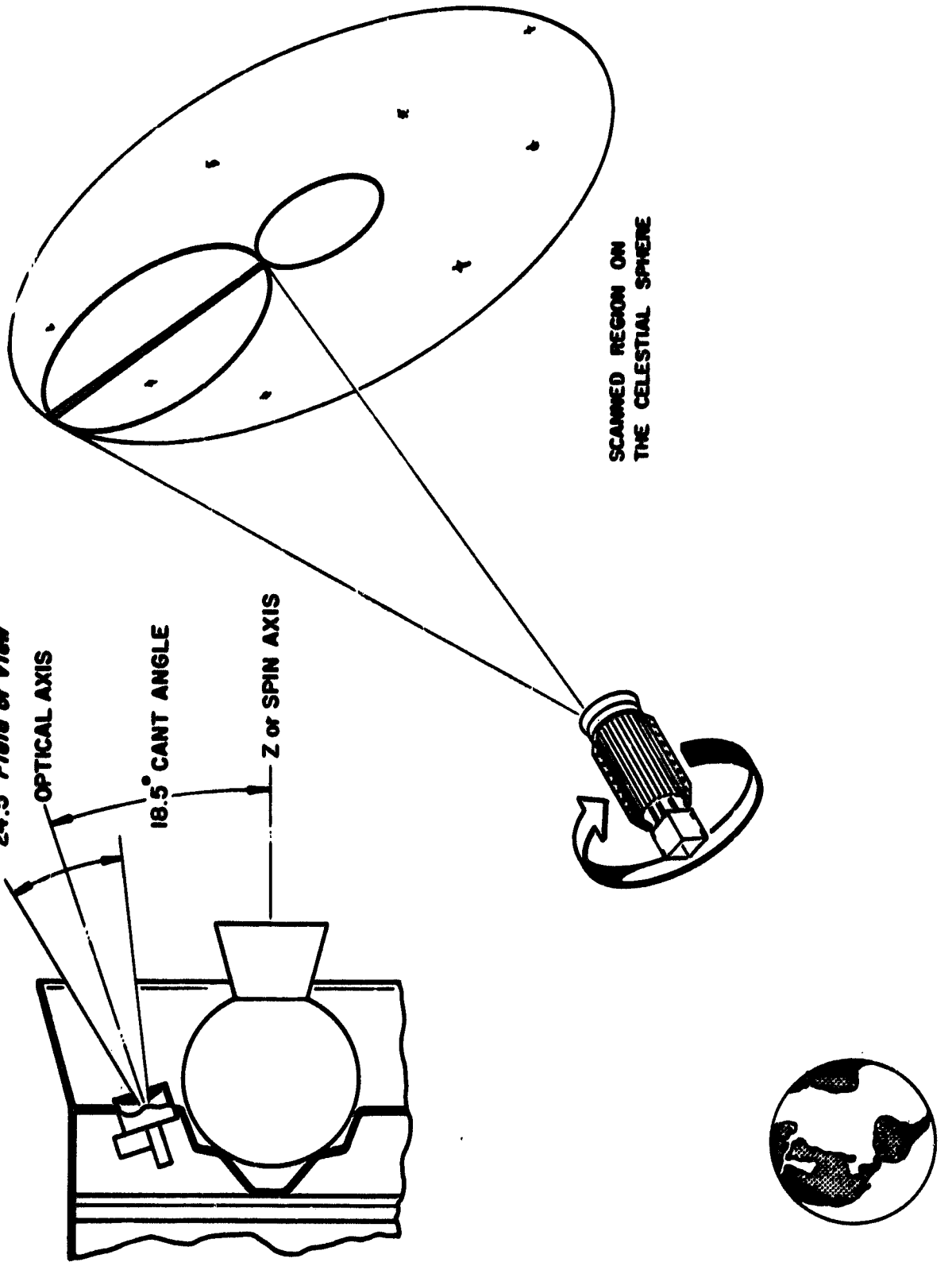


Figure 90: Pictorial Representation of Spin Mode Sensor Operation During Transfer Orbit. The inset shows a possible mounting configuration in the aft equipment module of the spacecraft.

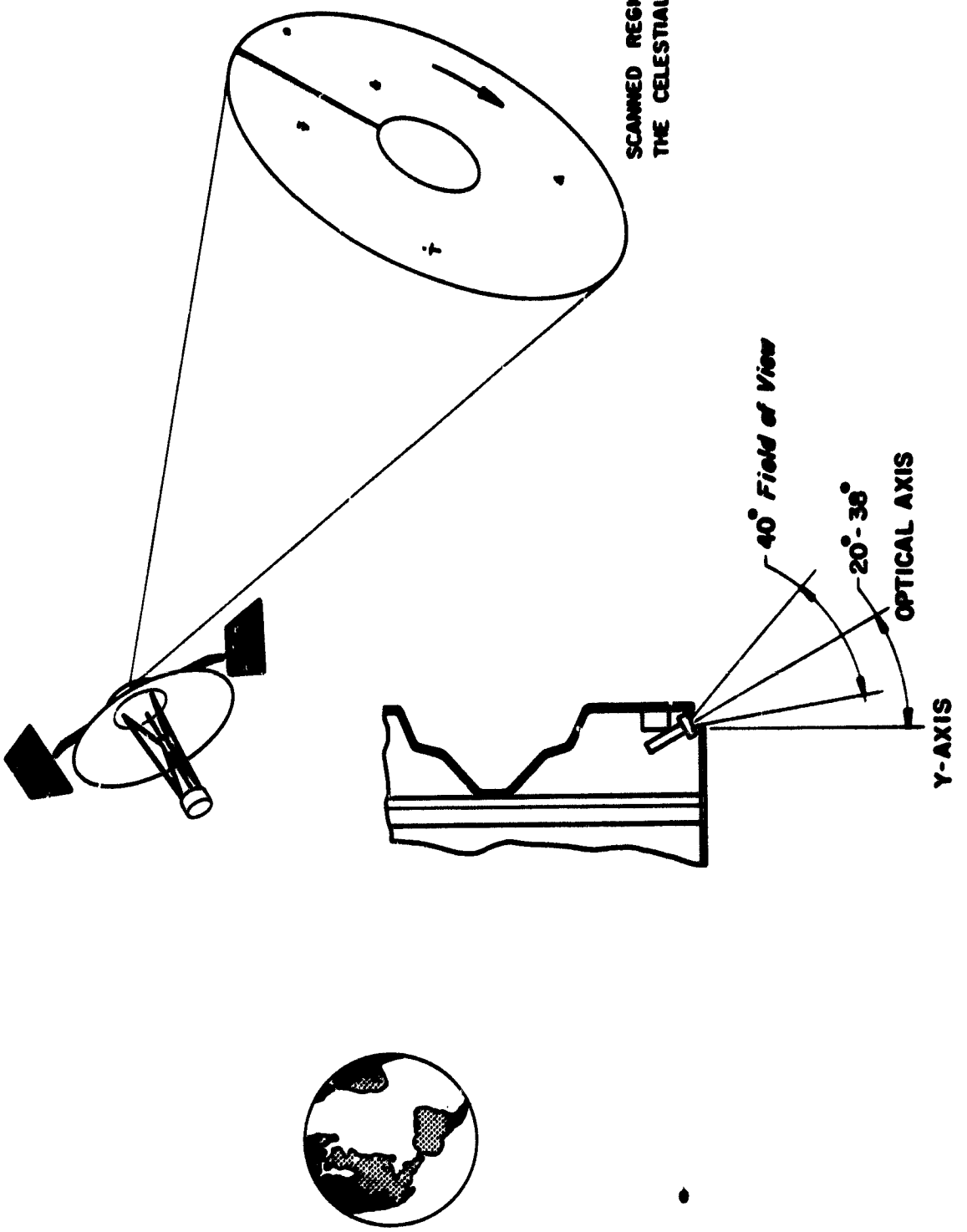


Figure 91: Pictorial Representation of Three Axis Sensor Operation. The inset shows a possible mounting configuration in the aft equipment module of the spacecraft.

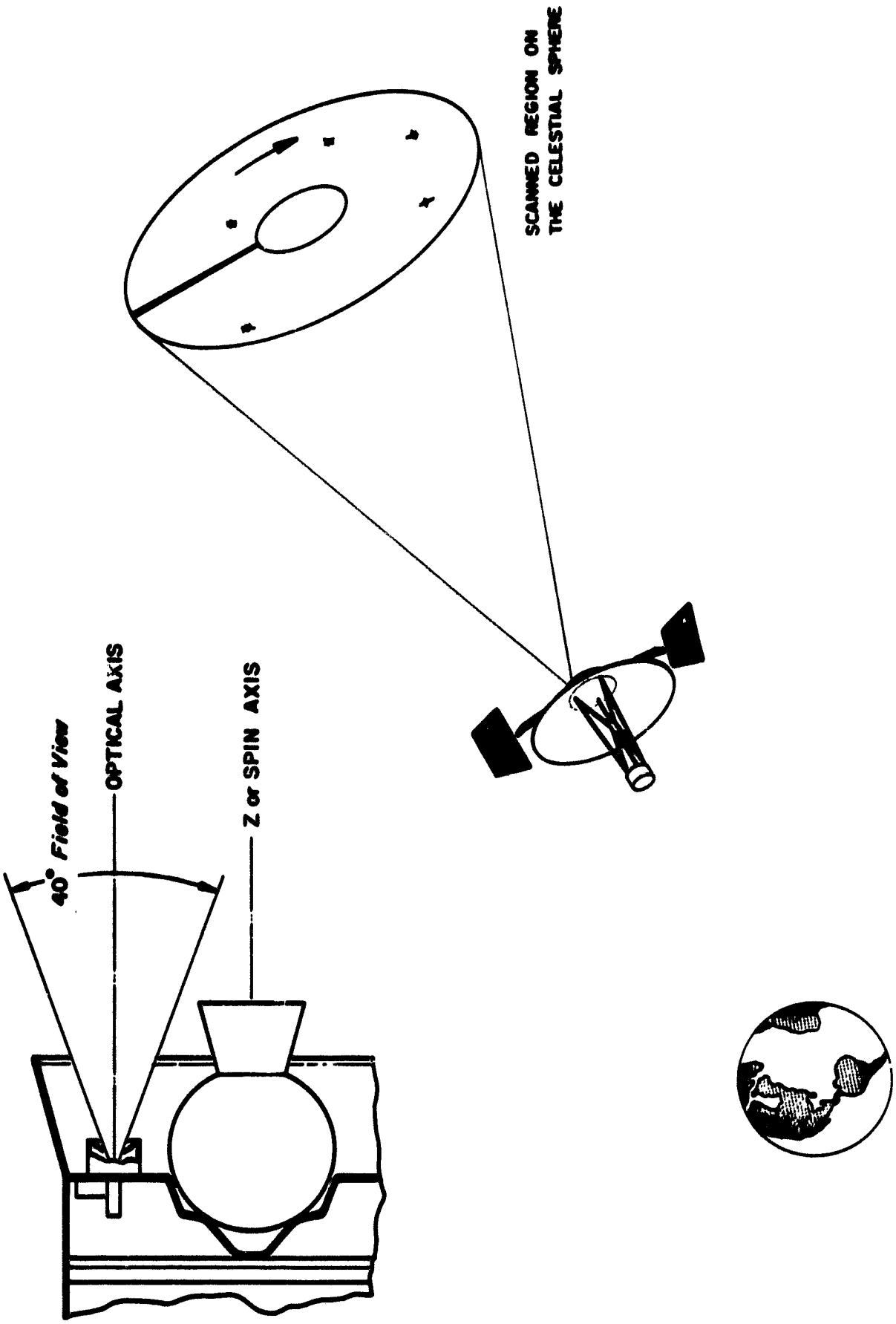


Figure 92: Pictorial Representation of Dual Mode Sensor Operation. The inset shows a possible mounting configuration in the aft equipment module of the spacecraft.

The preceding illustrations pictorially describe the recommended sensors for use during the ATS F and G missions. In each of the three systems, the designs were put through stages of optimization in order to provide the best design for the particular requirements. These optimizations were discussed in Section IV, SCADS Sensor Designs, and resulted in establishing the recommended system parameters for each of the configurations which were presented in Tables II, III, and IV.

On the basis of these parameters, the volume, weight, and power were estimated and presented in Tables V, VI, and VII for the spin stabilized mode sensor. Similar estimates made for the three axis controlled mode sensor were presented in Tables VIII, IX, and X; and for the dual mode sensor in Tables XI, XII, and XIII.

In Section V, a performance analysis was done for each of the systems to determine the probability of detection of the required number of stars on the basis of the minimum brightness, or limiting magnitude, of the stars that can be detected with each system. From this information, an error analysis was performed to give the probability of achieving the single-scan accuracy required for the spin mode and for the three-axis mode for each of the applicable sensor systems.

A complete system for the satellite to give the required attitude information throughout the mission consists of a spin mode sensor plus a three axis controlled mode sensor, or a single dual mode sensor. A comparison of the basic characteristics of these two system choices combining the appropriate data from the above mentioned tables is now summarized in Table XIV.

As seen from the entries in this table, the two configurations are remarkably similar in gross physical characteristics. However, the dual mode sensor has more difficult star detection requirements and its accuracy

TABLE XIV

Comparison of the Spin Mode Sensor-Three Axis Sensor Combination with the Dual Mode Sensor

Characteristic	Spin mode sensor Three-axis sensor (combined characteristics)	Dual mode sensor
Volume:		
sun shields excluded	95.2 cu. in.	95.4 cu. in.
sun shields included	672 cu. in.	653 cu. in.
Weight:	7.25 lbs.	7.37 lbs.
Power:	2.55 watts (three-axis mode)	2.55 watts
System Limiting Magnitude:		
Spin mode	3.84	4.65
Three-axis mode	4.21	4.65
Single-sca ccuracy:		
Spin mode ($\Sigma \leq 0.1^{\circ}$ with four stars)	97% of cases	97% of cases
Three-axis mode ($\Sigma \leq 0.01^{\circ}$ with six stars)	94% of cases	50% of cases

in the three-axis controlled state is marginal. Thus it does neither the detection task required in the spinning mode nor the precision measurement task required in the three axis mode as well as the corresponding single sensor counterpart.

A number of additional advantages accrue from the use of two sensors. First, partial redundance can increase the total system reliability over that found with the dual mode sensor. Second, the sun never intrudes into the field of view in the three-axis mode. Thus, possible solar heating of the

detector is avoided and the instrument is operational over the full synchronous orbit; this is not true for the dual mode sensor. Finally, the mounting location of the three-axis controlled mode sensor can be selected to avoid the possibility of sensor damage at the time of separation between the kick motor and the satellite.

In conclusion then, two separate SCADS sensors are recommended for the two operational phases of the ATS F & G missions.

PRECEDING PAGE BLANK NOT FILMED.

REFERENCES

1. Final Report: Feasibility Study for a Scanning Celestial Attitude Determination System, Contract No. NAS5-9577, prepared by Control Data Corporation, Research Division, for Goddard Space Flight Center, September, 1965.

2. Final Report: Breadboard Design of a Scanning Celestial Attitude Determination System (SCADS), Contract No. NAS5-9661, prepared by Control Data Corporation, Research Division, for NASA-Goddard Space Flight Center, November, 1966.

3. Final Report: Feasibility Study for a Scanning Celestial Attitude Determination System (SCADS) on the IMP Spacecraft, Contract No. NAS5-9439, prepared by Control Data Corporation, Research Division, for NASA-Goddard Space Flight Center, June, 1967.

4. Final Report: Feasibility Study of SCADS for Small Scientific Spacecraft (S^3), Contract No. NAS5-10367, prepared by Control Data Corporation, for NASA-Goddard Space Flight Center, September, 1967.

5. Grosh, C. B., "Orientation of a Rigid Torque-Free Body by Use of Star Transits," Journal of Spacecraft and Rockets, Vol. 4, No. 5, pages 562-566, 1967.

6. Battin, R. H., Astronautical Guidance, McGraw-Hill Book Company, Inc., pages 379-383, 1964.

7. Final Report: Special Techniques for Space Navigation, Subcontract 247 of Prime Contract NAS9-153, prepared by Control Data Corporation, Research Division, for Massachusetts Institute of Technology, Instrumentation Laboratory, Volume 2, page II-43, July, 1964.

8. Code, A. D., "Stellar Energy Distribution," Stellar Atmosphere, J. L. Greenstein, ed., University of Chicago Press, Chicago, Illinois, 1960.

9. Norton, R. H., "The Absolute Spectral Energy Distribution of Canopus," Technical Report No. 32-641, Jet Propulsion Laboratory, California Institute of Technology, August 15, 1964.

10. Final Report: A Theoretical Investigation of Information Limits of Scanning Optical Systems, Contract No. NAS1-4646, prepared by Control Data Corporation, Research Division, for NASA-Langley Research Center, December, 1965.

11. Skolnik, Merrill I., Introduction to Radar Systems, McGraw-Hill Book Company, Inc., page 410, 1962.

REFERENCES (continued)

12. Farrell, E. J. and C. D. Zimmerman, Optical and Electro-Optical Information Processing, MIT Press, Chapter 35, pages 642 and 646, 1965.

13. Schwartz, Misha, Information Transmission, Modulation, and Noise, McGraw-Hill Book Company, Inc., New York, page 507, 1959.

14. Papoulis, A., The Fourier Integral and its Applications, McGraw-Hill Book Company, Inc., 1962.

15. Hansen, Peter D., "New Approaches to the Design of Active Filters," The Lightning Empiricist, Vol. 13, No. 1-2, Philbrick Researches, Inc., Dedham, Massachusetts, 1965.

16. Churchill, R. V., Introduction to Complex Variables and Applications, McGraw-Hill Book Co., Inc., page 118, 1948.

17. Rice, S. O., "Mathematical Analysis of Random Noise," Bell System Technical Journal, Vols. 23 and 24, 1944-1945.

18. Technical Report AFAL-TR-322, Volume II: Space Testing of the Star Occultation Technique for Spacecraft Navigation, Contract No. AF33(615)-2127, prepared by Control Data Corporation, Research Division, for Air Force Avionics Laboratory, Wright-Patterson Air Force Base, Dayton, Ohio.

19. Reed, E. I., W. B. Fowler, C. W. Atkin, and J. F. Brun, "Some Effects of MeV Electrons on the OGO II Airglow Photometers," Goddard Space Flight Center, X-616-67-132.

20. Wolff, C., Applied Optics, Vol. 5, No. 11, page 1838, November, 1966.

GLOSSARY OF PRIMARY SCADS SYMBOLS

(Note: Symbols which are used only in specific sections of the report or in intermediate steps of a derivation are defined where they are used.)

a	clear aperture diameter of the SCADS optical system
d	overall diameter of the SCADS bright object shield
D	normalized diameter (d/a) of the bright object shield
D_{71}	integral number of elapsed days from midnight at the beginning of 1971 to midnight at the beginning of date $(D_{71} + 1)$.
e	the magnitude of the charge on the electron
$f(t)$	star pulse input to the SCADS electronic filter
Δf	noise equivalent bandwidth of the electronic filter
h	overall height of the SCADS bright object shield
H	normalized height (h/a) of the bright object shield
$H(s)$	frequency domain transfer function of the SCADS electronic filter
$h(t)$	impulse response of the SCADS electronic filter
k	argument of the error function to give a detection probability P_d
M	stellar magnitude (photographic magnitude assumed unless subscripted)
M_ℓ	limiting photographic stellar magnitude for the SCADS system
$\hat{n}$	unit vector normal to the plane of the SCADS slit as projected on the celestial sphere
N_B	number of equivalent tenth magnitude stars characterizing the background radiation
n_{BD}	the average number of photocathode emissions in time T_s due to background radiation plus dark current
N_F	the false detection rate characterizing the expected number of false star detections per scan period caused by random noise
n_s	the average number of photocathode emissions in time T_s due to a star of given magnitude
N_S	the number of radial slits in the SCADS reticle
n_T	the average number of photocathode emissions in time T_s required to reach the detection threshold level
P_d	detection probability (for a star of given magnitude)
P_{lim}	parametric stellar magnitude limit for star availability--threshold studies

GLOSSARY OF PRIMARY SCADS SYMBOLS

(continued)

$\hat{s}$	unit vector to a star of known position
S_K	sensitivity of the photomultiplier cathode to stellar radiation
$\widehat{SW}$	rotational slit width
$\frac{S}{N}$	peak signal-to-RMS noise ratio at the output of the SCADS filter
T	scan period
T_s	time interval required for the center of the star image to traverse the slit
t_{71}	fractional number of elapsed Julian days from Greenwich midnight at the beginning of 1971 to the current time in orbit
$y(t)$	star pulse output from the SCADS electronic filter
α	celestial right ascension
α^r_{spin}	reference right ascension of the spin axis at synchronous insertion
Γ	cant angle of the SCADS optical axis with respect to the scan axis
δ	celestial declination
δ^r_{spin}	reference declination of the spin axis at synchronous insertion
ϵ_u	angular uncertainty in the direction of the scan axis relative to its nominal direction
ϵ_o	efficiency of the SCADS optical system
Θ	SCADS optical field of view
Θ_{eff}	SCADS effective field of view in terms of the area scanned on the celestial sphere
θ_e	outer or exterior angular radius of the SCADS scan annulus on the celestial sphere
θ_i	inner angular radius of the SCADS scan annulus on the celestial sphere
θ_{slit}	angular length of the SCADS radial slit projected on the celestial sphere
ξ	SCADS bright object shield angle: minimum angle between the optical axis and the spacecraft-bright source line
σ	standard deviation

GLOSSARY OF PRIMARY SCADS SYMBOLS

(continued)

Σ	RMS total three-axis error in the SCADS attitude determination
Φ_{SS}	angle from the spacecraft spin axis to the sun line
ψ	angle from the SCADS scan axis to a bright celestial source
Ω	right ascension of the point of synchronous insertion
ω_c	radian frequency parameter for the SCADS electronic filter

APPENDIX A

ATTITUDE DETERMINATION FOR THE ATTITUDE CONTROLLED PHASE OF THE ATS F&G MISSION

1. GENERAL METHOD OF SOLUTION

The general problem is to find the orientation as a function of time, t, of a system fixed in a satellite whose roll, pitch, and yaw are slowly changing. This model may be applied to a satellite which is essentially stabilized along local vertical. The basic measurements which must be used to furnish this orientation are the times at which known stars lie in a slit and the angular position of the slit at these times. The method of attack of our problem used here is to derive a constraint equation of the form

$$f(\hat{s}_i, \beta_i, r(t_i), p(t_i), y(t_i)) = 0 \qquad (A\text{-}1)$$

where

$\hat{s}_i$ = unit vector in direction of the i^{th} star (known)

β_i = measured angular position of the slit at the time of transit (known)

t_i = time of transit (known)

$r(t_i)$, $p(t_i)$, and $y(t_i)$ = roll, pitch, and yaw at t_i (unknown).

Note that (A-1) is one equation in three unknowns, $r(t_i)$, $p(t_i)$, and $y(t_i)$. Hence, any number of equations of this form are useless in themselves, for new unknowns are introduced with each new measurement. To overcome this difficulty, we may assume that r(t), p(t), and y(t) are not randomly varying functions of time. Two courses are available to establish a systematic variation in roll, pitch, and yaw:

(1) Derive the differential equations that govern the motion of r, p, and y.

(2) Assume some empirical formula for r, p, and y.

APPENDIX A

We will apply the second method here; in fact, we assume

$$r = r_o + \dot{r}t$$

$$p = p_o + \dot{p}t$$

$$y = y_o + \dot{y}t$$

where r_o, p_o, y_o, $\dot{r}$, $\dot{p}$, and $\dot{y}$ are constants to be found.

Equation (A-1) is an algebraic statement of the geometry of the problem. This geometry is simply that the vector to the star, $\hat{s}_1$, and the slit plane's normal are perpendicular at the instant of transit. To write this equation then, we must express these two vectors in the same coordinate system.

2. COORDINATE SYSTEM

Seven coordinate systems will now be introduced: S_i, $i = 1, 2, \ldots, 7$. S_1 will be the celestial coordinate system. This system is most useful in order to specify the position of the stars. S_2 may be called the satellite system. Roll, pitch, and yaw will be defined with respect to this system. S_5 will then be a system fixed with respect to the satellite. Finally, S_7 will be a system fixed in the slit (which rotates with respect to the satellite).

Let us now define these coordinate systems. Let S_1 be the celestial system with associated unit vectors $\hat{i}_1$, $\hat{j}_1$, and $\hat{k}_1$ with $\hat{i}_1$ in the direction of the First Point of Aries, $\hat{j}_1$ in the equatorial plane, and $\hat{k}_1$ in the direction of the north celestial pole.

Let S_2 be a coordinate system which moves with the satellite (Figure A-1). Let $\hat{i}_2$ have the direction from the satellite to the earth's center; $\hat{j}_2$ perpendicular to $\hat{i}_2$, in the orbital plane, and such that the orbital motion is

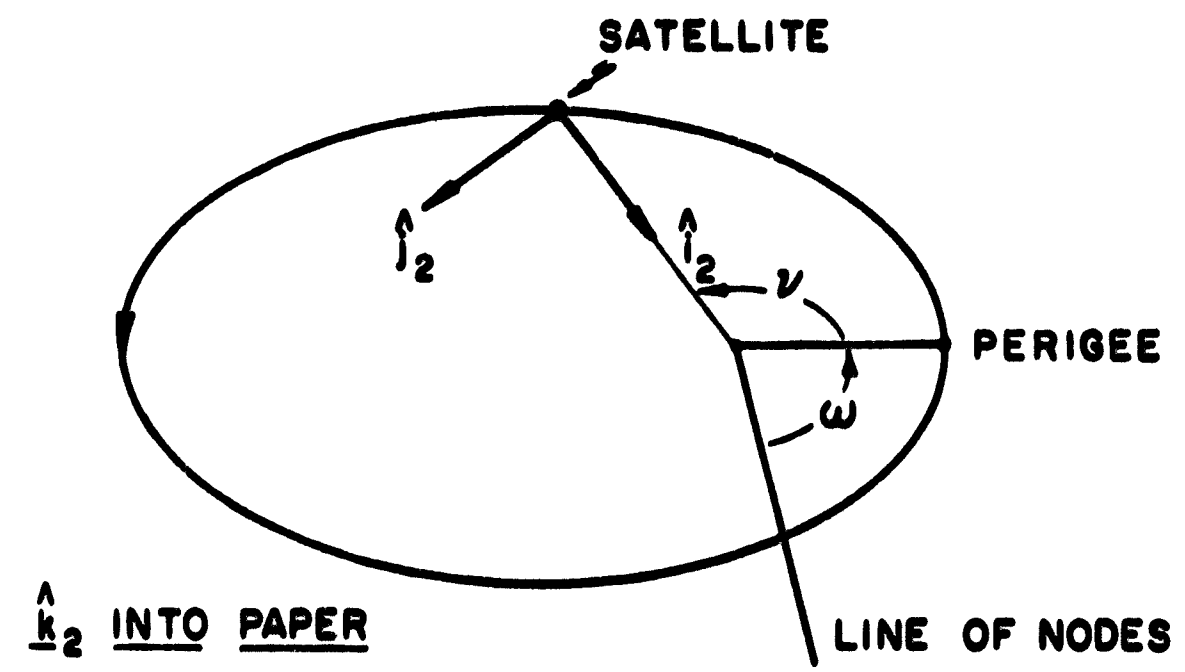


Figure A-1: The coordinate system S_2

in the direction of $\hat{j}_2$. Finally, $\hat{i}_2 \times \hat{j}_2 = \hat{k}_2$. Note that $\hat{k}_2$ has the direction of the negative orbital normal.

Now, let S_5 be a system fixed in the satellite. $S_2 \rightarrow S_5$ through three rotations: roll, pitch, and yaw (r, p, y). Thus,

$\hat{k}_2 \rightarrow \hat{k}_3$ rotation r about $\hat{j}_2 = \hat{j}_3$
$\hat{j}_3 \rightarrow \hat{j}_4$ rotation p about $\hat{k}_3 = \hat{k}_4$
$\hat{j}_4 \rightarrow \hat{j}_5$ rotation y about $\hat{i}_4 = \hat{i}_5$

The vectors $\hat{i}_5$, $\hat{j}_5$, and $\hat{k}_5$ are parallel to the position yaw, roll and pitch axes, respectively.

We now may write

$$\begin{pmatrix} \hat{i}_2 \\ \hat{j}_2 \\ \hat{k}_2 \end{pmatrix} = A \begin{pmatrix} \hat{i}_1 \\ \hat{j}_1 \\ \hat{k}_1 \end{pmatrix}, \qquad \begin{pmatrix} \hat{i}_5 \\ \hat{j}_5 \\ \hat{k}_5 \end{pmatrix} = B \begin{pmatrix} i_2 \\ j_2 \\ k_2 \end{pmatrix}$$

where

$$A = \begin{pmatrix} -\cos\Omega\cos(\omega+\nu) + \sin\Omega\cos i\sin(\omega+\nu) & -\cos\Omega\sin(\omega+\nu) - \sin\Omega\cos i\cos(\omega+\nu) & \sin\Omega\sin i \\ -\sin\Omega\cos(\omega+\nu) - \cos\Omega\cos i\sin(\omega+\nu) & -\sin\ \sin(\omega+\nu) + \cos\Omega\cos i\cos(\omega+\nu) & \cos\Omega\sin i \\ -\sin i\sin(\omega+\nu) & \sin i\cos(\omega+\nu) & -\cos i \end{pmatrix}$$

$$B = \begin{pmatrix} \cos p \cos r & \sin p & -\cos p \sin r \\ -\cos y \sin p \cos r + \sin y \sin r & \cos y \cos p & \cos y \sin p \sin r + \sin y \cos r \\ \sin y \sin p \cos r + \cos y \sin r & -\sin y \cos p & -\sin y \sin p \sin r + \cos y \cos r \end{pmatrix}$$

Here

Ω = argument of ascending node (known)

ω = argument of perigee (known)

ν = true anomaly (known)

i = inclination (known)

The angles Ω, ω, ν, and i can be calculated or are calculated as part of the satellite ephemeris. The angles r, p, and y are to be found.

The only coordinate system remaining to be defined is that which locates the slit plane with respect to S_5. To this end, let

$\hat{i}_5 \rightarrow \hat{i}_6$ rotation γ about $\hat{k}_5 = \hat{k}_6$

$\hat{k}_6 \rightarrow \hat{k}_7$ rotation β about $\hat{i}_6 = \hat{i}_7$ (Figure A-2).

Thus,

$$\begin{pmatrix} \hat{i}_7 \\ \hat{j}_7 \\ \hat{k}_7 \end{pmatrix} = C \begin{pmatrix} \hat{i}_5 \\ \hat{j}_5 \\ \hat{k}_5 \end{pmatrix}$$

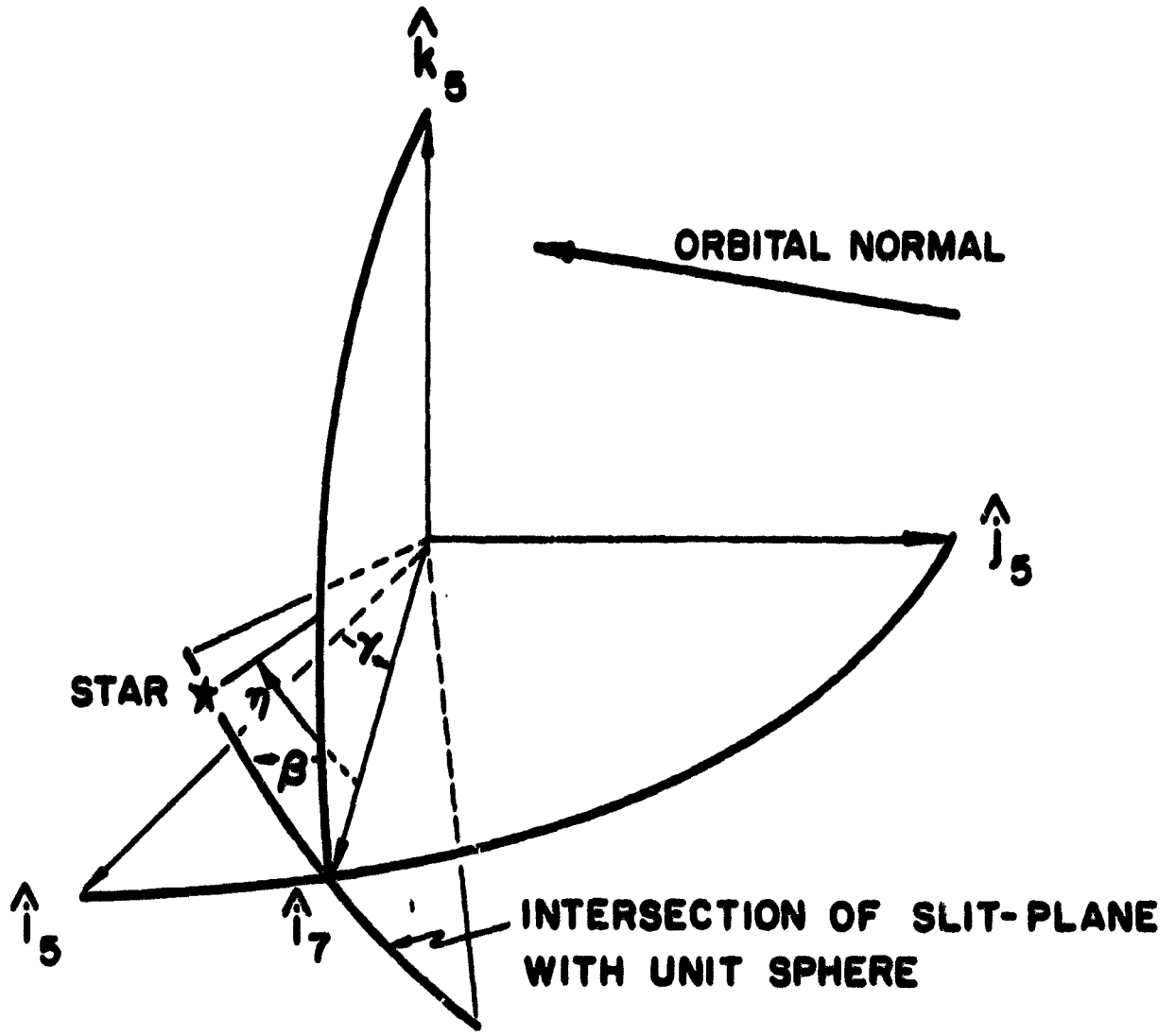


Figure A-2: The slit plane with respect to S

where

$$C = \begin{pmatrix} \cos\gamma & \sin\gamma & 0 \\ -\sin\gamma\cos\beta & \cos\gamma\cos\beta & \sin\beta \\ \cos\gamma\sin\beta & -\cos\gamma\sin\beta & \cos\beta \end{pmatrix}$$

The physical interpretation of S_7 and the angles γ and β are as follows: $\hat{i}_7$ will have the direction of the scan axis of the instrument; γ will be a fixed measured angle which defines the position of this axis in the yaw-pitch plane of the satellite; finally, the slit will be made to rotate about the scan axis and β will be computed by measuring the time a star transits the slit and utilizing the known rate of rotation of the slit about $\hat{i}_7$.

3. CONSTRAINT EQUATION

Now suppose a single slit as picture in Figure A-2 is utilized. Let this slit rotate with respect to S_5 with its axis of rotation coincident with $\hat{i}_7$. As this slit rotates stars will transit the slit, and at the instant of transit the rotational position of the slit, β (Figure A-2), may be computed by utilizing the known rotation rate of the slit. Thus, at the instant a star appears in the slit we may write

$$\hat{s} = \cos\eta\ \hat{i}_7 + \sin\eta\ \hat{k}_7$$

where η = elevation of star with respect to S_7 at the instant the star transits (not measured).

But we may also write

$$\hat{s} = \cos\delta\cos\alpha\ \hat{i}_1 + \cos\delta\sin\alpha\ \hat{j}_1 + \sin\delta\ \hat{k}_1$$

where δ = declination of the star (known)

α = right ascension of the star (known).

Thus, the instant the star appears in the slit, we may write

$$\begin{pmatrix} \cos \eta \\ 0 \\ \sin \eta \end{pmatrix} = C\ B\ A\ \hat{s} \qquad \text{(A-2)}$$

where $\hat{s}$ is expressed with components in S_1. Since η is not measured, we choose to eliminate this parameter from (A-2). Hence,

$$0 = C_2\ B\ A\ \hat{s} \qquad \text{(A-3)}$$

where C_i = i^{th} row of C.

Equation (A-3) now represents one equation in the three unknowns, r, p, y. These three angles are slowly varying functions of time. It appears we may write

$$\begin{aligned} r &= r_o + \dot{r}t \\ p &= p_o + \dot{p}t \\ y &= y_o + \dot{y}t \quad (t \text{ measured}) \end{aligned} \qquad \text{(A-4)}$$

where r_o, p_o, y_o, $\dot{r}$, $\dot{p}$, and $\dot{y}$ are constants. Equation (A-4) is a good approximation for time intervals on the order of five minutes. However, (A-4) may have to be revised after more information on the stabilization system is obtained. Thus, with this assumption, Equation (A-3) becomes one equation in six unknowns. A minimum of six transits of at least three stars is necessary for a solution. If more than six transits are obtained, a least squares solution may be sought.

APPENDIX B

DATA SHEETS FOR EMR-541N AND EMR-543N PHOTOMULTIPLIERS

PRECEDING PAGE BLANK NOT FILMED.

MODEL 541N-01-14
PRELIMINARY SPEC
MARCH, 1966

I PHYSICAL CHARACTERISTICS

Number and type of dynodes:	14; venetian-blind; Ag-Mg
Maximum overall length (unpotted):	3.94 inch (100 mm)
Typical weight (unpotted):	71 grams
Window material:	7056 glass
Cathode sensitive area:	1 in. (25 mm) diameter, area = .786 in^2
Cathode type:	Semitransparent: bi-alkali

	Note	Minimum	Typical	Maximum	Units
II. PHOTOCATHODE CHARACTERISTICS	1				
Quantum efficiency (Q) at 4100 Å		18	21.5		%
Cathode luminous sensitivity (S_k)		55	72.0		μA/lm
Cathode peak radiant sensitivity (σ_k)		.059	.071		A/W
Typical quantum efficiency					See Fig. 1
III. MULTIPLIER PHOTOTUBE CHARACTERISTICS, DC	1				
Voltage required for current amplification (G) of:					See Fig. 2
10^4			1690		V
10^5			2280		V
10^6			2950	3400	V
Dark current (i_D) at a current amplification of:					
10^5	1,2		2.6×10^{-12}		A
10^6			2.5×10^{-11}	1×10^{-10}	A
10^7			2.5×10^{-10}		A
Anode luminous sensitivity (S) at a current amplification of 10^6		55	72.0		A/lm
Anode peak radiant sensitivity (σ) at a current amplification of 10^6		59,000	71,000		A/W
Equivalent anode dark current input at current amplification of 10^6	1				
Luminous, (E_D)			3.5×10^{-13}	1.8×10^{-12}	lm
Radiant at 4200 Å ($\mathcal{E}_D$)			3.5×10^{-16}	1.7×10^{-15}	W

EMR PHOTOELECTRIC DIVISION
ELECTRO-MECHANICAL RESEARCH, INC.
BOX 44 • PRINCETON, NEW JERSEY 08540

APPENDIX B

MODEL 541N-01-14
PRELIMINARY SPEC
MARCH, 1966

		Note	Minimum	Typical	Maximum	Units
	Equivalent noise input at current amplification of 10^6	1				
	Luminous, (E_N)			3.9×10^{-14}	1.0×10^{-13}	lm
	Radiant at 4100 Å, ($\mathcal{E}_D$)			4.0×10^{-17}	1.0×10^{-16}	W
IV.	MULTIPLIER PHOTOTUBE CHARACTERISTICS, PULSE	1				
	Dark current counts at a current amplification of 10^6 at 20°C	2, 3		125		Pulses /sec
	Pulse height resolution (FWHM) for Cs^{137}, NaI (Tl)	4		8.0		%
	MAXIMUM RATINGS	5				
	Supply voltage				3600	V
	Anode current				.3	mA
	Ambient temperature				150	°C

I.	ENVIRONMENTAL	
	Shock	100 g, 11 millisecond duration
	Vibration	30 g, 20 to 3,000 cps
	Temperature	-55°C to 150°C
II.	PACKAGING	
	Potted weight (typical)	170 grams Normally packaged in a 1-3/8" O.D. x 4-1/4" length fiberglass housing.

NOTES:
1. All data at room temperature = 20°C.
2. Measured after dark current stabilization.
3. Discriminator bias at 1/4 of the average single electron pulse height.
4. Harshaw scintillation crystal, NaI (Tl) Type D, size: 1 in. x 1 in., S/N BY 591
5. Absolute maximum ratings, prolonged exposure at maximum ratings may result in permanent deterioration of tube performance.

EMR PHOTOELECTRIC DIVISION
ELECTRO-MECHANICAL RESEARCH, INC.
BOX 44 • PRINCETON, NEW JERSEY 08540

MODEL 541N-01-14
PRELIMINARY SPEC
MARCH, 1966

TYPICAL SPECTRAL RESPONSE CHARACTERISTICS

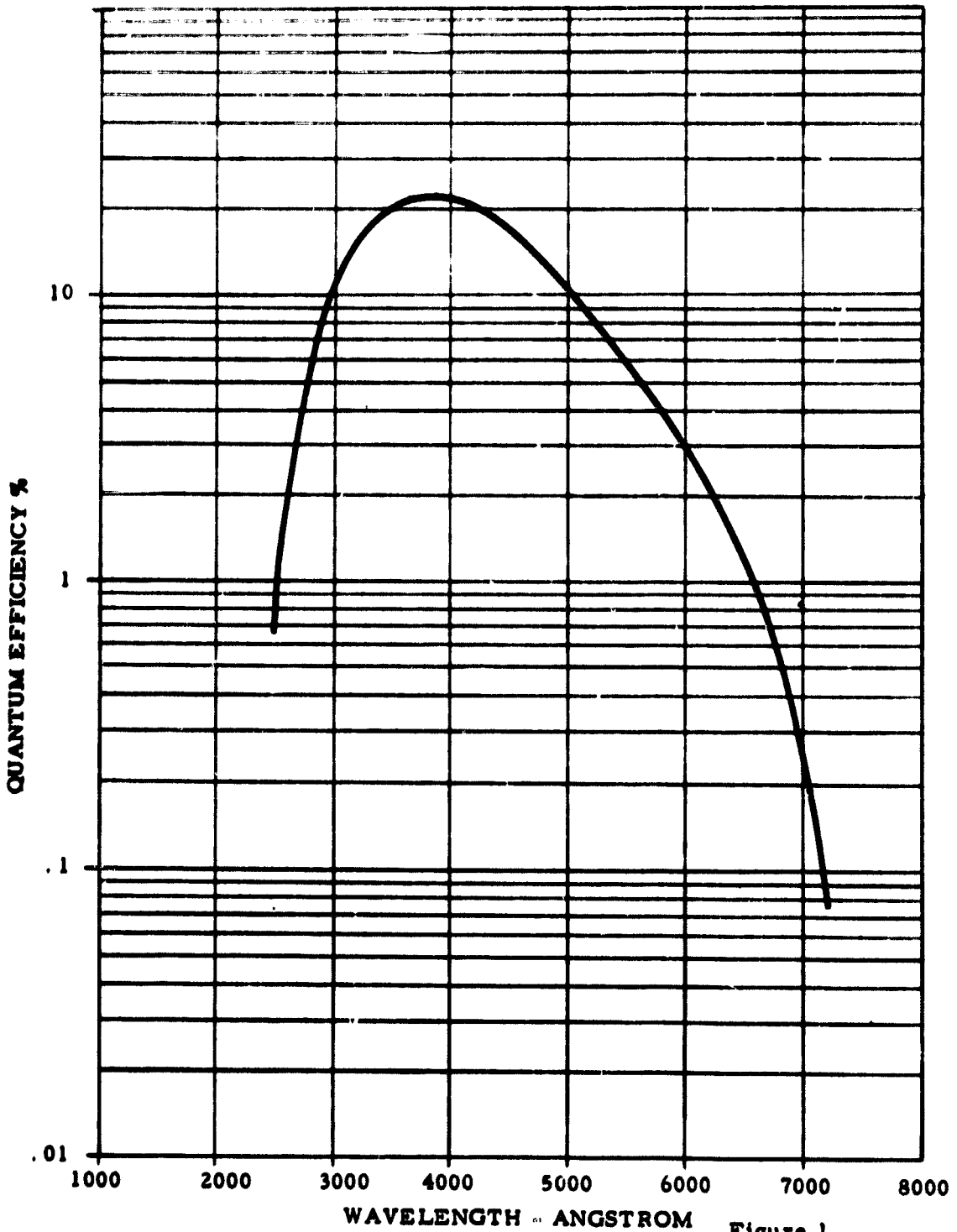


Figure 1

EMR PHOTOELECTRIC DIVISION

ELECTRO-MECHANICAL RESEARCH, INC
BOX 44 • PRINCETON, NEW JERSEY 08540

MODEL 541N-01-14
PRELIMINARY SPEC
MARCH, 1966

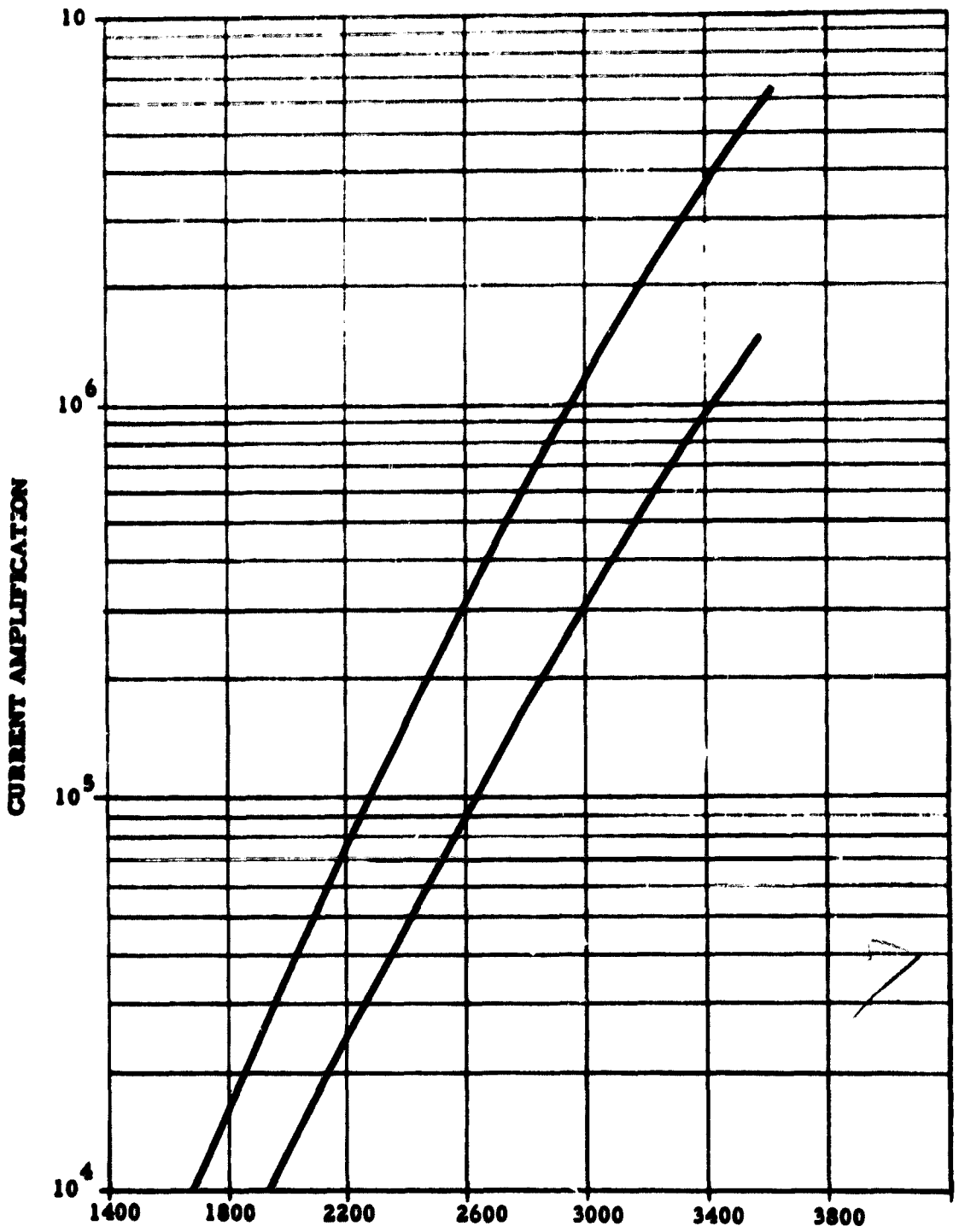
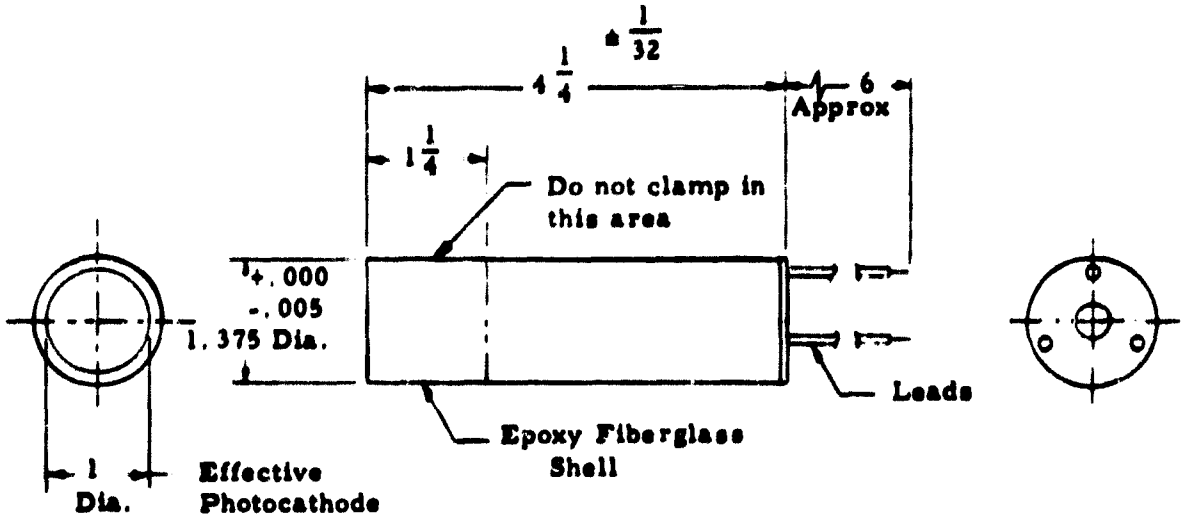


Figure 2

EMR PHOTOELECTRIC DIVISION
ELECTRO-MECHANICAL RESEARCH, INC.
BOX 44 • PRINCETON, NEW JERSEY 08540

MODEL 541N-01-14
PRELIMINARY SPEC
MARCH, 1966



NOTES:
1. Resistor values equal thru-out unit

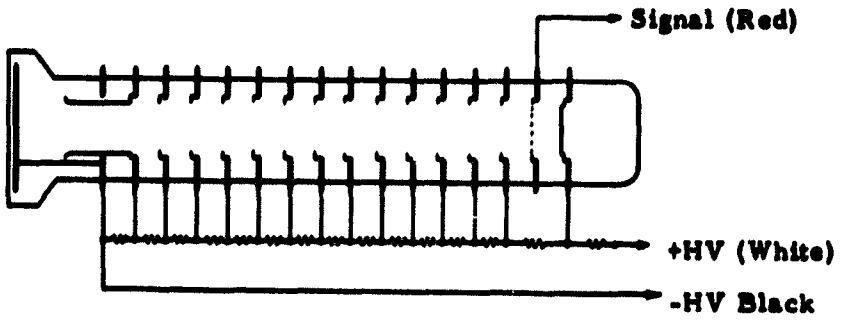


Figure 3

PHOTOELECTRIC DIVISION
ELECTRO-MECHANICAL RESEARCH, INC.
BOX 44 • PRINCETON, NEW JERSEY 08540

PRELIMINARY SPECIFICATION DATA
MODEL 543N-01-14 MULTIPLIER PHOTOTUBE

I. PHYSICAL CHARACTERISTICS

Number and type of dynodes:	14; venetian-blind; Ag-Mg
Maximum overall length (unpotted):	6.50 inch
Typical weight (unpotted):	188 grams
Window material:	7056 glass
Cathode sensitive area:	1.7 in. diameter (area = 2.5 sq. in.)
Cathode type:	Semitransparent: bi-alkali

II. PHOTOCATHODE CHARACTERISTICS

	Note 1	Minimum	Typical	Maximum	Units
Quantum efficiency (Q) at 4100 Angstroms			18.0		%
Quantum efficiency at 6300 Angstroms			.89		%
Cathode luminous sensitivity (S_k)			55.2		μA/lm
Cathode peak radiant sensitivity (σ_k)			.060		A/W
Typical Multiplier Phototube Response and Quantum Efficiency					See Fig. 1

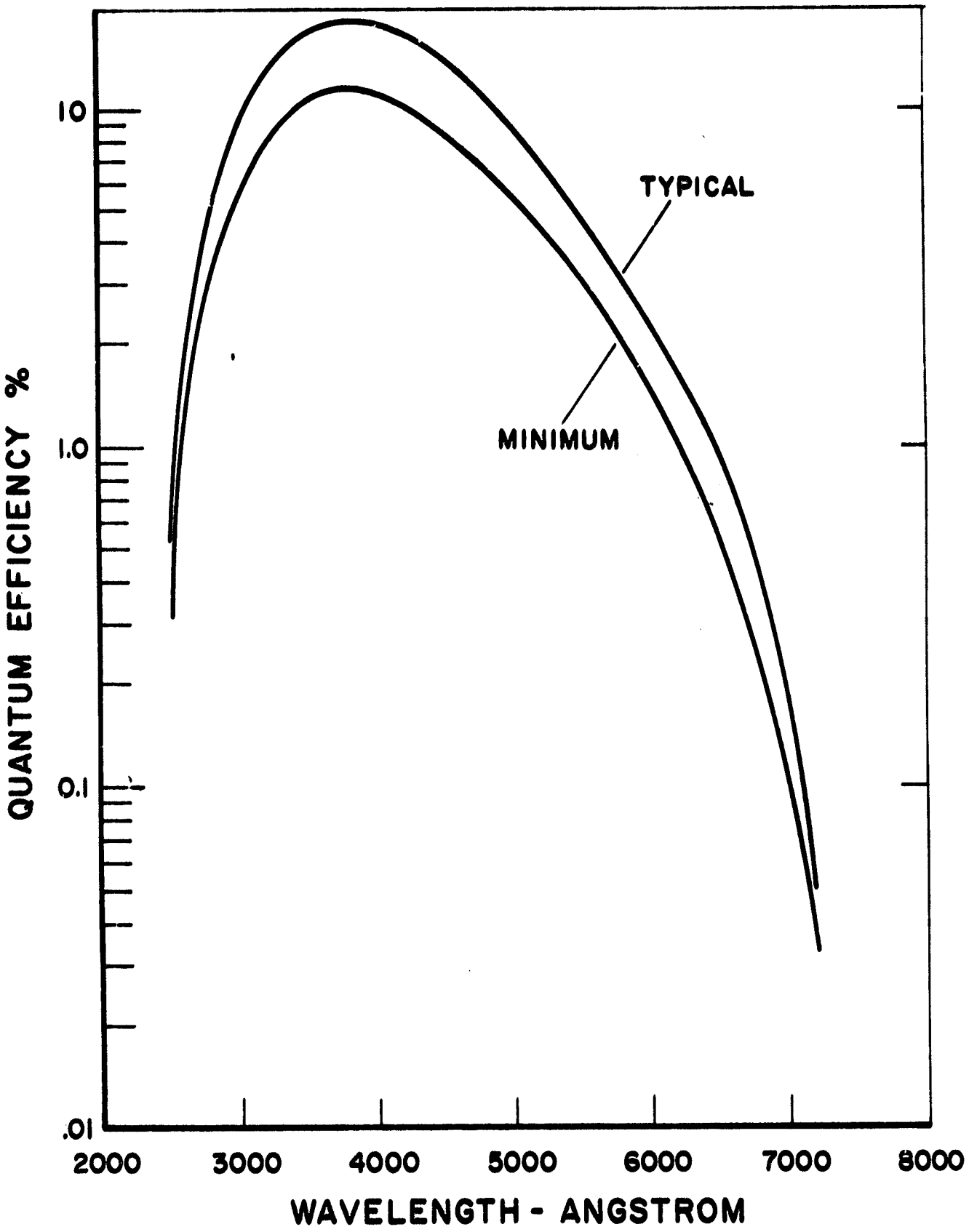
III. MULTIPLIER PHOTOTUBE CHARACTERISTICS, DC

		1			See Fig. 2
Voltage required for current amplification (G) of:	10^4		1418		V
	10^5		1951		V
	10^6		2657		V
	10^7		3313		V
Dark current (i_D) at a current amplification of:	10^5	1, 2	2.4×10^{-12}		A
	10^6		2.1×10^{-11}		A
	10^7		2.6×10^{-10}		A

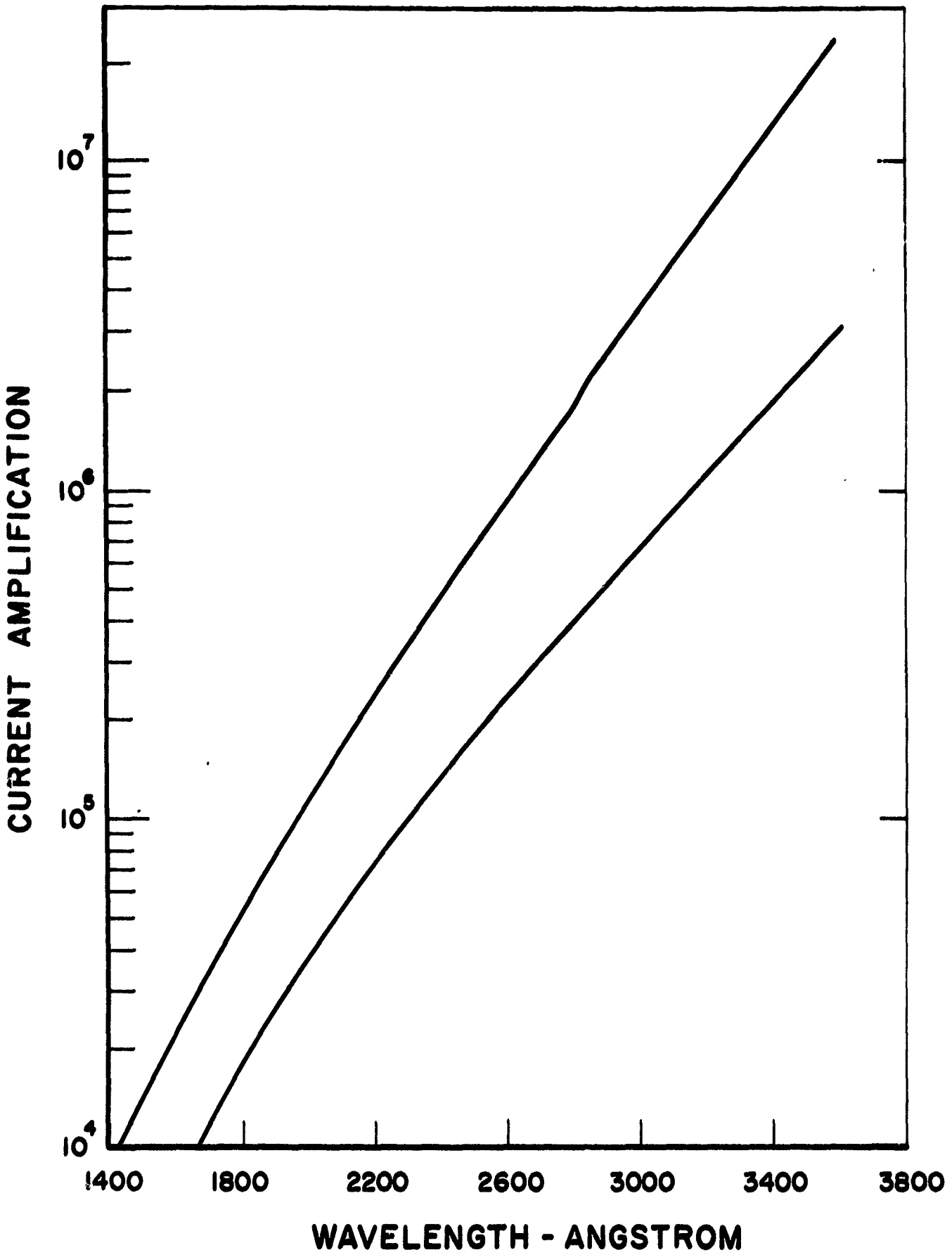
		Note	Minimum	Typical	Maximum	Units
	Anode luminous sensitivity (S) at a current amplification of 10^6			55.2		A/lm
	Anode peak radiant sensitivity (σ) at a current amplification of 10^6				60,000	A/S
	Equivalent anode dark current input at current amplification of 10^6	1				
	Luminous, (E_D)			3.8×10^{-13}		lm
	Radiant at 4100 Angstroms (ϵ_D)			3.5×10^{-16}		W
	Equivalent noise input at current amplification of 10^6					
	Luminous, (E_N)			4.6×10^{-14}		lm
	Radiant at 4100 Angstroms, (ϵ_D)			4.25×10^{-17}		W
IV.	MULTIPLIER PHOTOTUBE CHARACTERISTICS, PULSE	1				
	Dark current count at a current amplification of 10^6 at 20°C	2, 3		200		Pulses per sec.
	Pulse height resolution (FWHM) for Cs^{137}, NaI(Tl)	4		7.80		%
V.	MAXIMUM RATINGS	5				
	Supply voltage			3600		V
	Anode current			1.0		mA
	Ambient temperature			150		°C

		Note	Minimum	Typical	Maximum	Units
VI.	ENVIRONMENTAL					
	Shock			50 g, 11 millisecond duration		
	Vibration			20 g, up to 3,000 cps		
	Temperature			-55°C to 150°C		
VII.	PACKAGING			Normally packed in a 2" O.D. x 7-3/16 length Fiberglass housing		
	Potted weight (typical):			385 grams		

NOTES:
1. All data at room temperature = 20°C.
2. Measured after dark current stabilization.
3. Discriminator bias at 1/4 of the average single electron.
4. Harshaw scintillation crystal, NaI (Tl) Type D, size: 2 in. x 2 in.x S/N 7PA6.
5. Absolute maximum ratings, prolonged exposure at maximum ratings may result in permanent deterioration of tube performance.



SPECTRAL RESPONSE CHARACTERISTICS
EMR 543N-01-14



VOLT-AMPERE CHARACTERISTICS
EMR 543N-01-14

APPENDIX C

PHOTOMULTIPLIER NOISE INDUCED BY EXPOSURE TO THE VAN ALLEN BELTS

Here we may be guided by NASA Goddard experience with the OGO II air glow photometers. The main body photometer used a EMR 541 E-05M, a one inch diameter end-on tube with a tri-alkali cathode on a sapphire window [C1]. The orbit was polar with apogee near 1500 kilometers and perigee near 400 kilometers.

The photocathode current in this photometer was observed to vary from 5×10^{-16} to 3.3×10^{-9} amperes with the maximum occurring in low latitudes near 1500 kilometers (L = 1.23). "It was not a simple increase in dark current level, but consisted of a multitude of pulses and tended to persist after the radiation levels had decreased."

Since L = 1.23 corresponds about to the maximum of the inner belt of fast electrons from the "starfish explosion" it is natural to attribute the effects to these fast electrons. We thus examine some of the possible ways in which these could cause noise in the photomultiplier.

1. BREMSSTRAHLUNG

Bremsstrahlung (X-rays) due to fast electrons cause photo-emissions by the photoelectric effect (below .05 mc^2 in carbon, .1 mc^2 in aluminum), the Compton effect and by pair production (important at about 10 mc^2 in lead, 30 mc^2 in aluminum). This could be very serious in that the resulting X-rays are very penetrating and it could happen that attempts to shield against the fast electronics would only increase the X-ray production.

Consequently, we next estimate the amount of Bremsstrahlung we might expect from a given amount of shielding.

APPENDIX C

a. X-ray Production by Bremsstrahlung in Aluminum

We assume:

1) normally incident mono-energetic electrons of energy E_o on an infinite slab of thickness X_1 centimeters;

2) we can neglect all energy loss mechanisms except ionization and excitation.

Number of photons which appear at $X = X_1$ is

$$n = N \int_0^a \int_{E_{min}}^{E(X)} e^{-\frac{X_1 - X}{\tau(k)}} \phi_k \frac{dk}{E_o - \mu} dX \qquad (C\text{-}1)$$

where

$$\phi_k \frac{dk}{E_o - \mu} \cdot (\mu = mc^2)$$

is the cross section for emission of a photon in the range k, k + dk.

$\tau(k)$ is the range for photons in aluminum. $\tau(k)$ was actually taken from the graphs of range given by Johnson (Satellite Environment Handbook) [C2] and was approximated by

$$\log \tau(k) = .440 \log k + 1.224$$

$$k > 5.5 \times 10^{-2} \text{ MeV}$$

$$= 2.760 \log k + 4.126$$

$$k < 5.5 \times 10^{-2} \text{ MeV} \qquad (C\text{-}2)$$

To find E(X) recourse was had to an empirical equation for range given in the American Institute of Physics Handbook [C3].

$$R = .412\ E^{n}\ gm/cm^2$$

$$n = 1.265 - .0954\ \ell n\ E$$

$$.01 \leq E \leq 2.5\ MeV \qquad (C\text{-}3)$$

$$R = .530\ E - .106\ gm/cm^2$$

$$2.5 \leq E \leq 20\ MeV$$

We take n = 1.181 in first approximation and define,

$$H(X) = \left(\frac{X}{.412}\right)^{\frac{1}{1.181}} \qquad X < 1.219\ gm/cm^2$$

$$= \frac{X + .106}{.530} \qquad X \geq 1.219\ gm/cm^2 \qquad (C\text{-}4)$$

Then

$$E(X) = H(X_o - X) \qquad (C\text{-}5)$$

where X_o is the range of electrons of incident energy E_o.

E_{min} was taken as $.1\ mc^2$ reasoning that photons of energy much less than this would not excape. Finally, X_2 was taken as the solution of

$$E(X_2) = E_{min} = .1\ mc^2$$

and a was defined as

$$a = Min\ (X_1, X_2), \qquad (C\text{-}6)$$

which is just to say that an electron is followed until it either has energy less than $.1\ mc^2$ or it passes through the slab.

$\phi_k \frac{dk}{E_o - \mu}$ was taken from Heitler [C4]. The non-relativistic approximation and the extreme relativistic approximation with complete screening (Thomas-Fermi model) were used with the changeover at $E = mc^2$. The calculations were repeated for total photon energy radiation putting $k\phi_k$ for ϕ_k.

The number, N, of Bremsstrahlung photons coming through an aluminum shield of thickness $X_1 = .25, .688$, and 2.5 gms/cm^2 per incident fast electron is plotted in Figures C-1 through C-3 as is the energy radiated per incident fast electron, both as a function of incident energy.

The average photon energy as a function of incident energy appears in Figure C-4. It may be noted that the shielding is not very effective against the X-rays, and the number of photons per incident electron as a function of shielding thickness with incident energy as a parameter is plotted in Figure C-5.

The results indicate that photon energies of about an MeV are typical and that below 2.5 gms/cm^2 of aluminum less than one photon per incident electron is produced. There is a tendency for the number of photons to increase with shielding thickness up to a certain thickness for electrons of a given energy (i.e., thickness 1.6 gm/cm^2 at $E_o = 2$ MeV) and to decrease thereafter.

The nature of these results appears to rule out Bremsstrahlung as a major contribution, particularly when we consider the results of the Van de Graaff simulation of the OGO II environment by Reed et al. [C1]. On bombardment of the photometer by 2.6 MeV electrons the dark current is observed to decrease exponentially with the shielding thickness. (See their Figure 8.) If Bremsstrahlung were the major contribution an initial dark current increase would occur according to Figure C-5. Thus, fast electrons and protons which penetrate the shielding are the likely cause of the

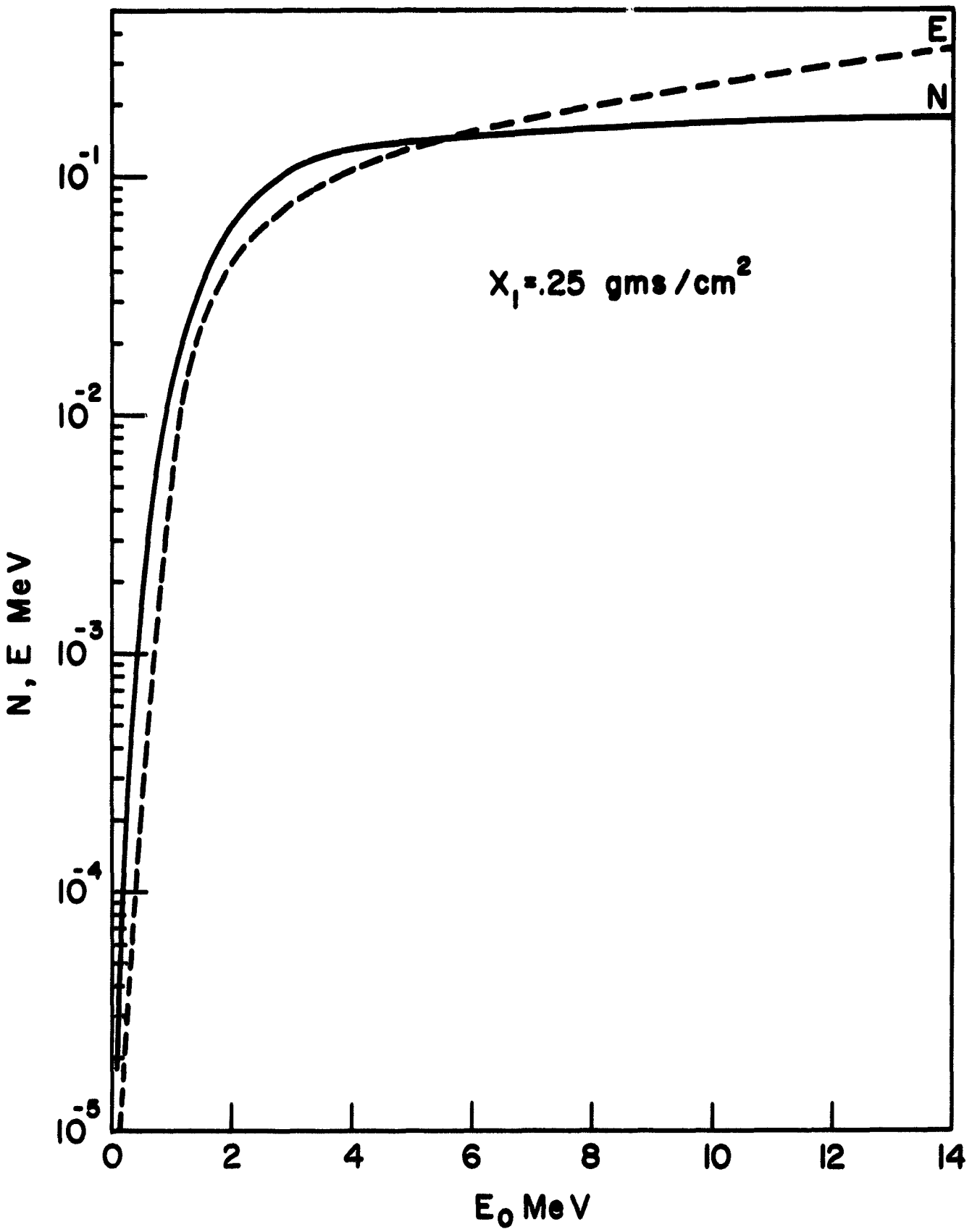


Figure C-1: Number (N) of photons and energy (E) radiated Bremsstrahlung. Data for X_1 = 0.688 gms/cm^2.

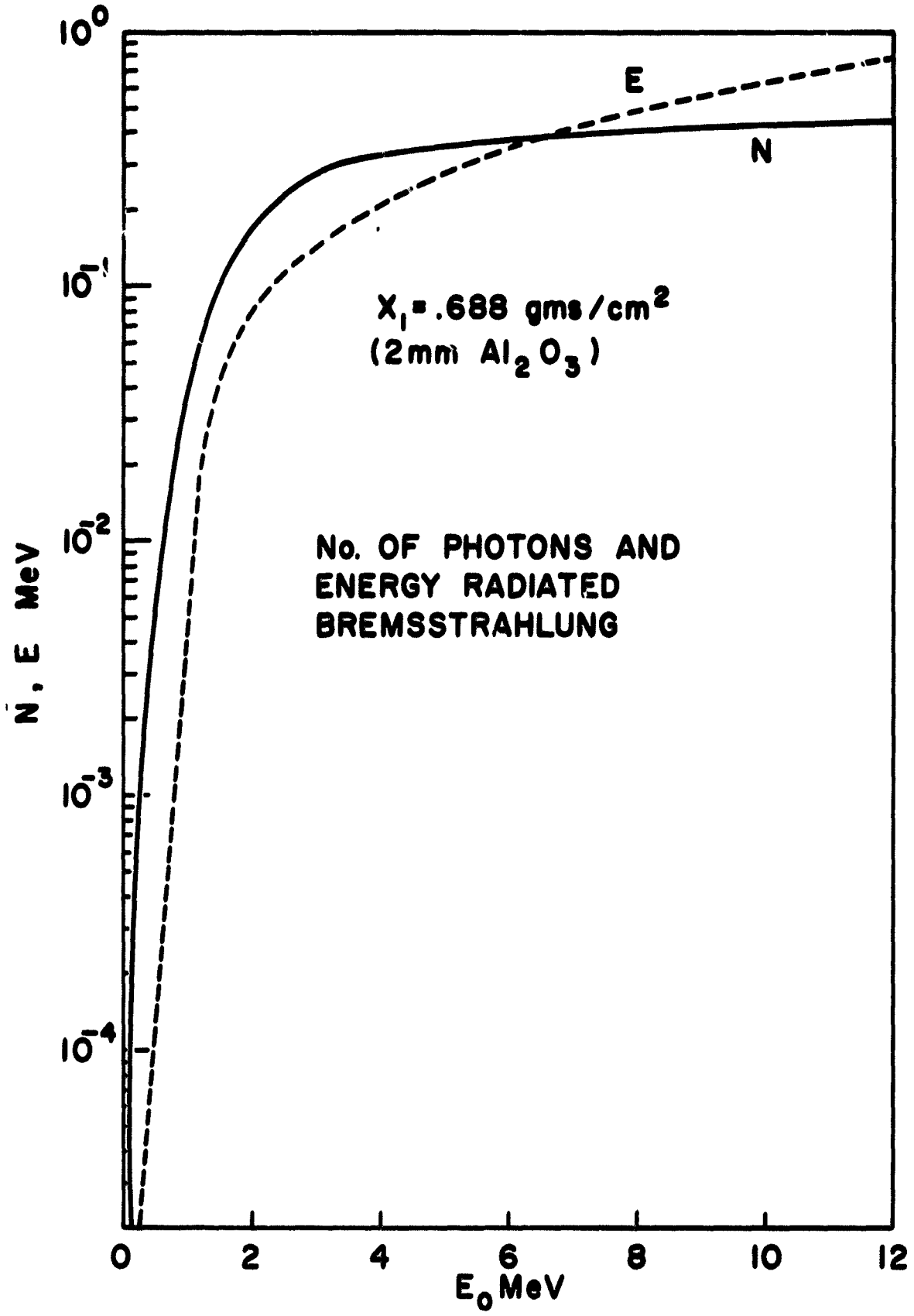


Figure C-2: Number (N) of photons and energy (E) radiated Bremsstrahlung. Data for X_1 = 0.688 gms/cm^2.

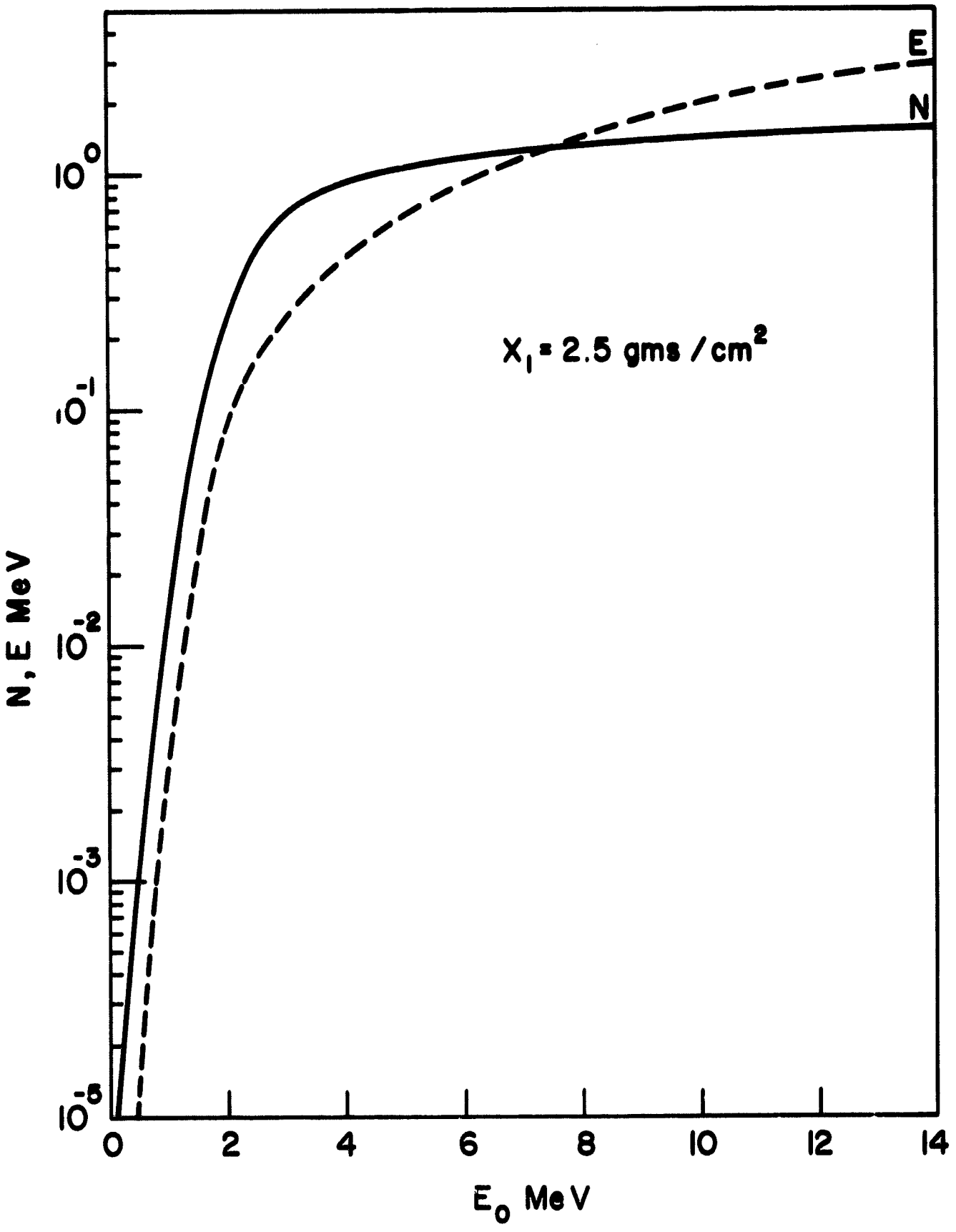


Figure C-3: Number (N) of photons and energy (E) radiated Bremsstrahlung. Data for X_1 = 2.5 gms/cm^2.

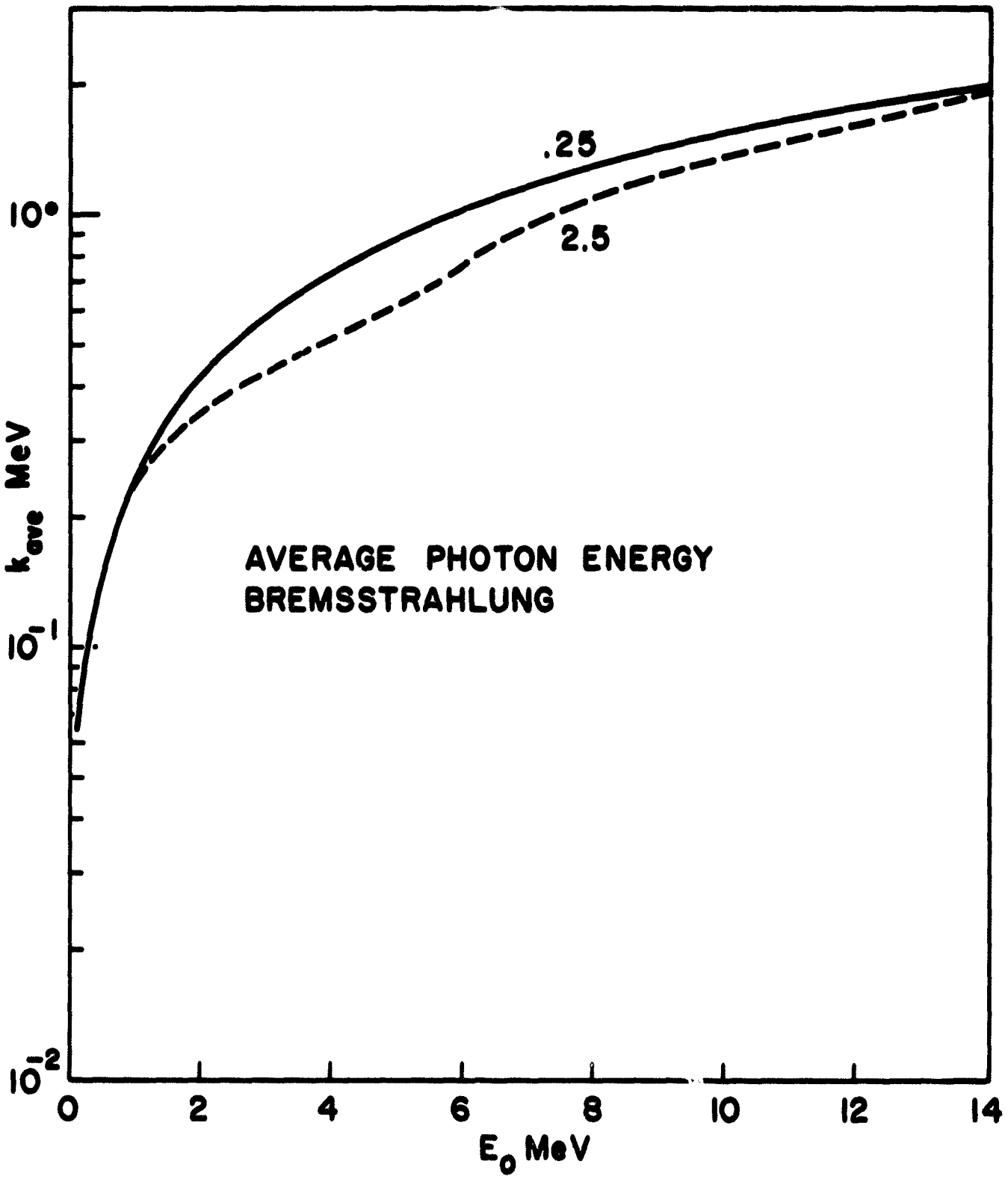


Figure C-4: Average photon energy Bremsstrahlung.

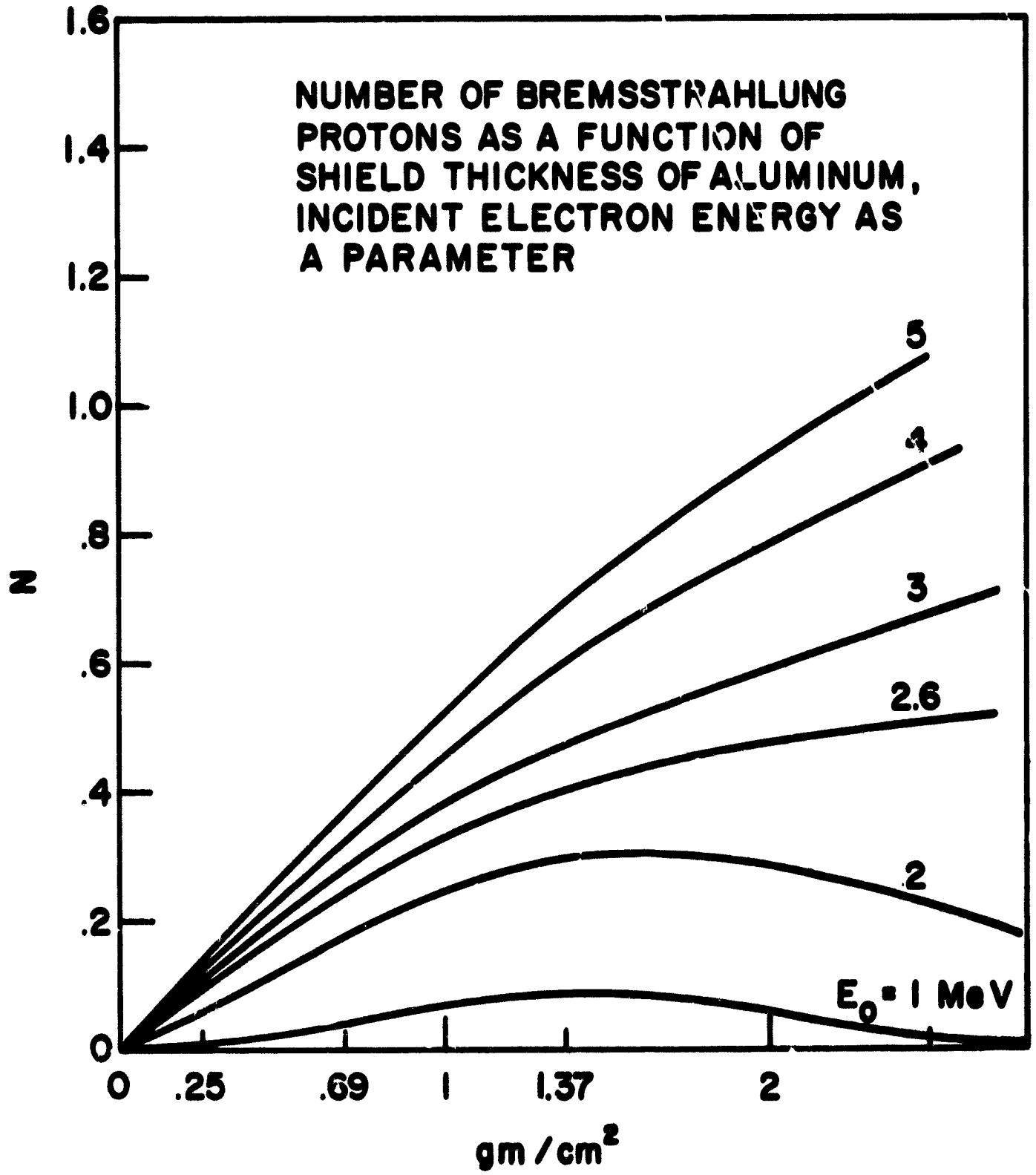


Figure C-5: Number of Bremsstrahlung protons as a function of shield thickness of aluminum. Incident electron energy is parametric.

observed noise.

2. CERENKOV RADIATION

A. T. Young [C5] has studied the noise due to Cerenkov pulses in an end-on photomultiplier caused by the muon component of cosmic rays traversing the face plate. He reports a minimum of about 50 photoelectrons for each Cerenkov pulse. Thus, the Cerenkov radiation caused by fast electrons in the face plate might have been a major factor in the photometer noise observed in the OGO photometer.

Moreover, the experiments of the NASA group clearly established that the photocathode and the first few dynodes were the sensitive element. C. Wolff [C6] finds the radiation induced noise proportional to cathode area and concludes that either the lens elements or the photocathode was the sensitive element. NASA experiments failed to detect luminescence of the optics.

The rate of Cerenkov radiation per unit path length in the wavelength band $(\omega, \omega + d\omega)$ is given (e.g. Schiff [C7]) by

$$\frac{dE}{dx} = \frac{e^2}{c^2}\left(1 - \frac{1}{n^2\beta^2}\right)\omega d\omega \qquad \text{(C-7)}$$

where n = refraction index

ω = angular frequency

$\beta = v/c$

v is electron velocity

c is light velocity

If n is the average number of photons produced at frequency ω

$$\frac{dn}{dx} = \frac{1}{\hbar\omega}\frac{dE}{dx} \qquad \text{(C-8)}$$

where $\bar{h} = \frac{6.62 \times 10^{-27}}{2\pi}$ erg sec.

Equations (C-7) and (C-8) given

$$\frac{dn}{dx} = \frac{2\pi e^2}{\bar{h}c} \left(1 - \frac{1}{n^2 \beta^2}\right) \Delta\nu_{12} \text{ photons/incident electron} \qquad \text{(C-9)}$$

where $\Delta\nu_{12} = \frac{1}{\lambda_1} - \frac{1}{\lambda_2}$

and $\lambda_{1,2}$ is the wavelength at angular frequency, $\omega_{1,2}$.

For a single electron incident on the photomultiplier window at energy E_o, the total number of photons generated would be

$$n = \frac{2\pi \Delta\nu_{12}}{137} \int_{E_{min}}^{E_o} \left(1 - \frac{1}{n^2 \beta^2(E)}\right) \frac{dx(E)}{dE} \, dE \qquad \text{(C-10)}$$

Of course,

$$\frac{E_{min}}{mc^2} = \sqrt{1 + \frac{1}{n^2 - 1}} - 1 \quad ,$$

$$\beta^2 = \frac{t(t+2)}{(t+1)^2} \quad ,$$

where $t = E/mc^2$, and we have put $e^2/\bar{h}c = 1/137$.

In evaluating (C-10) the relation between x and the energy E(x) would be the same as in the section on Bremsstrahlung.

Then, to find the total number of Cerenkov photons produced in the Van Allen belts it is necessary to average over the electron energy distribution and overall photocathode window orientations.

The computation can be simplified somewhat. In Figure C-6 the factor $1 = 1/n^2\beta^2$ appearing in Equation (C-10) is plotted for sapphire ($n_2 = 1.796$ at 5000 Angstroms), and noted to rise rapidly from zero at $E_{min} \approx .204\ mc^2$, reaching almost its asymptotic value at $E = 2mc^2$(1 MeV). We therefore approximate this factor as zero below E_{min} and constant thereafter. Then, Equation (C-10) becomes,

$$n \approx \frac{2\pi\ \Delta\nu_{12}}{137} \left(1 - \frac{1}{n^2}\right) L_{ave}, \qquad \text{(C-11)}$$

where L_{ave} must now be suitably chosen.

If the photocathode window thickness is ℓ and its radius R, the thickness (path length) averaged over all orientations is found to be,

$$\ell_{ave} = \frac{2\ell}{\pi\sqrt{1 + c^2}}\ \ell n\ \frac{(\sqrt{1 + c^2} + 1 - c)(\sqrt{1 + c^2} + c)}{(\sqrt{1 + c^2} - 1 + c)(\sqrt{1 + c^2} - c)}, \qquad \text{(C-12)}$$

where $c = \frac{2\ell}{\pi R}$.

If ℓ = 2 mm and R = ½ inch, ℓ_{ave} = .392 cm = 1.73 gm/cm^2 (sapphire with density 3.50 gms/cm^3).

In the radiation belts electron energy distributions seem to fit a relation like

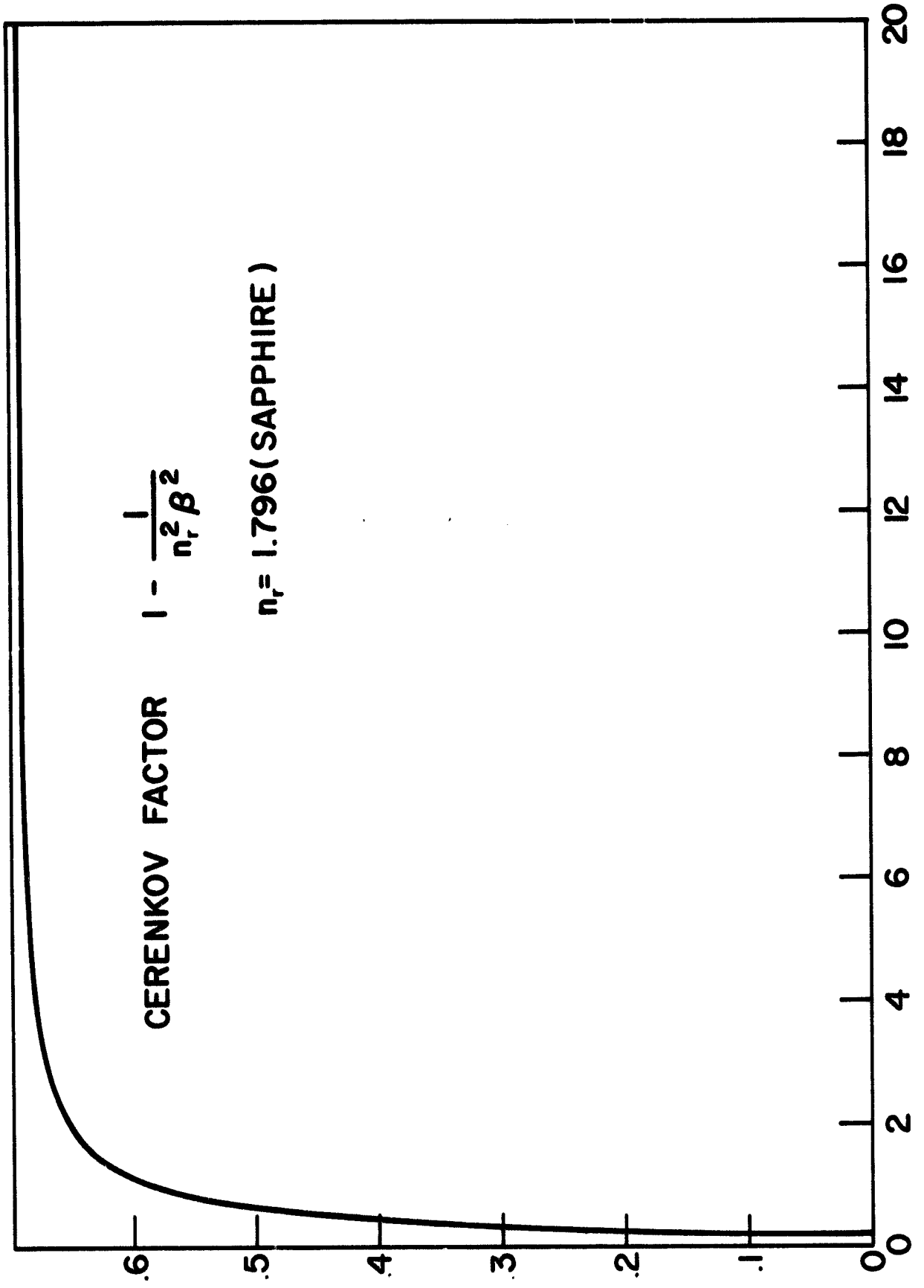


Figure C-6: Cerenkov factor for sapphire.

$$\frac{d\phi}{dE} = a\,\phi_o\, e^{-aE} \text{ electrons/cm}^2\text{sec MeV} \qquad \text{(C-13)}$$

We are thus led to put for L_{ave} in Equation (C-11) something like

$$L_{ave} = \frac{\int_{E_{min}}^{\infty} e^{-aE}\, X(E)\, dE}{\int_{E_{min}}^{\infty} e^{-aE}\, dE} \qquad \text{(C-14)}$$

X(E) is taken as in Equation (C-3) as,

$$X(E) = .412\, E^{1.181} \text{ gm/cm}^2, \quad E \leq 2/5 \text{ MeV}$$

$$= .530\, E - .106 \text{ mg/cm}^2, \text{ otherwise} \qquad \text{(C-3a)}$$

To Equation (C-3a) we further add the restriction that,

$$X(E) \leq \ell_{ave}, \qquad \text{(C-15)}$$

where ℓ_{ave} comes from Equation (C-12).

Then Equation (C-14) becomes

$$L_{ave} = \frac{\int_{E_{min}}^{E_{max}} e^{-aE}\, X(E)\, dE + \int_{E_{max}}^{\infty} e^{-aE}\, \ell_{ave}\, dE}{\int_{E_{min}}^{\infty} e^{-aE}\, dE} \qquad \text{(C-16)}$$

E_{max} is found using $\ell_{ave} = 1.73$ gm/cm^2 in (C-3a) as, $E_{max} = 2.79$ MeV, a

result which suggests that we can just as well use only the first of Equation (C-3a) in (C-16) and obtain,

$$L_{ave} = \frac{a^{-\alpha}\left\{\gamma(\alpha,\ aE_{max}) - \gamma(\alpha,\ aE_{min})\right\}}{\frac{\ell_{ave}}{a}\, e^{-aE_{max}} - \frac{1}{a}\, e^{-aE_{min}}} \qquad \text{(C-17)}$$

where $\alpha = 2.181$ and $\gamma(\alpha, X)$ is an incomplete gamma function.

Vette [C8] has published a model for the inner and outer belt electrons. From his Figure 36 (page 20), which we reproduced as Figure C-7, we find that at the peak of the inner belt the integral omnidirectional flux is,

$$\phi(> E) = 2.8 \times 10^{8}\ e^{-1.035E}/cm^{2}\ sec \qquad \text{(C-18)}$$

Thus, a = 1.035, and we find after evaluating the gamma functions,

$$L_{ave} = 16.74 \times 10^{-2}\ gm/cm^{2}$$
$$= 4.784 \times 10^{-2}\ cm\ ,$$

and the average path length is less than ½ millimeter.

The minimum amount of shielding around OGO II main body photometer was about 60 mils or .4 gm/cm^{2} (cf. their Figure 3). Thus, from Figure C-8, range of electrons in aluminum, they are shielded for about 1 MeV electrons. From Figure C-7 (Vette's AE-2 environment) at L = 1.25 there are about $\phi = 10^{8}$ electrons/cm^{2}sec of energy greater than 1 MeV. If A is the projected cathode area

$$A = \frac{\pi R^{2}}{2} \quad .$$

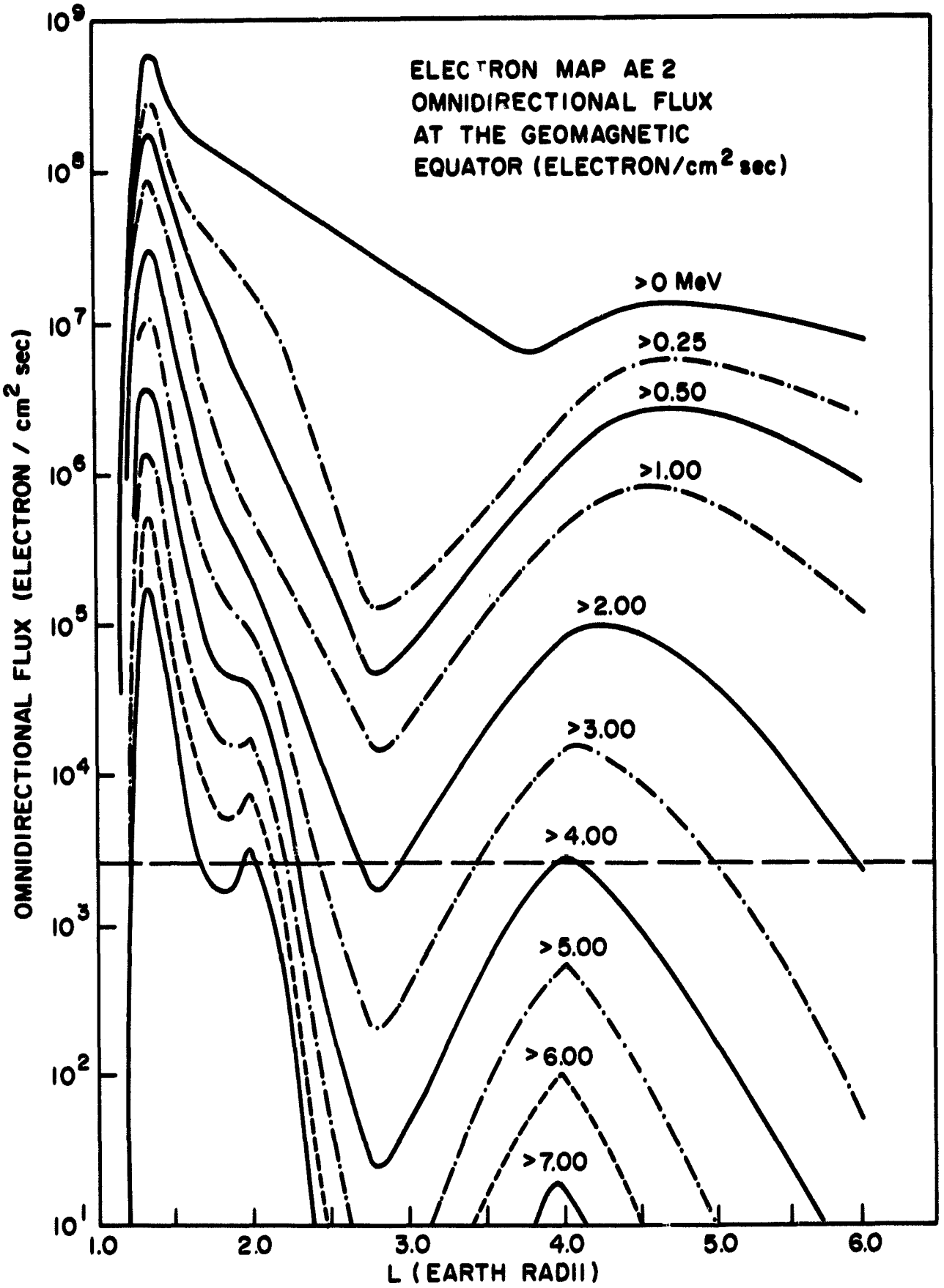


Figure C-7: Electron map AE2. Omnidirectional flux at the geomagnetic equator (electron/cm^2sec).

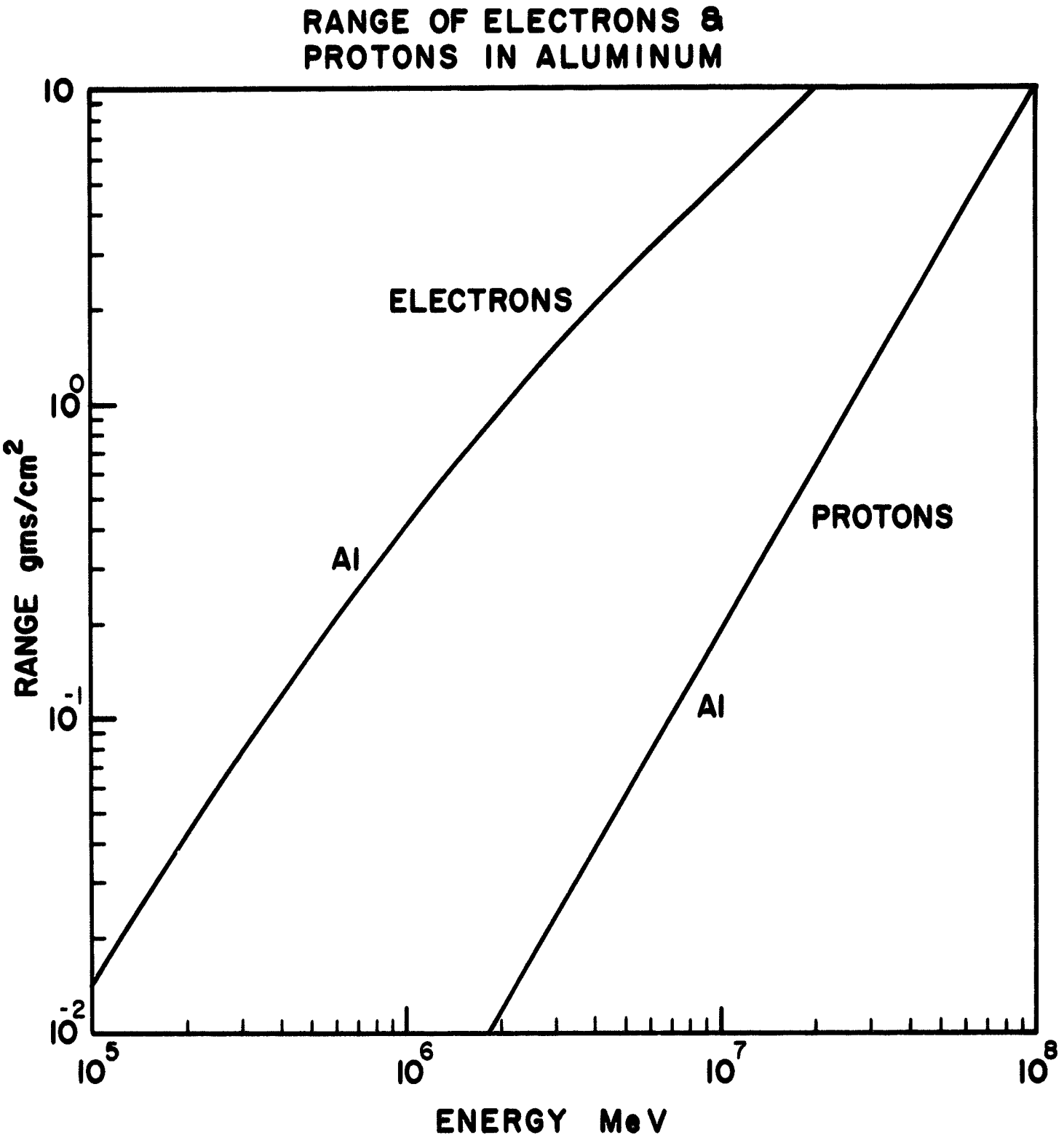


Figure C-8: Range of electrons and protons in aluminum

APPENDIX C

The Cerenkov wave fronts travel in the electron direction. Thus, only photons from electrons traveling toward the photocathode in the face plate cause photo-events.

The quantum efficiency, E_q, of the 541E-05M over the wavelength band 1500 to 5000 Angstroms is about 20%.* Then the number of expected photo-electrons due to Cerenkov radiation in the inner belt would be,

$$N = \phi_o \frac{\pi R^2}{4} E_q \frac{2\pi \nu_{12}}{137} \quad 1 - \frac{1}{n^2} \quad L_{ave} \tag{C-19}$$

Taking λ_1 = 1500 Angstroms, λ_2 = 5000 Angstroms we have with $\phi_o = 10^8$, R = 1.27, E_q = .2, n = 1.796, L_{ave} = .0478

$$N = 1.78 \times 10^9/\text{sec} \tag{C-20}$$

A photocathode current of 3.3×10^{-10} ampere or 2.06×10^{10} electrons per second was observed. We conclude the Cerenkov radiation fails by about a factor of 10 to explain the noise.

3. LUMINESCENCE

The NASA group [C1] tested the luminescence of various window materials on irradiation with 50 KeV electrons from an electron microscope and by a millicurie Sr^{90} source. We will use the data from each experiment, in turn testing whether luminescence of the cathode window material caused by fast electrons can account for the OGO II results.

According to Heitler [C4] in the region where the dominant loss mechanism for fast particles in matter is by collisions, the average energy loss is

---

* Figure C-9.

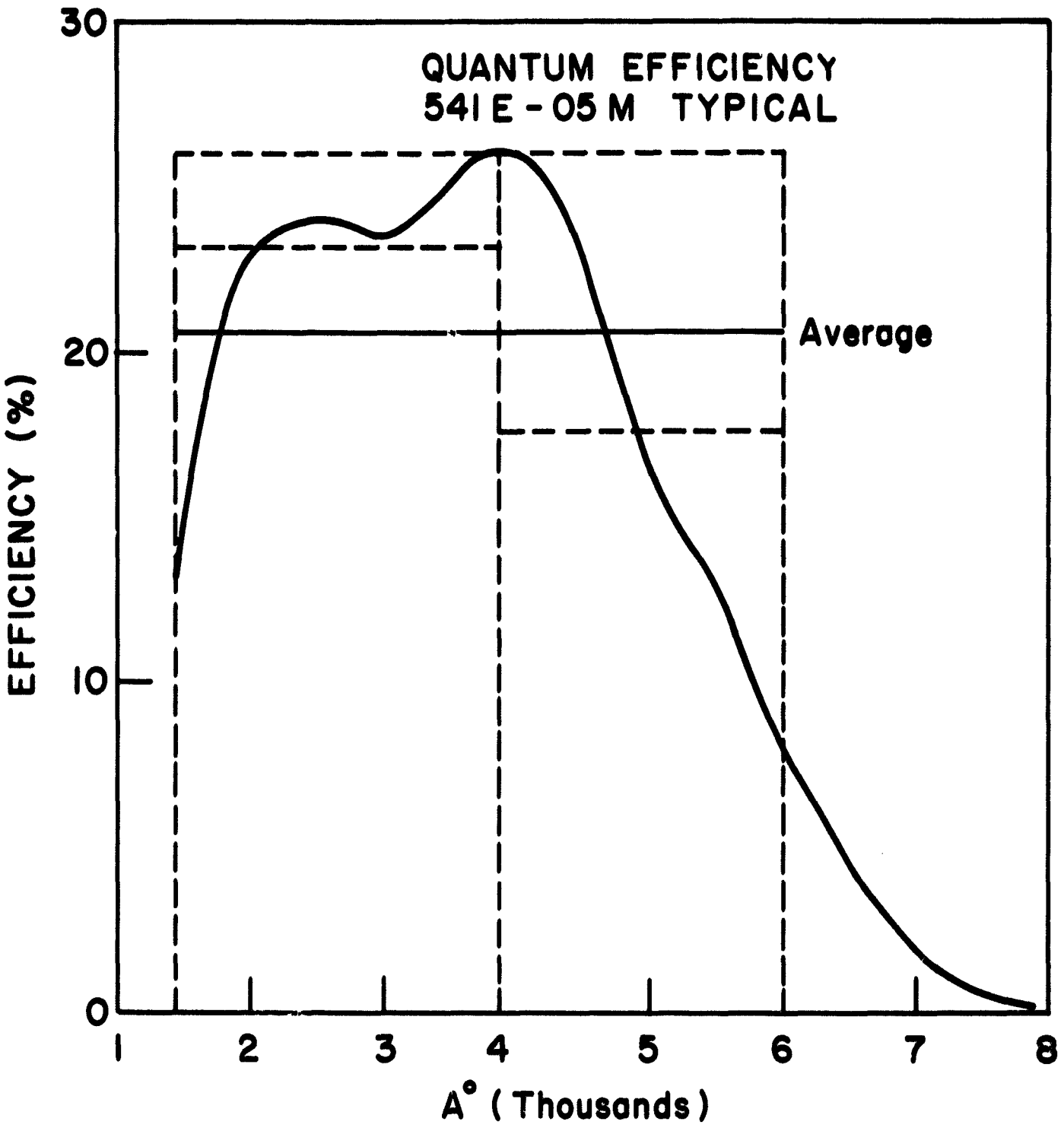


Figure C-9: Spectral quantum efficiency (typical) of the EMR 541E-05M photomultiplier tube.

"very nearly proportional" to the number of primary ion pairs formed. The ratio of ionizations to excitations and the average energy transfer per ion pair are nearly independent of primary energy. About one primary ion pair is formed for each 32 eV of energy loss practially independent of the particle type. Of course primary ions (or electrons) subsequently produce secondaries.

Mott and Gurney [C9] discuss the production of luminescence in solids. In speaking of irradiation with α and β rays (presumably at moderate energies) they observe that most of the energy dissipation is by production of electron-hole pairs which subsequently recombine at impurity centers, Frenkel and Schottky defects, or at the surface where they either transfer their energy to the lattice atoms or radiate on recombining. A discussion of the mechanisms by which electrons and holes lose their excess energy is given.

The assumption, which the preceding few paragraphs are used here to justify, is that the radiance per incident particle is proportional to its energy loss.

4. ELECTRON MICROSCOPE DATA

On irradiation of sapphire with 10^8 50 KeV electrons/cm^2sec, radiance of 10^{-4} ergs/sec cm^2 steradian was observed in the band 3500 to 4100 Angstroms. That is, per 50 KeV electron, an energy

$$E \approx \frac{\pi}{2} \times 10^{-14} \text{ ergs/Angstrom} \qquad \text{(C-21)}$$

was radiated into 2π steradians in the visible and ultra-violet.

We assume that the main body photometer is shielded for 1 MeV and that the energy distribution of electrons in the inner belt is given by Equation (C-13) and the environment is Vettes' AE-2. This neglects belt

decay as indeed we have previously done.

The average energy above an MeV is,

$$1 + \frac{1}{a}\ \text{MeV} = 1 + \frac{1}{1.035}\ \text{MeV} \quad .$$

Of this on the average, an MeV is lost in the shielding so that the average energy of electrons incident on the photometer cathode window was about

$$E_{ave} \approx 1/1.035\ \text{MeV} \qquad \text{(C-22)}$$

Over the wavelength band 1500 to 6000 Angstroms, the 541E-05M typically has a quantum efficiency E_q of about 20%. Midband wavelength, λ_{ave}, is 3750 Angstroms and band width is 3500 Angstroms. The density of electrons above an MeV is again taken as 10^8/sec cm^2. Then the expected number of photo-events is,

$$n_{pe} = \frac{\pi}{2} R^2 \phi_o E \left(\frac{E_{ave}}{5 \times 10^{-2}} \right) E_q \frac{\lambda_{ave}}{hC} \Delta\lambda \qquad \text{(C-23)}$$

Using (C-21) and (C-22) in (C-23) with the data of the previous paragraph,

$$n_{pe} \approx \frac{2}{3} \times 10^{10}/\text{sec} \quad . \qquad \text{(C-24)}$$

This is within a factor of 3 of the observed photocurrent.

APPENDIX C

5. Sr^{90} IRRADIATION

Here the NASA group[C1] placed a millicurie Sr^{90} source ¼ inch square in contact with various samples of window material. Within the wavelength band 1800 to 6300 Angstroms the radiance from the sapphire sample was 3.8×10^{-10} watts/cm^2 steradian. Sr^{90} with a ½ life of 25 years has a daughter, Y^{90}, with a ½ life of 65 hours. Thus, the Sr^{90} is in equilibrium with its daughter. The maximum β energy of the Sr^{90} is .545 MeV, that of the Y^{90} is 2.26 MeV. There is also 1.74 MeV gamma radiation at a rate of 6×10^2/sec cm^2 which will be neglected. There will be $2 \times 3.71 \times 10^7$ decay events per second, but only half of these would result in β rays through the sapphire.

In his discussion of β decay, Fermi [C10] gives for the probability that the emitted electron has momentum in p, p + dp,

$$P(p)\ dp = \text{Const.} \left(\sqrt{1 + \eta_o^2} - \sqrt{1 + \eta^2} \right)^2 \eta^2\ d\eta$$

where

$$\eta = \frac{p}{mc} = \sqrt{\frac{2E}{mc^2}} \quad ,$$

and

$$\eta_o = \frac{p_{max}}{mc} \quad .$$

The average energy carried away by a β particle will be,

$$E_{ave} = \frac{\int_0^{p_{max}} P(p)\ \frac{p^2}{2m}\ dp}{\int_0^{p_{max}} P(p)\ dp} \qquad \text{(C-25)}$$

The integral in the denominator of (C-25) is given by Fermi [C10] in terms of a function $F(\eta_o)$.

$$F(\eta_o) = -\frac{\eta_o}{4} - \frac{\eta_o^3}{12} + \frac{\eta_o^5}{30} + \frac{\sqrt{1+\eta_o^2}}{4} \sinh^{-1}\eta_o \qquad \text{(C-26)}$$

Defining,

$$E(\eta_o) = \int_0^{\eta_o} \left(\sqrt{1+\eta_o^2} - \sqrt{1+\eta^2}\right)^2 \eta^4 \, d\eta$$

$$= \frac{\eta_o}{8} + \frac{\eta_o^3}{24} - \frac{\eta_o^5}{60} + \frac{\eta_o^7}{105} - \frac{\sqrt{1+\eta_o^2}}{8} \sinh^{-1}\eta_o \,, \qquad \text{(C-27)}$$

$$E_{ave} = \frac{mc^2}{2} \frac{E(\eta_o)}{F(\eta_o)} \,. \qquad \text{(C-28)}$$

Using (C-26) to (C-28) we find

$$E_{ave}(.545 \text{ MeV}) = .087 \text{ MeV}$$

$$E_{ave}(2.26 \text{ MeV}) = .675 \text{ MeV} \,. \qquad \text{(C-29)}$$

There is a Cerenkov component in the radiance measured by the NASA group. Most of this is from the Y^{90} decay. The amount of this will first be estimated assuming a mono-energetic beam of energy given by (C-29). This is equivalent to neglecting the energy dependence of β in Equation (C-7) and the contribution of the Sr^{90}.

APPENDIX C

The Cerenkov radiation per electron will be from Equation (C-7)

$$E_c \approx 2\pi^2 e^2 \left(1 - \frac{1}{n^2}\right)\left(\frac{1}{\lambda_1^2} - \frac{1}{\lambda_2^2}\right) \ell_{ave} \qquad (C\text{-}30)$$

Below .204 MeV the Cerenkov radiation in sapphire ceases. The range of .2 MeV electrons is about .04 gms/cm^2. That of .675 MeV electrons about .250 gms/cm^2. Thus, we will use an average path length for Cerenkov radiation of .210 gm/cm^2 or (using a density of 3.5 gm/cm^3)

$$\ell_{ave} = .06 \text{ cm} \qquad (C\text{-}31)$$

Using (C-31), n = 1.796, λ_1 = 1800 Angstroms, λ_2 = 6300 Angstroms, e = 4.803 x 10^{-10} e.s.u.

$$E_c = 5.34 \times 10^{-10} \text{ erg/electron} \qquad (C\text{-}32)$$

The number of electrons emitted per square centimeter per second per steradian is,

$$n_e = \frac{3.71 \times 10^7}{\left(\frac{2.54}{4}\right)^2 \times 4\pi} = 7.32 \times 10^6/\text{cm}^2 \text{ second steradian} \qquad (C\text{-}33)$$

The product of (C-32) and (C-33) is the estimate of the amount of observed light from the sapphire due to the Cerenkov component. This is,

$$I_c = 3.91 \times 10^{-3} \text{ erg/sec cm}^2 \text{ steradian,} \qquad \text{(C-34)}$$

an amount sufficient in itself to account for the NASA observation.

Nonetheless, some of the observed light must have been due to scintillation. Let us use the electron microscope data to estimate this component. There we had that an amount of energy,

$$E_{e\nu} = \frac{\pi}{1.5} \times 10^{-19} \text{ ergs/Angstrom ev ,} \qquad \text{(C-35)}$$

was due to luminescence. Therefore, with .675 MeV electrons in the wavelength band 1800 to 6300 Angstroms we would have

$$E_e = \frac{\pi}{1.5} \times 10^{-19} \times 3.5 \times 10^3 \times .675 \times 10^6 \qquad \text{(C-36)}$$

$$= 4.95 \times 10^{-10} \text{ ergs/electron .}$$

This is almost the same as the Cerenkov component of Equation (C-32). Let us assume that the relative amounts of Cerenkov radiation and luminescence occurring in the Sr^{90} experiment are given by (C-32) and (C-36). There we had that,

$$3.71 \times 10^7/(2.54/4^2 \quad \frac{.675 \text{ MeV electrons}}{\text{cm}^2 \text{ sec}}$$

$$= 4\pi \times \frac{.675}{.675 + .087} \times \frac{.495}{4.95 + 5.34} \times 3.8 \times 10^{-3} \text{ ergs/cm}^2\text{sec .}$$

Where we use only the Y^{90} β particles in the computation, the energy radiated in luminescence is about

$$E_e = 2.21 \times 10^{-10} \text{ ergs/.675 MeV electron .}$$

The expected number of photo-events due to luminescence of the NASA photometer cathode window in the AE-2 environment would be,

$$n_{pe} = \phi \frac{\pi R^2}{2} E_e \left(\frac{E_{ave}}{.675}\right) E_q \frac{\lambda_{ave}}{hc}$$

Using R = 1.27 cm., $E_q = .2$, $\lambda_{ave} = 4050$ Angstroms, $E_{ave} = 1/1.035$ MeV, and $\phi_o = 10^8/cm^2 sec$,

$$n_{pe} \approx 3.27 \times 10^9/sec. \qquad \text{(C-37)}$$

This is within a factor of six of the observed rate.

Using the electron microscope data we came within a factor three of the observed rate, and Cerenkov radiation came within a factor eleven. Considering the crudity of the calculations, we perhaps have no right to expect better agreement. Nonetheless, none of these mechanisms has really accounted for all the observed noise. And since the belt decay was neglected, the discrepancy is even more.

It is likely that luminescence from the tube walls near the photocathode and scintillation of the tri-alkali itself are needed to fully explain all the noise, but it seems likely that fast electrons penetrating the shielding can account for most of the dark current increase observed on the OGO II main body airglow photometer.

The proton component has not been included. Shielding for MeV electrons also shields for 15 MeV protons (cf., Figure C-8). Above 15 MeV Vette's

HP 1-4 [C11] environment gives about 3 x 10^4 protons/cm^2sec at 1.3 to 1.4 Earth radii. This is orders of magnitude less than the electron density at the same place.

REFERENCES

[C1] Reed, E. I., W. B. Fowler, C. W. Atkin, and J. F. Brun, "Some Effects of MeV Electrons on the OGO II Air Glow Photometers," Goddard Space Flight Center, X-616-67-132.

[C2] Johnson, F. S., Satellite Environment Handbook, 2nd ed., Stanford University Press.

[C3] American Institute of Physics Handbook, 2nd ed., McGraw-Hill, pp. 8-43.

[C4] Heitler, W., The Quantum Theory of Radiation, 3rd ed., Oxford, pp. 246-249.

[C5] Young, A. T., Rev. Scientific Instr., 37, 11, 1472.

[C6] Wolf, C., Applied Optics, 5, 11, 1838 (October 1966).

[C7] Schliff, L. I., Quantum Mechanics, McGraw-Hill, 1949, pp. 262 ff.

[C8] Vette, J. I., A. B. Lucero, and J. A. Wright, "Models of the Trapped Radiation Environment," Vol. II, NASA-SP-3024.

[C9] Mott, N. F., and R. W. Gurney, Electronic Processes in Ionic Crystals, 2nd ed., Oxford, 1940.

[C10] Fermi, E., Nuclear Physics, rev. ed., University of Chicago Press, 1950.

[C11] Vette, Vol. I, Inner Zone.

PRECEDING PAGE BLANK NOT FILMED.

APPENDIX D

RADIATION DAMAGE TO CIRCUITRY

PAGE BLANK NOT FILMED.

1. Bulk Damage to Circuits

Damage to the semiconductor devices due to hard radiation will come about as a result of atomic displacement (bulk damage), formation of surface states, and ionization resulting in perturbation of the electronic band structure.

The common transistors and diodes are affected largely by bulk damage and this is considered first. Bulk damage occurs when a lattice atom is displaced by an incident particle into an interstitial site forming a vacancy and an interstitial atom.

For protons $\lesssim$ 100 Mev and electrons $\lesssim$ 50 Kev (non-relativistic range) the maximum energy, E_m, which can be transferred to a lattice atom by an elastic collision is,

$$E_m = \frac{4E_o Mm}{(M + m)^2} , \qquad (D\text{-}1)$$

where E_o is the energy of the incident particle, m is the mass of the incident particle, and M is the mass of the lattice atom. For Si and Ge the minimum energy to displace a lattice atom is 13 ev (electron volts)[D-1]. Thus, Equation (D-1) predicts that incident protons of 98 ev or more can cause bulk damage in Si.

If we use Equation (D-1) for electrons on Si we find E_o = .167 Mev; hence these electrons are relativistic and (D-1) does not apply. The appropriate relativistic form for electrons with the restrictions $E_o \ll Mc^2$ (usually true; for Si, Mc^2 = 26.1 Bev) is,

$$E_m = 2\frac{m}{M} E_o\left(\frac{E_o}{mc^2} + 2\right) . \qquad (D\text{-}2)$$

From Equation (D-2) an incident electron with energy of .145 Mev will just displace a Si atom, .324 Mev will just displace a Ge atom.

APPENDIX D

Both Equation (D-1) and (D-2) indicate that materials of larger atomic weights generally are less susceptible to radiation damage. However, since Si is the more common device material we shall confine ourselves to it and, consequently, need consider only electron energies above about .145 Mev.

Rosenzwieg [D-2] has discussed radiation damage in discrete Si components. The diffusion length of the minority carriers is the device parameter most easily effected by radiation. In Figure D-1 we display Rosenzwieg's data (for one ohm cm. Si) on the effect of mono-energetic electrons on the diffusion length. A flux of 10^{13} electrons per square centimeter at 1 Mev appears necessary to make an appreciable change.

The data may be fitted to the theoretical relation,

$$\frac{1}{L^2} = \frac{1}{L_o^2} + K \phi \qquad \text{(D-3)}$$

where L_o is the initial diffusion length, L is the diffusion length after irradiation with a total flux ϕ of electrons of energy E, and K is a parameter called the "damage coefficient", which depends on E and the material. More generally, K will also depend on the type of bombarding particle. Rosenzwieg asserts that p type Silicon has a damage coefficient 1/72 that for n type silicon. Thus, we consider only p on n devices.

It is to be expected that the damage will have a dependence on the energy of the incident particles. In Figures D-2 and D-3 we display the energy dependence of the damage coefficient for one ohm cm. n and p type silicon under electron and proton bombardment, respectively. It is also noted that neither n or p type material really follows the theoretical curve of displacement density variation with energy.

Following Rosenzwieg we shall use the concept of an "equivalent" amount

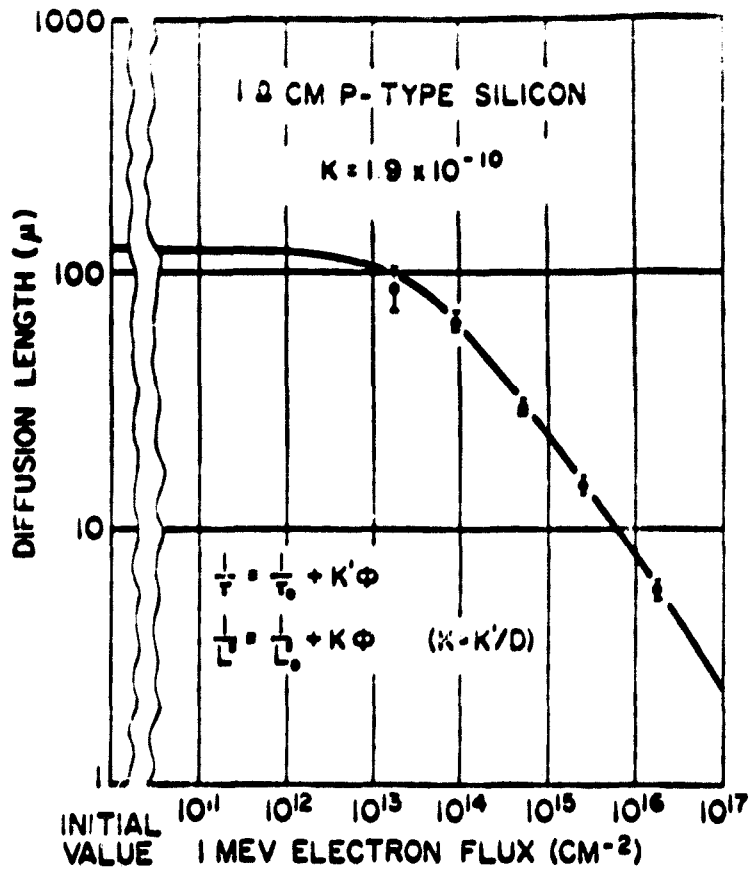


Figure D-1: Electron diffusion length.

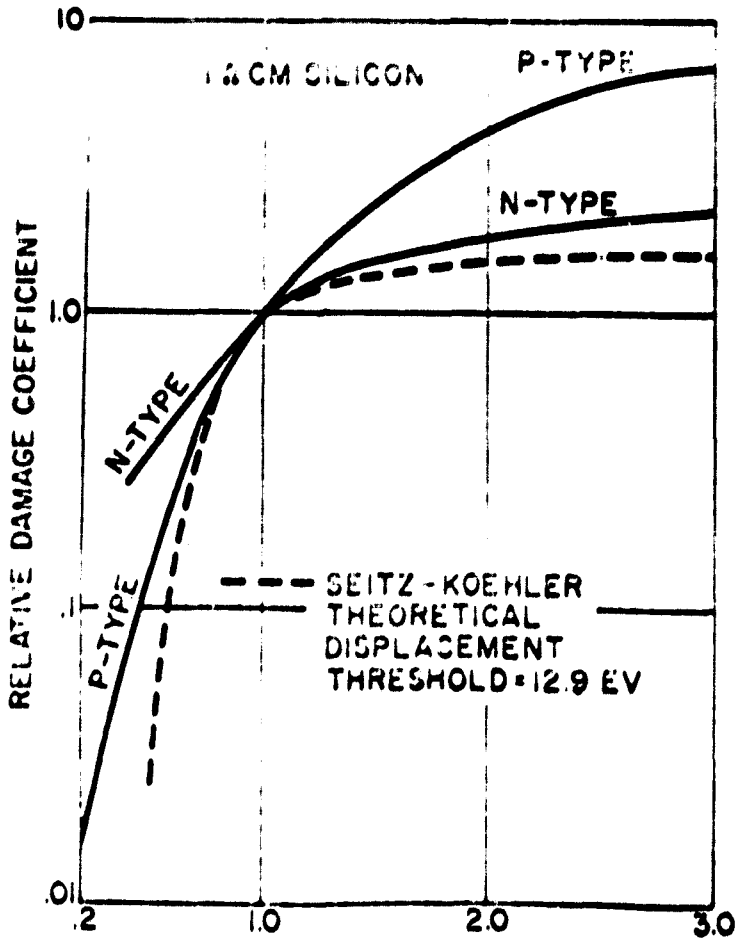


Figure D-2: Electron irradiation damage coefficient.

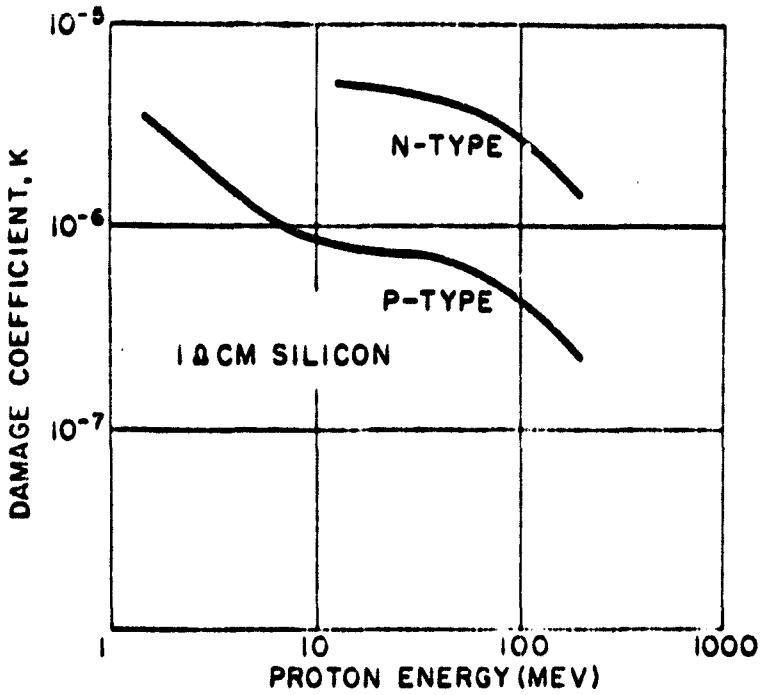


Figure D-3: Proton irradiation damage coefficient

of 1 Mev electron flux as being that flux consisting of electrons of energy E which produces the same change in diffusion length. The data of Figure D-1 gives a damage coefficient for 1 Mev electrons as 1.9×10^{-10}. At a flux of 1.9×10^{13} per square centimeter, 1 Mev electrons, the diffusion length has dropped to 80 percent of its initial value. Let this be the allowable change in diffusion length.

In the region 10 to 50 Mev (FigureD-3) the damage coefficient for protons in p type material (which we assume) is 8×10^{-7}. For an 80 percent change in diffusion length, we find using (D-3) that the allowable 10 to 50 Mev proton flux would be $\phi_p = 4.5 \times 10^{9}$ per square centimeter. However, the data of FigureD-3 is for carrier densities of 10^{10} per cubic centimeter, whereas transistors usually operate at 10^{16} to 10^{17} per cubic centimeter and so the damage coefficients are about a factor 4 to 10 times lower[D-2]. We can take the larger factor. Presumably the transistors can be selected for radiation resistance. Then the allowable 10 to 50 Mev proton flux would be

$$\phi_p = 4.5 \times 10^{10}/cm^2. \qquad \text{(D-4)}$$

FigureD-2 shows the damage coefficient for electron bombardment of p type silicon as increasing by about a factor 7 in the range 1 to 3 Mev. At 3 Mev the curve has fairly well leveled off. Though the data cuts off at 3 Mev we will assume that it is flat thereafter and take as a damage coefficient for an electron energy of 3 Mev and greater.

$$K = 1.26 \times 10^{-9}$$

Thus, using the 80 percent criteria for deterioration of diffusion length the allowable dose of 3 Mev and greater energy electrons is,

$$\phi_e = 3.2 \times 10^{12}/cm^2. \qquad \text{(D-5)}$$

2. Damage to Metal-Oxide-Semiconductor (MOS) Devices

MOS integrated circuits with their associated size and power consumption advantages are attractive for space applications. Unfortunately, the common MOS devices are also an order of magnitude more susceptible to radiation effects usually ascribed to ionization and surface effects [D-3]. MNS devices have higher damage thresholds but are not readily available.

Gordon and Wannemaker [D-4] have studied the effect of Co^{60}_{γ} radiation 2 Mev electrons and 22 Mev protons on MOS FET devices. They irradiated these devices with 2 Mev electrons and 22 Mev protons with various gate biases and measured the change in gate threshold voltage as a function of total dose. Figures D-4 and D-5 are a composite of their results.

In interpreting these results we shall assume, as do Gordon and Wannemacker, that the effects do not depend on the energy of the incident radiation and that a 30 percent change in the gate threshold voltage is allowed. If one-half of the change is allotted to electrons and one-half to protons the allowable electron flux is,

$$\phi_e = 2 \times 10^{11}/cm^2 \qquad (D\text{-}6)$$

and that due to protons is,

$$\phi_p = 4.3 \times 10^{10}/cm^2. \qquad (D\text{-}7)$$

We must shield for 4.7 Mev electrons and 45 Mev protons. We summarize the derived allowable fluxes for both discrete p type silicon devices and MOS FET in Table D-I.

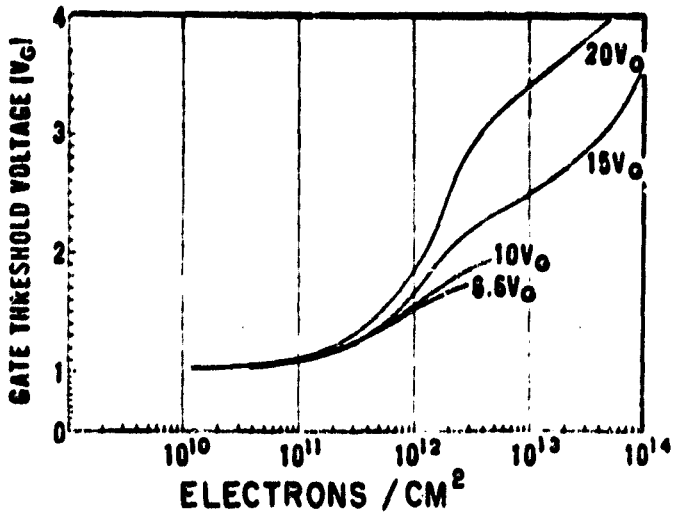


Figure D-4: Typical normalized gate threshold voltage versus electron dose with gate bias during exposure as a parameter.

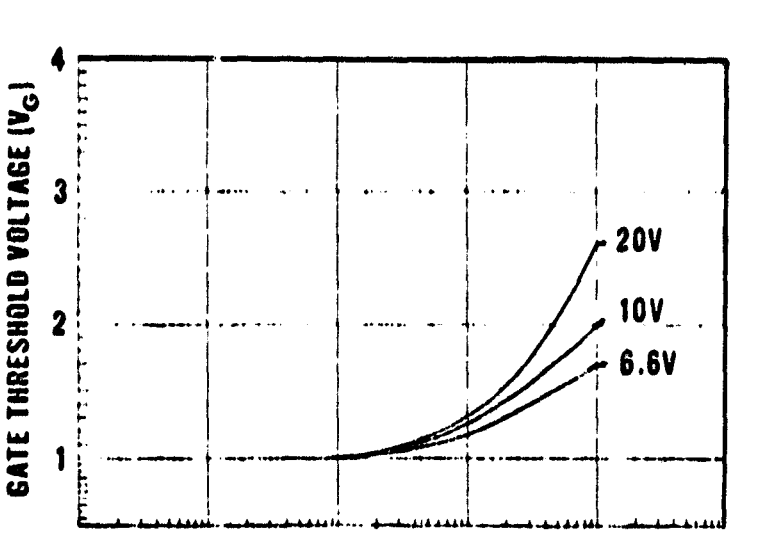


Figure D-5: Typical normalized gate threshold voltage versus proton dose.

TABLE D-I

	p type Si	MOS FET
Electron flux	3.2×10^{12}	2×10^{11}
Proton flux	4.5×10^{10}	4.3×10^{10}

Total Allowable Flux
Discrete and Integrated Circuits,
Units of cm^{-2}

APPENDIX D

REFERENCES

[D-1] Corbelt, J. W., "Electron Radiation Damage in Semiconductors and Metals," Solid State Physics Series, Academic Press (1966).

[D-2] Rosenzwieg, W., "Space Radiation Effects in Silicon Devices," IEEE Trans. Nuclear Science, NS-12, No. 5 18 (October 1965).

[D-3] Hamman, D. J., "Space Radiation Effects in Integrated Circuits," IEEE Trans. Nuclear Science, NS-13, No. 6 160(December 1966).

[D-4] Gordon, F., Jr. and H. E. Wannemacker, Jr., "The Effects of Space Radiation on MOS FET Devices and Some Application Implications of Those Effects," IEEE Trans. Nuclear Science, NS-13, No. 6 262 (December 1966).